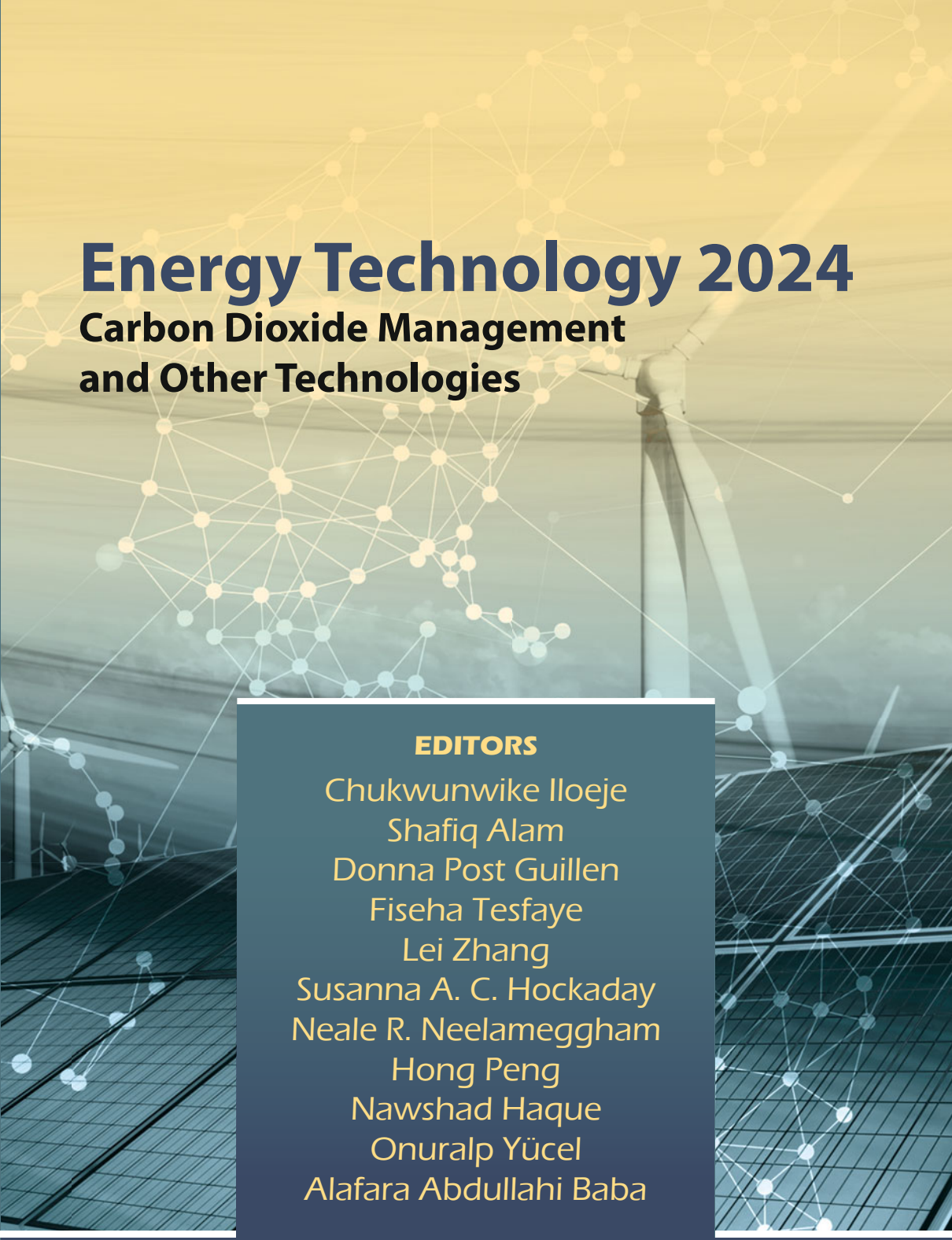

Energy Technology 2024

Carbon Dioxide Management and Other Technologies

EDITORS

Chukwunwike Iloeje
Shafiq Alam
Donna Post Guillen
Fiseha Tesfaye
Lei Zhang
Susanna A. C. Hockaday
Neale R. Neelameggham
Hong Peng
Nawshad Haque
Onuralp Yücel
Alafara Abdullahi Baba

TMS

Springer

The Minerals, Metals & Materials Series

Chukwunwike Iloeje · Shafiq Alam ·
Donna Post Guillen · Fiseha Tesfaye · Lei Zhang ·
Susanna A. C. Hockaday ·
Neale R. Neelameggham · Hong Peng ·
Nawshad Haque · Onuralp Yücel ·
Alafara Abdullahi Baba
Editors

Energy Technology 2024

Carbon Dioxide Management and Other Technologies

TMS

Springer

Editors
Chukwunwike Iloeje
Argonne National Laboratory
Lamont, IL, USA

Donna Post Guillen
Idaho National Laboratory
Idaho Falls, ID, USA

Lei Zhang
University of Alaska Fairbanks
Fairbanks, AK, USA

Neale R. Neelameggham
IND LLC
South Jordan, UT, USA

Nawshad Haque
Commonwealth Scientific and Industrial
Research Organisation (CSIRO)
Clayton, VIC, Australia

Alafara Abdullahi Baba
University of Ilorin
Ilorin, Nigeria

Shafiq Alam
University of Saskatchewan
Saskatoon, SK, Canada

Fiseha Tesfaye
Metso Outotec Metals Oy
Espoo, Finland

Susanna A. C. Hockaday
Curtain University
Perth, WA, Australia

Hong Peng
University of Queensland
Brisbane, QLD, Australia

Onuralp Yücel
Istanbul Technical University
İstanbul, Turkey

ISSN 2367-1181 ISSN 2367-1696 (electronic)
The Minerals, Metals & Materials Series
ISBN 978-3-031-50243-9 ISBN 978-3-031-50244-6 (eBook)
https://doi.org/10.1007/978-3-031-50244-6

© The Minerals, Metals & Materials Society 2024

This work is subject to copyright. All rights are solely and exclusively licensed by the Publisher, whether the whole or part of the material is concerned, specifically the rights of translation, reprinting, reuse of illustrations, recitation, broadcasting, reproduction on microfilms or in any other physical way, and transmission or information storage and retrieval, electronic adaptation, computer software, or by similar or dissimilar methodology now known or hereafter developed.
The use of general descriptive names, registered names, trademarks, service marks, etc. in this publication does not imply, even in the absence of a specific statement, that such names are exempt from the relevant protective laws and regulations and therefore free for general use.
The publisher, the authors, and the editors are safe to assume that the advice and information in this book are believed to be true and accurate at the date of publication. Neither the publisher nor the authors or the editors give a warranty, expressed or implied, with respect to the material contained herein or for any errors or omissions that may have been made. The publisher remains neutral with regard to jurisdictional claims in published maps and institutional affiliations.

This Springer imprint is published by the registered company Springer Nature Switzerland AG
The registered company address is: Gewerbestrasse 11, 6330 Cham, Switzerland

Paper in this product is recyclable.

Preface

It is with great pleasure that we present the peer-reviewed proceedings of the Energy Technology 2024: Carbon Dioxide Management and Other Technologies symposium organized in conjunction with the TMS 2024 Annual Meeting & Exhibition in Orlando, Florida, USA. This symposium was organized by the TMS Energy Committee which is part of the TMS Extraction & Processing Division and Light Metals Division, and co-sponsored by the TMS Recycling and Environmental Technologies Committee.

The increasing global mean surface temperature could have drastic, long-term, and irreversible impacts on our natural world, and affect sustainable economic development and public welfare. Limiting this warming to the 1.5°C target from the Paris Agreement would require developing and integrating clean energy and carbon management technologies to reduce greenhouse gas (GHG) emissions and decarbonize the energy and metal industries by 2050. With this goal in mind, the symposium invited submissions from participants from academia, industry, and government sectors to provide focused discussions on industrial energy sustainability and CO_2 management, covering technology areas such as clean energy technologies, innovative beneficiation, smelting technologies, process intensification, as well as CO_2 capture and conversion for industrial applications.

This proceedings volume presents outcomes from the incredible effort by all the authors and their respective organizations in conducting their research and preparing the manuscripts published in this book on energy technologies and CO_2 management. The research presented includes novel technology development, reports on innovative process improvements, system-level techno-economic and life cycle assessments, and broader policy discussions on methods and approaches for reducing industrial carbon dioxide and other greenhouse gas emissions. It is our hope that this proceedings volume of the record of the Energy Technology 2024: Carbon Dioxide Management and Other Technologies symposium will provide valuable content for scientists, engineers, and other stakeholders interested in innovative energy technologies, novel energy materials processing, and carbon management techniques.

The production of the proceedings volume was a major undertaking, and we are grateful to the several individuals and committee members who dedicated time over

the course of several months to design the symposium content, review manuscripts, and chair the symposium sessions. We would also like to thank the authors and invited speakers for their contributions and acknowledge the invaluable support from the TMS staff members in the production of this proceedings volume.

Chukwunwike Iloeje, Ph.D.
Lead Organizer

Energy Technology 2024 Carbon Dioxide Management and Other Technologies Editors

Chukwunwike Iloeje, Argonne National Laboratory, USA
Shafiq Alam, University of Saskatchewan, Canada
Donna Post Guillen, Idaho National Laboratory, USA
Fiseha Tesfaye, Metso Outotec Metals Oy, Åbo Akademi University, Finland
Lei Zhang, University of Alaska Fairbanks, USA
Susanna A. C. Hockaday, Curtin University, Australia
Neale R. Neelameggham, IND LLC, USA
Hong (Marco) Peng, University of Queensland, Australia
Nawshad Haque, Commonwealth Scientific and Industrial Research Organization, Australia
Onuralp Yücel, Istanbul Technical University, Turkey
Alafara Abdullahi Baba, University of Ilorin, Nigeria

Contents

Part V Poster Session

About the Editors

Chukwunwike Iloeje is a Principal Scientist in the Energy Systems and Infrastructure Analysis Division at Argonne National Laboratory (ANL), a CASE Scientist at the Pritzker School of Molecular Engineering at the University of Chicago, and the Strategic Analysis team Co-lead at ANL.

In his research, Dr. Iloeje uses computational modeling to explore questions at the intersection of sustainable energy conversion, manufacturing, and material transformations, with particular interest in critical materials separations and supply chain optimization, as well as carbon capture and conversion to high-value chemicals.

Dr. Iloeje has a bachelor's degree in mechanical engineering from the University of Nigeria, and an MSc and Ph.D. in Mechanical Engineering from Massachusetts Institute of Technology.

Shafiq Alam is an Associate Professor at the University of Saskatchewan, Canada. He is an expert in the area of mining and mineral processing with profound experience in industrial operations, management, engineering, design, consulting, teaching, research, and professional services. As a productive researcher, Dr. Alam has secured 2 patents and has produced over 185 publications. He is the lead/co-editor of 15 books and an editorial board member of two mining and mineral processing journals named *Minerals* (an Open Access journal by MDPI) and *The International Journal of Mining, Materials and Metallurgical Engineering*. He is the winner of the 2015 Technology Award from

the Extraction & Processing Division of The Minerals, Metals & Materials Society (TMS), USA.

With extensive relevant industry experience as a registered professional engineer, Dr. Alam has worked on projects with many different mining industries. He is an Executive Committee Member of the Hydrometallurgy Section of the Canadian Institute of Mining, Metallurgy and Petroleum (CIM) where he held the Office of Secretary. During 2015–2017, he served as the Chair of the Hydrometallurgy and Electrometallurgy Committee of the Extraction & Processing Division (EPD) of TMS. Currently, he is the Secretary of the Recycling and Environmental Technologies Committee of TMS and is serving on the TMS-EPD Awards Committee. He is a lead/co-organizer of at least 19 Symposia at the International Conferences through CIM and TMS. Dr. Alam is one of the founding organizers of the Rare Metal Extraction & Processing Symposium at TMS and since 2014, he has been involved in organizing this symposium every year with great success. In the past, he was involved in organizing the International Nickel-Cobalt 2013 Symposium and TMS 2017 Honorary Symposium on Applications of Process Engineering Principles in Materials Processing, Energy and Environmental Technologies. Dr. Alam was also a co-organizer of the 9^{th} and 10^{th} International Symposia on Lead and Zinc Processing (PbZn 2020, PbZn 2023) held in California and China, respectively. He co-organized the Pressure Hydrometallurgy Symposium at the Conference of Metallurgists (COM 2023) organized by CIM, which was held in Toronto, Canada. In 2022, he was involved in co-organizing the 2022 Energy Technologies and CO_2 Management Symposium while in 2023 he was the lead-organizer of Rare Metal Technology Symposium. In addition to co-organizing the current 2024 Energy Technologies and CO_2 Management Symposium, Dr. Alam is also co-organizing the 2024 Rare Metal Extraction and Processing Symposium co-located with the TMS 2024 Annual Meeting and Exhibition in Orlando, Florida.

Donna Post Guillen is the Group Lead for Modeling and Simulation in the Materials Science and Engineering Department at the Idaho National Laboratory. Dr. Guillen has over 35 years of research engineering experience and has served as principal investigator/technical lead for numerous multidisciplinary projects encompassing waste heat recovery, combustion, heat exchangers, power conversion systems, nuclear reactor fuels and materials experiments, waste vitrification, and advanced manufacturing. Her core area of expertise is computational modeling of energy systems, materials, and thermal fluid systems. She is experienced with X-ray and neutron beamline experiments, computational methods, tools and software for data analysis, visualization, application development, machine learning and informatics, numerical simulation, and design optimization. As Principal Investigator/Technical Lead for the DOE Nuclear Science User Facility Program, she has engaged in irradiation testing of new materials and performed thermal analysis for nuclear reactor experiments. She actively mentors students, serves in a leadership capacity as well as routinely chairs and organizes technical meetings for professional societies, provides subject matter reviews for proposals and technical manuscripts, has published over 100 papers and received three Best Paper awards, authored numerous technical reports and journal articles, and has written/edited several books.

Fiseha Tesfaye is a Process Metallurgist at Metso Corporation and Adjunct Professor of metallurgical thermodynamics at Åbo Akademi University, Finland. He received his M.Sc. degree in materials processing technology and Ph.D. degree in metallurgy from Aalto University. With expertise in metallurgy, Dr. Tesfaye's research activities are focused mainly on the thermodynamic characterization of inorganic materials as well as rigorous theoretical and experimental investigations that promote sustainable production of metals and renewable energy. In 2018, Dr. Tesfaye was also appointed as a visiting research scientist in Seoul National University, South Korea. Dr. Tesfaye is an active member of The Minerals, Metals & Materials Society (TMS), and is a winner of the 2018 TMS Young Leaders Professional Development Award. He is currently the Vice

Chair of the TMS Energy committee and serves as a subject editor for different journals including *JOM*, the member journal of TMS, and *Processes*, MDPI. Furthermore, he has co-edited many scientific research books and proceedings. His personal research achievements include remarkable improvement of experimental research applying the solid-state EMF technique for thermodynamic investigations of inorganic materials, as well as a noticeable contribution to realize the transition toward the circular economy. In his research areas, Dr. Tesfaye has disseminated over 100 publications.

Lei Zhang is an Associate Professor in the Department of Mechanical Engineering at the University of Alaska Fairbanks (UAF). Prior to joining UAF, she worked as a postdoctoral associate in the Department of Chemical and Biomolecular Engineering at the University of Pennsylvania. Dr. Zhang obtained her Ph.D. in Materials Science and Engineering from Michigan Technological University, and her M.S. and B.E. in Materials Science and Engineering from China University of Mining and Technology, Beijing, China. Her current research mainly focuses on the synthesis of nanomaterials and the manipulation of their properties and applications in gas storage, separation, energy storage, and water treatment. She is also working on the development and characterization of anti-corrosion coatings on metallic alloys for aerospace and biomedical applications. Dr. Zhang has served on the TMS Energy Committee since 2014, including the Vice-Chair role in 2018–2020 and the Chair role in 2020–2022. She also served on the Best Paper Award Subcommittee of the committee. She has served as a frequent organizer and session chair of TMS Annual Meeting symposia (2015– present). She was the recipient of the 2015 TMS Young Leaders Professional Development Award.

Susanna A. C. Hockaday has 18 years of pyrometallurgical research experience in the non-ferrous industry. She joined Mintek in 2002 after obtaining her B. Chem. Eng. (Minerals Processing) and M.Sc. in Extractive Metallurgy at the University of Stellenbosch in South Africa. During 2002 to 2010 she worked in the commercial projects group on various projects including the recovery of precious metals in liquid iron and the smelting of ores to produce design specifications of an industrial ferrochrome DC arc furnace. From 2011 to late 2015 she took a break from work and had two delightful children, now aged 13 and 10. From 2015 till 2021, she has been involved in research of new technologies for titanium metal production, chlorination of titanium dioxides in a fluidized bed, and the applications of concentrating solar energy in mineral processing. In 2023 she obtained her Ph.D. Mech Eng with the thesis entitled "Solar Thermal Treatment of Manganese Ores". She acted as a work package leader responsible for €2 million of research toward advancement of solar thermal process heating technology in manganese ferroalloy production for the PRÉMA project funded by the European Union's Horizon 2020 Research and Innovation Programme under Grant Agreement No 820561 and is part of the SPIRE group of projects. Dr. Hockaday was the coordinator and the main author for Mintek's Roadmap for Solar Thermal Applications in Minerals Processing (STAMP). Dr. Hockaday is a member of the South African Institute of Mining and Metallurgy (SAIMM). She was also head of the organizing committee for the SAIMM Colloquium on Renewable Energy Solutions for Energy Intensive Industry in 2020 and the Renewable Energy Solutions for Energy Intensive Industry Conference in 2021. Dr. Hockaday resigned from Mintek in June 2021 to move with her family to Perth, Australia. Since Oct 2022 she has been employed at Curtin University as a senior engineer and postdoctoral research fellow executing two HILT CRC projects involving the low-carbon upgrading of iron ores.

Neale R. Neelameggham, IND LLC, is involved in international technology and management licensing for metals and chemicals, thiometallurgy, energy technologies, Agricoal, lithium-ion battery, energy efficient low cost OrangeH2, Netzero sooner with Maroon gas and Pink hydrogen, rare earth oxides, etc. He has more than 38 years of expertise in magnesium production and was involved in the process development of its startup company NL Magnesium to the present US Magnesium LLC, UT when he was instrumental in process development from the solar ponds to magnesium metal foundry. His expertise includes competitive magnesium processes worldwide. In 2016, Dr. Neelameggham and Brian Davis authored the ICE-JNME award winning paper "Twenty-First Century Global Anthropogenic Warming Convective Model." He is working on Agricoal® to greening arid soils, and at present energy efficient Orange hydrogen, and turbine generator electric car with hydrocarbons and steam. He authored *The Return of ManmadeCO2 to Earth: Ecochemistry*. Dr. Neelameggham holds 16 patents and applications and has published several technical papers. He has served in the Magnesium Committee of the TMS Light Metals Division (LMD) since its inception in 2000, chaired in 2005, and since 2007 has been a permanent advisor for the Magnesium Technology Symposium. He has been a member of the Reactive Metals Committee, Recycling Committee, Titanium Committee, and Program Committee for LMD and LMD council. Dr. Neelameggham was the Inaugural Chair, when in 2008, LMD and the TMS Extraction and Processing Division (EPD) created the Energy Committee and has been a Co-Editor of the Energy Technology Symposium through the present. He received the LMD Distinguished Service Award in 2010. As Chair of the Hydrometallurgy and Electrometallurgy Committee, he initiated the Rare Metal Technology Symposium in 2014 and has been a co-organizer to the present. He organized the 2018 TMS Symposium on Stored Renewable Energy in Coal and initiated Light Elements Technology in 2023.

Hong Peng is currently an Amplify Senior Lecturer at the School of Chemical Engineering, University of Queensland (UQ). He gained his Ph.D. degree in Chemical Engineering at UQ with the OZ Minerals Award for Excellent Thesis (2014). Dr. Peng has industry experience as a chemical engineer from the Olympic Dam site and Newcastle Technology Centre, BHP Billiton (2006-2009). He was the recipient of the 2020 TMS Young Leaders Professional Development Award. Dr. Peng's research focuses on the fundamental aspects of mineral processing, interfacial colloid science, crystal kinetics, and precipitation as well as molecular dynamics simulation. These projects are of interest to nanobubbles, mine tailings, zeolite, clay minerals, and metal resource recovery.

Nawshad Haque is a Principal Research Scientist at the Commonwealth Scientific and Industrial Research Organisation (CSIRO) Australia and leads the Technoeconomics for Decarbonisation Team in the Energy Technologies Program. He manages a team of around 3 researchers, 2 post-docs, and 8 Ph.D. students. The Team is evaluating electrolyzers and other associated technologies for hydrogen energy systems. Dr. Haque has over 21 years of R&D experience since having a Ph.D. in Chemical Engineering from the University of Sydney. He has played a key role in the development of CSIRO's technology evaluation capabilities including flowsheeting, technoeconomic and life cycle assessment methodologies using various databases, tools, and software to aid in decision. In his current role, Dr. Haque has initiated several large international multiparty collaborative research relationships with governments and industries leading to the establishment of multi-million-dollar projects related to various technologies for science capacity development. Dr. Haque is the Leader for the CSIRO BCSIR Bangladesh and RMIT University long-term collaboration program for scientific research capability development in Bangladesh.

Dr. Haque leads India-Australia Minerals Scholar Network on Critical Minerals and Green Steel research to develop talents which was announced as part of the joint Prime Minister's statements of both nations. Dr. Haque has co-authored more than 100 publications attracting numerous citations. Dr. Haque is currently an

elected Fellow of the Australian Institute of Energy, Australasian Institute of Mining and Metallurgy, and a member of TMS. He has assisted several journals including *Minerals*, *Journal of Cleaner Production, Drying Technology*, and is a regular reviewer of *International Journal of Hydrogen Energy*. He has served as a Director of the Board of Australian Life Cycle Assessment Society for 10 years. Dr. Haque has co-supervised CSIRO sponsored 15 Ph.D. students and over 56 vacation scholarship projects to completion, many on technoeconomic and life cycle assessment. He is an adjunct academic at Swinburne University, Monash University, and RMIT University in Australia.

Onuralp Yücel completed his technical education with a Ph.D. in Metallurgical Engineering from Istanbul Technical University (ITU) where he has held the post of Professor since 2002. He was a Visiting Scientist at Berlin Technical University between 1987 and 1988. He carried out postdoctoral studies at the New Mexico Institute of Mining and Technology, Socorro, USA between 1993 and 1994. Prof. Yücel has as many as 400 publications/ presentations to his credit, which include topics like technological developments in the production of a wide range of metals, ferroalloys, advanced ceramic powders, and application of carbothermic and metallothermic processes, among others. He was the vice chairman of ITU, Metallurgical and Materials Engineering Department (MMED) between 2004 and 2007. He has been a director of ITU, Applied Research Center of Material Science & Production Technologies between 2006 and 2012. He was the chairman of ITU, MMED between 2016 and 2018.

Prof. Yücel is a member of the international advisory board of the International Symposium on Boron, Borides and Related Materials (ISBB), International Symposium on High-Temperature Metallurgical Processing organized by TMS, International Symposium on Self Propagating High-Temperature Synthesis (SHS), and International Metallurgy and Materials Congress (IMMC). Dr. Yücel's areas of interest include: *Pyrometallurgy*: Pretreatment of concentrates (production of WO3, Sb2 O3, As2 O3, MoO3, ZnO), smelting and reduction of slags, production ferroalloys, alloys and metals carbothermic and metallothermic processes

(SHS) in EAF or in ladle (Mg, Ca, Sr, Cu, Co, V, Cr, W, Zn, ferroboron, cobaltboron, nickelboron, ferronickel, nickel pig iron, ferrotungsten, ferromolybdenum, ferromanganese, silicomanganese, ferrovanadium, ferrochromium, iron-nickel-chromium- molybdenum, and aluminum-titanium-boron alloys); *Ceramic Powder Production and Processing*: Production of carbide, nitride, boride powders and their processing by explosive consolidation or sintering techniques (B4C, TiB2, ZrB2, SiC, CrB2,); and *Beneficiation of Industrial Wastes*: Production of metals and compounds from aluminum dross, steel scale and EAF dust, Waelz slag, galvanizing ash, brass production wastes, and vanadium sludge produced aluminum production, and grit production from aluminum, copper, and steel slags.

Alafara Abdullahi Baba is Professor of Analytical/ Industrial and Materials Chemistry and Dean, Faculty of Physical Sciences, University of Ilorin, Nigeria. He holds a Ph.D. in Chemistry from the University of Ilorin (2008). His dissertation entitled "Recovery of Zinc and Lead from Sphalerite, Galena and Waste Materials by Hydrometallurgical Treatments" was judged the best in the area of Physical Sciences at the University of Ilorin, Nigeria in 2009. In addition, he was a Ph.D. project supervisor of the Best Postgraduate Student of the University of Ilorin in the 2021/2022 academic session. His area of research covers analytical, industrial, and materials chemistry in general with special interests in solid minerals and materials processing through hydrometallurgical routes; reactions in solution for metallurgical applications; preparation of phyllosilicates, porous, and bio-ceramic materials; ore beneficiation including indigenous barite processing for oil and gas applications with developing eco-friendly-cum-low energy synthetic routes for industrial, technological utilities, among others. Professor Alafara has been cited in many internationally acclaimed journals of high impact. As an academically inclined scholar with many distinct awards, several of his research breakthroughs of more than 150 publications have been presented at both national and international conferences and workshops for wider recognition. His University of Ilorin 198th Inaugural Lecture (2021) titled "Sustainable National Development: Mineral and Material Resources to the

Rescue" affirmed the use of locally sourced minerals for industries, a condition for countries to save significant foreign earnings.

Professor Alafara has occupied various positions as a chairperson, secretary, and member of relevant academic and professional committees. He was Head, Department of Industrial Chemistry of the University of Ilorin between 2017–2020; Deputy Director, Central Research Laboratories (2014–2017); University of Ilorin Senate Representative for the Students' Disciplinary Committee (2019–2021); Secretary, Hydrometallurgy and Electrometallurgy Committee of the Extraction & Processing Division (2018–2021); Co-organizer of the Rare Metal Extraction & Processing Symposium and Lead Organizer, Energy Technologies & Carbon Dioxide Management Symposium (2021); Materials Characterization - Education Committee; EPD and Best Awards Committee Representative; appointed EPD Council Education Representative (2021–Date), and Subject Editor for *JOM* (TMS, 2023–Date). He is also the current National President of the Materials Science and Technology Society of Nigeria and a Fellow of many professional societies including the Chemical Society of Nigeria and the Materials Science and Technology Society of Nigeria. He has supervised and is still supervising many undergraduate and postgraduate research works and is currently serving as an External Examiner to Postgraduate researchers in universities within and outside Nigeria.

Part I
Decarbonizing Materials Processing

Research and Development on Low Carbon Technologies of Modern Blast Furnace Ironmaking

Fuming Zhang, Xiangfeng Cheng, Yanbo Chen, and Zhizheng Wang

Abstract Under the modern blast furnace process conditions, replace the coke or pulverized coal by hydrogen; improve the efficiency of hydrogen reduction in the blast furnace; realize carbon-hydrogen coupling reduction in different process section and temperature range; give full play to the advantages of carbon direct reduction, CO indirect reduction, and H_2 reduction in heat transfer, mass transfer, momentum transmission, and metallurgical reaction engineering, through process development and operation optimization; reduce carbon fuel consumption and blast furnace fuel ratio to below 460 kg/t; and realize rich hydrogenation and low carbonization of blast furnace iron making process. The changes of theoretical combustion temperature of tuyere raceway and bosh gas volume of the blast furnace are researched. The reduction thermodynamic parameters of different temperature range and zone of blast furnace are calculated. The process measures of improving hydrogen utilization ratio and hydrogen carbon replacement ratio in the operation of blast furnace are discussed.

Keywords Blast furnace · Ironmaking · Low carbon · Hydrogen metallurgy · High pellet ratio · Fuel ratio

Introduction

Developing Status of China's Steel Industry

The carbon emissions of China's steel industry account for approximately 15% of the total carbon emissions, which is the highest carbon emissions in the manufacturing industry. Facing the increasingly severe situation of ecological environment protection, the steel industry is facing great pressure of carbon emission reduction, an urgent need to develop can significantly reduce CO_2 emissions breakthrough low carbon

F. Zhang (✉) · X. Cheng · Y. Chen · Z. Wang
Shougang Group Co. Ltd., Shijingshan Road No.60, Beijing, China
e-mail: zhangfuming2018@163.com

© The Minerals, Metals & Materials Society 2024

C. Iloeje et al. (eds.), *Energy Technology 2024*, The Minerals, Metals & Materials Series, https://doi.org/10.1007/978-3-031-50244-6_1

metallurgy technology, to meet the "carbon peak" and "carbon neutrality" development strategy requirements [1]. In 2022, the China's crude steel output reached 1.013 billion tons (the global crude production was 1.878 billion tons accounting for 54%), and the carbon emission will account for more than 50% of the total global steel industry carbon emissions. Figure 1 shows the changes in hot metal and crude steel production of China in recent years; Fig. 2 shows the changes in crude steel production and CO_2 emissions of China in recent years.

At present, the steel manufacturing process in China is still dominated by blast furnace-converter (BF-BOF) process. In 2022, the output of hot metal reached 864 million tons, accounting for 65.46% of the world, and the ratio of crude steel produced by BOF accounted for around 90%. Currently, China's steel manufacturing process and energy structure show "high carbonization", and the energy consumption of fossil carbon such as coal and coke accounts for nearly 90% of the total energy. Reducing carbon consumption and reducing CO_2 emissions based on BF process

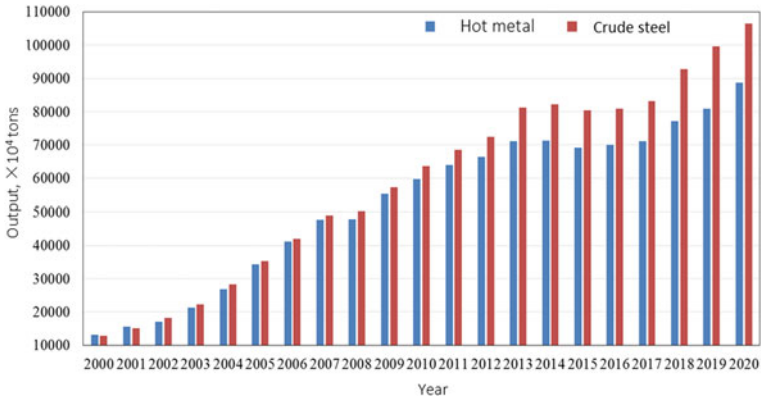

Fig. 1 Changes in hot metal and crude steel production of China in recent years

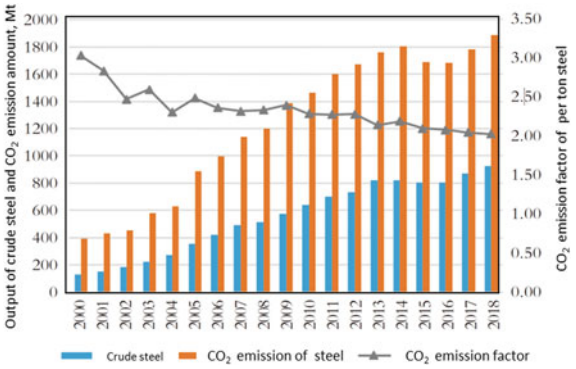

Fig. 2 Changes in crude steel production and CO_2 emissions of China in recent years

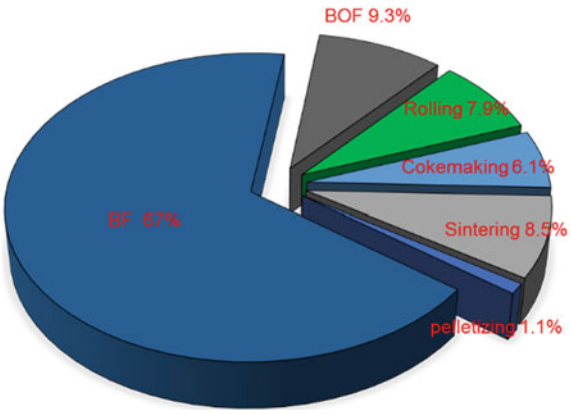

Fig. 3 Carbon emissions of BF + BOF steel manufacturing process

has become an important research topic and development direction of China's steel industry in the future.

CO_2 Emission in Steel Manufacturing

Blast furnace (BF) and cokemaking, sintering, and pelletizing processes are the key and core process section in the whole iron and steel manufacturing. BF ironmaking is a traditional metallurgical process based on carbon reduction, and the ironmaking process is the main source of CO_2 emissions in the steel industry. In the whole process of BF-BOF, the carbon emissions of the ironmaking system account for 82.79% of the total emissions of the full process, the BF accounts for 67%. The recent carbon emission reduction target is mainly focused on the energy saving and emission reduction of coking, sintering, and BF ironmaking, especially the carbon emission reduction of BF ironmaking process. Figure 3 shows the carbon emissions of BF-BOF steel manufacturing process.

Current Situation of BF Ironmaking Technology in China

According to incomplete statistics, there are about 1200 BFs in China in 2021, the average BF inner volume approximate 1400 m^3, and the total production capacity of BF ironmaking is about 1.2 billion tons per year (The parameters are given in Table 1). There are 9 huge BFs with the inner volume over 5000 m^3 in operation, ranking second in the world (32 sets 5000 m^3 BF in operation all over the world, including 12 in Japan, ranking first in the world). There are 17 sets 4000 m^3 class of BF in operation, that is, first rank in the world. In general, the main force of BF ironmaking in China is still small and medium-sized BFs of 450–1200 m^3, with the

capacity accounting for about 50% of the national ironmaking capacity [2]. There is great space for structural adjustment, process upgrading, and equipment progress. In the future, China will continue the steel industrial structure adjusting, the high-quality industrial development and equipment modernization are expected. Table 2 shows the main technical parameters of China's BF. Figure 4 shows the changes in the main technical parameters of BFs of China in recent years.

In recent years, the technical and economic indices of BF in China have been continuously improved and made steady progress:

- The BF average productivity is stable at above 2.6 t/(m^3·d), ranking in the international leading level.
- The BF fuel ratio enters the platform stage, the coke rate and PCI rate do not change much, and the carbon consumption does not decrease much, so there is still space for carbon reduction.
- The hot blast temperature is stagnated between 1100 and 1150 °C, which is far from the international advanced level (with a difference of about 100 °C).
- The energy consumption of the BF ironmaking process changes smoothly, decreasing to 387.9 kgce/t.H.M (standard coal, approximately 11.37 GJ/t.H.M)

Table 1 Distribution and capacity of BFs in China (estimate)

Volume/ m^3	≥ 5000	4000–5000	3000–4000	3000–2000	2000–1200	1200–450	≤ 450
Quantity/ sets	9	17	23	76	135	452	213
Capacity/ (Mt a^{-1})	34	79.60	126.60	151.72	172.27	364.33	112.40

Table 2 Main technical parameters of China's blast furnace

Item	2022	2021	2020	2019	2018	2017	2016	2015
Productivity/(t·m^3·d^{-1})	2.67	2.64	2.63	2.59	2.58	2.51	2.48	2.46
Fuel ratio/ kg·t^{-1}	527	531	529	528	536	544	543	526
Coke rate/kg·t^{-1}	347	355	355	356	372	363	363	358
PCI rate/kg·t^{-1}	151	147	148	145	139	148	140	142
Hot blast temperature/ °C	1149	1100	1115	1147	1140	1142	1139	1134
TFe of burden/%	57.54	56.60	57.73	57.85	57.4	57.3	57.0	57.0
Agglomeration ratio/%	81.05	89.67	91.78	84.7	89.9	89.1	84.9	89.3
Stopped blast ratio/%	2.75	2.68	1.92	2.15	1.86	1.93	2.57	2.27
Productivity of labour/t (person a)$^{-1}$	8771.4	8549.1	8366.7	8518.7	7263.9	7227.2	6998.1	6093.8
Energy consumption of BF/kgce·t^{-1}	387.9	387.9	385.2	388.5	392.1	390.8	390.6	387.3

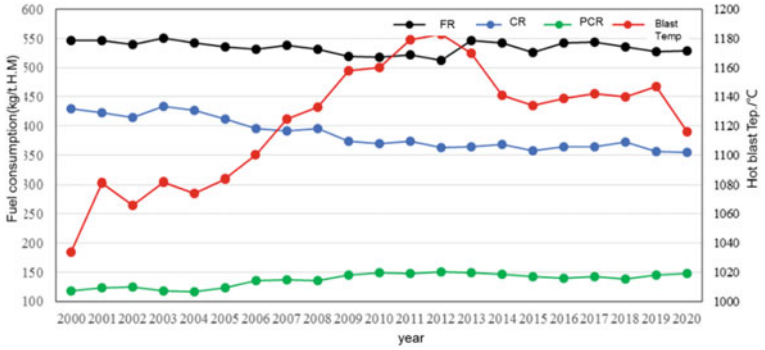

Fig. 4 Changes in the main technical parameters of BFs of China in recent years

in 2022. The government proposed extreme energy consumption standard of BF process is 361 kg/t.H.M (10.58 GJ/t.H.M), which still has some difference for reduce.

- The labor productivity increased greatly, reaching more than 8500 t.H.M/(person year).

Development Status of BF Ironmaking Technology

Technical Concept of BF Ironmaking

- Modern BF technology progress and operation optimization, the main technical indicators have been close to the theoretical carbon consumption, the future development space is limited.
- The theoretical value of the fuel ratio (solid carbon consumption) is about 390–410 kg/t, some advanced BF fuel ratio has been reached 470–490 kg/t.
- Adopt burden composition and fuel structure reform to reduce carbon fuel consumption and CO_2 emission.
- Hydrogen-based gas fuel injection to replace solid carbon fuel and realize carbon-hydrogen coupled metallurgy, thus reducing carbon consumption and CO_2 emission.

Advanced Operational Indices

For the BF ironmaking process, the coke, pulverized coal, heavy oil, and natural gas are used as reducing agent and fuel. Therefore, under the existing raw material conditions, the fuel consumption is generally 470–550 kg/t.H.M. For some BFs with good raw material conditions, high technical equipment level and high operation

level, the fuel ratio can be reduced to less than 470 kg/t.H.M. In BF smelting process, only coke and pulverized coal adopted as fuel, the theoretical fuel ratio is about 460 kg/t.H.M [3]. Under the BF actual operating conditions, when the pulverized coal injection rate reaches 150–200 kg/t.H.M, the fuel ratio is generally maintained at 480–540 kg/t.H.M, and the O/C (Ore/Coke charging burden ratio) of BF can reach more than 5.5–6.0.

Highlights of BF Ironmaking

The BF oxygen enrichment with pulverized coal injection (PCI) technology is actively adopted in China, the blast oxygen enrichment ratio has been reached 3.5–8.5%, and the advanced BF PCR has been reached 180–200 kg/t.H.M. With the increase of BF volume, the technical level increases correspondingly, and the BF fuel consumption is even lower. Increasing the hot blast temperature can provide higher physical heat; thus, the higher temperature physical heat can significantly reduce the fuel ratio and coke rate and promote the PCI.

Under the condition of full BF gas combustion, the hot blast temperature of dome combustion hot blast stove and the blast temperature of some advanced large BFs has reached 1200 °C. Due to the improvement of oxygen enrichment ratio and the fuel ratio reduced, the blast volume is reduced correspondingly, which effectively reduces the BF bosh gas volume and power energy consumption. The BF permeability is the most critical restriction of ultra-high efficient smelting and ultra-low carbon smelting in the future. Increasing the oxygen enrichment ratio, the BF bosh gas volume is decreased, which is helpful to improve the reduction potential of CO and H_2, it will play an important role in improving BF permeability, promoting the indirect reduction process and improving the production efficiency. High oxygen enrichment ratio will become an important approach to achieve low carbon BF smelting in the future. Improving the oxygen enrichment ratio can significantly reduce the blast volume, improve the BF permeability and reduce the process energy consumption. When the oxygen enrichment ratio reaches 7.5%, the blast volume per ton hot metal can be reduced to 850 Nm^3/t.H.M. Improving the blast oxygen enrichment ratio can improve the theoretical combustion temperature in the raceway of the tuyere, which is conducive to the combustion of pulverized coal, and contributes to the hydrogen-based gas fuel injection.

Raising the BF top pressure is conducive to stabilizing the BF operation and reducing the fuel ratio. As a result from statistics, the top pressure of large BF is higher. Practice confirmation and statistics show that improve the BF top pressure, improve the gas utilization ratio effectively, reduce fuel consumption and carbon emissions. Improving the efficiency mainly depends on improving the concentrate level, oxygen enrichment blast, reducing the fuel ratio, and improving the BF stable and smooth operation. Increasing the top pressure has little influence on improving

the productivity, mainly to improve the dynamics of indirect reduction of BF (diffusion and gas–solid reaction process), which has a significant effect on reducing the fuel consumption and improving the gas utilization ratio.

Technical Innovation of BF Ironmaking Process

High Pellet Charging Proportion Smelting

For a long time, the burden structure of BF in China is mainly high basicity sinter + acid pellet + lump ore, and the average pellet proportion is approximate 18–20%. The energy consumption of pellet process is much lower than sintering process, and the CO_2 emission of pellet process is about 37% of sintering. The pellet can achieve low silicon (SiO_2 content to 2.0%), the sintering minimum of SiO_2 content is about 5%, improve the pellet proportion, the BF fuel consumption and CO_2 emission can be significantly reduced. For full pellet smelting, compared with full sintering smelting, the CO_2 emission can be reduced by more than 11.5%. Figure 5 shows the comparison of operational specification for sintering and pelletizing process; Table 3 shows the comparison of pollutant emission of sintering and pelletizing process. Increase the pellet charging proportion can improve the burden grade, reduce the slag amount and fuel consumption, and then reduce the operational cost of hot metal (Figs. 6 and 7). It is beneficial to reduce the total amount of flue gas and dust from the ironmaking system, NO_x, SO_2, and other pollutants emission, to achieve green, low carbon, and clean requirements.

Hydrogen-Based Gas Injection into BF

Theoretical research and production practice shows that injecting natural gas into BF is beneficial to improve the BF output and reduce the fuel ratio. Amount of methane and hydrogen contained in natural gas, after natural gas injected into BF, the methane is decomposed and transformed into H_2 and CO under high temperature conditions, which can improve the volume percentage of H_2 and CO in bosh gas and improve the reduction potential of BF gas. Taking the 5500 m^3 BF as an example, according to the theoretical calculation, the natural gas injection rate is 30 kg/t.H.M, the BF is expected to reduce the annual emission reduction of CO_2 of about 0.145 million tons per year. If coke oven gas is injected, because the volume percentage of H_2 is higher (volume percentage > 50%), in the effect of CO_2 emission reduction will be more significant. Taking hydrogen as reducing agent to replace carbon and reducing is the technical core of BF hydrogen metallurgy. The function of coke as a reducing agent depends on hydrogen replacement, which is the essence of carbon-hydrogen coupled metallurgy in BF.

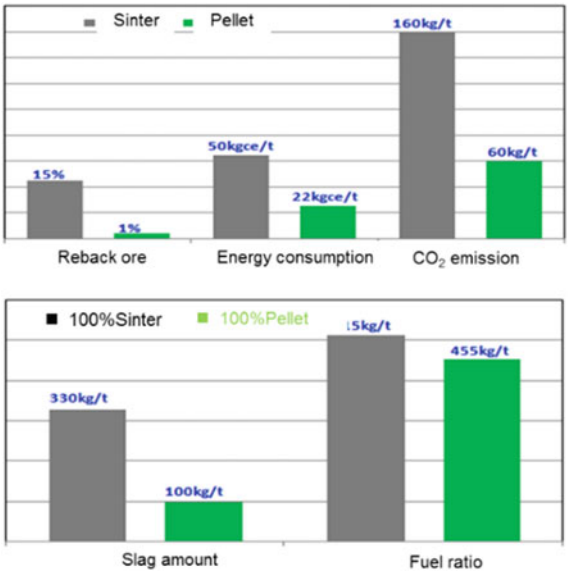

Fig. 5 Comparison of operational specification for sintering and pelletizing process

Table 3 Comparison of pollutant emission of sintering and pelletizing process

Item	Dust, g/t	SO_2, g/t	NO_x, g/t	Waste gas volume, Nm^3/t
Sintering	80	360	600	2000
Pelletizing	52	234	390	1300

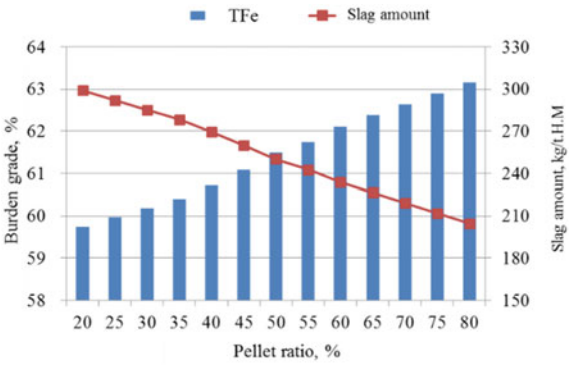

Fig. 6 Relationship between pellet ratio and burden grade and slag amount

Hydrogen-based fuel such as natural gas and coke oven gas injection into BF is a new technical method to reduce carbon fuel consumption and CO_2 emissions [4]. Under the current technical conditions, the massive preparation and use of "green hydrogen" is still in the research and exploration stage, and the large-scale and commercial application will take some time. At the same time, the economy of

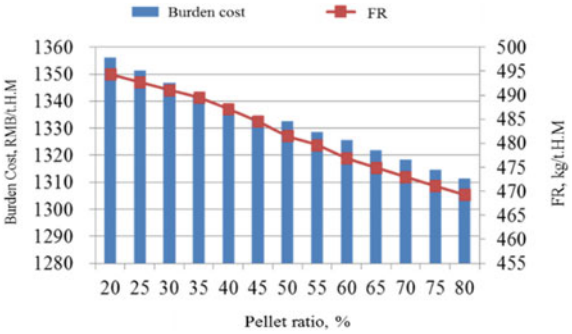

Fig. 7 Relationship between pellet ratio and burden cost and fuel ratio

hydrogen metallurgy also needs to be promoted steadily according to the carbon emission reduction policy and system. Carbon-hydrogen coupled metallurgy is an important technical feature of the new generation of BF, and the hydrogen metallurgy technology has a broad development prospect.

Carbon-Hydrogen Coupled Metallurgy in BF Ironmaking Process

Technical Theory and Reduction Thermodynamics

With increase the blast temperature and oxygen enrichment ratio, it helps to improve the reduction potential of H_2 and CO, promote the indirect reduction process, and improve the production efficiency. High blast temperature is the initial fundamental reaction (gas generation) and the primary energy of BF process. Figure 8 is the H_2 and CO reduction potential diagram; it can find the H_2 and CO different reduction advantage region in the different temperature zone.

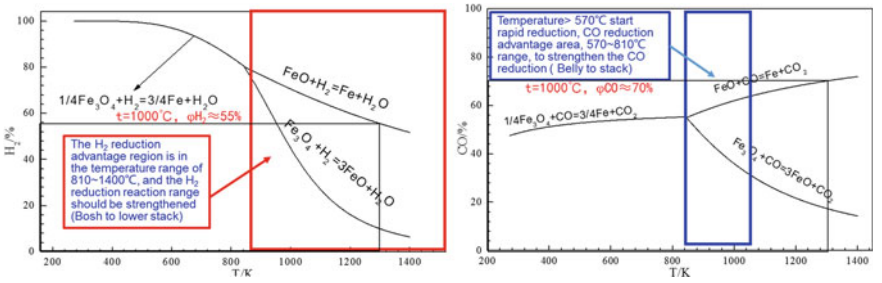

Fig. 8 H_2 and CO reduction potential diagram

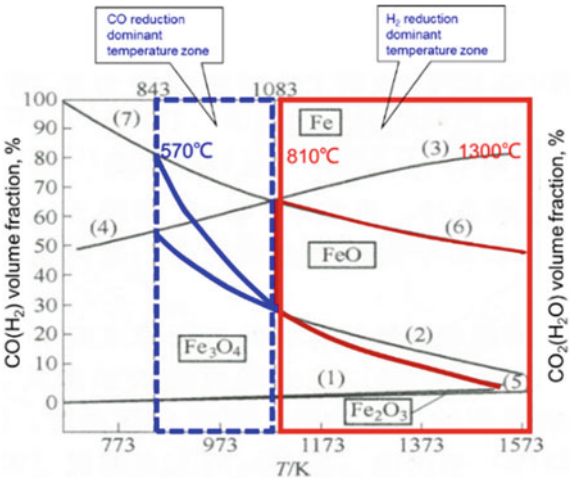

Fig. 9 H_2 and CO coupled reduction potential diagram

The iron oxides reduction follows the hierarchical reduction rules. The required volume fraction of reduction gas (reduction potential) varies under different temperature conditions. There exists the reducing dominance temperature zone for H_2 and CO. Multiple reduction media are characterized by competitive reduction. The water vapour and gas displacement reaction in BF makes H_2 contribute to the CO reduction effect and promote the reduction reaction between FeO and CO. In the BF smelting process, due to the existence of carbon dissolution reaction ($C + CO_2 = 2CO$), there are direct reduction and indirect reduction reactions in the BF ironmaking process. Direct reduction and indirect reduction of BF are synergistic coupled process systems, which are interdependent and indispensable. Water vapour and gas replacement reaction ($CO_2 + H_2 = CO + H_2O$) is the core of carbon-hydrogen coupled metallurgy, using H_2 to reduce CO_2 into CO, CO to reduce iron oxide (exothermic reaction). The H_2 reduction process is the coupling reaction superposition of Fe–H–C–O multiplex and multimorphic complex system (Shown in Fig. 9).

Under the condition of excess coke in the BF, the process operation window is extremely harsh, and the BF smelting process needs to be reconstructed. The hydrogen metallurgy process of BF is the reduction process of H_2 driven carbon, and the heat supply becomes the key link, that is the mass transfer must first solve the problem of heat transfer.

Key Subject of Hydrogen Metallurgy Technology in BF

Some technical problems of hydrogen metallurgy in the future BF process still need to be further explored and studied, mainly including:

- Thermodynamic and kinetic mechanisms of liquid iron oxide reduction by H_2.

- Problems of endothermic and heat compensation for the H_2 reduction process.
- Collaborative improvement of H_2 and CO utilization ratio under BF smelting conditions.
- Heating the H_2 temperature to 1000 °C inject into the BF.
- Economic problems of full hydrogen or hydrogen-rich reducing gas injection.

Under the laboratory conditions, the effect of reduced gas with different H_2 volume fraction on the reduction degree of different raw materials was investigated. Sintering reducibility is the best, basic pellet reducibility is good, and acid pellet reducibility is the worst. Increases with the volume fraction of H_2 in the reduction atmosphere, consistent with the thermodynamic and kinetic theory of the reduction process.

Reaction for Hydrogen-Based Fuel Injection into BF

Natural gas (NG) injection in the BF tuyere first causes the reforming reaction and changes into H_2 and CO in the tuyere raceway and hearth. When H_2 is injected into the BF tuyere, because the free energy of H_2 and O_2 is higher than that of C and O_2 reaction. Figure 10 shows the Ellingham chart of fuel combustion in BF tuyere raceway.

Natural gas at high temperatures produces CO and H_2. In the high temperature region above 1000 °C, the reduction of FeO is essentially a direct reduction of carbon. At 810–1000 °C, H_2 starts preferentially CO with carbon involved in the reduction of FeO. At temperatures below 810 °C, CO preferentially H_2 participates in the reduction reaction of FeO, and after temperatures below 666 °C, CO and H_2 reduction capacity goes beyond carbon for indirect reduction. The theoretical combustion temperature (RAFT) caused by natural gas injection can be compensated by increasing the oxygen enrichment ratio and reducing the blast humidity, while the increasing blast temperature is difficult to fully compensate for the reduction of RAFT. In order to compensate for the heat loss of natural gas cracking in the tuyere

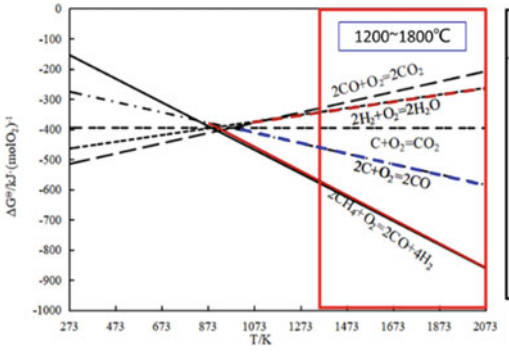

Reaction	$\Delta G^{\ominus}$
$2H_2+O_2=2H_2O(g)$	$\Delta G^{\ominus}$=-495000+111.76T
$2C+O_2=2CO$	$\Delta G^{\ominus}$=-228800-171.54T
$C+O_2=CO_2$	$\Delta G^{\ominus}$=-395350-0.54T
$2CO+O_2=2CO_2$	$\Delta G^{\ominus}$=-561900+170.46T
$2CH4+O_2=2CO+4H_2$	$\Delta G^{\ominus}$=-46712-392.88T

Fig. 10 Ellingham chart of fuel combustion in BF tuyere raceway

raceway, the natural gas can be tried to carry out high temperature cracking and reforming through process analysis. Then, the modified gas can be injected into the BF with the hot blast [5].

Figure 11 shows the influence of oxygen enrichment ratio on the bosh gas volume and RAFT; Fig. 12 shows the influence of blast temperature on bosh gas and RAFT under different hydrogen-based fuel injection amount and oxygen enrichment ratio conditions; Fig. 13 shows the influence bosh gas volume and RAFT on different natural gas injection rate.

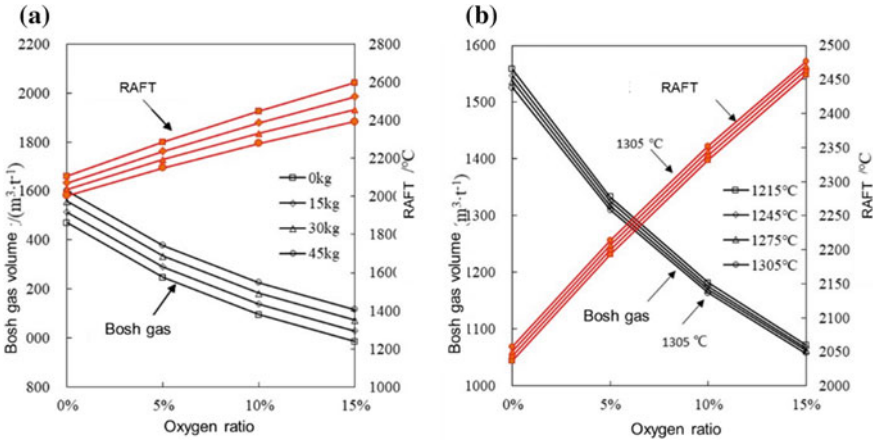

Fig. 11 Influence of oxygen enrichment ratio on the bosh gas volume an RAFT

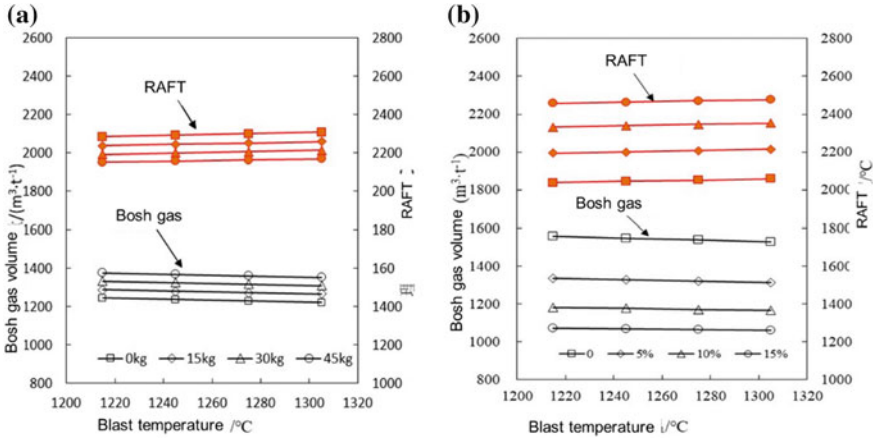

Fig. 12 Influence of bosh gas and RAFT on different blast temperature

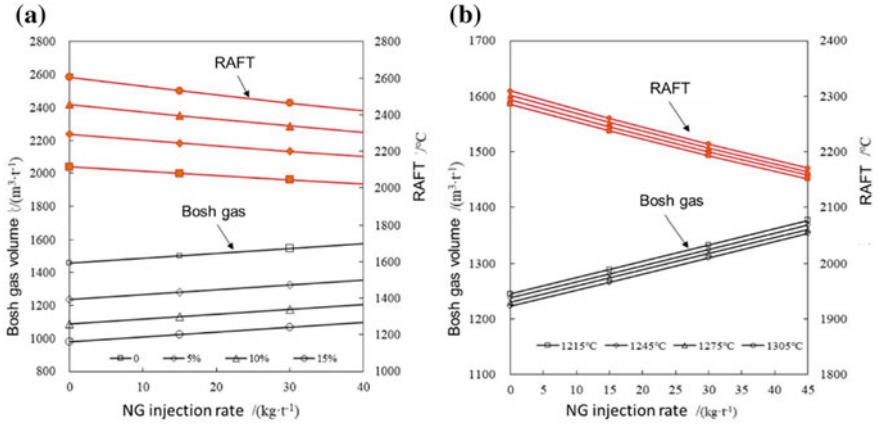

Fig. 13 Influence bosh gas volume and RAFT on different NG injection rate

Conclusions

In the future, China's iron and steel industry will still focus on the BF-BOF process. Blast furnace, as an efficient ironmaking device, the realization of the BF carbon reduction is an important direction of carbon reduction in steel industry.

The development of hydrogen metallurgy in China should still be based on the BF hydrogen-rich process. Considering carbon emission reduction and fuel gas economy, natural gas and other hydrogen base gas should be selected to reduce carbon consumption, and green hydrogen is the key to the ultimate carbon emission reduction of BF ironmaking.

BF hydrogen metallurgy is carbon-hydrogen coupled metallurgy, which has competitive reduction in different areas and temperature ranges of BF; one of the key technologies to realize low carbon ironmaking in BF is to improve the utilization rate of hydrogen and reduce the fuel ratio.

Hydrogen reduction of iron oxide in BF hydrogen enrichment smelting is a heat absorption reaction in which the gas reformation and heat supply of the hearth are in the best state.

Controlling the reasonable direct reduction degree and theoretical combustion temperature is the key to realize low carbon ironmaking technology. It is necessary to investigate the increase of hydrogen content on the BF performance, the maximum difference of pressure, slag, and other effects to ensure the BF stable and smooth operation.

References

1. Fuming Z, Xiangfeng C, Guangyu Y et al (2021) Development of low-carbon and green ironmaking technology at home and abroad. Ironmaking 40(5):1–8 (in Chinese)
2. Fuming Z (2012) Technical characteristics of giant blast furnaces in the early 21st century. Ironmaking 31(2):1–8 (in Chinese)
3. Luengen HB, Schmoele P (2018) Comparison of blast furnace operation modes in the world. In: 8th international congress on science and technology of ironmaking—ICSTI 2018 proceedings, 1054–1063
4. Shiga A, Miyaoka S, Suzuki M et al (2020) Latest plant engineering of blast furnaces. Nippon Steel Techn Rep 123(3):141–147
5. Cheng X, Zhang Fuming Q et al (2022) Study on the main process parameters of blast furnace under natural gas injection. J Steel Res 34(9):944–951 (in Chinese)

Pathways to Reduce Operational Carbon Footprint in Secondary Aluminum Melting

Anand Makwana, Valmiro Sa, Jason Kabarowski, Yue Huang, Renato Pereira Da Silva Junior, and Xiaoyi He

Abstract Economic and environmental pressures are driving change in the modern aluminum industry, compelling manufacturing sites to optimize their processes to drive down costs and reduce environmental impact. Secondary aluminum melting (recycling) requires only 5–10% of the energy needed to produce primary aluminum—reducing carbon emissions and providing cost savings for the producer and consumer but is still a major source of greenhouse gases because of the growing size of the secondary market. Significant improvements in carbon footprint and energy efficiency can be made to aluminum remelting by using smart oxy–fuel burners, low carbon intensity fuels, and Industry 4.0 tools. In this paper, we discuss different pathways to reduce total CO_2 emissions from secondary melting furnaces. First, a novel smart burner will be discussed. This next-generation oxy–fuel burner helps to reduce specific fuel consumption. The burner is a 'transient heating' burner that enables automatic control of energy into various locations of the furnace, based on feedback from furnace sensors. Second, we discuss how the use of low carbon intensity fuels like hydrogen and ammonia can help reduce or eliminate CO_2 emissions. Finally, we present how the use of oxy–fuel combustion technology combined with low carbon intensity fuel can help optimize overall energy cost for secondary melting furnaces. These pathways can assist manufacturers in choosing the optimal solution to decarbonize their melting furnaces.

V. Sa (✉)
Air Products and Chemicals Inc., 27136 Regal Scott Dr, Magnolia, TX 77354-4583, USA
e-mail: SAVC@airproducts.com

A. Makwana · J. Kabarowski
Air Products and Chemicals Inc., 1940 Air Products Blvd., Allentown, PA 18106, USA

Y. Huang
Air Products and Chemicals Inc., Room 101, No. 87, Lane 887, Zuchongzhi Road, Shanghai 201203, China

R. P. Da Silva Junior
Air Products and Chemicals Inc., Av de La Fama, 1, 08940 Cornellà de Llobregat, Spain

X. He
Air Products and Chemicals Inc., 1940 Air Products Blvd, Allentown, PA 18106, USA

© The Minerals, Metals & Materials Society 2024

C. Iloeje et al. (eds.), *Energy Technology 2024*, The Minerals, Metals & Materials Series, https://doi.org/10.1007/978-3-031-50244-6_2

Keywords Decarbonization · Oxy-fuel combustion · Hydrogen · Ammonia · Secondary melting

Introduction

Secondary aluminum melting furnaces provide an energy-efficient pathway to recycle used aluminum products and scrap. These secondary aluminum processes consume about 5–10% of the energy needed to manufacture primary aluminum, thereby providing environmental and economic benefits. The focus on decarbonization of the industrial sector to achieve net-zero carbon emissions has bolstered interest from producers in diverse ways to reduce and/or eliminate the carbon footprint of their secondary melting furnaces. This paper focuses on how the use of next-generation oxy–fuel burners and low carbon intensity fuels can help lower the carbon footprint of secondary melting furnaces.

Pathways to Reduce Carbon Footprint of Secondary Melting Furnaces

A major source of carbon generation from secondary melting furnace operation is the use of carbon-containing fuels that are used for process heating. Most of the fuels used currently for process heating with combustion systems contain carbon and hydrogen which get converted into carbon dioxide (CO_2) and water vapor (H_2O) as major products of combustion, in addition to minor species like NOx, CO, PAHs, unburnt hydrocarbons, or fuel leaving the flue, etc. The CO_2 emissions from combustion are the major source of greenhouse gas (GHG) emitted from secondary melting furnace operations.

Oxy–fuel combustion is a good pathway to achieve partial decarbonization of secondary melting furnaces. The use of oxy–fuel combustion systems in reverb and rotary furnaces allows for the reduction of the fuel usage and, therefore CO_2 emissions, by as much as 40% as compared to conventional cold air–fuel combustion systems because oxy–fuel flames are more effective in transferring energy to the melt. In oxy–fuel systems, the higher heat transfer rate to the melt is due to higher flame temperatures, higher flame emissivity, and the absence of diluent nitrogen (that carries the heat with it out of the flue) [1].

Given the need to achieve net-zero carbon emissions from furnace operations, producers can switch to biofuels or alternative fuels like hydrogen (H_2) or ammonia (NH_3) that don't contain carbon. While the combustion of H_2 or NH_3 will not produce any CO_2 leaving the flue, it is critical to take into account the pathway by which these fuels are produced and how much CO_2 emissions are associated with the production of these fuels. Carbon capture at the furnace exhaust is another potential route to

reduce CO_2 emissions. However, the use of carbon capture, storage, and transport or utilization would be very challenging to implement on reverb furnaces as compared to switching the fuel type to non-carbon-based fuels or biofuels. Carbon capture is difficult in secondary melting because of the smaller scale of reverb furnaces and the need to utilize or sequester the captured CO_2. Lastly, N_2O and unburnt fuel like CH_4 have higher lifetime GHG potential as compared to CO_2 [2]. The use of alternative fuels like hydrogen and ammonia can increase the NO_x and N_2O emissions from combustion processes due to thermal NO_x formation and/or fuel-bound NO_x formation [3]. Therefore, it is critical for the burner to be designed to minimize the NO_x formation from use of these alternative fuels, and the GHG potential of N_2O should be accounted for when switching the fuel type.

Partial Decarbonization: Use of Oxy–Fuel Burners

Oxy–fuel burner technology can be used in current reverb and rotary furnaces to achieve either of two goals: increase the furnace production rate or decrease the fuel usage per ton of material produced. Rotary furnaces have higher efficiencies than reverb furnaces [4] due to a higher heat transfer rate driven by direct contact between the hot refractory and the melt, and the mixing action of rotation. As a result, use of oxy–fuel is a natural fit for rotary furnace as the maximum available energy from oxy–fuel can be absorbed by the melt. The use of multiple burners in a rotary furnace [5] can provide enhanced process benefits by providing a means to reduce uneven heat distribution in the furnace and incomplete combustion products leaving the furnace flue.

In reverb furnaces, the oxy–fuel burner operation can be tuned to match the producer needs to either partially convert the furnace operation to oxy–fuel (boost application) or convert to a full oxy–fuel system. The effective use of oxy–fuel combustion has two critical aspects associated with it, design of the burner, and the correct installation location to maximize its benefits. The remainder of this discussion focuses on the use of smart oxy–fuel burners in reverb furnaces.

Oxy–fuel burners need to be designed in such a way that they can provide efficient heat transfer to the melt while minimizing any adverse impacts of using oxygen as the oxidizer and its inherently higher flame temperatures as compared to air–fuel burners. These devices can be designed as smart burners using Industry 4.0 tools to automatically regulate firing rate, equivalence ratio, and/or the amount of energy input from individual burners (in the case of multiple burners used in a furnace).

Proper location and installation of oxy–fuel burners in the furnace is equally important to extract the maximum theoretical benefits that this technology can deliver. Computational fluid dynamics modeling (CFD) is a good tool to simulate the whole furnace operation and identify the optimal location to install the burners.

Horizontal Transient Heating Burner Technology (HTHB)

The Air Products Horizontal Transient Heating Burner (HTHB) technology [6] is a smart technology that allows directional control of flames in a furnace based on feedback from smart sensors positioned within the furnace. Figure 1 presents photographs of flames (natural gas (NG) as fuel and oxygen (O_2) as oxidizer) showing directional change of the flame from the left to the right side of the furnace. Figure 1a shows the left side flame (active flame) is providing about 80% of the total heat output from the burner to the left, and Fig. 1b shows the right-side flame is delivering the major portion of the burner thermal output to the right.

The modulation of the flame direction from left to right and vice versa can be based on a fixed frequency or on feedback from sensors installed in the furnace. This ability to regulate the flame direction helps to solve several challenges faced by typical stationary flame oxy–fuel or conventional regenerative (regen) burners. In particular, the ability to move the flame around the furnace helps to achieve more uniform energy distribution in the furnace and minimize localized heating of the melt.

Figure 2 shows CFD results of the comparison of temperature profiles near the aluminum melt surface in a reverb furnace for two different burners: stationary conventional oxy–fuel burner versus HTHB technology. In both cases, the reverb furnace has two burners installed that operate at identical firing rates and global equivalence ratios. The comparison of the two plots shows that HTHB technology is able to achieve a more uniform temperature distribution throughout the melt surface. The more uniform temperature in the furnace helps to reduce the peak temperatures on the melt surface and reduce cold spots as compared to the conventional oxy–fuel burner systems. The HTHB technology can produce lower peak temperatures due to delayed mixing through both fuel and oxidizer staging, and these reduced peak temperatures help to decrease metal losses due to oxidation and reduce cold spots, helping to improve the energy efficiency of the furnace.

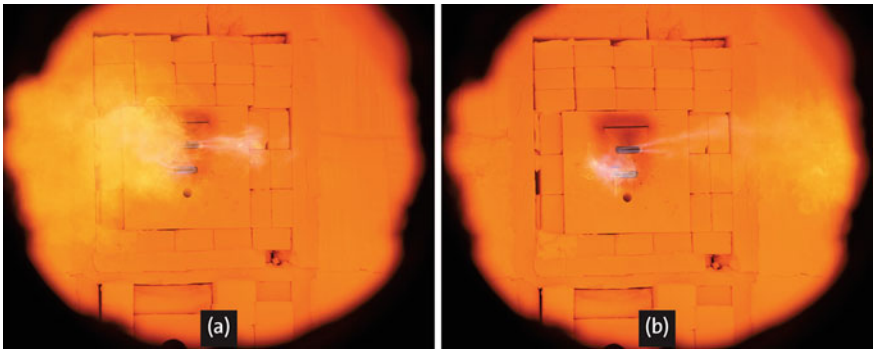

Fig. 1 Two-nozzle HTHB technology operating in a reverb furnace **a** 100% NG-O_2 flame image with left flame active, **b** 100% NG-O_2 flame image with right flame active

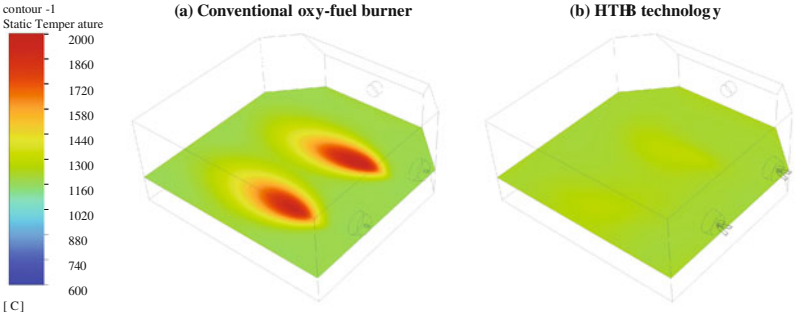

Fig. 2 Comparison of temperature profile at the aluminum melt surface **a** conventional oxy–fuel burner, **b** HTHB technology

Additionally, this next-generation transient heating technology produces lower nitrogen oxides (NO_x) by up to 40% as compared to conventional oxy–fuel burners, for both conventional fuels (NG) and mixtures of conventional (NG) and alternative fuels (H_2) [6]. Lastly, staging of the oxidizer away from the melt surface can assist in reducing the oxygen near the bath surface, which can help to reduce metal oxidation and increase metal yield.

Furnace Simulation Using CFD

The design of new generation oxy–fuel burners is the first part of the equation to solve the challenge of implementing oxy–fuel combustion in reverb furnaces. CFD can be used to answer several critical questions such as how and where in the furnace should the burner be installed? How will the installation of this burner impact the flow field in the furnace? In the case of a boost application, how does the operation of two burners impact the flame development from each individual burner? Additionally, in the case of larger furnace sizes, multiple burners or a combination of different burners (roof-mounted transient burners or sidewall mounted transient burners) can be used in the same furnace. CFD plays a critical role in identifying optimal locations of these burner systems.

A reverb furnace of 15-ton capacity was simulated using CFD to find the optimal location of the oxy–fuel burner for a secondary aluminum melting operation. The aim of the study was to either reduce the fuel usage or increase the production rate, as needed, based on customer-specific goals. The HTHB technology was evaluated for a boost application study with a target to replace about 50% of energy input to the furnace with an oxy–fuel burner. The existing air–fuel system is a two-burner regen system and uses natural gas as fuel. Figure 3a displays this air–fuel case and shows the temperature field in the burner plane when the left side of the burner is operating. Figure 3b shows the boost application and the temperature field in the HTHB flame plane. The figure shows the evolution of two flames (one from the regen burner and the second from the HTHB) in the furnace with minimal interaction. The development

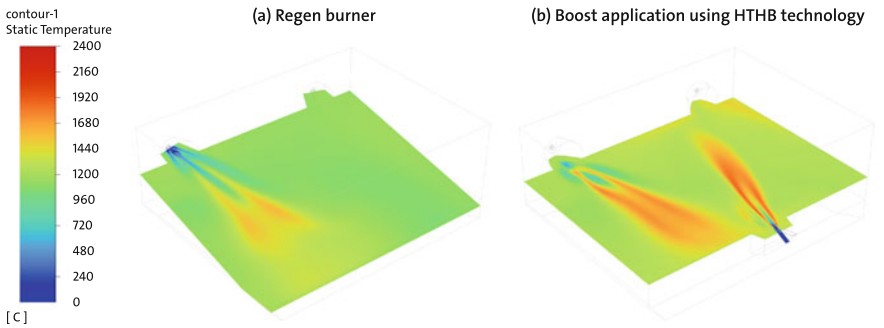

Fig. 3 Comparison of temperature profile in the burner plane **a** regen system, **b** boost application using HTHB technology

of the flames in two different directions is intentional to achieve more uniform heat transfer throughout the melt surface and reduce cold spots in the furnace. The CFD results demonstrate that when the total firing rate was maintained between the two cases, the melting thermal efficiency improved by 7% and the melting time was reduced by 14%.

HTHB Installed in a Reverb Furnace

A HTHB burner was installed in a reverb furnace with a regen burner in a boost application at a secondary aluminum melting operation in Europe. The burner and related installation allow a transition to a system with energy input almost exclusively from the oxy–fuel combustion system. This flexibility allows the customer to meet increased production demand.

Figure 4 shows an image of the HTHB technology installed on a furnace wall. The installation at the site involved supply of oxygen, new fuel, and oxygen flow control skids, as well as a burner control system.

The burner has been commissioned, and operation has been smooth to date. Figure 5 shows the flame images from HTHB technology during the start of the melt cycle and at the end of the melt cycle. The flame from the transient heating burner is long, covering about 2/3 of the reverb furnace width, and is sootier due to fuel rich combustion from the individual flames. This allows the energy from the flames to penetrate much deeper along the furnace width and increase the radiative heat transfer from the soot particles to the melt. The authors are waiting to collect more data in the coming months and the results will be shared once this data has been analyzed.

A roof-mounted version of the Air Products Transient Heating oxy–fuel burner system has been installed in several reverb furnaces [4, 7]. The operations have achieved productivity increases of up to 35%, up to 20% lower metal losses, and decreases in fuel consumption of up to 45% [4, 7]. The increase in thermal efficiency

Fig. 4 HTHB mounted on a reverb furnace wall

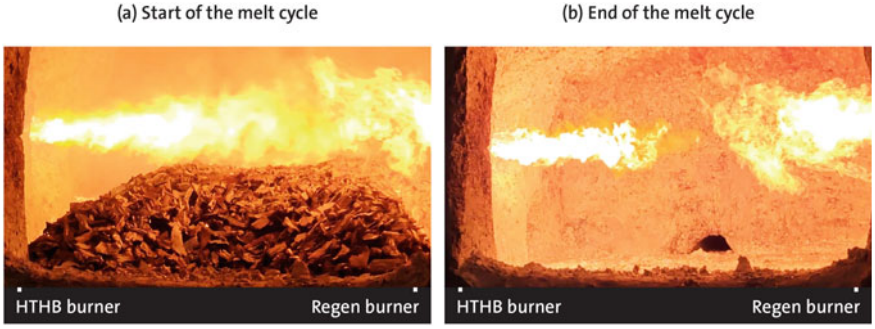

Fig. 5 Flame images from reverb furnace: **a** start of the cycle, **b** end of the melt cycle

helps to reduce the specific fuel consumption (SFC) and lower the carbon footprint of the furnace operation. These examples of using oxy–fuel combustion illustrate that the secondary aluminum industry can benefit from the use of next-generation smart oxy–fuel burners to reduce their carbon footprint from combustion processes, while improving furnace performance (furnace thermal efficiency, improved productivity, improved furnace yield) to obtain economic benefits.

Impact of the Use of Low Carbon Intensity Fuels on Decarbonization of Melting Furnaces

The use of oxy–fuel combustion can help accomplish partial decarbonization of secondary melting furnaces. However, to reduce the carbon footprint further, use of alternative fuels like low carbon intensity hydrogen or ammonia are attractive options. Fuel consumption directly relates to CO_2 emissions, e.g., for every million Btu (MMBtu) of natural gas burned, 116 lbs of CO_2 are released into the atmosphere [8]. These exhaust flue CO_2 emissions are eliminated when we change the fuel to H_2 or NH_3. The major products of combustion of H_2 and NH_3 are water–vapor (H_2O), and water vapor (H_2O) and nitrogen (N_2), respectively. No CO_2 is emitted, thereby achieving zero exhaust flue CO_2 emissions.

Figure 6 shows theoretical CO_2 emissions reduction potential from flue exhaust for different fuel blends of natural gas-hydrogen and natural gas-ammonia. The base fuel used in these calculations is natural gas. The figure doesn't consider CO_2 associated with the production of H_2 and NH_3 and any NG leaks in the supply chain. Hydrogen and ammonia fuels have carbon intensity associated with their production, and this carbon intensity depends on the production route used. It is important to check with the fuel supplier regarding the carbon intensity associated with the fuel production and calculate 'actual' CO_2 reduction possible when switching the fuel type to NG-H_2 or NG-NH_3 blends. For hydrogen and ammonia to be considered low carbon, they must be produced by emitting less than a certain limit of CO_2 emission/MJ of fuel; for example, in Europe for hydrogen this limit is fewer than 20 g CO_2e/MJ of hydrogen (46.5 lbs CO_2e/MMBtu) [9]. Additionally, Fig. 6 displays that for a given volumetric blend of H_2 or NH_3 with NG, NG-NH_3 the fuel blend has a slightly higher CO_2 emission reduction potential as compared to the NG-H_2 fuel blend due to the higher heating value (HHV) value of ammonia (435 Btu/scf) is greater than hydrogen (343 Btu/scf). As a result, at a fixed volumetric fuel blend ratio, the NG volumetric flow rate is reduced more in NG-NH_3 mixture as compared to the NG-H_2 mixture.

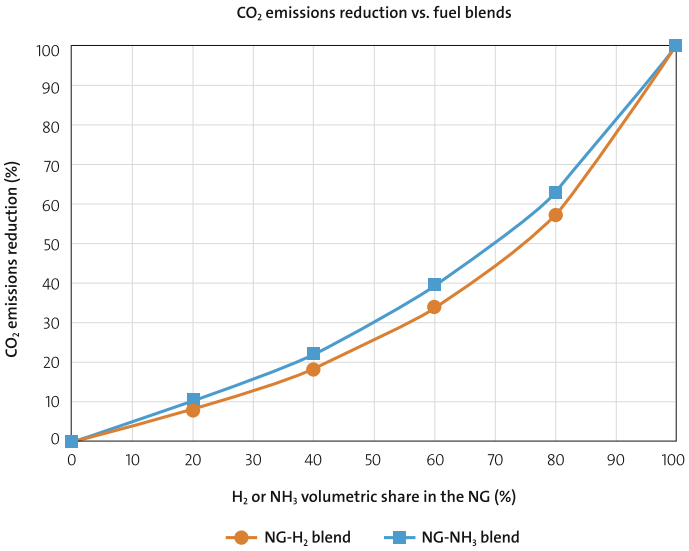

Fig. 6 CO_2 emission reduction for NG-H_2 and NG-NH_3 blends

Considerations for the Use of H_2: Air–Fuel, Oxy–Fuel, or Air–Oxy–Fuel Burner Systems

Another important consideration is whether to use an oxy–hydrogen burner, air–oxy–hydrogen, or an air–hydrogen burner. Oxy–fuel flames are more effective in transferring energy to the melt as compared to those from air–fuel burners. The absolute improvement in thermal efficiency and therefore, fuel usage per lb of material processed, depends on several factors, including (but not limited to) type of furnace, air leakage in the furnace, whether it has undergone a full or partial conversion to oxy–fuel combustion. The previous field results show that the fuel usage with oxy–fuel burners can be reduced by as much as 45% [4, 7]. This is important as hydrogen, in particular low carbon intensity hydrogen that has low carbon associated with its production, is more expensive as compared to conventional fuels. Therefore, with the use of oxy–fuel combustion systems, the total fuel cost can be reduced as compared to air–fuel systems.

Another consideration is that the furnace atmosphere composition when using air–fuel burners versus oxy–fuel burners is significantly different. Figure 7 compares the major species produced from combustion of NG-H_2 fuel blends for both air–fuel and oxy–fuel burners. At any particular fuel composition, the use of oxy–fuel burners increases the volume fraction of CO_2 and H_2O in the furnace atmosphere. Additionally, as the fraction of hydrogen in the fuel increases, the concentration of water vapor increases inside the furnace. This increase in the concentration of water vapor, associated with an increase in the use of hydrogen and/or change to an oxy–fuel system, in the furnace may impact the product quality and increase the

metal oxidation rate. This should be considered when evaluating various fuels and combustion systems.

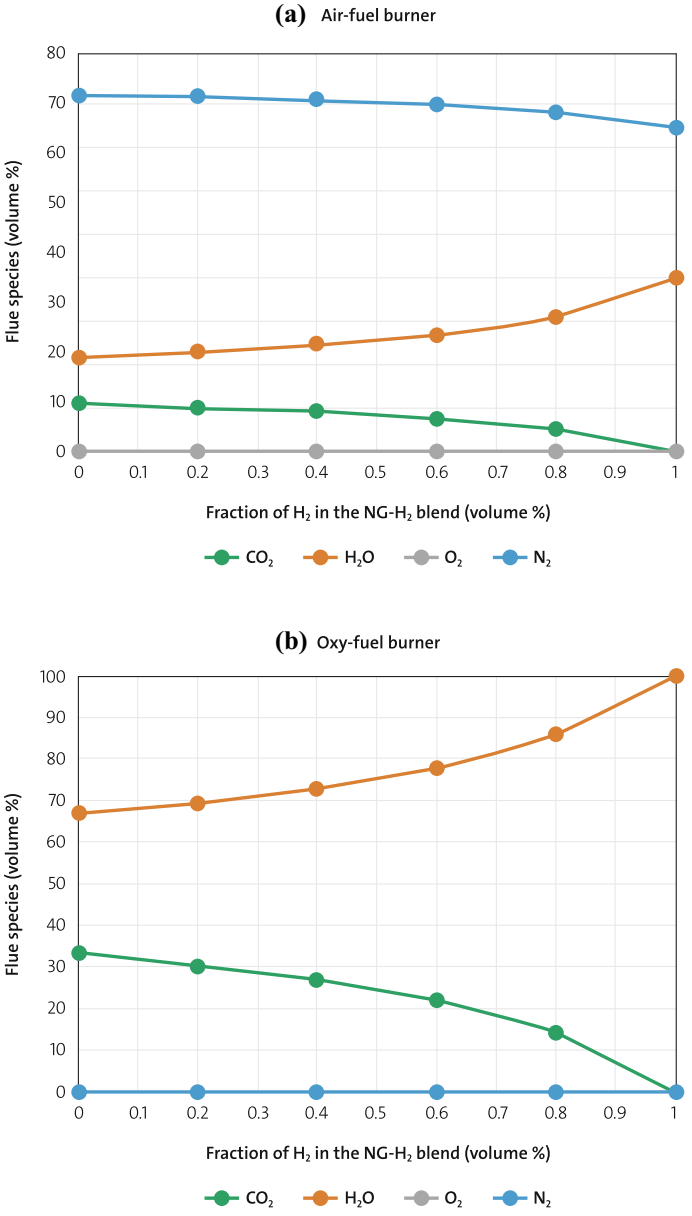

Fig. 7 Comparison of change in major products of combustion for different NG-H_2 fuel blends **a** air–fuel burner, **b** oxy–fuel burner

Furthermore, NO_x emission is another parameter that could be different for oxy–fuel and air–fuel burners. The use of oxy–fuel burners can help reduce the total NO_x emissions as compared to an air–fuel burner primarily, because of the absence of nitrogen in the oxidizer stream. Practically, due to the pressure balance in the furnace, oxy–fuel burners may produce NO_x as a function of air leakage in the furnace.

Lastly, use of an air–oxy–fuel burner can be an interesting option to consider as well. Air–oxy–fuel burners can provide operational flexibility, allowing the combustion system to accommodate the varying needs of different furnace cycles and the ability to switch operation from oxy–fuel mode (melting mode) to air–oxy–fuel mode (holding mode).

Conclusion

Decarbonization of secondary melting furnaces can be achieved by use of oxy–fuel combustion systems and low carbon intensity fuels, like hydrogen and ammonia. The use of smart oxy–fuel transient heating technology provides a practical way to achieve partial decarbonization of furnace operations. Alternative fuels like hydrogen and ammonia further provide a route to eliminate exhaust flue CO_2 emissions, thereby achieving full decarbonization of combustion processes. The 'actual' CO_2 reduction potential using these fuels will depend on the hydrogen and ammonia production route, which would in turn depend on the local geographic conditions (availability of renewable energy or average carbon associated with electricity available in the region, carbon intensity of hydrogen production, etc.).

References

1. Baukal CE (2013) Oxygen-enhanced combustion, 2nd edn. CRC Press
2. Yoro KO, Daramola MO (2020) CO_2 emission sources, greenhouse gases, and the global warming effect. In: Advances in carbon capture. Woodhead Publishing, 3–28
3. Chai WS, Bao Y, Jin P, Tang G, Zhou L (2021) A review on ammonia, ammonia-hydrogen and ammonia-methane fuels. Renew Sustain Energy Rev 147:111254
4. Gangoli S, Kenworthy JB, Buragino G, Hewertson R, Sane A, Mocsari J (2017) Oxy–fuel technologies and strategies for secondary aluminum melting operations. Light Metal Age 75(4):22
5. Hewertson RJ, Gangoli SP, Kenworthy JB, He X, Sane AV, Air Products and Chemicals Inc. (2023) Multi-burner rotary furnace melting system and method. U.S. Patent 11,598,522
6. Makwana A, He X, Hewertson R, Lawrence M (2022) Decarbonization of Secondary aluminum melting. Light Metal Age, p 32
7. Sane A, Gangoli S, He X, Lawrence M, Hewertson R (2018) Effective use of oxy–fuel combustion in aluminum reverberatory furnaces. Light Metal Age, 36
8. https://www.eia.gov/environment/emissions/co2_vol_mass.php. Assessed in Sept 2023
9. UK Low Carbon Hydrogen Standard: emissions reporting and sustainability criteria—GOV.UK (www.gov.uk). Assessed in Sept 2022

Reduction and Carbonization of Iron Concentrate with Hydrogen-Rich Gas

Run Zhang, Chao Wang, Yang You, and Jie Dang

Abstract Iron concentrate can be obtained from vanadium titanium bearing magnetite ore through beneficiation, which mainly recovers iron and vanadium resources through the process of blast-furnace ironmaking and converter vanadium extraction. However, this process has the bottleneck problems of large carbon emission and high process energy consumption, which does not meet the development trend of green and low-carbon smelting. Based on hydrogen metallurgy technology, the reduction and carbonization of iron concentrate in hydrogen-rich gas system (CH_4–H_2 gas mixture) was studied in this paper. The theoretical calculation results show that the Fe-containing phase in iron concentrate could be completely reduced and carbonized to Fe_3C above 709 °C, while Fe_3C cannot exist stably below 900 °C. The experimental results are basically consistent with the thermodynamic results. The results preliminarily confirm the feasibility of producing high value-added product Fe_3C from iron concentrate by hydrogen-rich gas, which provides a possible way of smelting iron concentrate.

Keywords Iron concentrate · Hydrogen-rich gas · Fe_3C

R. Zhang · C. Wang · Y. You (✉) · J. Dang (✉)
College of Materials Science and Engineering, Chongqing University, Chongqing 400044, China
e-mail: youyang@cqu.edu.cn

J. Dang
e-mail: jiedang@cqu.edu.cn

Y. You · J. Dang
Chongqing Key Laboratory of Vanadium-Titanium Metallurgy and New Materials, Chongqing University, Chongqing 400044, China

© The Minerals, Metals & Materials Society 2024

C. Iloeje et al. (eds.), *Energy Technology 2024*, The Minerals,
Metals & Materials Series, https://doi.org/10.1007/978-3-031-50244-6_3

Introduction

Vanadium titanium bearing magnetite ore, as a complex mineral resource containing a variety of metal elements, mainly contains valuable metal components of iron, titanium, and vanadium[1, 2]. Vanadium titanium bearing magnetite ore is widely distributed in the world, and its reserves are also very rich. China has the most abundant vanadium titanium bearing magnetite resources in the world, and more than 90% of which are concentrated in Panzhihua area [3]. The vanadium titanium bearing magnetite resources in Panzhihua have lower iron grade and higher TiO_2 content, which does not belong to one of the high-quality iron ore resources. In the practical application of vanadium titanium bearing magnetite ore, the valuable phase in the ore is usually divided into different types of products according to its properties through complex beneficiation process [4–7]. After the separation of the ore, the useful products obtained are mainly divided into three kinds: the first kind is iron concentrate, which is mainly used to extract iron and vanadium; the second is titanium concentrate, which is mainly used for titanium extraction; the third is sulfide, which can recover valuable metals such as cobalt and nickel. Among these three products, iron concentrate mineral rate is the highest, while the enrichment degree of valuable elements is also relatively high.

The process of blast-furnace ironmaking and converter vanadium extraction is the main method of smelting Panzhihua iron concentrate, which can effectively recover iron and vanadium from vanadium titanium bearing magnetite ore. Although this process has the advantages of complete process, high production efficiency and large production capacity, there are also many limitations, such as waste of titanium resources, excessive consumption of coke, large carbon emissions, long process, and high energy consumption [2]. It is worth noting that the proposed targets of "carbon peaking" and "carbon neutrality" make these shortcomings more prominent. Therefore, the development of new low-carbon metallurgy technology is imminent [8].

Hydrogen metallurgy technology, as a green and low-emission smelting process, has been widely welcomed in the steel industry [9]. At present, the main sources of hydrogen-rich gas are natural gas, coke oven gas, and so on. In addition to hydrogen, natural gas and coke oven gas also contain a large amount of methane gas, which as another efficient and clean reducing agent, has been widely concerned by relevant researchers in recent years. At present, researchers have successfully used methane gas as a reducing agent to reduce metal oxides such as MnO_2, SiO_2, Cr_2O_3, TiO_2, and so on [10–17]. These studies showed that methane gas could not only reduce metal oxides at relatively low temperatures, but also further convert metal elements into metal carbides. However, there were few reports about the direct reduction of Panzhihua iron concentrate to form Fe_3C by using hydrogen-rich gas containing methane. Therefore, the present study aimed to explore the feasibility of direct reduction of iron concentrate in Panzhihua to produce high value-added iron products (Fe_3C).

Table 1 Main chemical components of iron concentrate in Panzhihua area (wt%)

Phase	TFe	FeO	Fe_2O_3	TiO_2	V_2O_5	SiO_2
Content	53.48	33.83	39.88	12.70	0.566	3.73
Phase	Al_2O_3	CaO	MgO	P	S	As
Content	4.12	1.08	2.93	< 0.01	0.852	< 0.01

Experimental

Materials

The raw material used in this study is iron concentrate obtained from vanadium titanium bearing magnetite ore in Panzhihua area. The main chemical components of iron concentrate are given in Table 1. The employed gases were CH_4 (99.99 vol% Chongqing Ruixin Gas Co., Ltd.), H_2 (99.999 vol% Chongqing Ruixin Gas Co., Ltd.), and Ar (99.999 vol% Chongqing Ruixin Gas Co., Ltd.).

Experimental Procedure

The experimental equipment employed in this study mainly includes vertical sealed furnace (heated by silicon–molybdenum heater) and gas flow controllers (Alicant, Model MC-500SCCM-D and MC-1SLPM-D), as shown in Fig. 1.

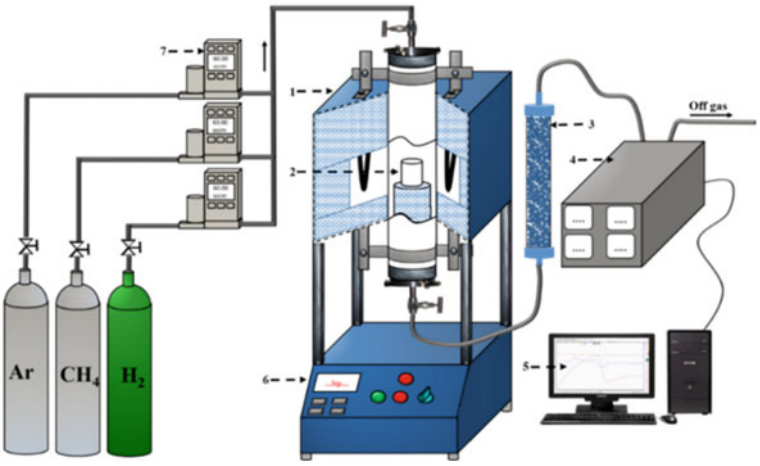

Fig. 1 Schematic diagram of the experimental apparatus: 1—furnace, 2—Al_2O_3 crucible, 3—filter, 4—infrared spectrometer, 5—data collector, 6—temperature controller, 7—mass flow controller

First, 1g iron concentrate powder was weighed with a balance and put into the corundum crucible and installed in the furnace tube constant temperature zone according to standard operation. Ar gas was injected into the furnace tube as a protective gas during the heating process. When the temperature reached the experimental temperature, the intake of Ar gas was stopped, and the CH_4–H_2 mixed gas was injected into the furnace tube at a flow rate of 500 sccm/min. When the reaction ended and began to cool down, the intake of CH_4–H_2 gas mixture was stopped, and Ar gas was injected into the furnace tube as a protective gas. And the reaction product was removed from the furnace tube after falling to room temperature.

Part of the reduced sample was fully ground, and then the phase composition analysis was performed by X-ray diffractometer (Cu-Kα, PANalytical X 'Pert Powder, PANalytical B.V.). The unground reduced sample was set in epoxy resin and then polished. The micro-morphology of the polished surface was analyzed by scanning electron microscope (SEM, TESCAN VEGA 3 LMH, Tescan VEga 3 LMH).

Thermodynamic Analysis

The main iron-bearing phases in iron concentrate are Fe_2O_3, Fe_3O_4, FeO, and $FeTiO_3$. Mastering the theoretical reduction carbonization conditions of these iron-bearing phases will be helpful to the subsequent experimental research. Therefore, the Gibbs reaction free energy variation of these iron-containing phases in hydrogen-rich systems (CH_4–H_2 gas mixture) was calculated by using the reaction module of FactSage software, and the calculation results are shown in Fig. 3. The partial pressure of CH_4 and H_2 in the systems was set to 0.25 and 0.75 atm (refer to the gas composition of coke oven gas).

As can be seen from Fig. 2, the possible chemical reactions of iron concentrate in hydrogen-rich systems are as follows:

$$FeTiO_3 + 4/3CH_4 = 1/3Fe_3C + 8/3H_2 + TiO_2 + CO \quad (1)$$

$$FeO + 4/3CH_4 = 1/3Fe_3C + CO + 8/3H_2 \quad (2)$$

$$Fe_2O_3 + 11/3CH_4 = 2/3Fe_3C + 3CO + 22/3H_2 \quad (3)$$

$$Fe_3O_4 + 5CH_4 = Fe_3C + 4CO + 10H_2 \quad (4)$$

Equations (1)–(4) do not consider the reducibility of hydrogen because the reduction product of H_2, H_2O, will spontaneously react with CH_4 above 620 °C:

$$H_2O + CH_4 = 3H_2 + CO \quad (5)$$

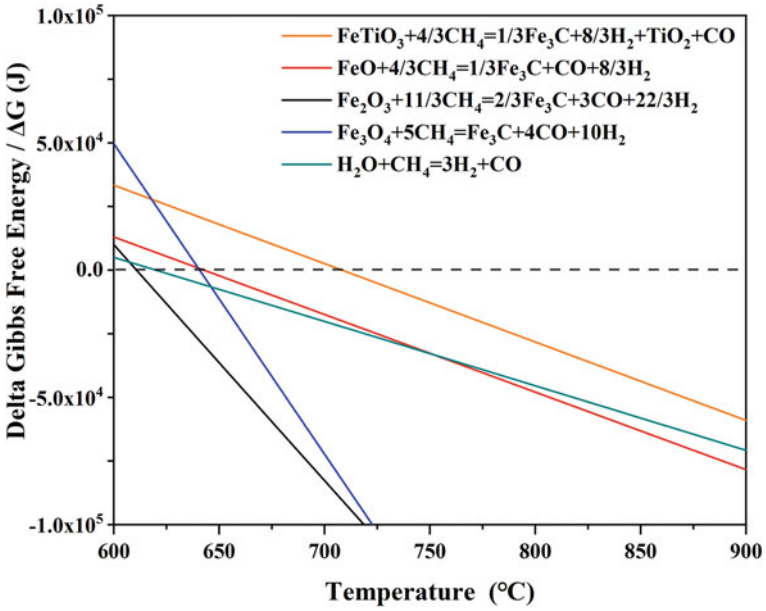

Fig. 2 Gibbs reaction free energy of iron concentrate reacted in hydrogen-rich system

Figure 2 shows that Fe_2O_3 can be spontaneously reduced and carbonized to Fe_3C by CH_4–H_2 mixture gas at above 610 °C, which is the most easily reduced and carbonized iron-bearing phase in iron concentrate. In contrast, $FeTiO_3$ is the most difficult one to be reduced and carbonized to Fe_3C, and its lowest reduction carbonization temperature is 709 °C.

Results and Discussion

Effect of Reaction Temperature

Thermodynamic calculation results have shown that the iron concentrate can be gradually reduced and carbonized to Fe_3C by CH_4–H_2 gas mixture at above 610 °C, while the increase of temperature is helpful to the reaction in thermodynamics. Therefore, in order to determine the actual reduction and carbonization conditions of iron concentrate, the reduction and carbonization reaction of iron concentrate samples was carried out with CH_4–H_2 gas mixture at different temperatures.

Figure 3 shows the XRD results of iron concentrate reduced for 3 h at different temperatures. As seen from Fig. 3, the presence of Fe_3C was not detected in the reduced sample after 3 h of reaction when the temperature was lower than 800 °C, which indicates that CH_4–H_2 gas mixture may not further carbonize the metal iron

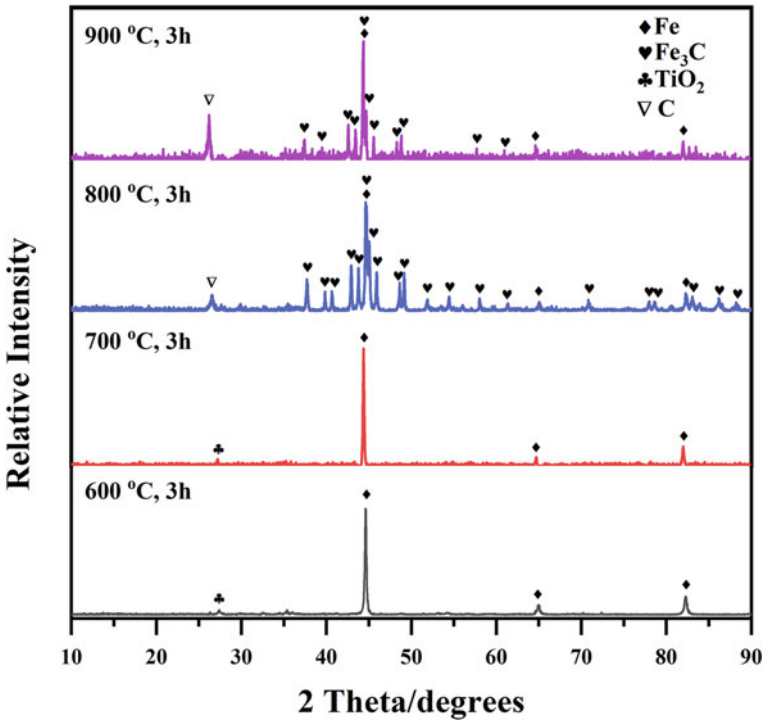

Fig. 3 XRD patterns of iron concentrate reduced at different temperatures for 3 h

in the reduced sample to Fe_3C below 800 °C. After the reaction at 800 °C for 3 h, a large amount of Fe_3C was generated in the reduced sample, accompanied by the generation of deposited carbon. However, there was still a large amount of metallic iron remained in the reduced sample. It preliminarily indicates that although the CH_4–H_2 gas mixture can reduce and carbonize iron concentrate into Fe_3C at 800 °C, the carbonization rate was not high enough. With the temperature rising to 900 °C, there was still a large amount of metal iron in the reduced sample which has not been reduced to Fe_3C, and a large amount of deposited carbon was generated. It seems that the carbonization rate has not changed significantly. The experimental results suggest that the CH_4–H_2 gas mixture may not be able to completely reduce and carbonize the iron oxide in the iron concentrate to Fe_3C.

Figure 4 shows the BSE images of iron concentrate reduced at different temperatures for 3 h. As can be seen from the figure, when the temperature was lower than 800 °C, there was no significant difference in the micro-morphology between the samples after 3 h reduction. The metal iron in the reduced sample was closely combined with TiO_2, resulting in the overall particle morphology of the reduced sample without changing significantly, while the pyroxene phase also did not separate. With the temperature rising above 800 °C, the formation of Fe_3C caused the original bright white massive microstructure in the reduced sample to break up, forming some small

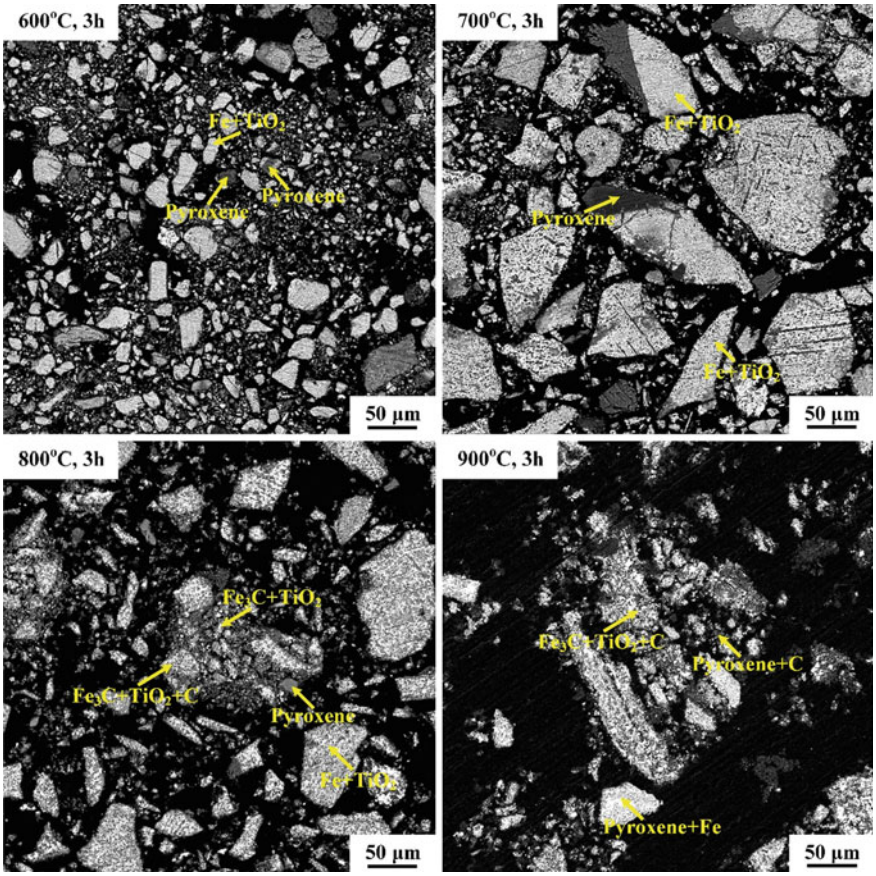

Fig. 4 BSE images of iron concentrate reduced at different temperatures for 3 h

gray particles (Fe_3C), which were loosely reunited with the surrounding bright white particles (metallic iron and TiO_2 phases).

Effect of Reduction Time

In order to further investigate the reduction law of iron concentrate by CH_4–H_2 gas mixture, the reduction and carbonization reaction of iron concentrate samples was carried out for different time. The XRD results of iron concentrate reduced at 800 °C for different time are shown in Fig. 5.

As shown in Fig. 5, the iron oxide in the iron concentrate was basically reduced to iron after 1 h reduction, but the presence of Fe_3C was not detected. A large amount of Fe_3C was produced in the sample after 2 h reduction, while the diffraction peak

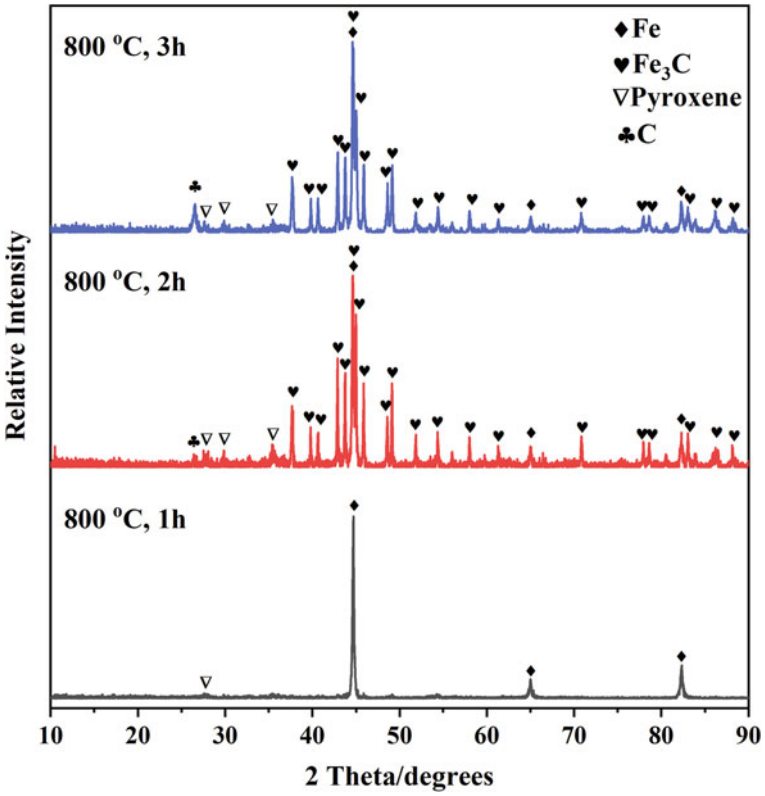

Fig. 5 XRD pattern of iron concentrate reduced at 800 °C for different time

of Fe was also obvious, indicating that quite a lot of Fe in the sample has not been carbonized into Fe_3C at this time. Meanwhile, the formation of deposited carbon indicates that the pyrolysis rate of CH_4 gas was higher than the carburizing rate of Fe at this temperature. With the reduction carbonization time extending to 3 h, the relative intensity of diffraction peaks of Fe_3C and Fe in the samples did not change much, while the relative intensity of diffraction peaks of deposited carbon increased significantly. This means that the CH_4–H_2 gas mixture at this time could not further carbonize the residual Fe in the sample to Fe_3C. Combined with the reduction results of the iron concentrate sample reacted at 900 °C for 3 h (shown in Fig. 3), it can be inferred that the large amount of residual Fe and deposited carbon in the reduced sample may be caused by the decomposition of the generated Fe_3C during the cooling process (the cooling type of the heating furnace is air cooling, and the cooling rate is relatively slow).

Conclusions

The reduction and carbonization behavior of Panzhihua iron concentrate by hydrogen-rich gas was preliminarily studied by theoretical calculation and experiment. The theoretical calculation results show that the iron concentrate can be partially reduced and carbonized to Fe_3C by CH_4–H_2 gas mixture at above 610 °C, while the complete reduction and carbonization to Fe_3C is above 709 °C. The experimental results show that the iron concentrate can be reduced and carbonized to Fe_3C above 800 °C, while there was always a large amount of metallic iron in the reduced sample. Neither the increase of temperature nor the extension of reaction time can convert all the iron in the sample to Fe_3C. It is speculated that the reason may be partly caused by the decomposition of Fe_3C.

Acknowledgements Thanks are given to the financial support from the National Natural Science Foundation of China (52074057, 52222408) and Chongqing Natural Science Foundation (cstc2021jcyj-msxmX0049).

References

1. Chen D, Zhao H, Hu G, Qi T, Yu H, Zhang G, Wang L, Wang W (2015) An extraction process to recover vanadium from low-grade vanadium-bearing titanomagnetite. J Hazard Mater 294:35–40. https://doi.org/10.1016/j.jhazmat.2015.03.054
2. Sui Y-l, Guo Y-f, Jiang T, Qiu G-z (2017) Reduction kinetics of oxidized vanadium titanomagnetite pellets using carbon monoxide and hydrogen. J Alloy Compd 706:546–553. https://doi.org/10.1016/j.jallcom.2017.02.264
3. Zhang J-l, Xing X-d, Cao M-m, Jiao K-x, C-l W, Ren S (2013) Reduction kinetics of vanadium titano-magnetite carbon composite pellets adding catalysts under high temperature. J Iron Steel Res Int 20:1–7. https://doi.org/10.1016/S1006-706X(13)60048-5
4. Wang WZ, Meng QL, Yang CG (2013) Experimental research on comprehensive recovery of iron and titanium from the vanadium-titanium magnetite ore. Adv Mater Res 641–642:381–384. https://doi.org/10.4028/www.scientific.net/AMR.641-642.381
5. Liu W, Zhang J, Wang W, Deng J, Chen B, Yan W, Xiong S, Huang Y, Liu J (2015) Flotation behaviors of ilmenite, titanaugite, and forsterite using sodium oleate as the collector. Miner Eng 72:1–9. https://doi.org/10.1016/j.mineng.2014.12.021
6. Laxmi T, Srikant SS, Rao DS, Bhima Rao R (2013) Beneficiation studies on recovery and in-depth characterization of ilmenite from red sediments of badlands topography of Ganjam District, Odisha, India. Int J Min Sci Technol 23:725–731. https://doi.org/10.1016/j.ijmst.2013.08.017
7. Bulatovic S, Wyslouzil DM (1999) Process development for treatment of complex perovskite, ilmenite and rutile ores. Miner Eng 12:1407–1417. https://doi.org/10.1016/S0892-6875(99)00130-2
8. Bataille C, Åhman M, Neuhoff K, Nilsson LJ, Fischedick M, Lechtenböhmer S, Solano-Rodriquez B, Denis-Ryan A, Stiebert S, Waisman H, Sartor O, Rahbar S (2018) A review of technology and policy deep decarbonization pathway options for making energy-intensive industry production consistent with the Paris agreement. J Clean Prod 187:960–973. https://doi.org/10.1016/j.jclepro.2018.03.107
9. Tang J, Chu M-s, Li F, Feng C, Z-g L, Zhou Y-s (2020) Development and progress on hydrogen metallurgy. Int J Miner Metall Mater 27:713–723. https://doi.org/10.1007/s12613-020-2021-4

10. Liu B, Zhang Y, Su Z, Peng Z, Li G, Jiang T (2017) Thermodynamic analysis and reduction of MnO_2 by methane-hydrogen gas mixture. JOM 69:1669–1675
11. Anacleto N, Ostrovski O (2004) Solid-state reduction of chromium oxide by methane-containing gas. Metall Mater Trans B 35:609–615
12. Zhang G, Ostrovski O (2001) Reduction of ilmenite concentrates by methane containing gas, part II: effects of preoxidation and sintering. Can Metall Q 40:489–497
13. Ksiazek M, Tangstad M, Dalaker H, Ringdalen E (2014) Reduction of SiO_2 to SiC using natural gas. Metall Mater Trans E 1:272–279
14. Ostrovski O, Zhang G (2010) Reduction and carburization of metal oxides by methane-containing gas. AIChE J 52:300–310
15. Dang J, Fatollahi-Fard F, Pistorius PC, Chou KC (2017) Synthesis of titanium oxycarbide from concentrates of natural ilmenite (weathered and unweathered) and natural rutile, using a methane-hydrogen gas mixture. Metall Mater Trans B 48:1–7
16. Zhang R, Liu D, Fan G, Sun H, Dang J (2019) Thermodynamic and experimental study on the reduction and carbonization of TiO_2 through gas-solid reaction. Int J Energy Res 43:4253–4263. https://doi.org/10.1002/er.4551
17. Fan GQ, Hou YL, Huang DJ, Dang J, Zhang R, Xiang JY, Lv XW, Ding XM (2021) Synthesis of Ti(C, N, O) ceramic from rutile at low temperature by CH_4–H_2–N_2 gas mixture. Int J Refract Metal Hard Mater 101:105659. https://doi.org/10.1016/j.ijrmhm.2021.105659

Adsorption Kinetics of Carbon Dioxide in Polymer-Inorganic Powder Composite Materials

Dragutin Nedeljkovic

Abstract One of the major problems in modern society is the huge demand for energy which has as a consequence an enormous amount of waste gas production. Composite materials based on polyethylene oxide matrix and inorganic zeolite powders have been observed to show good properties in the field of carbon dioxide separation. In previous experiments, it has been shown that PEO-zeolite-based membranes show good performance at temperatures up to 398K both in dry and wet conditions. In this work, the influence of the pressure of the waste gases as well as the influence of the partial pressure of the carbon dioxide in the mixture on the overall performance of the membrane were tested.

Keywords Composites · Waste gas treatment · Polymers · Environmental effect · Carbon dioxide capture

Introduction

Recent developments in industrialization, urbanization, and the increased number of inhabitants on the Earth together with a modern way of living have caused an increased demand for energy in all aspects of everyday life. Currently, the majority of energy demand is supplied by fossil fuel sources. Fossil fuels exothermally react with oxygen from the air (combustion) producing carbon dioxide and water as main products and oxides of elements present in crude oil (nitrogen, sulphur, phosphorus) as by-products. Emitted flue gasses (mainly carbon dioxide) have a strong impact on the global warming process causing the "greenhouse effect" [1, 2]. With the increased amount of carbon dioxide in the atmosphere, Earth cannot emit excess heat which results in the increase of the temperature on the surface (thus the name "greenhouse") negatively affecting all biosphere [3]. Carbon dioxide emission is not

D. Nedeljkovic (✉)
College of Engineering and Technology, American University of the Middle East, 54200 Egaila, Kuwait
e-mail: Dragutin.Nedeljkovic@aum.edu.kw

© The Minerals, Metals & Materials Society 2024

C. Iloeje et al. (eds.), *Energy Technology 2024*, The Minerals, Metals & Materials Series, https://doi.org/10.1007/978-3-031-50244-6_4

limited to large-scale combustion plants (heating plants, power plants, metallurgy plants, etc.), but is also produced by everyday communal activity (traffic, transport, etc.). The problem of carbon dioxide concentration has reached such a serious level that it came to the debate by the General Assembly of the United Nations resulting in the 2016 Paris Protocol that calls for drastic reduction of carbon dioxide emission on the global level. However, the current situation is that the concentration of carbon dioxide in the atmosphere reached 420 ppm in 2021 with an increasing trend [4].

Despite constant development and improvements in renewable energy technology (solar, geothermal, wind, etc.) fossil, and non-renewable fuels (coal, crude oil and its derivatives, and natural gas) will remain the main source of energy in the foreseeable future. Therefore, the main goal of future environmental efforts should be in the direction of carbon dioxide emission reduction by its separation from flue gases rather than a decrease in use of the fossil fuels [5, 6]. Several possible solutions for carbon dioxide separation are (i) physical adsorption in which carbon dioxide is physically adsorbed on the surface of the adsorbent. After the adsorbent is saturated, it is recovered by the desorption process and ready for reuse. The main disadvantage of this procedure is a very unfavorable energy balance and a relatively long time for the recovery process. (ii) Chemical adsorption in which carbon dioxide reacts with adsorbent (usually basic solution). The main disadvantage is that the process is often irreversible and even if adsorbent recovery is possible, the energy consumption is too high. Also, in many cases, products of the chemical reaction between adsorbent and carbon dioxide are environmentally hazardous and require further treatment. (iii) Fractional condensation in which carbon dioxide is turned to the liquid state at appropriate pressure–temperature conditions while other combustion products remain as gases. The main disadvantage of this process is the huge amount of energy that is required for cooling to the appropriate temperature [7, 8]. As a feasible alternative to the aforementioned procedures, membrane technologies emerged in recent years. In this type of separation, flue gases are separated by the different permeation properties of the suitable membrane material. In general, membrane separation of carbon dioxide is not limited to the products of combustion in which carbon dioxide is separated from hydrogen, oxygen, and nitrogen (the main topic of this work). In a broader sense, membrane treatment may include carbon dioxide separation from other gas mixtures: synthetic gas treatment (separation from hydrogen only); natural gas production (separation from methane) [9, 10].

A suitable membrane for this application should have the highest possible permeability of carbon dioxide and the lowest possible permeability of all other flue gases. Traditional sieve-like membranes are not suitable for this purpose as the separation should occur at the molecular size which makes synthesis of the porous membrane with suitable sieve openings practically impossible [11–13]. Another potential approach is to use a non-porous (also called dense) membrane. In this type of membrane, separation is based on the adsorption of the components of the mixture on the surface of the membrane, molecular diffusion through the bulk of the membrane, and desorption of the molecules on the permeate side of the membrane. The driving force for the diffusion is the pressure gradient between the two sides of the membrane [14–16]. In the ideal case, the adsorption and diffusion of carbon dioxide

should be as high as possible, while the adsorption and diffusion of other components in the mixture should be as low as possible. Both adsorption and diffusion processes are strongly affected by the temperature and pressure. As this procedure is usually tested at pressures near atmospheric pressure, one of the research directions is to determine the conditions that would enhance the diffusivity of carbon dioxide but reduce the diffusivity of all other components. Theoretical analysis using the Hansen solubility rule on a level of molecular interactions indicates that the presence of ethylene oxide units in the polymer material increases the solubility of carbon dioxide while keeping the solubility of oxygen and hydrogen relatively constant [18]. This prediction was confirmed by experimental results [17]. Therefore, polymers that contain poly(ethylene oxide) (PEO) block were chosen as a suitable material for the membrane. In a series of previous experiments, polymer under the commercial name PEBAX 1657 supplied by Arkema has shown good results in separation [19–23]. Technically, the PEBAX family of bloc co-polymers are thermoplastic elastomers with a nylon block as a mechanical carrier and a PEO block as a rubbery component that also acts as an active component of the membrane [24, 25]. The number in the PEBAX name (in this case 1657) indicates fractions of both blocks. PEBAX 1657 corresponds to 60 mass % of PEO. This particular polymer has been selected based on the previous experiments [19, 26].

Analysis on the molecular level shows that small, almost round, non-polar molecules of hydrogen will have a significantly higher diffusion coefficient than carbon dioxide if all other parameters are equal (which is always the case for gas mixtures). As diffusion is determined by molecular properties, and therefore cannot be used as a selectivity parameter, the main efforts are in the direction of increasing the solubility of carbon dioxide while keeping the solubility of hydrogen (and other gases) as low as possible. Although both molecules of oxygen and nitrogen are non-polar and smaller than carbon dioxide, the difference in size (and consequently, in diffusion coefficient) is not as high as in the case of hydrogen, so the main effort is to decrease the solubility of hydrogen [27–30].

The solubility of carbon dioxide can be further increased by the addition of various additives like zeolite powder. By chemical structure, zeolites are inorganic compounds of aluminum and silicon which in some cases contain other transition metals. Microscopically, zeolite powder contains frameworks with structures similar to a “cage”. The main characterization data for those structures are maximum diffusion diameter—the diameter of the biggest sphere that can freely diffuse through the structure, and maximum sphere diameter—the diameter of the biggest sphere that can be accommodated inside the framework. As a general rule of thumb, the presence of the zeolite powder in the membrane increases the selectivity of the membrane for carbon dioxide versus other gases [31].

The optimal properties of the composite membrane will only be achieved if zeolite powder is evenly distributed through the bulk of the membrane. Therefore, the main challenge is to synthesize a membrane that contains no pin-holes or voids between polymer and zeolite particles, without clusters of powder. As polymer chains and zeolites are hydrophobic and hydrophilic respectively, providing good contact between them is one of the main challenges. The most suitable procedure is to

dissolve both polymer and zeolite in a liquid which is a good solvent for both and to add an appropriate homogenizing agent to the solution. This additive should be compatible with both polymer and solvent and would act as a connector between the two (the working mechanism is similar to the mechanism of detergent) [32].

Materials and Methods

In this paper, influence of different pressures with different partial pressures of carbon dioxide on the permeation properties of carbon dioxide was tested. Commercially available polymer PEBAX 1657 supplied by Arkema was used as received. The structure of this co-polymer of nylon-6 and PEO is presented in Fig. 1.

Based on previous experiments, IWS type of zeolite was selected for the experiments [19]. This type of zeolite contains three-dimensional pores with a diffusion diameter of 87 pm, a maximum sphere diameter of 67 pm, and a specific surface of 800 m^2/g. A specific surface determines the surface that is available for the diffusion of carbon dioxide. IWS zeolite was selected based on good results obtained in previous measurements as well as in tests with repeated measurements under different conditions. An additional advantage of a three-dimensional framework is that molecules can diffuse through it regardless of the orientation. Frameworks with a lower number of dimensions have shown weaker permeation properties as the direction of pores can influence the direction of diffusion. Zeolite powder was supplied by NanoScape and used as received. Characterization of the zeolite powder is supplied by the producer unless stated otherwise.

The homogenizing agent was a detergent-structured compound, *n*-tetradecane trimethyl ammonium bromide (n-C14-TMABr-NTAB), based on the previous research. It was supposed that its polar "head" at the nitrogen atom would serve as a connector to the very polar, electrically zeolite particle. At the same time, a long, normal, alkane, non-polar chain should be compatible with the polymer bulk of the membrane. As a molecule contains both polar and non-polar parts, it was expected that it would serve as a good connector between matrix and powder. NTAB was supplied by Sigma-Aldrich and used as received.

The synthesis procedure for the membrane was as follows:

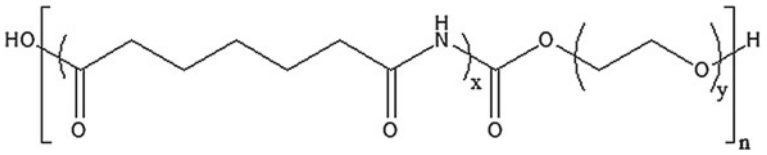

Fig. 1 Structure of the PEBAX 1657 used as a matrix of the membranes

A mixture of water and ethanol (70/30 wt%) at the temperature of 80 °C under reflux was used as a solvent. PEBAX 1657 was added to the solvent. After a homogenous solution was obtained, zeolite powder followed by NTAB was added and ultrasound mixing was performed. The frequency of the ultrasound mixer was 40 kHz, and the power was 90 W. The New solution was stirred overnight at 80 °C under reflux. Amounts of polymer, zeolite, and NTAB were measured in a manner that they form 72%, 20%, and 8% of the membrane by mass, respectively. After stirring resulting viscous solution was casted on the Teflon surface and covered by a non-woven textile. Such conditions were necessary in order to prevent the stitching of the membrane to the surface and the potential formation of the pinhole by dust or similar impurities. Drying was performed overnight under slight underpressure (working hood). If the pressure drop was higher (e.g. vacuum pump) evaporation might be too rapid, and, consequently, residual bubbles may remain in the bulk of the membrane reducing its permeation properties. On the other hand, if the drying process was too slow (e.g. by natural convection), drying would take too long time, and this may cause sedimentation of zeolite particles resulting in their uneven distribution and, consequently, a decrease in permeation properties. Just before the first round of measurements membrane was evacuated on the high vacuum line for approximately one hour in order to remove potential residual solvent.

Measurements of permeability and selectivity were performed using the time-lag method which is based on constant pressure on the permeate side. The following equations were used in order to determine solubility and diffusivity [33–35]:

$$\alpha_{A/B} = \frac{P_A}{P_B} = \frac{D_A S_A}{D_B S_B}$$

$\alpha_{A/B}$ is the selectivity of gas A versus gas B, P is permeability, D is diffusivity, and S is solubility. Index A and B refer to gases A and B, respectively.

$$D = \frac{l^2}{6\theta}$$

l is the thickness of the membrane and θ is the time lag (time required to reach constant pressure on the permeate side)

$$P = D \cdot S = \frac{V_\mathrm{p} l \left(p_{\mathrm{p}_2} - p_{\mathrm{p}_1}\right)}{\mathrm{ART}\Delta t \left(p_\mathrm{f} - \frac{\left(p_{\mathrm{p}_2} + p_{\mathrm{p}_1}\right)}{2}\right)}$$

V_p is the permeate volume, R is the universal gas constant, Δt is for the time required for permeate pressure to increase from value $p_{\mathrm{p}1}$ to value $p_{\mathrm{p}2}$, p_f is feed pressure, A is the surface area of the membrane, T is the temperature at which measurements were conducted, and p_f is initial pressure on the retentive side.

Measurements were performed at four different initial pressures on the retention side (50; 75; 100; and 125 kPa). At each pressure, there is a mixture of carbon

dioxide with another gas. In each of the measurements set for the total pressure, four different compositions (and consequently, four different partial pressures of carbon dioxide) were tested. The composition of the measuring mixture in each measurement was 5, 10, 20, and 30% (mol%) of carbon dioxide with a balance of other gas in the mixture. The membrane was put in the measuring chamber on the steel mash support. Preparation of the measuring mixture was performed in the preparation chamber by measuring pressures of carbon dioxide and other measured gas. The permeate side was initially at the vacuum, and the gas mixture was applied to the feed (retention) side, creating a pressure gradient that acted as the driving force for the diffusion. The pressure was monitored on both sides and the measurement was considered finished when the pressure on the permeate side reached a constant value. After the constant value was reached and the measurement was concluded, the membrane was put on the high vacuum line before the next measurement. The reason is to eliminate any potential residuals of the adsorbed gases in the bulk of the membrane. The composition of the gas mixture on the permeate side was determined by dissolving it in a solution of $Pb(NO_3)_2$ and determination of total amount of carbon dioxide as $PbCO_3$. The complete apparatus for measurement is presented in Fig. 2.

Besides common flue gases, additional measurement was performed with pure helium. The goal was to test the membrane for pin-holes, voids, or any other damage that is invisible by the bare eye. Helium was chosen as it is a very small, non-polar perfectly round molecule with very low safety risk during measurements which makes it a perfect choice for any damage detection. Mixtures of gases with carbon dioxide were measured in such a sequence that the risk of the formation of an explosive or flammable mixture was minimal. The order of measurements was as follows:

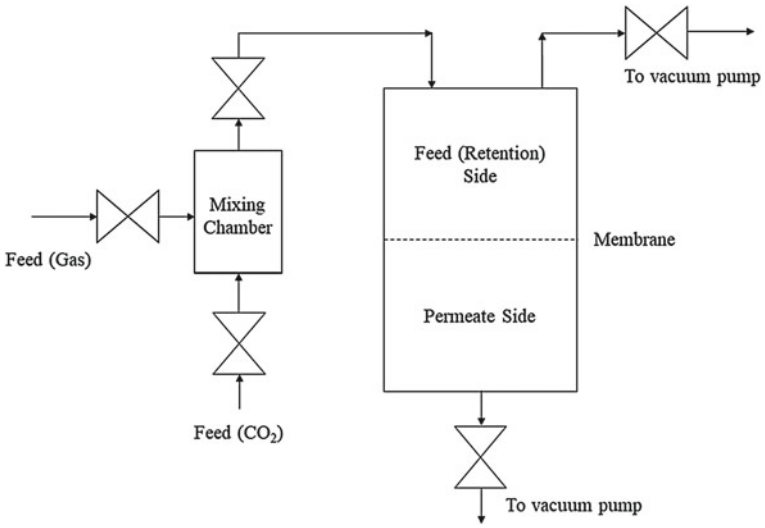

Fig. 2 Scheme of the apparatus for the permeability measurements

He (pure); $CO_2 + H_2$; $CO_2 + N_2$; $CO_2 + O_2$. Each combination was measured three times and the arithmetic mean value was taken as a result.

Results and Discussion

Prepared membranes were transparent to slightly opaque with no visible damage or zones of particle aggregation. The white color of the membrane indicates voids between zeolite particles and polymer bulk due to the light refraction on the surface. Unevenly distributed zeolite particles can be observed by the presence of zones of different opacity or color of the membrane. Any presence of voids or uneven distribution of the particles results in a membrane that cannot be applied for separation. The thickness of the membranes varied between 166 and 241 μm. Permeability is defined as the volume of the gas that passes through the membrane of defined thickness through a defined surface area under a defined pressure gradient in a defined period of time. However, due to practical reasons common unit for permeability is Barrer. The relation between Barrer and the analogous unit in the SI system is given as

$$1\ \text{Barrer} = 3.35 \times 10^{-16} \frac{\text{m}^3}{\text{m}^2\ \text{Pa}\ \text{s}\ \text{m}}$$

Permeation of 1 Barrer means that 1 cm^3 of oxygen at STP conditions diffuses through the 1 cm thick membrane with a surface area of 1 cm^2 in 1 s with a pressure gradient of 1 mmHg.

Results of all selectivity measurements of a mixture of carbon dioxide with hydrogen are presented in Table 1.

As can be seen from Table 1, an increase in pressure gradient increases the permeability of carbon dioxide but plays no significant role in the permeability of hydrogen. This behavior can be attributed to the fact that the permeability of hydrogen is mainly determined by diffusion which is, in return, influenced by temperature much more than by pressure gradient. This leads to a slight increase in selectivity with an increase in pressure gradient. However, further increases in pressure can cause rupture of other types of mechanical failure of the membrane. If measurement sets within the same pressure gradient are compared, it can be seen that an increase in the fraction of carbon dioxide in the mixture causes a very slight decrease in the selectivity. However, the differences are within the error margin of the measurement equipment, and no statistical significance can be observed.

Results of all selectivity measurements of a mixture of carbon dioxide with oxygen are presented in Table 2.

Comparing the results of the membrane selectivity versus oxygen, it can be observed that selectivity is lower than in similar measurements performed on gases separately [21]. This trend is observed for all pressure gradients and feed compositions. Although lower, measured values for oxygen selectivity are in an acceptable

Table 1 Selectivity measurement of mixtures of carbon dioxide in mixture with hydrogen

Pressure gradient (kPa)	Fraction of CO_2 in feed (mol%)	$P(CO_2)$, Barrer	$P(H_2)$, Barrer	$\alpha(CO_2/H_2)$
50	5	105	11.7	9.0
	10	103	11.3	9.1
	20	100	10.1	9.9
	30	97	11	8.8
75	5	110	12	9.2
	10	104	11.5	9.0
	20	106	11.7	9.1
	30	101	11.6	8.7
100	5	115	11.3	10.2
	10	110	11	10.0
	20	105	10.7	9.8
	30	107	10.5	10.2
125	5	117	11.4	10.3
	10	110	11.3	9.7
	20	107	11	9.7
	30	107	10.5	10.2

Table 2 Selectivity measurement of mixtures of carbon dioxide in mixture with oxygen

Pressure gradient (kPa)	Fraction of CO_2 in feed (mol %)	$P(CO_2)$, Barrer	$P(O_2)$, Barrer	$\alpha(CO_2/O_2)$
50	5	103	6	17.2
	10	102	5.9	17.3
	20	98	5.6	17.5
	30	97	5.7	17.0
75	5	105	6.2	16.9
	10	100	5.9	16.9
	20	99	5.7	17.4
	30	96	5.7	16.8
100	5	110	6.4	17.2
	10	105	6.1	17.2
	20	102	6	17.0
	30	103	5.7	18.1
125	5	115	6.6	17.4
	10	107	6.4	16.7
	20	104	6.1	17.0
	30	103	6	17.2

Table 3 Selectivity measurement of mixtures of carbon dioxide in mixture with nitrogen

Pressure gradient (kPa)	Fraction of CO_2 in feed (mol%)	$P(CO_2)$, Barrer	$P(N_2)$, Barrer	$\alpha(CO_2/N_2)$
50	5	110	2.4	45.8
	10	108	2.3	47.0
	20	105	2.3	45.7
	30	102	2.1	48.6
75	5	115	2.2	52.3
	10	109	2	54.5
	20	108	1.9	56.8
	30	106	1.9	55.8
100	5	120	2.3	52.2
	10	115	2.1	54.8
	20	110	2	55.0
	30	108	1.8	60.0
125	5	122	2.4	50.8
	10	115	2.2	52.3
	20	112	2.1	53.3
	30	108	2.1	51.4

range. An increase in pressure gradient slightly increases the permeability of carbon dioxide (similar to the case of hydrogen), but the permeability of oxygen is increased as well. This supports the assumption that pressure gradient is the main driving force for the permeation of bigger molecules, while diffusion is the main cause of permeation for smaller molecules. The composition of the feed stream played no role in the permeation properties of the oxygen.

Results of all selectivity measurements of a mixture of carbon dioxide with nitrogen are presented in Table 3.

Similar to the case of oxygen, the permeability of both carbon dioxide and nitrogen increases with an increased pressure gradient. As the dimensions of oxygen and nitrogen molecules are similar, it is reasonable to conclude that pressure gradient is the main driving force for the permeation of nitrogen. As in the case of oxygen, selectivity versus nitrogen is lower in comparison to measurements of pure gases, but values are still acceptable for future research and developments.

Conclusion

In this work, permeation properties of dense, composite membranes based on PEBAX polymer and IWS zeolite powder with NTAB as an additive were investigated. The main task of this experiment was to test the permeability and selectivity properties of

the membranes if they were exposed to a mixture of gases. Previous measurements were performed on gases separately, so the aim was to see how the membrane would behave in the case of competitive permeation. Three different gas mixtures were measured, each of them with four different compositions and with four different pressure gradients as a driving force. Results that were obtained indicate that an increase in the driving force causes an increase in the permeability of carbon dioxide, oxygen, and nitrogen, but does not influence the permeability of hydrogen. The possible reason for this is that the permeability of small molecules is mainly determined by the diffusion coefficient, while the permeability of bigger molecules is determined by a pressure gradient. In the cases of nitrogen and oxygen, the selectivity of the membrane with the gas mixture was slightly lower in comparison to measurements of the pure gases, possibly because there is competition between different molecules for the positions within the zeolite frame. Having all this in mind, this system has promising potential for future development. In the next steps, measurements of gas mixtures under wet conditions (gas mixture saturated with water vapor) as well as measurements with repeated pressurization and depressurization are planned.

References

1. Desideri U, Corbelli R (1998) CO_2 capture in small size cogeneration plants: technical and economical considerations
2. Rao AB, Rubin ES (2002) A technical, economic, and environmental assessment of amine-based CO_2 capture technology for power plant greenhouse gas control. Environ Sci Technol 36(20):4467–4475. https://doi.org/10.1021/es0158861
3. Mitsch WJ, Bernal B, Nahlik AM, Mander Ü, Zhang L, Anderson CJ, Jørgensen SE, Brix H (2013) Wetlands, carbon, and climate change. Landsc Ecol 28(4):583–597. https://doi.org/10.1007/s10980-012-9758-8
4. Walsh B, Ciais P, Janssens IA, Peñuelas J, Riahi K, Rydzak F, van Vuuren DP, Obersteiner M (2017) Pathways for balancing CO_2 emissions and sinks. Nat Commun 8(1):14856. https://doi.org/10.1038/ncomms14856
5. Chang P-H, Lee T-J, Chang Y-P, Chen S-Y (2013) CO_2 sorbents with scaffold-like Ca•Al layered double hydroxides as precursors for CO_2 capture at high temperatures. Chemsuschem 6(6):1076–1083. https://doi.org/10.1002/cssc.201200910
6. Kuppan CS, Chavali M (2019) CO2 sequestration: processes and methodologies. In: Martínez LMT, Kharissova OV, Kharisov BI (eds) Handbook of ecomaterials. Springer International Publishing, Cham, pp 619–668. https://doi.org/10.1007/978-3-319-68255-6_6
7. Lin Y-J, Pan T-H, Wong S-H, Jang S-S. Plantwide control of CO_2 capture by absorption and stripping using monoethanolamine solution
8. Duarte GS, Schürer B, Voss C, Bathen D (2017) Adsorptive separation of CO_2 from flue gas by temperature swing adsorption processes. ChemBioEng Rev 4(5):277–288. https://doi.org/10.1002/cben.201600029
9. Villalobos LF, Hilke R, Akhtar FH, Peinemann K-V (2018) Fabrication of polybenzimidazole/palladium nanoparticles hollow fiber membranes for hydrogen purification. Adv Energy Mater 8(3):1701567. https://doi.org/10.1002/aenm.201701567
10. Li J-R, Ma Y, McCarthy MC, Sculley J, Yu J, Jeong H-K, Balbuena PB, Zhou H-C (2011) Carbon dioxide capture-related gas adsorption and separation in metal-organic frameworks. Coord Chem Rev 255(15):1791–1823. https://doi.org/10.1016/j.ccr.2011.02.012

11. Vericella JJ, Baker SE, Stolaroff JK, Duoss EB, Hardin JO, Lewicki J, Glogowski E, Floyd WC, Valdez CA, Smith WL, Satcher JH, Bourcier WL, Spadaccini CM, Lewis JA, Aines RD (2015) Encapsulated liquid sorbents for carbon dioxide capture. Nat Commun 6(1):6124. https://doi.org/10.1038/ncomms7124
12. Lee HJ, Kang SW (2020) CO_2 separation with polymer/aniline composite membranes. Polymers 12(6):1363. https://doi.org/10.3390/polym12061363
13. Živković LA, Pohar A, Likozar B, Nikačević NM (2016) Kinetics and reactor modeling for CaO sorption-enhanced high-temperature water-gas shift (SE–WGS) reaction for hydrogen production. Appl Energy 178:844–855. https://doi.org/10.1016/j.apenergy.2016.06.071
14. Živković L, Pohar A, Likozar B, Nikačević N (2019) Reactor conceptual design by optimization for hydrogen production through intensified sorption- and membrane-enhanced water-gas shift reaction. Chem Eng Sci 211:115174. https://doi.org/10.1016/j.ces.2019.115174
15. Ješić D, Lašič Jurković D, Pohar A, Suhadolnik L, Likozar B (2021) Engineering photocatalytic and photoelectrocatalytic CO_2 reduction reactions: mechanisms, intrinsic kinetics, mass transfer resistances, reactors and multi-scale modelling simulations. Chem Eng J 407:126799. https://doi.org/10.1016/j.cej.2020.126799
16. Nunes SP, Peinemann KV (2001) Membrane technology in the chemical industry. Weinheim, New York, Wiley-VCH
17. Koros WJ, Fleming GK, Jordan SM, Kim TH, Hoehn HH (1988) Polymeric membrane materials for solution-diffusion based permeation separations. Prog Polym Sci 13(4):339–401. https://doi.org/10.1016/0079-6700(88)90002-0
18. Akhtar FH, Kumar M, Vovusha H, Shevate R, Villalobos LF, Schwingenschlögl U, Peinemann K-V (2019) Scalable synthesis of amphiphilic copolymers for CO_2—and water-selective membranes: effect of copolymer composition and chain length. Macromolecules 52(16):6213–6226. https://doi.org/10.1021/acs.macromol.9b00528
19. Nedeljkovic D (2021) Homogenization of the dense composite membranes for carbon dioxide separation energy technology 2021: carbon dioxide management and other technologies. 51
20. Lin H, Freeman BD (2004) Gas solubility, diffusivity and permeability in poly(ethylene oxide). J Membr Sci 239(1):105–117. https://doi.org/10.1016/j.memsci.2003.08.031
21. Lin H, Freeman B (2005) Materials selection guidelines for membranes that remove CO_2 from gas mixtures. J Mol Struct 739:57–74. https://doi.org/10.1016/j.molstruc.2004.07.045
22. Jankowski A, Grabiec E, Nocoń-Szmajda K, Marcinkowski A, Janeczek H, Wolińska-Grabczyk A (2021) Polyimide-based membrane materials for CO_2 separation: a comparison of segmented and aromatic (co)polyimides. Membranes 11(4):274. https://doi.org/10.3390/membranes11040274
23. Esposito E, Bruno R, Monteleone M, Fuoco A, Ferrando Soria J, Pardo E, Armentano D, Jansen JC (2020) Glassy PEEK-WC vs. Rubbery Pebax®1657 polymers: effect on the gas transport in CuNi-MOF based mixed matrix membranes. Appl Sci 10(4):1310. https://doi.org/10.3390/app10041310
24. Baker RW (2012) Membrane technology and applications, 3rd edn. Wiley, Chichester, West Sussex, Hoboken
25. Baker RW (2002) Future directions of membrane gas separation technology. Ind Eng Chem Res. https://doi.org/10.1021/ie0108088
26. Nedeljkovic D (2021) The effect of the temperature and moisture to the permeation properties of PEO-based membranes for carbon-dioxide separation. Polymers 13(13):2053. https://doi.org/10.3390/polym13132053
27. Chen JC, Feng X, Penlidis A (2005) Gas permeation through poly(ether-b-amide) (PEBAX 2533) block copolymer membranes. Sep Sci Technol 39(1):149–164. https://doi.org/10.1081/SS-120027406
28. Bondar VI, Freeman BD, Pinnau I (1999) Gas sorption and characterization of poly(ether-b-amide) segmented block copolymers. J Polym Sci Part B Polym Phys 37(17):2463–2475. https://doi.org/10.1002/(SICI)1099-0488(19990901)37:17<2463::AID-POLB18>3.0.CO;2-H.

29. Bondar VI, Freeman BD, Pinnau I (2000) Gas transport properties of poly(ether-b-amide) segmented block copolymers. J Polym Sci Part B Polym Phys 38(15):2051–2062. https://doi.org/10.1002/1099-0488(20000801)38:15<2051::AID-POLB100>3.0.CO;2-D
30. Kupka V, Dvořáková E, Manakhov A, Michlíček M, Petruš J, Vojtová L, Zajíčková L (2020) Well-blended PCL/PEO electrospun nanofibers with functional properties enhanced by plasma processing. Polymers 12(6):1403. https://doi.org/10.3390/polym12061403
31. Asghari M, Mosadegh M, Riasat Harami H (2018) Supported PEBA-Zeolite 13X nanocomposite membranes for gas separation: preparation, characterization and molecular dynamics simulation. Chem Eng Sci 187:67–78. https://doi.org/10.1016/j.ces.2018.04.067
32. Chen XY, Nik OG, Rodrigue D, Kaliaguine S (2012) Mixed matrix membranes of aminosilanes grafted FAU/EMT zeolite and cross-linked polyimide for CO_2/CH4 separation. Polymer 53(15):3269–3280. https://doi.org/10.1016/j.polymer.2012.03.017
33. Yoshino M, Ito K, Kita H, Okamoto K-I (2000) Effects of hard-segment polymers on CO_2/N_2 gas-separation properties of poly(ethylene oxide)-segmented copolymers. J Polym Sci Part B Polym Phys 38(13):1707–1715. https://doi.org/10.1002/1099-0488(20000701)38:13<1707::AID-POLB40>3.0.CO;2-W
34. Buttersack C, Rudolph H, Mahrholz J, Buchholz K (1996) High specific interaction of polymers with the pores of hydrophobic zeolites. Langmuir 12(13):3101–3106. https://doi.org/10.1021/la950727e
35. Car A, Stropnik C, Yave W, Peinemann K-V (2008) Tailor-made polymeric membranes based on segmented block copolymers for CO_2 separation. Adv Funct Mater 18(18):2815–2823. https://doi.org/10.1002/adfm.200800436

Part II
Energy Efficiency, Electrification and Carbon Management

Benchmarking of Energy Consumption and CO_2 Emissions in Cement Production: A Case Study

Shoaib Sarfraz, Ziyad Sherif, Mark Jolly, and Konstantinos Salonitis

Abstract In the pursuit of economic growth and value creation, foundation industries including cement, metals, glass, chemicals, paper, and ceramics face formidable challenges related to energy usage, emissions, and resource consumption in their manufacturing operations, all while striving to achieve ambitious Net Zero carbon and green targets. To overcome these challenges and propel sustainable progress, benchmarking emerges as a powerful ally. This study performs a benchmarking analysis of energy use and CO_2 emissions for a UK cement plant as well as best available techniques (BAT) investigation to identify opportunities for performance improvement in crucial areas such as energy usage and environmental sustainability. The research utilises industrial data from a 2850 tonne per day capacity dry process cement plant. Key energy and emissions parameters, including thermal and electrical energy intensity, recovered energy and CO_2 intensity, are computed per tonne of cement produced along with capacity utilisation across major process stages including raw material grinding, clinkerisation, and cement grinding. Comprehensive data sourced directly from the manufacturer is compared against literature benchmarks for global averages and best practices. Although surpassing global average values, the plant lags European best practices across all metrics, signalling room for substantial improvement. Assessment of relevant BATs for the cement industry reveals prospects to integrate vertical roller mills for cement grinding and use Organic Rankine Cycle

S. Sarfraz (✉) · Z. Sherif · M. Jolly · K. Salonitis
Sustainable Manufacturing Systems Centre, School of Aerospace, Transport and Manufacturing, Cranfield University, Cranfield, Bedfordshire MK43 0AL, UK
e-mail: shoaib.sarfraz@cranfield.ac.uk

Z. Sherif
e-mail: z.sherif@cranfield.ac.uk

M. Jolly
e-mail: m.r.jolly@cranfield.ac.uk

K. Salonitis
e-mail: k.salonitis@cranfield.ac.uk

© The Minerals, Metals & Materials Society 2024

C. Iloeje et al. (eds.), *Energy Technology 2024*, The Minerals, Metals & Materials Series, https://doi.org/10.1007/978-3-031-50244-6_5

(ORC) at the clinkerisation stage. Adopting these techniques could reduce the electrical energy intensity of clinkerisation by 51% and cement grinding electrical intensity by 30%, surpassing benchmarks. While limited to a single cement plant, the study provides a standardised methodology that could be replicated across foundation industries to enable performance tracking and highlight efficiency gaps. The benchmarking approach developed can guide the implementation of energy conservation measures and the adoption of best practices by the cement industry to reduce its carbon footprint.

Keywords Sustainable manufacturing · Benchmarking · Energy efficiency · Foundation industries · Net zero

Introduction

Foundation industries including cement, metals, glass, chemicals, paper, and ceramics serve as crucial industries, generating wealth and significantly representing a nation's economy and overall strength. These industries provide £52 billion to the UK economy by producing 28 Mt of materials annually [1]. However, while meeting human demands through the production of goods and services, the foundation industries consume substantial amounts of limited energy and materials, often with low energy efficiency and resource conversion rates. This inefficiency leads to significant waste and severe environmental damage [2]. The foundation industries are responsible for around 10% of total CO_2 emissions [3]. Significant energy consumption and emissions growth have led to severe environmental pollution. The 2017 energy efficiency survey report indicates that the global demand for fossil energy continues to rise, resulting in a general increase of over 30% in global energy consumption [4]. Notably, the industrial sector is a major contributor to this escalating energy demand, accounting for more than 53% of the nation's total energy consumption [5]. In this context, it is critical for foundation industries to improve their environmental sustainability and reduce their resource consumption. Benchmarking is a powerful tool that helps industries identify and prioritise opportunities to improve energy efficiency and environmental sustainability [6–8]. This tool has been well-developed for more than 40 years, after first being used by Xerox Corporation in the early 1980s. Xerox's approach involved studying and learning from various industries, not just its direct competitors, in order to identify best practices and innovative strategies that could be applied to their operations [9].

The cement industry ranks as the third-largest consumer of industrial energy worldwide, responsible for approximately 7% of global industrial energy consumption and ~ 7% of global CO_2 emissions, faces particular challenges in achieving sustainability due to its inherent energy- and emissions-intensive production processes [10, 11]. Although the cement industry recognises the need to reduce its environmental impacts, benchmarking initiatives remain limited [12]. Global studies reveal wide variability in energy efficiency and carbon emissions between different

cement plants, suggesting major potential for improvement through systematic benchmarking [12]. However, comprehensive data is lacking, as cement producers are often reluctant to share detailed operational insights.

This study focuses on benchmarking the energy usage and carbon emissions of a UK cement plant to pinpoint opportunities for enhancing efficiency and reducing environmental impacts. A tailored benchmarking methodology that incorporates BAT analysis has been developed to evaluate the cement plant's thermal energy intensity, electrical energy intensity, waste heat recovery, CO_2 intensity and capacity utilisation. Metrics are compared against industry best practices to highlight potential areas for improvement. The primary objective of this study is to enhance the sustainability of energy and emission intensive manufacturing processes, with a strong focus on environmental considerations and resource efficiency. Therefore, this study aims to achieve this by introducing a benchmarking approach, which offers a systematic method for evaluating and enhancing the sustainability of manufacturing systems. Ultimately, this endeavour is expected to foster the growth and advancement of the manufacturing industry while promoting environmentally friendly practices and resource conservation.

Benchmarking Approach Development

This section outlines the steps involved in the benchmarking approach development process and provides the rationale behind each step.

Understanding the Manufacturing Operations of Foundation Industries

A generic process model has been developed to elucidate the key elements involved in manufacturing operations across various foundational industries (Fig. 1). This model illustrates the typical inputs and outputs that are inherent to production processes. Inputs encompass raw materials, electricity, and fuel, which provide the physical components, energy, and power needed to enable manufacturing activities. Outputs include the desired final manufactured products, as well as waste streams and carbon dioxide emissions, which tend to be unavoidable by-products of industrial production.

A salient feature of the model is its illustration of process heat recovery as a key component. Many manufacturing processes intrinsically generate significant waste heat, which represents a loss of energy efficiency if not harnessed. Thus, incorporating heat capture and reuse into process designs can dramatically improve the energy efficiency and environmental profile of manufacturing. Additionally, the model highlights machine capacity utilization as a vital parameter in optimising industrial

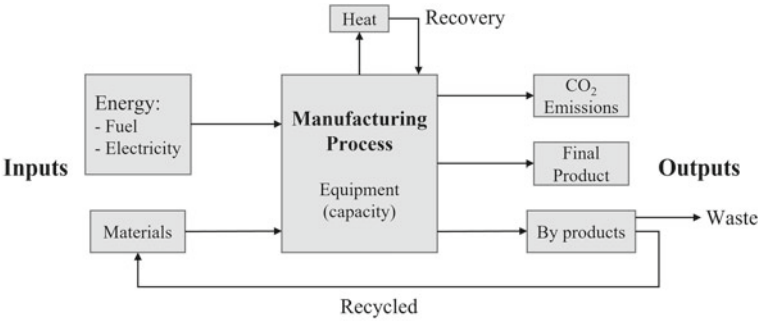

Fig. 1 Generic manufacturing process model of inputs–outputs

production. Running machines at maximum capacity boosts productivity and diminishes per unit costs. However, energy, materials, and labour must be balanced to avoid inefficiencies associated with over-capacity.

Identification of Key Process Metrics

Both intensity and performance-based metrics have been utilised in this work to evaluate manufacturing efficiency from complementary perspectives. As noted by Jaller and Matthews [13], intensity-based measures that quantify emissions per unit output offer valuable insight into efficiencies, as declining emissions per product indicate improved environmental performance over time. Though intensity metrics do not directly correlate with overall emission reductions, they enable critical trend analyses. Furthermore, performance metrics that gauge the achievement of economic and regulatory targets are essential, as highlighted by Ogunsiji and Ladanu [14]. In a manufacturing context, performance indicators provide insights into operational performance while highlighting performance gaps and continuous improvement opportunities. Thus, this study employs intensity metrics for their utility in tracking efficiency gains, alongside performance metrics to assess broader goal attainment. This dual intensity and performance-based approach thereby enables a multidimensional assessment of manufacturing efficiency. The chosen metrics along with description and units are provided in Table 1.

Table 1 Vital sign metrics for manufacturing sustainability

Metric	Description	Formula	Unit
Thermal energy intensity	The amount of thermal energy used to produce a unit of output	(Thermal energy consumed)/(unit mass produced)	kWh/t
Electrical energy intensity	The amount of electrical energy used to produce a unit of output	(Electrical energy consumed)/(unit mass produced)	kWh/t
Energy recovered (heat)	The amount of energy recovered or reused from the process	(Recovered energy)/(total energy waste)	%
CO_2 intensity	Total direct emissions per unit mass produced	(CO_2 emissions)/(unit mass produced)	tCO_2/t
Capacity utilisation	The extent to which production capacity is being used	(Actual output rate)/(max possible output rate)	%

Data Collection Points

Industry Data Collection

Based on the selected metrics, a data template was developed to facilitate the benchmarking process, as given in Table 2. This will capture and organise multiple entries, such as product type, equipment used, process conditions, process specification, and measurement methods used which is an important part of data collection.

The measurement method used to collect data affects the accuracy of the data. For example, collecting data using sensors on the machine or equipment (such as an energy meter) can provide more accurate data than using bill data or production output data. Additionally, it pinpoints the extent of the data presented, whether it directly results from the process or encompasses other aspects beyond the process (such as indirect emissions or auxiliary energy consumption). The current value represents the value provided by the manufacturer which was compared with the global average and best practice values.

Table 2 Data collection template

Process data form				
	Process			
	Product type			
	Equipment used			
	Process conditions			
	Process specification			
	Metrics	Unit	Measurement method	Current value
1	Thermal energy intensity			
2	Electrical energy intensity			
3	Energy recovered			
4	Capacity utilisation			
5	CO_2 intensity			

Literature Data Collection

This section outlines the procedure adopted to collect essential data from the literature, comprising global average and best practice values, as well as best available techniques (BATs) and their associated impacts and costs. The gathered information is instrumental in assessing company performance, comparing it with industry standards, and exploring potential avenues for efficiency improvement. This establishes the basis for evaluating manufacturing processes and the potential adoption of BATs.

Global and Best Practice Values The procedure employed in this study follows a comprehensive approach to gather data concerning global average values, as well as best practice benchmarks, relevant to the various identified metrics. A literature review was conducted to collect relevant information from articles, industry reports, and government publications. The primary aim of this data collection was to establish a solid foundation for benchmarking the manufacturing processes under investigation. By analysing these averages and best practice standards, this study intends to assess company performance and compare operational data against industry norms, facilitating the identification of areas for potential improvement and efficiency enhancement.

BATs, Their Impact, and Associated Cost of Implementation Within the approach, a thorough exploration of BATs for the manufacturing processes under scrutiny was undertaken. A comprehensive examination of BATs, including their associated impacts, as well as the estimated costs of implementation, was conducted. This analysis drew upon data derived from various studies, governmental bodies, and environmental agencies. The main objective of this analysis was to provide a comprehensive understanding of the potential benefits and economic implications associated with the adoption of BATs. By evaluating the feasibility and cost-effectiveness of BAT implementation, this study aims to assist companies in making informed decisions concerning process improvements, while also quantifying the resulting savings in energy consumption.

Developed Benchmarking Approach

The benchmarking approach adopted in this study (Fig. 2) is structured around three key pillars. The first pillar involves an extensive literature review, which encompasses the collection of data on best practices, global averages, and BATs along with their associated environmental and cost considerations. The second pillar centres on the acquisition of industry-specific data, including production, processing, and equipment-related information within the manufacturing processes under examination. The final pillar revolves around data analysis, which includes the comparative assessment of industry data against benchmarks, an evaluation of the potential impact of best practices and BATs, and the estimation of cost savings. This holistic

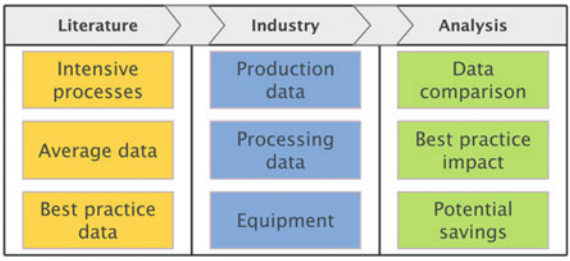

Fig. 2 Benchmarking approach overview

approach equips the study with the necessary insights to evaluate manufacturing processes objectively, identify areas for enhancement, and make informed decisions concerning efficiency improvements and sustainability.

Case Study Results and Discussion

Utilising the developed benchmarking approach, a case study was conducted with a prominent cement manufacturer based in the UK having a plant capacity of 2850 t/day. Notably, the cement manufacturing industry, one of the major foundation industries, stands as a significant consumer, demanding nearly 15% of the total industrial energy use due to its energy-intensive processes [15]. The case study reveals significant relevance for advancing sustainable practices within this vital sector.

Industry Versus Literature Metrics Data

A detailed comparison was conducted between data sourced from the industry, employing the developed data collection template, and data obtained from the literature. The dataset encompasses three pivotal processes: raw meal grinding, clinkerisation, and finish grinding, collectively constituting 20%, 25%, and 40% of the total energy demand in cement production, respectively [16]. Specifically, the clinkerisation stage is scrutinized for thermal energy intensity, heat energy recovery, CO_2 intensity, and capacity metrics. In contrast, electrical energy intensity is analysed across all stages. The data are presented in Fig. 3. This evaluation revealed that the performance of the plant in question surpasses global average values in all aspects for all stages. However, there is still room for improvement as their values fall short of best practice benchmarks both globally and in Europe.

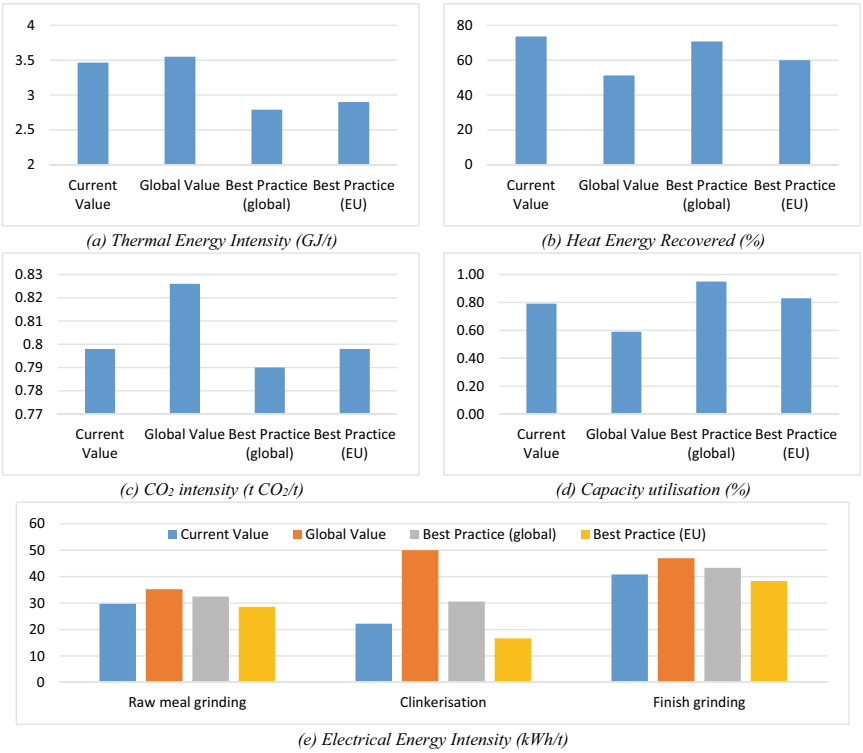

(a) Thermal Energy Intensity (GJ/t)

(b) Heat Energy Recovered (%)

(c) CO_2 intensity (t CO_2/t)

(d) Capacity utilisation (%)

(e) Electrical Energy Intensity (kWh/t)

Fig. 3 Industry versus literature data visualisation. **a**–**d** represents the Clinkerisation stage only while, **e** shows all three stages [16–26]. *Note* The current values of all metrics i.e., thermal energy intensity, heat energy recovered, CO_2 intensity, capacity utilisation, and electrical energy intensity are directly obtained from the industry.

BATs Identification and Analysis

The subsequent step entailed the acquirement of BATs relevant to cement manufacturing. Tackling energy consumption was prioritised, and for this reason, BATs related to energy consumption were examined. This includes detailed data on their associated electrical and thermal energy savings, as well as implementation costs, sourced from literature. The dataset comprises BATs tailored to the three production stages, in addition to generic techniques with broader applicability across the entire cement plant. This compilation phase establishes the groundwork for the evaluation of potential improvements within the studied industry (Table 3).

Table 3 Cement BAT, their energy impact, and associated cost [27–31]

	BAT applicable to the cement sector (Energy)	Savings		Implementation cost (M€)
		Electric (MJ/t)	Thermal (MJ/t)	
1	Replacing a ball mill with a vertical roller mill in raw material grinding	40	0	29.9
2	Use of gravity-type homogenising silo for raw material blending	10	0	6
3	Changing from long kilns to kilns with cyclone preheaters and pre-calciner	18	1800	85
4	Organic Rankine Cycle (ORC) for power generation through waste energy recovery	41	0	20
5	Changing from rotary or satellite coolers to modern grate coolers	−18	200	17.5
6	Using 5 or 6 stage cyclone preheater	0	90	6.5
7	Replacing ball mills with vertical roller mills in cement grinding	43	0	25
8	Using high efficiency separator for cement grinding	12	0	1.5
9	Using variable speed drives for all fans	6	0	0.16
10	Introduction of process control optimisation (Advanced plant control systems)	8.5	95	2.6
11	Replace low efficiency motors with premium and super premium efficiency motors (IE3 and IE4)	14.5	0	0.5

The negative sign (−) denotes an increase in energy consumption cause by implementing a technology

Industry BAT Adoption and Impact

Following the identification and assessment of the applicable BATs employed by the company, a commendable adoption of many recognised techniques was revealed. Nevertheless, two notable exceptions emerged. The first pertains to the untapped

potential of harnessing power through waste energy recovery at the clinkerisation stage, a prospect offered by the Organic Rankine Cycle (ORC). The second involves the integration of vertical roller mills (VRM) for cement grinding, showcasing opportunities for further refinement in the company's manufacturing processes.

The potential energy intensity values are computed based on the savings conceivable by adopting the lacking BATs and compared to the best practice values. In the case of clinker production, the potential electrical intensity could be reduced by 51%. Furthermore, utilising VRM for cement grinding could potentially reduce the electrical energy consumption by 30%. This will allow the company to surpass best practice energy use values, as shown in Fig. 4.

The potential total energy savings of each stage have been compared with the implementation cost of the identified BATs. As seen from Fig. 5, it is evident that the BAT for clinker production incurs lower implementation costs but yields less energy savings. However, the additional EUR 5 million needed for implementing the cement grinding BAT may not justify the possible 0.5 kWh/t extra savings. Therefore, implementing ORC for energy generation maybe the more economical option.

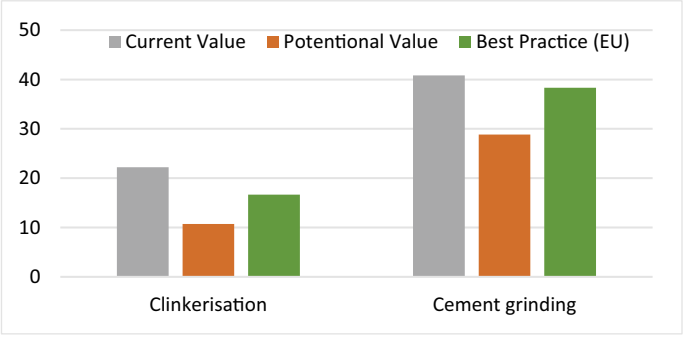

Fig. 4 Current and potential electrical energy values (kWh/t) comparison

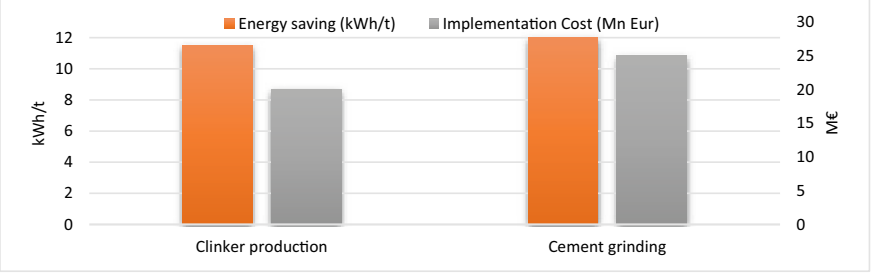

Fig. 5 Energy saving (GJ/t) versus cost (M€)

Conclusion

This study demonstrates the value of benchmarking as a tool for assessing and improving the energy efficiency and carbon footprint of energy-intensive manufacturing processes, using a UK cement plant as a case study. The benchmarking analysis quantified the plant's energy intensity and CO_2 emissions per tonne of cement produced across key process stages including raw material grinding, clinker production, and cement grinding. Performance gaps were revealed relative to current global averages and best practices.

The study also compiled relevant best available techniques (BATs) for the cement sector, revealing additional prospects to integrate vertical roller mills for cement grinding and use Organic Rankine Cycle to increase waste heat recovery. Adopting these BATs could reduce the electrical energy intensity of cement grinding by 30% and clinkerisation by 51%, surpassing global benchmarks. A preliminary economic analysis further showed clinker production improvements may offer a more economical energy saving option. This is due to the considerably lower implementation cost (EUR 5 million) while providing a relatively similar energy saving potential ($\pm$5 kWh/t).

Overall, this research demonstrates the usefulness of a benchmarking procedure that incorporates BATs for cement manufacturers to identify performance gaps, best practices, and efficiency opportunities. Although limited to a single cement plant, the standardised methodology could be replicated across multiple sites to support step-change improvements industry wide. The approach could also be adapted to enhance sustainability in other foundation industry sectors.

The study acknowledges certain limitations in its methodology. While BATs affecting energy consumption are thoroughly examined, their impact on emissions is not included in this analysis. Additionally, while energy savings are compared to initial implementation costs, long-term cost-effectiveness is a factor that warrants further consideration. Moreover, the study considers the cost of implementation in a generalised sense, without delving into the specific costs that may be influenced by plant layout and other site-specific factors. These limitations serve as areas for potential refinement and consideration in future analyses.

Acknowledgements Authors are grateful to managers in the UK cement company who participated in this study and provided us the required information and data. We would also like to acknowledge the UK EPSRC-funded project "Transforming Foundation Industries Research and Innovation Hub (TransFIRe)" (EP/V054627/1) for the support of this work. All data supporting this study are provided in full in this paper.

References

1. Jolly M, Velenturf APM, Salonitis K, Paddea S (2022) The UK transforming the foundation industries research and innovation hub (TransFIRe), pp 341–353

2. Cai W, Liu C, Lai K, Li L, Cunha J, Hu L (2019) Energy performance certification in mechanical manufacturing industry: a review and analysis. Energy Convers Manag 186:415–432. https://doi.org/10.1016/j.enconman.2019.02.041
3. Griffin PW, Hammond GP, McKenna RC (2021) Industrial energy use and decarbonisation in the glass sector: a UK perspective. Adv Appl Energy 3:100037. https://doi.org/10.1016/j.adapen.2021.100037
4. IEA (International Energy Agency) (2017) World energy outlook 2017 [online]. Available https://iea.blob.core.windows.net/assets/4a50d774-5e8c-457e-bcc9-513357f9b2fb/World_Energy_Outlook_2017.pdf
5. Garwood TL, Hughes BR, Oates MR, O'Connor D, Hughes R (2018) A review of energy simulation tools for the manufacturing sector. Renew Sustain Energy Rev 81:895–911. https://doi.org/10.1016/j.rser.2017.08.063
6. Rogers JG, Cooper SJ, Norman JB (2018) Uses of industrial energy benchmarking with reference to the pulp and paper industries. Renew Sustain Energy Rev 95:23–37. https://doi.org/10.1016/j.rser.2018.06.019
7. Menghi R, Papetti A, Germani M, Marconi M (2019) Energy efficiency of manufacturing systems: a review of energy assessment methods and tools. J Clean Prod 240:118276. https://doi.org/10.1016/j.jclepro.2019.118276
8. Cai W et al (2022) A review on methods of energy performance improvement towards sustainable manufacturing from perspectives of energy monitoring, evaluation, optimization and benchmarking. Renew Sustain Energy Rev 159:112227. https://doi.org/10.1016/j.rser.2022.112227
9. Adewunmi YA, Iyagba R, Omirin M (2017) Multi-sector framework for benchmarking in facilities management. Benchmarking Int J 24(4):826–856. https://doi.org/10.1108/BIJ-10-2015-0093
10. Mittelman E (2018) The cement industry, one of the world's largest CO_2 emitters, pledges to cut greenhouse gases. Yale E360. 24 Nov 2018 [online]. Available https://e360.yale.edu/digest/the-cement-industry-one-of-the-worlds-largest-co2-emitters-pledges-to-cut-greenhouse-gases
11. Junianto I, Sunardi DS (2023) The possibility of achieving zero CO_2 emission in the Indonesian cement industry by 2050: a stakeholder system dynamic perspective. Sustainability 15(7):6085. https://doi.org/10.3390/su15076085
12. IEA (2018) Technology roadmap: low-carbon transition in the cement industry. Accessed 17 Aug 2023 [online]. Available https://www.iea.org/reports/technology-roadmap-low-carbon-transition-in-the-cement-industry
13. Jaller M, Matthews S (2021) Can carbon intensity metrics help achieve net carbon reductions [online]. Available https://faculty.engineering.ucdavis.edu/jaller/wp-content/uploads/sites/298/2021/06/92021-Jaller-and-Matthews-Can-Carbon-Intensity-Metrics-Help-Achieve-Net-Carbon-Reductions.pdf
14. Ogunsiji AS, Ladanu WK (2017) A theoretical study of performance measures in the strategic and corporate entrepreneurship of firms. Int J Life Sci 1(1):49–57. https://doi.org/10.21744/ijls.v1i1.23
15. Gholipour Khajeh M, Iranmanesh M, Keynia F (2014) Energy auditing in cement industry: a case study. Energy Equip Syst 2(2):171–184
16. Madlool NA, Saidur R, Hossain MS, Rahim NA (2011) A critical review on energy use and savings in the cement industries. Renew Sustain Energy Rev 15(4):2042–2060 [online]. Available https://doi.org/10.1016/j.rser.2011.01.005
17. IEA (2022) Cement [online]. Available https://www.iea.org/reports/cement
18. Austrian Energy Agency (2014) industrial energy efficiency project: benchmarking report for cement sector. United Nations Industrial Development Organization. Accessed 01 Sept 2023 [online]. Available https://www.unido.org/sites/default/files/files/2019-05/BenchmarkingReportCementSector.pdf
19. Prakasan S, Palaniappan S, Gettu R (2020) Study of energy use and CO_2 emissions in the manufacturing of clinker and cement. J Inst Eng Ser A 101(1):221–232. https://doi.org/10.1007/s40030-019-00409-4

20. Afkhami B, Akbarian B, Beheshti N, Kakaee AH, Shabani B (2015) Energy consumption assessment in a cement production plant. Sustain Energy Technol Assessments 10:84–89. https://doi.org/10.1016/j.seta.2015.03.003
21. Omotayo JSO (2023) Economic impacts of optimizing energy recovery in clinker cooler using clinker cooler bed as a case study. J Eng Technol Res 15(1):17–26. https://doi.org/10.5897/JETR2022.0737
22. Rasul MG, Widianto W, Mohanty B (2005) Assessment of the thermal performance and energy conservation opportunities of a cement industry in Indonesia. Appl Therm Eng 25(17–18):2950–2965. https://doi.org/10.1016/j.applthermaleng.2005.03.003
23. CEMBUREAU (2023) Waste-to-energy. CEMBUREAU, The European Cement Association. https://www.cembureau.eu/policy-focus/environment/waste-to-energy/. Accessed 16 Aug 2023
24. Sousa V, Bogas JA (2021) Comparison of energy consumption and carbon emissions from clinker and recycled cement production. J Clean Prod 306:127277 [online]. Available https://www.sciencedirect.com/science/article/pii/S0959652621014967
25. Czigler T, Reiter S, Schulze P, Somers K (2020) Laying the foundation for zero-carbon cement. McKinsey & Company
26. European Union (2013) Establishing the best available techniques (BAT) conclusions under Directive 2010/75/EU of the European parliament and of the council on industrial emissions for the production of cement, lime and magnesium oxide. Official J Euro Union. Accessed 14 Aug 2023 [online]. Available https://eippcb.jrc.ec.europa.eu/sites/default/files/2019-11/CLM_BATC_Published.pdf
27. Zuberi MJS, Patel MK (2017) Bottom-up analysis of energy efficiency improvement and CO_2 emission reduction potentials in the Swiss cement industry. J Clean Prod 142:4294–4309. https://doi.org/10.1016/j.jclepro.2016.11.178
28. Huang YH, Chang YL, Fleiter T (2016) A critical analysis of energy efficiency improvement potentials in Taiwan's cement industry. Energy Policy 96:14–26. https://doi.org/10.1016/j.enpol.2016.05.025
29. Brunke JC, Blesl M (2014) Energy conservation measures for the German cement industry and their ability to compensate for rising energy-related production costs. J Clean Prod 82:94–111. https://doi.org/10.1016/j.jclepro.2014.06.074
30. ECRA (2022) State of the Art cement manufacturing: current technologies and their future development. European Cement Research Academy. Accessed 01 Sept 2023 [online]. Available https://ecra-online.org/fileadmin/redaktion/files/pdf/ECRA_Technology_Papers_2022.pdf
31. Kourti I, Sancho LD, Schorcht F, Roudier S, Scalet BM (2013) Best available techniques (BAT) reference document for the production of cement, lime and magnesium oxide: industrial emissions directive 2010/75/EU (integrated pollution prevention and control). Publications Office [online]. Available https://data.europa.eu/doi/10.2788/12850

Low-Energy Processing of a Local Boltwoodite Ore as Intermediate in Nuclear Fuel Cell

Alafara A. Baba, Mustapha A. Raji, Kehinde I. Omoniyi, Shemang Y. Chindo, Aduagba G. Kareem, Abhilash, Pratima Meshram, Amudat Lawal, and Folahan A. Adekola

Abstract The industrial demand for pure uranium and uranium compounds is tremendously increasing due to its wide array of utilities most especially in nuclear industries. Consequently, the treatment of a local boltwoodite ore containing *albite* ($Na_{2.00}Al_{2.00}Si_{6.00}O_{16.00}$: 96-900-1634), *boltwoodite* ($Na_{2.00}K_{2.77}U_{3.00}Si_{6.00}O_{9.00}H_{4.00}$: 96-900-7219), *thorite* ($Th_{4.00}Si_{4.00}O_{16.00}$: 96-900-7625), and *quartz* ($Si_{6.00}O_{6.00}$: 96-900-5019) was examined in sulphuric acid media. The experimental parameters such as leachant concentration, reaction temperature, and particle size on uranium ore dissolution were investigated. At optimal leaching conditions (2.5 mol/L H_2SO_4, 75 °C, and 75 μm), an 89.1% dissolution rate was achieved within 120 min. The estimated activation energy of 20.70 kJ/mol supported the diffusion control reaction mechanism as the rate-determining step. The leach liquor obtained at established conditions was further beneficiated to produce an industrial grade *sodium diuranate* ($Na_2U_2O_7$: 00-064-0473, density = 6.51 g/cm^3, melting point = 1654 ± 2 °C) proposed to serve as intermediate raw-material in a nuclear fuel cell.

A. A. Baba (✉) · M. A. Raji (✉) · F. A. Adekola
Department of Industrial Chemistry, University of Ilorin, P.M.B. 1515, Ilorin 240003, Nigeria
e-mail: baalafara@yahoo.com; alafara@unilorin.edu.ng

M. A. Raji
e-mail: mustaphaadekunle48@gmail.com

K. I. Omoniyi · S. Y. Chindo
Department of Chemistry, Ahmadu Bello University, P.M.B. 06, Zaria 810211, Nigeria

A. G. Kareem
Aeronautics and Air Vehicle Development Institute, Kaduna, Nigeria

National Agency for Science and Engineering Infrastructure, Abuja, Nigeria

Abhilash · P. Meshram
National Metallurgical Laboratory (CSIR), Jamshedpur, Jharkhand 831007, India

A. Lawal
Department of Chemistry, University of Ilorin, P.M.B. 1515, Ilorin 240003, Nigeria

© The Minerals, Metals & Materials Society 2024

C. Iloeje et al. (eds.), *Energy Technology 2024*, The Minerals, Metals & Materials Series, https://doi.org/10.1007/978-3-031-50244-6_6

Keywords Boltwoodite ore · Leaching · Intermediate · Low energy · Nuclear fuel cell

Introduction

In recent years, and as the global appreciable demand for energy continues to rise due to population growth coupled with a fast-growing economy, nuclear energy is likely to play a major role in reducing over-reliance on fossil fuels while achieving supply security and reducing carbon emissions that often contribute to climate change. However, uranium and uranium compounds are very attractive and robust sources of energy due to their efficiency, high energy density, reliability, and eco-friendliness [1]. Uranium, one of the most versatile strategic metals finds wide arrays of applications in the nuclear industry, catalysis, armored piercing, scientific research, and medical treatment, among others [2, 3].

In addition, before uranium can attain nuclear fuel cell grade, it has to go through different processing stages including comminution, leaching, concentration, purification by solvent extraction, and chemical precipitation [4]. There are several methods of leaching uranium ores depending on the mineralogical compositions of the ore. However, acid and alkaline leaching is the most commonly employed route for the leaching of uranium ores. Generally, the acid leach process has been reported to have rapid dissolution kinetics with high uranium recovery, and short leaching time and can be performed at a lower temperature compared with the alkaline leach method [5]. Presently, the most common acid-leaching agents employed for uranium ore dissolution are sulphuric acid (H_2SO_4), nitric acid (HNO_3), or hydrochloric acid (HCl) solutions [6, 7]. Due to the corrosive nature of HNO_3 coupled with the chloro-complex formation of HCl, H_2SO_4 is typically used due to its distinct property of high solubility of uranyl sulfate complexes [8, 9].

Given the aforementioned, the present investigation is aimed at evaluating the dissolution kinetics using sulphuric acid for the separation and recovery of the uranium from a local boltwoodite ore sourced from Bra district, Nigeria. The influence of sulphuric acid concentration, reaction temperature, particle size, and leaching time on the extent of uranium ore dissolution before appropriate beneficiation operations was considered.

Materials and Method

Material

The boltwoodite ore used for this investigation was obtained from Bra district (10° 0′ 3″ North, 9° 30′ 58″ East), Ningi Local Government Area of Bauchi State, Nigeria. The raw boltwoodite ore was crushed, ground, and sieved into three (3) particle sizes: − 90 + 75 μm, − 112 + 90 μm, and − 300 + 112 μm, respectively. However, the smallest particle size − 90 + 75, assumed to have a larger surface area was used throughout the leaching tests.

Leaching Experiments

The leaching investigation was carried out in a 1000 mL three-necked glass reactor equipped with a thermometer to control the reaction temperature and a mechanical stirrer for stirring the solution. The leaching reactor was heated thermostatically and the required temperature was maintained within ± 2 °C. For each run, 100 mL of prepared H_2SO_4 solution (0.1–2.5 mol/L) at predetermined concentrations was charged into the leaching glass and heated to the desired temperature at various leaching times (5–120 min). After the dissolution process, the pregnant leach solution (PLS) was filtered, water-washed, and oven-dried. The uranium and other associated impurities present in the PLS were determined by ICP-MS and the fraction of uranium ore dissolved at different parameters was recorded. The activation energy, *Ea*, was estimated from the Arrhenius plot, and the residual product obtained at established conditions was accordingly analyzed [10–12].

Results and Discussion

Ore Characterization

The mineralogical composition of the raw ore under study affirmed that it mainly consisted of *albite* ($Na_{2.00}Al_{2.00}Si_{6.00}O_{16.00}$: 96-900-1634), *boltwoodite* ($Na_{2.00}K_{2.77}U_{3.00}Si_{6.00}O_{9.00}H_{4.00}$: 96-900-7219), *thorite* ($Th_{4.00}Si_{4.00}O_{16.00}$: 96-900-7625), and *quartz* ($Si_{6.00}O_{6.00}$: 96-900-5019); and thus supported by photomicrography analysis [13] (Fig. 1).

The elemental composition of the raw boltwoodite ore analyzed by EDXRF gave: 51.46 wt% SiO_2, 26.45 wt% Al_2O_3, 4.27 wt% Fe_2O_3; 3807.5 mg/L UO_3, 104.4 mg/L ThO_2, and 70.9 mg/L Pr_2O_3 [13]. However, the SEM image of the raw boltwoodite ore was characterized by cloudy-*cum*-cluster surfaces as depicted in Fig. 2.

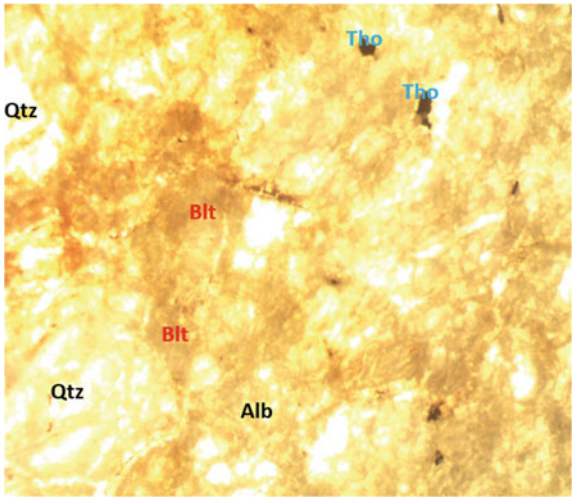

Fig. 1 Photomicrography analysis of the raw ore {*Alb* = Albite, *Blt* = Boltwoodite, *Tho* = Thorite, *Qtz* = Quartz}

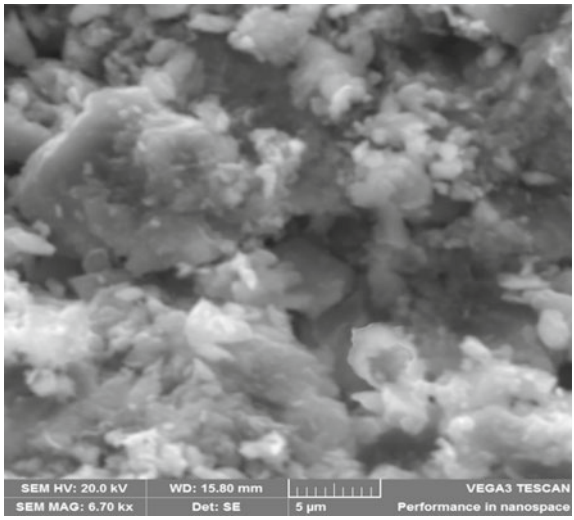

Fig. 2 SEM image of raw boltwoodite ore

Leaching Investigation

The leaching investigations confirmed that the uranium ore dissolution in sulphuric acid solution increases with increasing lixiviant concentration, reaction temperature, and decreasing particle fraction as summarized:

(i) ***Effect of lixiviant concentration***: H_2SO_4 concentrations varied between 0.1–2.5 mol/L at 55 °C within 5–120 min using the particle size − 90 + 75 μm. Increasing the lixiviant concentration tremendously increases the uranium ore

Table 1 Established parameters of the prepared $Na_2U_2O_7$ at optimal conditions

Parameters	Standard (%) *ASTM C* 788-03	$Na_2U_2O_7$ (%) 00-064-0473 This study
Density (g/cm^3)	6.44	6.51
Melting point (°C)	1646	1645 ± 2

dissolution up to 2.5 mol/L. Here, about 52.7% of the uranium ore dissolved within 120 min.

(ii) ***Effect of reaction temperature***: The effect of reaction temperature on the extent of uranium ore dissolution was carried out from 27 to 75 °C while keeping other parameters constant. However, increasing the reaction temperature from 27 to 75 °C tremendously increases the fraction of uranium ore dissolution yielding 89.1% at established conditions.

(iii) ***Effect of particle size***: The effect of particle size on the degree of uranium ore dissolution varied between − 90 + 75 and − 300 + 112 μm while keeping other parameters constant. It was affirmed that increasing the particle diameter from − 90 + 75 to − 300 + 112 μm appreciably decreases the level of uranium ore reacted from 89.1 to 67.3% at established conditions.

Hence, the estimated activation energy (Ea) of 20.70 kJ/mol supported the diffusion control reaction mechanism as the rate-determining step.

Beneficiation Test

At established conditions, the pregnant leach solution (PLS) obtained was further purified and beneficiated to produce an industrial grade *sodium diuranate* ($Na_2U_2O_7$: 00-064-0473), recommended to serve as intermediate in a nuclear fuel cell as compared to *ASTM C 788-03* international standard (Table 1) [13].

Conclusion

This research developed low-energy feasibility to enhance uranium extraction from boltwoodite ore for industrial value addition. Here, the processing and extraction of indigenous boltwoodite ore are feasible, and eco-friendly and could put the country among the global uranium and uranium compounds producers most especially in Sub-Saharan African countries including Nigeria. At established conditions, the preparation of an industrial grade *sodium diuranate* ($Na_2U_2O_7$: 00-064-0473, density = 6.51 g/cm^3, melting point = 1654 ± 2 ℃) recommended to serve as intermediate in the nuclear fuel cell has been proposed.

Acknowledgements The authors sincerely thank the (i) Executive Vice Chairman/Chief Executive of the National Agency for Science and Engineering Infrastructure (NASENI), Mr. Khalil Suleiman Halilu; (ii) University of Ilorin administration under a dynamic Vice-Chancellor, Professor Wahab Olasupo Egbewole, SAN; and (iii) TETFund, Nigeria for their immeasurable support to attend and present this distinct research at the 153rd Annual Meeting and Exhibition of The Minerals, Metals and Materials Society (TMS2024) held in Orlando, Florida, USA between 3rd–7th March 2024. Also, one of the authors (*Prof. Alafara A. Baba, the Dean, Faculty of Physical Sciences, University of Ilorin, Nigeria*) is grateful to the TMS EPD Council for their kind support.

References

1. Satybaldiyev B, Lehto J, Suksi J, Tuovinen H, Uralbekov B, Burkitbayev M (2015) Understanding sulphuric acid leaching of uranium from ore by means of $^{234}U/^{238}U$ activity ratio as an indicator. Hydrometallurgy 155:125–131
2. Lu BQ et al (2018) Immobilization of uranium into magnetite from aqueous solution by electrodepositing approach. J Hazard Mater 343:255–265
3. Li M, Huang C, Zhang X, Gao F, Wu X, Fang Q, Tan W, Zhang D (2018) Extraction mechanism of depleted uranium exposure by dilute alkali pretreatment combined with acid leaching. Hydrometallurgy. https://doi.org/10.1016/j.hydromet.2018.07.021
4. Zakrzewska G, Herdzik-Koniecko I, Cojocaru C, Chajduk E (2014) Experimental design and optimization of leaching process for recovery of valuable chemical elements (U, La, V, Mo and Yb and Th) from low-grade uranium ore. J Hazardous Mater. https://doi.org/10.1016/j.jhazmat.2014.04.066
5. Kim J, Cho H, Han K (2014) Leaching behavior of U and V from a Korean uranium ore using Na_2CO_3 and KOH. Geosyst Eng 17(2):113–119
6. Bai Z, Zhao X, Zhang J, Wu F, Quan Tang Q (2023) Optimisation of uranium–radium co-leaching from uranium ore. J Radioanal Nucl Chem 332:1841–1845
7. Ding D et al (2010) Two-stage column leaching of uranium from uraninite ore. Adv Sci Lett 5:96–100
8. Radwan HA, Faheim AA, El-Sheikh EM, Abd El-Wahab ZH, Gado MA (2021) Optimization of the leaching process for uranium recovery and some associated valuable elements from low-grade uranium ore. Int J Environ Anal Chem. https://doi.org/10.1080/03067319.2021.1936513
9. Kim JS, Chung KW, Lee HI, Yoon HS, Kumar JR (2014) Leaching behavior of uranium and vanadium using strong sulfuric acid from Korean black shale ore. J Radioanal Nucl Chem 299:81–87
10. Raji MA, Baba AA, Bale RB, Alabi AGF, Ghosh MK (2020) Removal of Iron impurities from a Nigerian biotite-rich kaolinite ore by a sulphuric acid solution. J Chem Technol Metall 55(6):2128–2135
11. Raji MA, Baba AA, Ibraheem L, Alabi AGF, Ghosh MK, Bale RB (2020) Preparation of industrial alumina from a biotite-rich kaolinite (BRK) ore by Cyanex®272. Indian Chem Eng 63(3):231–239
12. Baba AA, Raji MA, Muhammed OM, Abdulkareem AY, Olasinde FT, Ayinla IK, Adekola FA, Bale RB (2019) Potential of a Nigerian biotite-rich kaolinite ore to industrial alumina by hydrometallurgical process. J Metall Res Technol 116:222
13. Raji MA (2023) Hydrometallurgical processing of a boltwoodite ore as mediator in nuclear fuel cell and catalytic applications. Ph.D. thesis. Department of Industrial Chemistry, University of Ilorin, Ilorin, Nigeria, 238 pp

Low Energy Process Development for Chibuluma Copper Tailings

Nachikode Fumpa, Yotamu Rainford Stephen Hara, Makwenda Thelma Ngomba, Phenny Mwaanga, Gershom Mwandila, Bawemi Sichinga Mtonga, and Rainford Hara

Abstract Copper froth flotation tailings containing 1.19 and 0.97 wt% total and acid-soluble copper, respectively, from Chibuluma mines in the Copperbelt province of Zambia were characterized by SEM and XRD techniques. The major phases in the feed material were malachite, chrysocolla, pseudo malachite, chalcocite, quartz, biotite, orthoclase, calcite, etc. Screen analysis revealed that the tailings were coarse as only 9.17 wt% were less than 0.075 mm. With the purpose of establishing a low energy processing route, gravity concentration, froth flotation, and flotation–leach tests were carried out on the material. Gravity concentration upgraded copper up to 15.32 wt% at a cumulative recovery of 59.6%. On the other hand, a concentrate grade of 21.59 wt% was obtained via froth flotation but recovery was lower (49.68%). Therefore, the tailings from froth flotation were leached out and a leach efficiency of 97.92% was obtained such that the final tailings only had 0.02 wt%. As a result, it was concluded that the tailings should be processed via flotation–leach process to ensure maximum recovery of copper (both sulphide and oxide).

Keywords Tailings · Chibuluma · Flotation

Introduction

Chibuluma Mines Plc is a copper mining company that is located in Lufwanyama district of the Copperbelt province of Zambia. The company mines copper ore and treats it via froth flotation. However, froth flotation is more effective in processing copper sulphide minerals such that most of the copper oxide bearing minerals are lost to the tailings. In addition, some of the copper sulphide minerals are lost to the

N. Fumpa · Y. R. S. Hara (✉) · M. T. Ngomba · P. Mwaanga · G. Mwandila · B. S. Mtonga · R. Hara
School of Mines and Mineral Sciences, Copperbelt University, Kitwe, Zambia
e-mail: yotamuhara@gmail.com

© The Minerals, Metals & Materials Society 2024

C. Iloeje et al. (eds.), *Energy Technology 2024*, The Minerals, Metals & Materials Series, https://doi.org/10.1007/978-3-031-50244-6_7

tailings owing to poor chemical performance, dosing rates, and grinding. Consequently, Chibuluma tailings contain an average grade of 0.39–1.19 and 0.01–0.03 wt% cobalt.

Considering the high demand for both copper and cobalt in the world, it is important to establish an efficient method for recovering copper and cobalt from Chibuluma tailings. It is worth noting that there are no studies that have been reported on the recovery of copper and cobalt from Chibuluma copper flotation tailings. One of the major challenges of recovering valuable elements from the tailings is the energy demand owing to the fact that it is a secondary resource.

Froth Flotation of Copper

Froth flotation is a technique used in mineral processing to extract, separate, and concentrate metals from their ores with the use of chemical reagents [1–3]. This deals with the surface properties of the mineral to be separated or concentrated by altering its hydrophilic or hydrophobic condition [3, 4]. It is mainly suitable for sulphide ores. The variables that affect the operation of froth flotation are pulp density, mineralogy, particle size, pH, reagents, etc. [1, 4, 5].

Froth flotation has proven to be a versatile mineral separation technique used to enrich both sulphide and oxide copper-bearing ores with an expansion in technology [5]. It has permitted the mining and processing of low-grade ores for economic benefit. Copper oxide minerals are important resources which include malachite, azurite, cuprite, chrysocolla, etc.

The flotation of copper oxide is achieved through methods such as direct flotation by use of chelating agents; sulphidization process (use of Na_2S, NaSH, and collectors) to alter the surface characteristics of the mineral; and activation flotation by using amines [5]. Furthermore, oxide flotation is controlled by a number of factors which include surface potential, pH, residence time, solubility of the mineral, and chemical adsorption properties [2]. The recovery of oxide concentrates poses a challenge as the above factors play a significant role. The principle of oxide flotation involves sulphidization (at – 500 to 600 mV) followed by the use of xanthates (collectors) and frother which aids the formation of bubbles when air is induced [6]. A wide variety of oxide collectors have been proposed in the past without the use of sulphidizing agents such as organic complexing agents; fatty acids; or amines, respectively.

Gravity Separation

This is the separation and concentration of minerals from their ores based on the difference in the density or specific gravity in relative movement in response to the force of gravity [7]. The process has been employed for the concentration of precious minerals such as gold in the ancient years [8]. Nonetheless, it is still used

to concentrate other valuable minerals such as iron, tungsten, and coal [7]. The main advantage of gravity separation is that the process is not energy-intensive.

Experimental

Materials

The tailings material was obtained from Chibuluma Mine Limited. About 100 samples were carried from each of the three tailings dams at Chibuluma mine. The samples were homogenized to obtain a composite sample. All chemicals for flotation such as sodium ethyl xanthate (SEX), sodium sulphide (Na_2S), and pine oil were obtained from Curechem Zambia Limited.

Gravity Separation

Gravity separation was carried out using table shaking. The as-received material was ground to different particle sizes.

Froth Flotation

The flowsheet that was employed during froth flotation is shown in Fig. 1 from which it can be observed that the material was scavenged and cleaned twice, and the purpose was to increase recovery and concentrate grade, respectively. Sodium ethyl xanthate (SEX) and sodium amyl xanthate were used as collectors with a dosing rate of 500 and 185 g/t, respectively. On the other hand, pine oil was used as a frother at a rate of 0.07 g/t.

Mineralogical Examination

X-Ray Diffraction

A mineralogical examination of the sample was conducted using X-ray diffraction. XRD analysis was carried out using Rigaku Miniflex benchtop XRD with Cu K_α (0.15417 nm) radiation, at an acceleration voltage of 40 kV, current of 15 mA, and step size of $2\theta = 0.02$. The samples were analyzed for 2θ between 5° and 80°. The phases present in the powder diffraction patterns were identified by using the X'pert

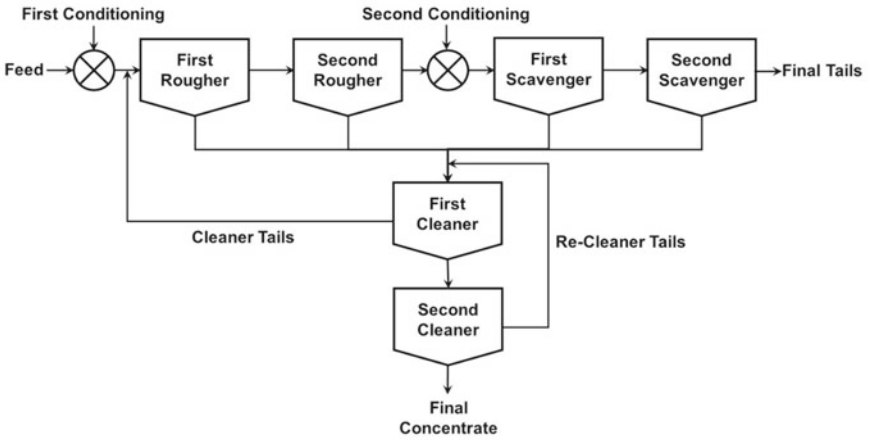

Fig. 1 Bulk flotation flowsheet that was used in the test works

high score plus software which is supported by the JCPDS PDF-4 + database (RDB 2012).

Scanning Electron Microscopy

The sample portion was screened on sieve size 1.7 mm, 100% passing, and a 90° transverse epoxy block was made and re-casted in epoxy for analysis on the TESCAN Integrated Mineral Analyser (TIMA). The TIMA is an automated mineralogy system for fast quantitative analysis of samples such as rocks, ores, concentrates, tailings, leach residues, or smelter products. TIMA combines BSE and EDX analysis to identify minerals and create mineral images that are analyzed to determine mineral concentrations, element distributions, and mineral texture properties such as grain size, association, liberation, and locking parameters.

Chemical Analysis

Chemical analysis was carried out on the feed and processed samples and the aim was to understand the efficiency of the process. A representative sample was taken from each portion of the sample. Several techniques such as atomic absorption spectroscopy (AAS), X-ray fluorescence (XRF), titration, and inductively coupled plasma-optical emission spectroscopy (ICP-OES) techniques were employed.

Table 1 Chemical analysis results of the as-received sample

Cu	ASCu	Co	Fe	SiO_2	Al_2O_3	K_2O	CaO	TiO_2	S	MnO
1.19	0.97	0.01	1.13	84.64	5.47	2.9	1.94	1.69	0.34	0.14

Results and Discussion

Characterisation of the As-Received Material

Chemical Analysis

Chemical analysis of the as-received sample is shown in Table 1 from which it can be observed that the sample has 1.19 wt% total copper of which 0.97 wt% is acid-soluble. The results in Table 1 further show that cobalt content is very low in the material (0.01 wt%). The major gangue constituent in the material is SiO_2 as it is 84.64 wt%. The other gangue constituents in the sample are Al_2O_3, K_2O, CaO, TiO_2, Fe, etc.

Mineralogical Examination

XRD pattern for the as-received sample is shown in Fig. 2 from which high-intensity peaks for quart can be observed. The other XRD peaks in the material are biotite ($K(Mg,Fe)_3AlSi_3O10(F,OH)_2$) and orthoclase ($KAlSi_3O_8$). The intensity peaks for copper-bearing minerals could not be observed as they are below the detection limit of the instrument.

Scanning electron microscopy mineralogical data is presented in Table 2 from which it can be seen that 71.09 wt% of the material is quartz. Biotite and orthoclase are 8.23 and 7.24 wt%, respectively. Malachite is the dominant copper-bearing mineral,

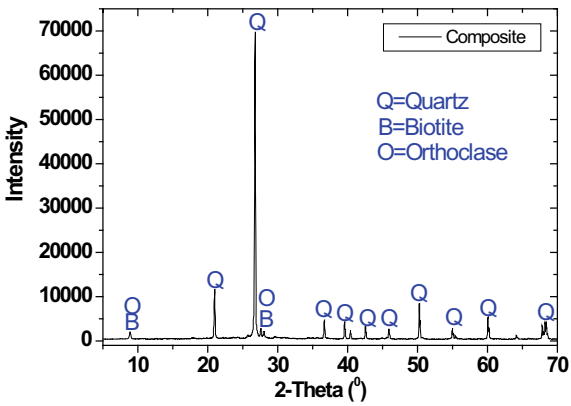

Fig. 2 X-ray diffraction pattern of the as-received sample

Table 2 Mineralogical analysis results of the as-received sample

Mineral	Composite
Quartz	71.09
Biotite	8.23
Orthoclase	7.24
Albite	4.12
Muscovite	2.4
Calcite	1.3
Malachite	1.27
Hematite/magnetite	0.61
Kaolinite	0.51
Chrysocolla	0.33
Chlorite-high Fe	0.28
Chrysocolla-Fe	0.3
Pseudo malachite	0.21
Fayalite	0.22
Dolomite	0.25
Chlorite-Clinochlore	0.12
Chalcocite	0.01
[Unclassified]	0.52
The rest	1.01
Total	100

while chrysocolla and pseudo malachite are the other copper-bearing minerals. Chalcocite is the main copper sulphide mineral. There is broad agreement between chemical analysis data and mineralogical examination as copper is predominantly in the oxide form.

Screen Analysis

Screen analysis of the as-received sample is shown in Table 3 from which it can be noted that the material is generally coarse as 39.45 wt% of the material has a particle size of more than 0.300 mm. On the other hand, only 9.17 wt% of the material has a particle size of less than 0.075. The minus 0.038 size fraction has a slightly higher grade of copper, cobalt, and iron.

Table 3 Detailed metal distribution results for Chibuluma composite sample

Fraction (mm)	Weight		Cumulative		% grade				Contained Cu (g)	% rec. Cu	Specific gravity
	(g)	%	Wt. Rtd	% passing	Cu	ASCu	Co	Fe			
+ 0.60	11.6	1.91	1.91	98.09	1.22	1.05	0.03	1.48	0.14	2.14	2.49
− 0.60 + 0.425	37.5	6.19	8.10	91.90	1.24	1.01	0.06	1.35	0.46	7.02	2.49
− 0.425 + 0.355	31.7	5.23	13.33	86.67	1.21	1.03	0.02	1.40	0.38	5.81	2.78
− 0.355 + 0.212	158.3	26.12	39.45	60.55	1.04	0.82	0.01	1.03	1.64	24.82	2.56
− 0.212 + 0.15	121.4	20.03	59.48	40.52	1.00	0.89	0.01	1.10	1.21	18.36	2.53
− 0.15 + 0.106	96.0	15.84	75.32	24.68	1.04	0.82	0.01	1.12	1.00	15.13	2.59
− 0.106 + 0.075	70.9	11.70	87.02	12.98	1.06	0.84	0.01	1.45	0.75	11.39	2.71
− 0.075 + 0.063	23.1	3.81	90.83	9.17	1.01	0.69	0.01	1.28	0.23	3.53	2.54
− 0.063 + 0.038	32.1	5.30	96.12	3.88	1.15	0.85	0.03	1.41	0.37	5.59	2.55
− 0.038 (Pan)	23.5	3.88	100.00	0.00	1.75	1.54	0.03	1.91	0.41	6.21	2.42
Total	606.1								6.60	100.00	
Calculated					0.96	0.78	0.01	1.08			2.67
Assays					1.19	0.97	0.01	1.13			2.57

Gravity Test Work

Gravity test works results for the sample are shown in Table 4. A concentrate grade of 8.54 and 15.32 wt% copper was obtained at a particle size of 0.300 mm and 0.212 mm, respectively. In short, recovery improved with a decrease in particle size and this is due to increased liberation at finer particle size. Cobalt was only upgraded from 0.01 to 0.07 wt% thereby representing an upgrade factor of 7. Nonetheless, some of the copper remained in the tailings after gravity separation hence representing poor recovery or extraction.

Flotation Test Work

Flotation test results for the samples that were conducted in the absence and presence of sulphidiser are shown in Tables 5 and 6, respectively. A concentrate grade of 10.40 wt% copper and cumulative % recovery of 62.69 were obtained for the sample that

Table 4 Gravity concentration results at different particle sizes

Fraction (mm)	Stream	Weight (g)	% grade			Contained Cu	% recovery Cu
			Cu	Co	Fe	(g)	
0.3	Concentrate	19.8	8.54	0.04	2.88	1.69	27.79
	Cleaner tails	48.7	1.32	0.02	1.18	0.64	10.55
	Middlings	244.3	0.86	0.01	0.88	2.10	34.50
	Final tails	261.4	0.63	0.02	0.96	1.65	27.16
	Total	574.2				6.09	100.00
	Calculated		1.06	0.01	1.01		
	Assayed		1.19	1.13	0.01		
0.212	Concentrate	7.0	15.32	0.07	5.10	1.06	24.49
	Middlings	164.6	0.92	0.00	0.89	1.52	34.97
	Final tails	247.3	0.71	0.02	0.97	1.76	40.54
	Total	418.8				4.35	100.00
	Calculated		1.04	0.01	1.01		
	Assayed		1.19	1.13	0.01		

was floated in the absence of sulphidiser (sodium sulphide). Most of the copper exists in the oxide state which was why recovery of copper was lower in the absence of sulphidiser. A higher grade copper concentrate (29.46 wt% copper) was attained when the sample was floated in the presence of sulphidiser and a % cumulative recovery of 89.46% recovery was obtained. Based on the results in Tables 5 and 6, it can be concluded that the material responds favorably to flotation in the presence of sulphidiser.

Table 5 Detailed metal balance flotation results in the absence of sulphidiser

Stream	Weight (g)	% weight	% grade		% Cu recovery	% Cu cumulative recovery
			Cu	Co		
Concentrate	1.1	0.4	10.40	0.05	3.62	62.69
Re-cleaner tails	19.2	6.3	1.99	0.00	11.98	
Cleaner tails	60.2	19.9	1.33	0.00	25.08	
Scavenger 1	28.6	9.4	1.40	0.00	12.53	
Scavenger 2	26.4	8.7	1.14	0.02	9.48	
Final tails	167.6	55.3	0.71	0.02	37.31	
Total	303.2					
Calculated			1.05	0.01		
Assayed			1.19			

Table 6 Detailed metal balance flotation results in the presence of sulphidiser

Stream	Weight (g)	% weight	% grade		% Cu recovery	% Cu cumulative recovery
			Cu	Co		
Concentrate	3.0	1.01	29.46	11.7846	25.26	89.46
Re-cleaner tails	9.2	3.06	4.62	0	12.05	
Cleaner tails	85.8	28.64	1.38	0	33.73	
Scavenger 1	33.9	11.32	1.27	88.2154	12.22	
Scavenger 2	25.2	8.40	0.87	0	6.20	
Final tails	142.4	47.56	0.26	0	10.54	
Total	299.5					
Calculated			1.17	0.01		
Assayed			1.19			

Table 7 Float–leach results

	Initial wt. (g)	Final wt. (g)	% Cu	% recovery	Acid consumption (kg/t)
Flotation tails (feed)	100	0.85	0.85	97.92	92.7
Float–leach final tails	88.5	0.02	0.02		

Leaching of the Flotation Tailings

The final tailings from flotation were leached and the results are shown in Table 7. It can be observed that 97.92 of the copper in the flotation tailings was extracted. Therefore, the final tailings had 0.02 wt% copper.

Conclusions

1. The as-received tailings material contains 1.19 and 0.97 wt% total and acid-soluble copper, respectively. Therefore, about 82% of the material is acid-soluble.
2. The as-received tailings material is generally coarse as only 9.17 wt% has a particle size of less than 0.075 mm.
3. The as-received material contains 84.64 weight SiO_2 of which 71.09 wt% is quartz. The other SiO_2 is contained in biotite and orthoclause.
4. Malachite is the dominant copper-bearing mineral while chrysocolla and pseudo malachite are the other oxide copper-bearing minerals. On the other hand, chalcocite is the main copper sulphide mineral.

5. Copper was upgraded to a concentrate grade of 8.54 and 15.32 wt% copper at a particle size of 0.300 and 0.212 mm. However, the tailings had 0.63 and 0.71 wt% copper.
6. A concentrate grade of 29.46 wt% copper at a cumulative recovery of 89.46% was attained during froth flotation in the presence of sulphidiser.
7. A combination of froth flotation and leaching yields a final tailing of 0.02 weight copper, hence representing an overall recovery of 97.58%.

Acknowledgements The authors thank the National Science and Technology Council (NSTC) for the financial support.

References

1. Mondal S et al (2021) Froth flotation process and its application. Vietnam J Chem 59(4):417–425
2. Kime M, Ntambwe J, Mwamba J (2015) Laboratory evaluation of the flotation response of a copper cobalt oxide ore to gasoil-rinkalore mixtures
3. Reyes-Bozo L et al (2014) Assessment of the floatability of chalcopyrite, molybdenite and pyrite using biosolids and their main components as collectors for greening the froth flotation of copper sulphide ores. Miner Eng 64:38–43
4. Rao SR (2013) Surface chemistry of froth flotation, volume 1: fundamentals. Springer Science & Business Media
5. Brest KK et al (2021) Statistical investigation of flotation parameters for copper recovery from sulfide flotation tailings. Res Eng 9:100207
6. Kiraz E (2014) Recovery of copper from oxide copper ore by flotation and leaching. Middle East Technical University
7. Burt RO (1984) Gravity concentration technology
8. Veiga MM, Gunson AJ (2020) Gravity concentration in artisanal gold mining. Minerals 10(11):1026

Production of FeCr and FeCrNi Alloys with an Energy Saving Route

Hasan Güney, Selçuk Kan, Kağan Benzeşik, and Onuralp Yücel

Abstract The stainless steel industry is increasing at a great pace every day. In addition, there is a need to increase the production capacities of FeCr and FeNi, which are the main input raw materials of stainless steel. However, FeCr and FeNi production processes with intensive energy consumption and high carbon dioxide emission values pose a problem when evaluated within the framework of the Paris Climate Agreement. As a result of these reasons, more environmentally friendly and more economical methods are sought. In this study, FeCr is produced by aluminothermic reaction to reduce the carbon footprint to almost zero in the smelting process and energy saving is aimed by exothermic reaction. In addition, FeCrNi production conditions were investigated by smelting in a single crucible instead of separately produced FeCr and FeNi. In addition, energy saving is achieved as it is fed in powder form without applying any agglomeration process as a preliminary preparation.

Keywords Ferro alloy · Low CO_2 emission · Energy saving · Aluminothermic

Introduction

Stainless steel (SS) is an alloy comprising iron and carbon, with a minimum chromium content of 11%, and may contain other alloying elements such as nickel and molybdenum. The addition of chromium leads to the formation of a thin film layer that enhances the material's corrosion resistance. Also, an enhancement in heat resistance can be observed. Alloying elements may enhance several physical and chemical properties [1].

Due to the demand for stainless steel, there has been a notable increase in production each year. Between 1980 and 2019, an average annual increase of 5.33% was observed. However, world stainless steel production decreased by 2.54% in 2020

H. Güney · S. Kan · K. Benzeşik · O. Yücel (✉)
Department of Metallurgical and Materials Engineering, Faculty of Chemical and Metallurgical Engineering, Istanbul Technical University, 34469, Maslak Istanbul, Turkey
e-mail: yucel@itu.edu.tr

© The Minerals, Metals & Materials Society 2024

C. Iloeje et al. (eds.), *Energy Technology 2024*, The Minerals, Metals & Materials Series, https://doi.org/10.1007/978-3-031-50244-6_8

due to the COVID-19 pandemic, which is a comparably low rate compared to other production decreases [2].

The primary materials used in the production of stainless steel include pig iron, ferrochrome, and ferronickel. The production of ferroalloys is associated with high energy consumption and significant CO_2 emissions. These effects are also evident in the "cradle to grave" analysis of stainless steel production. Data from a life cycle assessment (LCA) provides information on the inputs and outputs required for manufacturing 1 kg of 304-grade stainless steel, which accounts for 50% of stainless steel production. Looking at the data provided by LCA, it is found that for the production of 1 kg of 304-grade stainless steel, the energy consumption is 110 MJ for ferronickel, 56 MJ for ferrochrome, 22 MJ for iron, and 75 MJ for the EAF and AOD route. The emission of CO_2 is 8.9 kg for ferronickel, 5.1 kg for ferrochrome, 2 kg for iron, and 6.6 kg for the EAF and AOD route. In other words, the energy consumption and CO_2 emission values of ferroalloys play a crucial role in stainless steel production [3].

Ferrochrome is a type of ferroalloy containing between 50 and 70% chromium. Chromium used as an alloying element in steels is usually added to the alloy in the form of ferrochrome [4]. Approximately 80% of the ferrochrome produced in the world is used as an input during stainless steel production. The corrosion resistance of stainless steel is thanks to the chromium which is coming from ferrochrome. As a result of the differences in production methods, ferrochrome is divided into three groups according to the carbon content: High Carbon Ferrochrome (4–10% C), Medium Carbon Ferrochrome (0.5–4% C), and Low Carbon Ferrochrome (0.01–0.5% C). Another type is FeCr, called "charge chrome", which contains lower Cr (approximately 50%) and higher Fe than HC FeCr. Based on LCA data, 3534 kWh of electricity is required for the production of 1 t of ferrochrome. According to Global Warming Potential (GWP) data, 5.3 kg of CO_2 is emitted during the production of 1 kg of ferrochrome [5].

Nickel is the second most important alloying element in stainless steel production. As with chromium, alloying of nickel is carried out in the form of ferroalloy. Approximately 66% of the ferronickel produced in the world is consumed for stainless steel production. There are two types of sources used for nickel production; the first is nickel sulphide and the second is lateritic nickel. With the near depletion of nickel sulphide resources, techno-economic studies of lateritic nickel resources are gaining momentum. Because obtaining nickel from lateritic nickel ore causes high energy consumption and intense CO_2 emissions [6].

Many approaches and scenarios have been developed to measure and reduce GWP impacts and CO_2 emission values of ferronickel production. The most important of these is the LCA. According to the results of the LCA approach, while 1 kg of ferronickel is produced, an average of 8.9 kg of CO_2 is emitted. This approach involves multiple scenarios. For ferronickel produced with the Baseline Scenario (BL scenario) including metallurgy routes, 12.60 tons of CO_2 was calculated in the production of 1 ton of ferronickel. It was observed that 8.24 tons of CO_2 emission was observed in the production of 1 ton of ferronickel produced with Green Energy (GE scenario), which is a more sustainable scenario. In another scenario, which is more environmentally friendly, the Waste Use scenario (WU scenario), 10.92 tons

of CO_2 is emitted for 1 ton of ferronickel produced [7]. Although various scenarios have been developed to reduce CO_2 emission and energy consumption, consumption and emission values still show at dangerous levels [8].

In this study, it was aimed to save energy and reduce CO_2 emission values by producing FeCrNi instead of FeCr and FeNi separately, which are the raw materials of stainless steels. Also, FeCr was produced by the metallothermic method, and not only CO_2 emission value from the reductant was reduced to zero but also energy saving was achieved due to the high energy released due to the exothermic reaction.

Experimental

Experimental studies are divided into two different titles; carbothermic FeCrNi production and metallothermic FeCr production.

In this study, a 270 kVA DC Electric Arc Furnace was used for the smelting process. It has two electrodes, top and bottom, and has a depth of 50 cm and a diameter of 30 cm. The schematic view of the furnace is given in Fig. 1. In the experiments, an 8–9 cm electrode was used for the bottom electrode, and a 10 cm electrode was used for the top electrode.

The common point in the raw materials for both experimental groups is the KEF Concentrate used as a chromium source. In FeCrNi production, lateritic nickel ore calcined at 650 °C for 5 h is used as a nickel source. While the reductant used for carbothermic FeCrNi production was coke coal, aluminum was used as a reductant in metallothermic reaction. Two different products were selected as the aluminum source. One is an industrial pure aluminum powder (Al_{Powder}) and the other is metallic aluminum dross (Al_{Dross}) which is an aluminum recovery material. The results of the

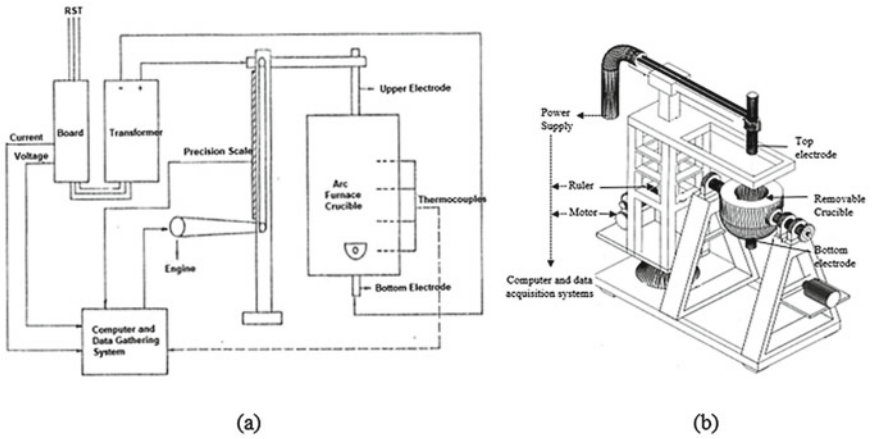

Fig. 1 **a** Logic layout and **b** schematic view of the laboratory size 270 kVA DC EAF

Table 1 Chemical analysis of the raw materials

Raw materials	Cr_2O_3	NiO	Fe_2O_3	SiO_2	Al_2O_3	MgO	CaO	Cr/Fe
LNO*	0.7	2.85	33.6	31.7	1.53	10.2	3.44	
CLNO*	0.82	3.35	39.53	37.29	1.80	12.00	4.05	
KEF 42-44 Al_{max}	43.57	0.19	14.04	4.7	17.35	18.9	0.28	3.07
KEF 42-44 Al_{min}	44.85	0.17	14.85	10.88	8.6	2.6	0.34	3.08
KEF 30-32	32.47	0.22	12.44	13.41	12.19	26.36	0.25	2.58
KEF concentrate	40.57	0.19	16.10	7.43	12.21	19.12	0.13	2.42

LNO Lateritic nickel ore
CLNO Calcined lateritic nickel ore

Table 2 Chemical analysis of coke (carbothermic reaction reductant)

	Carbon	Ash	Volatile matter	Moisture	S	P
Coke	83.66	13.53	2.24	0.57	0.76	0.024

Table 3 Chemical analysis of aluminum sources (metallothermic reaction reductants)

	Al_{Me}	Al_2O_3	Si	SiO_2	Fe	Fe_2O_3	Na_2O	K_2O	Ca	S	P
Al_{Powder}	98.1	Trace	0.52	–	1.0	–	–	–	0.15	0.018	0.007
Al_{Dross}	64.87	18.12	–	4.45	–	3.69	3.60	1.20	–	–	–

chemical analyses of the raw materials are given (Tables 1, 2 and 3). It was aimed to produce 55–60% Cr containing FeCr and, 2% Ni containing FeCrNi.

Carbothermic FeCrNi Production

Four different chromite concentrate sources were used for carbothermic FeCrNi production. Calcined lateritic nickel ore (CLNO) was used in different percentages to balance the nickel content in the product. Coke was used as a reductant to obtain a sufficient amount of C to reduce the Cr, Ni, and Fe elements in the ores. Experiments parameters are given in Table 4.

Metallothermic FeCr Production

Only KEF Concentrate was used as a chromium source for metallothermic FeCr production. In this part of the study, the focus was on the reduction with aluminum. Two different types of aluminum were used for this. One is pure metallic aluminum

Table 4 Calcined lateritic nickel ore, chromite, and coke amounts used in experiments

Exp. No.		KEF conct. (g)	KEF 42-44 Al_{Max} (g)	KEF 42-44 Al_{Min} (g)	KEF 30-32 (g)	CLNO (g)	Coke (g)	CLNO/ Crt*
3		3000				1500	700	50/100
11		9000				4500	2100	50/100
13		6000				3000	1400	50/100
		6000				3000	1400	50/100
		6000				120 (NiO)	551	
15		6000				3000	1500	50/100
		6000				3000	1500	50/100
17			–	7200	–	1800	1550	25/100
18			7200	–	–	1800	1500	25/100
19	Mix.1		–	–	7650	1350	1230	17/100
	Mix.2		–	–	7650	1350	1230	17/100
24	Mix.1	–	7650	–	–	1350	1530	17/100
	Mix.2	–	7650	–	–	1350	1530	17/100

powder (Al_{Powder}) and the other is Al_{Dross}, which is separated from the waste product in the aluminum industry and sent for recycling. The use of Al_{Dross} as a direct raw material input by eliminating the recycling process was evaluated in terms of economic and environmental approaches. The experiment parameters for the production of FeCr are given in Table 5.

Experiments 1 and 2: In these two experiments, the charge mix was fed into the furnace at once. Metal and slag pouring was not carried out, the smelted product was cooled in the furnace.

Experiment 3: In this experiment, the charge was prepared in two batches, but smelted together. In the first group, 6 kg of KCC and Al_{Powder} were used with a 100% stoichiometric ratio. In the second group, 5 kg of KCC and Al_{Dross} were used with a stoichiometric ratio of 120%. These two charge mixes were fed sequentially.

Experiment 4: Since the metal and slag will be poured from the furnace to the ladle in this experiment, CaO up to 15% by weight of chromite was added to increase the slag fluidity**.**

Experiments 5, 6, and 7: This experiment was carried out to optimize the amount of CaO addition.

Experiment 7: In this experiment, unlike the others, in order to determine the effect of the two different types of aluminum used, two consecutive pours were taken for the feeding and smelting processes of each charge. After the first pouring, the second smelting process could be continued without any difficulties.

Table 5 Experiment parameters for the production of FeCr

Exp. No.		KCC*, g	Al_{Dross}		Al_{Powder}		CaO		Total charge, g
			g	Stc, %	g	Stc, %	g	CaO/KCC %	
1		5000	1390	100	–	–	–	–	6390
2		5000	–	–	1280	140	–	–	6280
3		11,000	1710	120	1139	100	–	–	13,849
4	Mix 1	1000	–	–	184	100	–	–	20,645
	Mix 2	7000	2335	120	–		1110	13.47	
	Mix 3	7000	–	–	1291	100	725	8.80	
5	Mix 1	1000	–	–	184	100	35	2.97	19,350
	Mix 2	7000	2335	120	–		250	3.03	
	Mix 3	7000	–	–	1291	100	250	3.03	
6	Mix 1	1000	–	–	184	100	35	2.97	19,350
	Mix 2	7000	2335	120	–		250	3.03	
	Mix 3	7000	–	–	1291	100	250	3.03	
7	Run 1	6000	–	–	1102	100	353	5	15,808
	Run 2	6000	2000	100	–	–	353	5	

*KCC** KEF Concentrate
– Not used
* The limestone used contains 85% wt. active CaO

Results and Discussion

Carbothermic FeCrNi Production

The chemical analysis of the products and metal yields are given in Table 6. The energy and electrode consumption values are given in Table 7.

Metallothermic FeCr Production

The chemical analysis of the products and Cr yields are given in Table 8. Fe and Cr were successfully reduced to produce FeCr. Al and C contamination was also observed. Metallic Al can react with the oxygen inside the steel and Al_2O_3 can be collected in the slag. The energy and electrode consumption values are given in Table 9.

Table 6 Chemical analysis and recovery rates of metal samples produced by carbothermic smelting experiments

Exp. No.	Metal weight (g)	Chemical analysis (wt%)					Recovery rates (%)		
		Si	Fe	Ni	Cr	Total C	Cr	Ni	Fe
3	1275	5.66	41.35	2.12	45.18	6.58	69.17	68.39	70.05
11	2900	0.21	45.46	2.47	42.49	6.82	49.32	60.41	58.38
13	1298	4.29	40.74	1.86	46.60	6.33	36.31	30.54	35.13
	3104	2.89	41.41	2.01	46.05	6.37	85.82	78.93	85.39
	2120	0.74	27.65	2.30	55.74	8.69	70.95	51.70	86.73
15	5434	8.25	42.12	1.90	45.30	5.57	74.54	81.63	76.02
17	2587	8.07	30.31	1.29	52.74	6.77	61.75	58.50	62.95
18	2832	3.74	34.25	1.53	53.55	7.55	70.65	74.48	80.51
19	2010	5.14	35.15	1.42	52.70	6.16	62.33	58.50	68.01
	1939	4.63	36.05	1.47	51.83	7.20	60.13	58.42	67.29
24	2458	2.02	35.64	1.11	56.42	8.22	60.60	58.12	77.89
	2879	2.31	34.49	1.05	56.08	7.9	70.45	64.40	88.26

Table 7 Energy and electrode consumption values of carbothermic FeCrNi production

Exp. No.	Time, min	Electrode consumption, g, cm		kWh	Temp, °C
3	30	356	7.9	22.5	1580
11	30	140	2.5	35.5	1500
13	119	563	3.9	93	1560
15	107	613	5.5	71.5	1550
17	41	442	1.5	40	1600
18	46	375	2	45	1580
19	45	683	5.5	35	1550
	40			35	1600
	40			30	1540
24	45	846	5	35	1696
	45			35	1707

Table 8 Chemical analysis of metal samples produced by metallothermic smelting experiments

Exp. No.		Metal weight, g	Chemical analysis (wt%)						Cr recovery, %
			Al	Si	Fe	Ni	Cr	C	
1		1361	1.01	0.94	30.74	0.54	57.73	6.92	56.61
2		1620	3.02	6.14	31.54	0.35	54.95	6.93	64.13
3		4064	1.72	6.42	30.59	0.38	57.65	5.72	76.73
4		4078	2.86	4.31	35.97	0.60	55.58	2.64	54.43
5		2620	3.40	4.24	31.74	0.47	57.34	4.67	36.08
6		2977	2.94	4.78	28.84	0.41	55.80	7.93	39.90
7	C.1	1986	4.60	1.18	28.44	0.50	59.52	8.13	70.97
	C.2	2029	2.29	0.98	26.93	0.56	57.76	8.62	70.36

Table 9 Details such as smelting time and temperatures, electrical energy, and electrode consumption values of the metallothermic FeCr production experiments

Exp. No.	Smelting, kWh	Time, min	Electrode consumption, g cm		Temp, °C
1	19	40	170	2.4	1700
2	28.5	30	473	12.6	1900
3	58.5	60	663	18.9	1850
4	41.5	54	263	1.54	1800
5	33.5	38	423	3.5	1891
6	38	60	461	4	1875
7	64	100	530	1.5	1700

Conclusion

In this study, FeNiCr and FeCr are produced with carbothermic and metallothermic methods, respectively. A one-step production process is suggested for FeNiCr production. The metallic part of the Al can be used for the production of FeCr. Since the metallothermic method is an exothermic process, this method is economical not only for energy saving but also for using recycled Al as a reductant.

Acknowledgements This research was supported by ETİ Krom INC., Turkey which is a subsidiary of YILDIRIM Group of Companies and the European Bank for Reconstruction and Development (EBRD).

References

1. Singh R (2016) Applied welding engineering. Elsevier
2. ISSF website—stainless steel meltshop production 2021. https://www.worldstainless.org/statistics/stainless-steel-meltshop-production/stainless-steel-meltshop-production-2021/. Accessed 11 July 2023
3. Norgate T, Jahanshahi S, Rankin W (2004) Alternative routes to stainless steel—a life cycle approach. In: Tenth international ferroalloys congress. Cape Town, South Africa
4. Gasik M (2013) Handbook of ferroalloys. Elsevier
5. Habashi F (1997) Handbook of extractive metallurgy. Wiley-Vch
6. Selivanov EN, Sergeeva SV (2019) Prospects for the Ferronickel production development from the Urals oxidized nickel ores. KnE Mater Sci: 77–91
7. Bartzas G, Komnitsas K (2015) Life cycle assessment of ferronickel production in Greece. Resour Conserv Recycl: 113–122
8. Güney H, Güner Ö, Boncuk FF, Kan S, Benzeşik YO (2023) A decarbonization approach for FeCr. Sustain Metall 9(1):216–229

Part III
Sustainable Production

Seawater Enables High-Quality Carbon Removal

Erika Callagon La Plante, Dante A. Simonetti, David Jassby, Lorenzo Corsini, and Gaurav N. Sant

Abstract We present the mass balances associated with carbon dioxide (CO_2) removal (CDR) using seawater as both the source of reactants, and as the reaction medium via electrolysis following the "*Equatic*™" (*formerly known as "SeaChange"*) process (La Plante et al. in ACS EST Eng. https://doi.org/10.1021/acsestengg.3c00004, 2023). This process, extensively detailed in La Plante et al. (Chem Eng. https://doi.org/10.1021/acssuschemeng.0c08561, 2021), involves the application of an electric overpotential that splits water to form H^+ and OH^- ions, producing acidity and alkalinity, i.e., in addition to gaseous co-products, at the anode and cathode, respectively. The alkalinity that results, i.e., via the "continuous electrolytic pH pump" results in the instantaneous precipitation of calcium carbonate ($CaCO_3$),

E. C. La Plante (✉)
Department of Materials Science and Engineering, University of California, Davis, Davis, CA 95616, USA
e-mail: erika.laplante@uta.edu

E. C. La Plante · D. A. Simonetti · D. Jassby · G. N. Sant (✉)
Institute for Carbon Management, University of California, Los Angeles, Los Angeles, CA 90024, USA
e-mail: gsant@ucla.edu

E. C. La Plante · D. A. Simonetti · D. Jassby · L. Corsini · G. N. Sant
Equatic Inc., Los Angeles, CA 90024, USA

D. A. Simonetti
Department of Chemical and Biomolecular Engineering, University of California, Los Angeles, Los Angeles, CA 90024, USA

D. Jassby · G. N. Sant
Department of Civil and Environmental Engineering, University of California, Los Angeles, Los Angeles, CA 90024, USA

G. N. Sant
California Nanosystems Institute, University of California, Los Angeles, Los Angeles, CA 90024, USA

Department of Materials Science and Engineering, University of California, Los Angeles, Los Angeles, CA 90024, USA

© The Minerals, Metals & Materials Society 2024

C. Iloeje et al. (eds.), *Energy Technology 2024*, The Minerals, Metals & Materials Series, https://doi.org/10.1007/978-3-031-50244-6_9

hydrated magnesium carbonates (e.g., nesquehonite: $MgCO_3 \cdot 3H_2O$, hydromagnesite: $Mg_5(CO_3)_4(OH)_2 \cdot 4H_2O$, etc.), and/or magnesium hydroxide ($Mg(OH)_2$) depending on the CO_3^{2-} ion-activity in solution. This results in the trapping, and hence durable and permanent (at least ~ 10,000–100,000 years) immobilization of CO_2 that was originally dissolved in water, and that is additionally drawn down from the atmosphere within: (a) mineral carbonates, and/or (b) as solvated bicarbonate (HCO_3^-) and carbonate (CO_3^{2-}) ions (i.e., due to the absorption of atmospheric CO_2 into seawater having enhanced alkalinity). Taken together, these actions result in the net removal of $\approx$ 4.6 kg of CO_2 per m^3 of seawater catholyte processed. Overall, this analysis provides direct quantifications of the ability of the *Equatic*™ process to serve as a means for technological CDR to mitigate the worst effects of accelerating climate change.

Keywords Carbon dioxide mineralization · Calcium carbonate · Brucite · Electrolysis

Introduction and Background

Recently, in La Plante et al., we proposed an approach to rapidly precipitate Ca- and Mg-carbonates and hydroxides from seawater to achieve CDR [2]. This *Equatic*™ process electrolytically forces mineral carbonate precipitation thereby consuming prevalent CO_2 that is dissolved in seawater by locking it within carbonate minerals, and simultaneously producing alkaline mineral hydroxides that when dissolved in seawater enable the drawdown of atmospheric CO_2 into the seawater ensuring net CO_2 removal [2]. As such, previously, in La Plante et al., we have carefully examined and assessed the *Equatic*™ approach via detailed evaluations of energy demands, process cost, implementation schemes, and the achievable scale of carbon removal [2]. Therefore, in the current paper we particularly (only) focus on describing the geochemical basis, and the CO_2 (mass) balances of the *Equatic*™ process to enable CDR. Two scenarios are presented: (1) the precipitation of calcium carbonate and magnesium hydroxide ($Mg(OH)_2$: brucite), with $Mg(OH)_2$ dispersed as solids or dissolved in seawater and pre-equilibrated with CO_2 under dilute conditions, and (2) the precipitation of calcium and hydrated magnesium carbonates, i.e., when $Mg(OH)_2$ is carbonated under non-dilute conditions. Special focus is paid to offer detailed quantifications of carbon mass balances based on equilibrium calculations. The analysis, therefore, offers a quantitative basis for assessing the CDR potential of the technology and for developing a robust measurement, reporting, and verification (MRV) strategy. This manuscript provides limited discussion around the full life cycle of the process, including electrolyzer materials and systems, balance-of-plant equipment, operational considerations, etc. These aspects represent ongoing work that will be addressed in future publications. Taken together, these efforts contribute to the mitigation of ongoing climate change, which poses enormously negative effects on ecosystems and people's quality of life [3].

Table 1 Composition of seawater used in the analysis

Species	Molality (m, mol/kg) based on reference composition [5]	Molality (m, mol/kg) after equilibration at 420 ppm $CO_{2(g)}$
Na^+	0.4860597	0.4860597
Mg^{2+}	0.0547421	0.0547421
Ca^{2+}	0.0106568	0.0106568
K^+	0.0105797	0.0105797
Sr^{2+}	0.0000940	0.0000940
Cl^-	0.5657647	0.5657647
SO_4^{2-}	0.0292643	0.0292643
HCO_3^-	0.0017803	0.0021002
Br^-	0.0008728	0.0008728
CO_3^{2-}	0.0002477	0.0000312
F^-	0.0000708	0.0000708
B [$B(OH)_4^-$, $B(OH)_3$]	0.0004303	0.0004303
$H_2CO_3^*$	0.0000100	0.0000124
ΣCO_2	2.038 mmol/kg	2.141 mmol/kg
pH	8.352	8.170
pCO_2 (in atm)	–3.78	–3.38

Methods

We use PHREEQC [4] to carry out detailed geochemical simulations. The seawater composition used is based on Millero et al. [5] (Table 1), adjusted to pCO_2 (in atm) $= -3.38$ (420 ppm) [6] by charge balancing for the presence of inorganic C (carbon) species.

Results and Discussion

The *Equatic*™ process consists of the following steps (Fig. 1):

Step 1. The precipitation of brucite ($Mg(OH)_2$) and aragonite ($CaCO_3$) at the catholyte, consuming 100% of initial [Mg] and 20% of initial [Ca] in seawater,
Step 2. Catholyte processing, either:

Step 2a: The solids are separated from the catholyte effluent. Residual Ca^{2+} in the catholyte precipitates as $CaCO_3$ in a carbonation reactor, while $Mg(OH)_2$ solids (a) are discharged into the ocean, or (b) pre-equilibrated with seawater and carbonated inside the plant's battery limits under dilute (mass) conditions (Case 1),

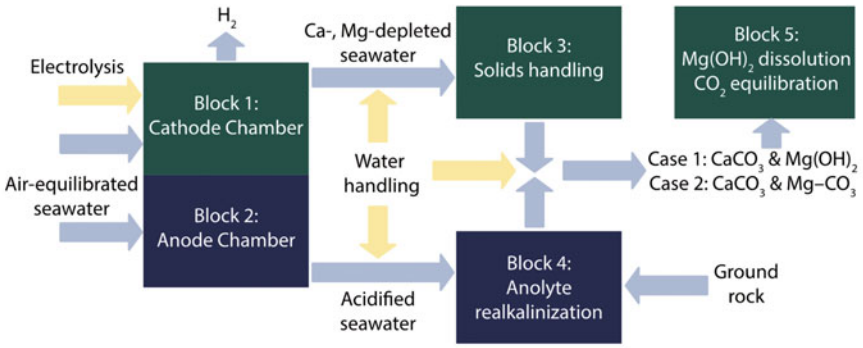

Fig. 1 Schematic of the *Equatic*™ process showing the inlet and outlet feeds and the energy requirements of the primary steps for CO_2 removal associated with the formation of: carbonate solids and (aqueous) dissolved CO_2 (Case 1) and carbonate solids only (Case 2). The major energy inputs include electrolysis, water processing and pumping, and rock grinding [2]

Step 2b: The catholyte effluent containing both solids and ions is carbonated inside plant limits, resulting in the dissolution of $Mg(OH)_2$ and equilibration with a CO_2 enriched vapor under non-dilute (mass) conditions to produce hydrated Mg-carbonates, while the residual Ca^{2+} in solution precipitates as $CaCO_3$ (Case 2),

Step 3. The realkalinization of the anolyte stream to neutralize its acidity and replenish divalent cations that are consumed (and do not redissolve) during mineral precipitation, and

Step 4. The discharge of the processed anolyte and catholyte streams back into the ocean [2].

We can consider a process configuration wherein air is sparged into the brucite-containing catholyte within a high surface-to-volume (s/v, m^{-1}), high mass transfer rate aeration reactor, i.e., inside-the-battery limit ("ISBL" approach) of an industrial plant. Careful analysis shows that herein all residual Ca^{2+} in solution in fact precipitates as $CaCO_3$, while the dissolution of $Mg(OH)_2$ in the presence of CO_2 results in the precipitation of hydromagnesite and nesquehonite (Fig. 2).

The net extent of CDR (CO_2 removal) accomplished by the *Equatic*™ process must be measurable, verifiable, reportable, additional (i.e., it would not have occurred without a market for carbon credits), and durable (permanent). In addition, the potential for leakage, harm, and co-benefits must be considered. Using the analysis presented in the sections above and in alignment with a recent approach suggested by CarbonPlan [7], we can calculate the net extent of CO_2 removal effected by the *Equatic*™ process as follows:

$$\text{Total Carbon Removal}_{CO_2e} = \text{Drawdown}_{CO_2e} - \text{Emissions}_{CO_2e},$$

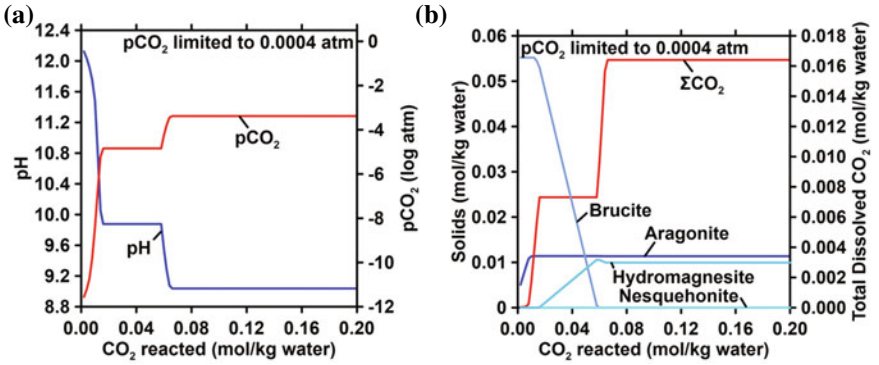

Fig. 2 Changes in **a** pH, **b** solid phase assemblage, and total dissolved CO_2 in the catholyte during reaction with CO_2 to achieve equilibrium pCO_2 equivalent to atmospheric conditions at 25 °C. These simulations show that the catholyte solids discharged include hydromagnesite and aragonite, in general agreement with our experiments

where Emissions_{CO_2e} includes the total embodied CO_2 emissions from material and energy use (e.g., the grid emissions factor of electricity, and the amount of energy embodied in the co-produced hydrogen assuming typical purification demands and conversion efficiencies), and:

$$\text{Drawdown}_{CO_2e} = \text{Equatic}_{\text{Dissolved},CO_2e} + \text{Equatic}_{\text{Solid},CO_2e} - \text{Evasion from seawater.}$$

The CO_2 sequestered as dissolved HCO_3^- and CO_3^{2-} ions, and solid carbonates can be quantified unambiguously by weighing the masses of $Mg(OH)_2$ and $CaCO_3$ produced, and multiplying these masses by a *carbon removal factor*, as follows (in units of g CO_2 per m^3 of water processed):

$$\begin{aligned}&\text{Equatic}_{\text{Dissolved},CO_2e}\left(\text{g } CO_2/\text{m}^3 \text{ water}\right)\\&\quad = \text{mass \% } Mg(OH)_2 \times \text{total mass of solids } \left(\text{g}/\text{m}^3 \text{ water}\right)\\&\qquad \times \left(1.7 \text{ mol } CO_2/\text{mol } Mg(OH)_2\right) \times \left(44.01 \text{ g } CO_2/\text{mol } CO_2\right)\\&\qquad \times \left(1 \text{ mol } Mg(OH)_2/58.3197 \text{ g } Mg(OH)_2\right),\end{aligned}$$

$$\begin{aligned}&\text{Equatic}_{\text{Solid},CO_2e}\left(\text{g } CO_2/\text{m}^3 \text{ water}\right)\\&\quad = \text{mass \% } CaCO_3 \times \text{total mass of solids } \left(\text{g}/\text{m}^3 \text{ water}\right)\\&\qquad \times \left(1 \text{ mol } CO_2/\text{mol } CaCO_3\right) \times \left(44.01 \text{ g } CO_2/\text{mol } CO_2\right)\\&\qquad \times \left(1 \text{ mol } CaCO_3/100.0869 \text{ g } CaCO_3\right),\end{aligned}$$

Summary and Conclusions

The total mass of the solids can be measured by separating the solids from the catholyte effluent stream, and the mass percentages of $Mg(OH)_2$ and $CaCO_3$ quantified—online and in real-time—using thermogravimetric analysis (TGA). The mass percentages of $Mg(OH)_2$ and $CaCO_3$ are taken from the mass loss between 300–500 °C and 600–900 °C, respectively. The carbon removal factor for $Equatic_{Dissolved,CO_2e}$ is affected by the extent of $Mg(OH)_2$ dissolution and the extent of CO_2 absorption (into water) from air. The ISBL approach discussed above eliminates these uncertainties. The evasion of CO_2 from seawater may result from secondary $CaCO_3$ precipitation or the mixing of un-neutralized acid (anolyte), albeit only in the case of the "in ocean" approach, considerations of which are addressed above. While there are uncertainties regarding increasing the dissolved inorganic carbon (DIC) content of the oceans, notably, the *Equatic*™ approach counteracts ocean acidification, which poses a significant risk to ocean ecosystems via a multitude of ways [8, 9].

References

1. La Plante EC, Chen X, Bustillos S, Bouissonnie A, Traynor T, Jassby D, Corsini L, Simonetti DA, Sant GN (2023) Electrolytic seawater mineralization and the mass balances that demonstrate carbon dioxide removal. ACS EST Eng. https://doi.org/10.1021/acsestengg.3c00004
2. La Plante EC, Simonetti DA, Wang J, Al-Turki A, Chen X, Jassby D, Sant GN (2021) Saline water-based mineralization pathway for gigatonne-scale CO_2 management. ACS Sustain Chem Eng 9(3):1073–1089. https://doi.org/10.1021/acssuschemeng.0c08561
3. Intergovernmental Science-Policy Platform on Biodiversity and Ecosystem Services (2022) Summary for policymakers of the methodological assessment of the diverse values and valuation of nature of the Intergovernmental Science-Policy Platform on Biodiversity and Ecosystem Services (IPBES). Zenodo, Bonn. https://doi.org/10.5281/zenodo.7410287
4. Parkhurst DL, Appelo CAJ (2013) Description of input and examples for PHREEQC Version 3—a computer program for speciation, batch-reaction, one-dimensional transport, and inverse geochemical calculations. US Geol Surv Tech Methods Book 6:497
5. Millero FJ, Feistel R, Wright DG, McDougall TJ (2008) The composition of standard seawater and the definition of the reference-composition salinity scale. Deep Sea Res Part Oceanogr Res Pap 55(1):50–72. https://doi.org/10.1016/j.dsr.2007.10.001
6. NOAA US Department of Commerce. Global Monitoring Laboratory—carbon cycle greenhouse gases. https://gml.noaa.gov/ccgg/trends/mlo.html. Accessed 08 Sept 2021
7. Chay F, Klitzke J, Hausfather Z, Martin K, Freeman J, Cullenward D (2022) Verification confidence levels for carbon dioxide removal. CarbonPlan. https://carbonplan.org/research/cdr-verification-explainer
8. Doney SC, Busch DS, Cooley SR, Kroeker KJ (2020) The impacts of ocean acidification on marine ecosystems and reliant human communities. Annu Rev Environ Resour 45(1)
9. Kroeker KJ, Kordas RL, Crim R, Hendriks IE, Ramajo L, Singh GS, Duarte CM, Gattuso J-P (2013) Impacts of ocean acidification on marine organisms: quantifying sensitivities and interaction with warming. Glob Change Biol 19(6):1884–1896. https://doi.org/10.1111/gcb.12179

A Clean Production Metallurgy—Chlorine Metallurgy: A Review

Haiyue Xue, Guozhi Lv, Ting-an Zhang, and Long Wang

Abstract The progress of global industrialization is inextricably intertwined with the development of metallurgical technologies. Chlorine metallurgy is a pivotal technology that plays a crucial role in enhancing the utilization of intricate mineral resources, thereby facilitating their efficient processing. Chlorine metallurgy employs chlorinating agents to convert metals in raw materials into chlorides, thereby affecting the separation and purification of polymetals in an eco-friendly manner. The utilization of metallurgical chloride can concurrently achieve a substantial enhancement in the rates of recovery, purity, and cleanliness. The article examines advancements in the implementation of various chlorine metallurgy techniques, including processes such as chlorination roasting, chlorination melting, and chlorination refining. The challenges associated with chlorine metallurgy applications are presented, along with the identification of potential avenues for future research in the field of chlorine metallurgy.

Keywords Chlorination metallurgy · Clean utilization · Complex mineral · Metal recovery

Introduction

Global industrialization is growing rapidly, accompanied by a boom in the metallurgical industry. In recent years, countries around the world have been paying more and more attention to green development, focusing on environmental development along with industrial development. Therefore, a green and healthy metallurgical technology, chlorinated metallurgy, is especially important. Chlorometallurgy is the technology of extracting metals from minerals in the form of chlorides by means of chlorinating agents [1]. Compared to metal oxides, metal chlorides are more active physicochemically, which is favorable for the extraction and separation of

H. Xue · G. Lv (✉) · T. Zhang · L. Wang
School of Metallurgy, Northeastern University, Shenyang 110819, China
e-mail: lvgz@smm.neu.edu.cn

© The Minerals, Metals & Materials Society 2024

C. Iloeje et al. (eds.), *Energy Technology 2024*, The Minerals,
Metals & Materials Series, https://doi.org/10.1007/978-3-031-50244-6_10

mineral metals. In the sixteenth century, it was discovered that the addition of table salt increased the extraction rate of gold and silver from ores [2]. The chlorinated roasting-leaching method was used in the eighteenth century to treat precious metal ores [2]. The application of chlorinated metallurgy took a major turn in the nineteenth century when it was discovered that the technology could be used to treat low-grade copper ores [2]. Since the twentieth century, chlorinated metallurgy has been widely used in the extraction and separation of magnesium, copper, tin, titanium, and other metals [2]. The chlorinated metallurgy technology is still being explored and developed to this day.

Chlorinated metallurgy includes chlorinated roasting, chlorinated dissociation, chlorinated leaching, chlorinated smelting, chlorinated refining, and other methods. Chlorinated metallurgy technology has the advantages of lower requirements for raw materials, lower temperature of the reaction process, and higher efficiency of metal separation than the traditional metallurgy technology.

Current Status of Chlorinated Metallurgy Research

Chloride Roasting

Chlorination roasting is a method of extracting useful elements from ores by reacting the chlorinating agent with the metals in the ore at 800–1200 °C. The principle of separation lies in the control of the reaction temperature according to the difference in the melting and boiling points of the different chlorinated compounds, thus enabling the separation and recovery of the chlorinated metals. The chlorinated metals are soluble in acid or water, so the separation products can be leached. The different chlorinated compounds are then separated by applicable extraction methods.

Chlorination roasting is one of the more commonly used chlorination methods (Fig. 1). A number of scholars have studied this process. Guo et al. [3] recovered zinc and lead metals from copper smelting slag by chlorine roasting. Under the optimum conditions, the recoveries of zinc and lead were 74.74% and 94.72%, respectively. It was found that high reaction temperatures and long roasting times reduced metal recovery. Xu et al. [4] extracted valuable metals from complex sulfide ore concentrates by chlorinated roasting-water leaching. Under the optimal experimental conditions, the recoveries of nickel, copper, and cobalt were as high as 95%, 98%, and 88%, respectively. The process recovered multiple metals from the ore material simultaneously. Chlorination roasting is a simple process with lower energy consumption and higher metal recovery than conventional thermal ore treatment processes. However, there is the problem of higher corrosion resistance requirements for equipment in the leaching process.

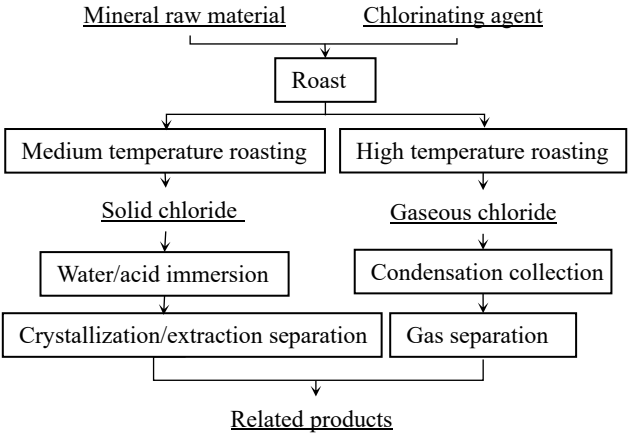

Fig. 1 Chlorination roasting flowchart

Chlorinated Precipitation

Chlorine dissociation, also known as chlorination reduction roasting. This is a chlorination reaction. A chlorinating agent and a reducing agent are added to the ore. When the reaction reaches a certain temperature, the metal chloride volatilizes. It is reduced directly to a single metal on the surface of the reducing agent. Finally the metal is recovered by magnetic separation (Fig. 2).

Chlorination isolation method is very suitable for the extraction of effective components in difficult-to-treat ores, which can get very good extraction results. Yu et al. [5] mixed high-grade manganese ore, carbonaceous reductant, chloride, and performed reduction roasting at 1000 °C. The results showed that 89.4% of the

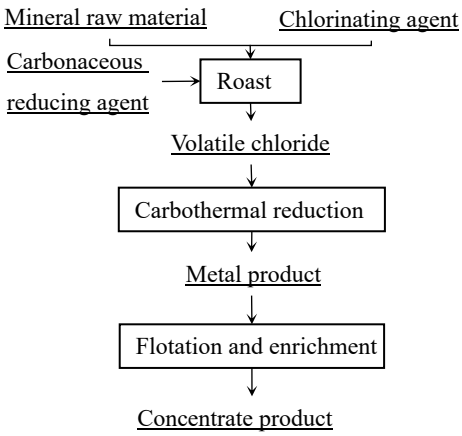

Fig. 2 Chlorination segregation flowchart

manganese could be recovered in an aqueous solution as chloride, while the dissolution rate of iron impurities was only 3%. The addition of calcium chloride further facilitates the reduction of iron. Chlorination reduction roasting of high magnesium and low nickel ores using sodium chloride as the chlorinating agent and coal as the reducing agent was studied by Zhou et al. [6]. The nickel recovery was as high as 98.31% under the optimal experimental conditions. Chlorine dissociation has the advantage of a relatively simple process and a low rate of loss of metals.

Chloride Leaching

Chlorine leaching is a wet chlorination method. In this method, the ore is immersed in a solution that reacts with a chlorinating agent (Fig. 3) [7]. The chlorinated leaching process relies primarily on the multiple effects of chloride ions in solution. Chlorine ions can both bind and separate metal ions from minerals and act as an ion exchanger to displace ions from their adsorbed state in minerals.

Scholars have also worked in the field of chlorine leaching. Wang et al. [8] were able to achieve a 92.8% gold leaching rate by immersing waste printed circuit boards in a sodium chlorate-sodium chloride-sulfuric acid solution. They found that the potential difference of ions in solution affects the leaching behavior of gold. Oxygen produced during the reaction passivates the gold to form $Au(OH)_3$. Pak et al. [9] carried out pressurized oxidative pretreatment, chlorination and hydrogenation leaching of high sulfur refractory metallurgical concentrates. Under the optimal conditions, the leaching rate of gold can reach 96.54%. From the research of scholars, it can be seen that the advantage of the chlorinated leaching method lies in the good extraction effect. Compared with chlorination roasting method and chlorination dissociation method, it does not need high-temperature treatment and has lower energy consumption. However, hydrochloric acid is too corrosive to the

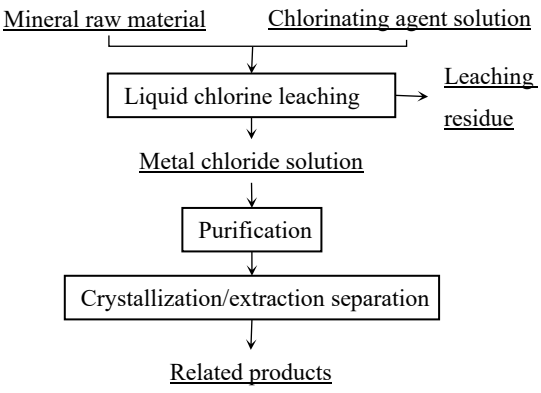

Fig. 3 Chlorination leaching flowchart

equipment. The reaction process will produce chlorine ion waste liquid, forming secondary pollution.

Melt Chlorination

Melt chlorination is one of the typical pyrochlorination technologies. It is less selective for raw materials than traditional pyrometallurgy [10]. Molten chlorination is a process in which the raw ore is reacted in a molten state with the addition of a chlorinating agent (Fig. 4). This method is commonly used for the extraction of gold from difficult-to-treat gold ores.

Huang et al. [11] investigated the destructive behavior of molten state metal chlorides on the structure of $ZnFe_2O_4$ with respect to the difficulty of separating zinc and iron in electric arc furnace dust. It was found that the mixed system of calcium chloride and magnesium chloride was more favorable to promote zinc chlorination and inhibit iron chlorination. In this system, zinc can be chlorinated at a rate of more than 90% and iron at a rate of less than 5%. The chlorination behavior of magnesium chloride towards rare earth oxides in molten chlorides was studied by Wang et al. [12]. Experiments showed that lanthanum oxide was chlorinated by magnesium chloride to form lanthanum chloride. As can be seen from the studies of scholars, the fusion chlorination method does not require much raw material. However, the samples obtained from the experiments are often of insufficient purity and have low metal recoveries.

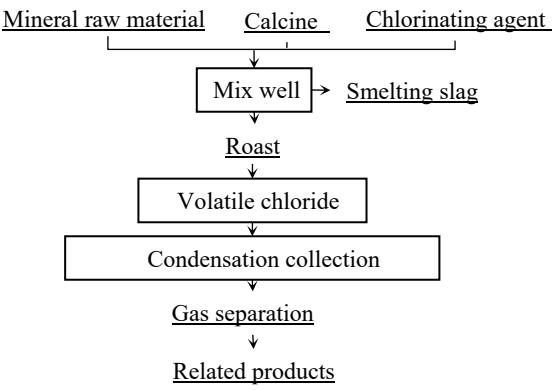

Fig. 4 Chlorination melting flowchart

Chlorine Refining

Chlorination refining differs from the methods described above in that the chlorinating agent forms impurity chlorides with impurities in the ore, thus extracting the metal. The method requires that the binding of chlorine to impurities to be superior to the binding of chlorine to metals. It is required that the impurity chlorides do not intermelt with the refined metal.

The kinetic behavior of magnesium impurities removed from aluminum chips by chlorination was discussed by Vieira et al. [13]. The results showed that the addition of chlorine either alone or in combination with an inert gas increased the magnesium removal. The chlorination process was used in the field of benzene refining by Molony et al. [14]. They use benzene fraction as raw material and remove paraffin and naphthene from crude benzene by adding chlorinating agent. The recovery of benzene was about 95% after chlorination reaction under the combined effect of UV light and peroxide. The chlorination refining method has the advantage of a simple process. However, its process parameters are difficult to control, the resulting product is not pure enough, and the experimental cost is high.

Progress in the Application of Chlorinated Metallurgy

Natural Ore

Natural ores are ores whose main metal composition is natural elements such as gold and silver. Carbonaceous gold ore is a kind of gold ore which is more difficult to treat. The common treatment methods of gold ore are leaching method, biological method, and so on. However, these methods have problems such as environmental pollution and low efficiency. Wang et al. [15] proposed the simultaneous recovery of gold and zinc elements in the ore by chlorine roasting using difficult carbonaceous gold ore as raw material and sodium chloride as chlorinating agent. The method obtained gold and zinc extraction rates up to 92% and 92.56%, respectively. This method expands a new way of thinking for the multi-element extraction of carbonaceous gold ore. Russian black shale gold ores containing platinum and palladium elements are an important natural resource. Kononova et al. [16] studied the effect of chlorination leaching of black shale gold ores in HCl/NaCl solution in the presence of manganese dioxide. The results showed that the extraction of each precious metal was above 90%. Difficult-to-treat gold ores are usually recovered by leaching after pretreatment, and various means of pretreatment have problems such as high energy consumption and long residence time requirements [17]. Therefore, the study of subsequent leaching is of great significance. Cyanide leaching and high-pressure chlorination leaching have the problems of toxicity and high equipment requirements, respectively. Compared with cyanide method, chlorination method has the advantages of high recovery rate and fast reaction speed.

Compared with the traditional cyanidation and biological methods, chlorination technology has the advantages of high metal recovery rate and simple reaction process. The application of chlorination technology in the field of natural ores is promising.

Sulphide Ore

Sulphide ores are ores in which metallic elements are present in the form of sulphides, such as nickel sulphide and chalcopyrite. Nickel metal is a very important strategic metal, which usually exists in the form of sulfide in ores. How to efficiently extract nickel metal from low-grade nickel ores is a very important research direction. Compared with the traditional hydrometallurgical technology, the chlorination roasting method has a simple process flow, uncomplicated post-treatment, and higher metal recovery. Xu et al. [4] explored the feasibility of low-temperature chlorination roasting of nickel sulfide concentrates by using hydrogen chloride produced by pyrolysis of ammonium chloride as the chlorinating agent. The recoveries of nickel, copper, and cobalt in the experiment were as high as 95%, 98%, and 88%, respectively. Pyrite usually coexists with nickel sulfide, and its separation is technically difficult. The commonly used separation processes are blowing conversion and sulfuric acid leaching [18]. Xiong et al. [18] investigated the reaction mechanism of pyrite with ammonium chloride by combining density functional theory and experiment. They found that the reaction could be carried out in three ways. Eventually, pyroxene were successfully converted to metal chlorides.

Chlorination is one of the potential technologies for the separation and recovery of sulphide ores. It has a lower reaction temperature compared with conventional pyrometallurgy. Chlorination for recovery of sulphide ores allows simultaneous recovery of associated elements within the ore. It tolerates lower ore grades and is applicable to a wide range of complex sulfide ores. The study of the mechanism of sulfide ore chlorination treatment will be an important direction for future research.

Oxidized Ores

Ores in which metallic elements are present in the form of oxides are oxidized ores, such as chromite, limonite, etc. Chromium powder is expensive and has high application value. Chromite is a good source of chromium but is accompanied by impurities such as iron and magnesium. High-temperature selective chlorination is a good way to eliminate impurities. Martirosyan et al. [19] reacted chromite with a chlorinating agent by heating. The impurities are dissolved in water in the form of chlorides and the insoluble material is the chromium concentrate. The concentrate contains 77.23% chromium oxide. Limonite is a type of nickel laterite ore which is commonly treated by high-pressure acid leaching, reductive roasting-ammonia

leaching with low extraction rate. Fan et al. [20] proposed a reductive roasting-selective chlorination-water leaching method for the extraction of nickel and cobalt. In this process, nickel and cobalt were dissolved in water in the form of chlorides and the extraction rates reached 91% and 90%, respectively. Iron remains in the slag and the leaching rate was less than 4%. The raw material for the titanium industry is mainly ilmenite, and the removal of iron impurities is the focus of the process. Early processes generally had many steps for removing impurities, heavy pollution and high cost [21]. Selective chlorination process can remove iron in one step, saving time and cost. However, there exists a small amount of titanium that is lost by chlorination.

The chlorination process is simple for treating oxidized ores. The simplicity of the process enables the cost of the experiment to be reduced. From the studies of the above mentioned scholars, it is found that the chlorination technique is ideal for recovering metals from oxidized ores and has a high impurity removal rate. It is superior to other methods of oxidized ore treatment such as thermal and wet methods.

Mixed Ores

Minerals in which metal oxides coexist with metal sulfides are called mixed ores. Copper oxide-sulfide ores contain useful elements such as nickel and copper. The commonly used flotation-fire smelting process has the disadvantages of high energy consumption and high cost. Therefore, scholars have proposed wet leaching [22] and biological treatment [23]. However, there are problems such as low productivity and low metal recovery. With the advancement of equipment material performance, chlorination has returned to the scholars' view. Mu et al. [24] studied a new process of simultaneous extraction of nickel and copper from mixed sulfur oxide copper-nickel ores by chlorination-water leaching. The nickel and copper recoveries of this method were greater than 92.33% and 89.43%, respectively. Xu et al. [25] investigated the effect of chlorination roasting on the co-extraction of nickel and copper from low-grade nickel sulfide ores as raw materials. The extraction rates of nickel and copper could reach 83.6% and 81.3%. The percentage of iron impurities in the leach solution was less than 3%.

Compared with the traditional process, chlorination technology has a short process flow and good effect. The special characteristics of the chlorination process, such as the insufficiently in-depth study of the mechanism and the high requirements for equipment and materials, have limited its industrialized development. With the continuous progress in the field of materials, chlorination technology in industrialized treatment of complex mixed ores will be a major trend in the future.

Rare Earth Minerals

Rare earths are valuable strategic resources that can be utilized in many industries such as medical, military, and chemical. Common rare earth ores include cerium fluorocarbon, monazite, and yttrium phosphorite. The traditional process chooses direct sulfuric acid roasting to recover rare earths, which is complicated and generates wastewater and exhaust gas. Zhu et al. [26] developed a new process, in which they immobilized elemental fluorine with magnesium oxide, and calcined rare earth oxides with ammonium chloride as a chlorinating agent. Finally, the rare earth elements were recovered by water leaching. When the reaction was carried out at 500 °C for 25 min, the recovery of rare earths was 75%. The apparent activation energy was 36.8 kJ/mol. Yu et al. [27] chlorinated the Baiyun Ebo rare earth tailings in China to synchronize the recovery of multiple elements such as rare earths, niobium, thorium, and iron from the ore. The results showed that the recovery of rare earths, niobium, thorium, iron, and fluorine reached 76–93%, 65–78%, 72–92%, 84–91%, and 81–94%, respectively.

Rare earth ores have a complex composition and are usually accompanied by phosphorus, fluorine, and other impurities. Chlorination technology has a higher metal recovery rate than traditional oxidation roasting and wet leaching processes. It can synchronize the recovery of multiple metals in low-grade rare earth ores, which is difficult to be achieved by traditional technologies under the same conditions. Chlorination technology is a promising rare earth ore recovery technology.

Conclusions

Chlorometallurgy can be used to process a wide range of complex ores, tailings, low-grade ores, and more. This process allows for the simultaneous recovery of associated elements while recovering useful metals. This article mainly describes the current status of the development of chlorometallurgy, the classification of methods of chlorometallurgy technology, as well as the application of chlorometallurgy in major ores. Chlorometallurgical technology initially suffered from the problem of high corrosiveness of the equipment. Recent advances in the field of materials have allowed this disadvantage to be ameliorated. Compared with traditional pyrometallurgy, chlorometallurgy has a lower reaction temperature and uses less energy. At the same time, chlorides are more soluble in water, resulting in higher metal recovery. Compared with traditional hydrometallurgy, chlorometallurgy has a great advantage in the field of difficult-to-treat mineral raw materials. The hydrometallurgical technology for difficult-to-treat minerals has the disadvantages of complex processes, many waste liquids, and poor recovery effect. Compared with the traditional wet process, the chlorometallurgy process is short and produces less waste liquid. Part of the waste liquid can be recycled to the process after treatment. Usually, chlorometallurgy only treats minerals by chlorine roasting and leaching, which is a simple

process with high metal recovery. In the chlorine reduction roasting technology, segmented condensation according to the differences in the melting and boiling points of different metal chlorides can achieve the simultaneous recovery of a variety of elements. Therefore, chlorometallurgy is a promising mineral treatment technology.

At present, chlorometallurgy has a few problems that need to be solved. The first is the problem of equipment corrosion. Although the emergence of corrosion-resistant materials has improved this problem, there is still the disadvantage of low equipment life. Secondly, it is the problem of efficient use of the chlorinating agent. Attention should be paid to the efficiency of chlorinating agents. Gas chlorinating agents require attention to gas leakage and gas recovery. Solid chlorinating agents need to be recovered after reacting. The last challenge is the industrialization of the process. Mechanism research needs to be deepened. How to improve the cycle efficiency of the whole chlorination process system should be the focus, which will lay the foundation for industrialization.

References

1. Xing Z, Cheng G, Yang H et al (2020) Mechanism and application of the ore with chlorination treatment: a review. Miner Eng 154:106404. https://doi.org/10.1016/j.mineng.2020.106404
2. Metallurgical Research Laboratory, Central South Institute of Mining and Metallurgy (1978) Chlorination metallurgy. Metallurgical Industry Press, Beijing, China (in Chinese)
3. Guo X, Zhang B, Wang Q et al (2021) Recovery of zinc and lead from copper smelting slags by chlorination roasting. JOM 73(6):1861–1870. https://doi.org/10.1007/s11837-021-04680-4
4. Xu C et al (2017) Extraction of metals from complex sulfide nickel concentrates by low-temperature chlorination roasting and water leaching. Int J Miner Metall Mater 24(4):377–385. https://doi.org/10.1007/s12613-017-1417-2
5. Yu D, Cui F, Cong Y et al (2019) Simultaneous selective chlorination and carbothermic reduction of high-iron manganese ore for the recovery of manganese chloride and metallic iron. Metals 9(10):1124. https://doi.org/10.3390/met9101124
6. Zhou S, W Yei, Li B et al (2016) Chloridization and reduction roasting of high-magnesium low-nickel oxide ore followed by magnetic separation to enrich ferronickel concentrate. Metall Mater Trans B 47(1):145–153. https://doi.org/10.1007/s11663-015-0478-8
7. Huang D, Huang J, Zhang Y et al (2023) Short-process preparation of high-purity V_2O_5 from shale acid leaching solution via chlorination. Processes 11(4):1270. https://doi.org/10.3390/pr11041270
8. Wang J, Zhang M, Lu Y (2021) Study of gold leaching behavior in the chlorination process from waste printed circuit boards. ACS Sustain Chem Eng 9(1):284–290. https://doi.org/10.1021/acssuschemeng.0c07165
9. Pak K-S, Zhang T-A, Kim C-S et al (2020) Research on chlorination leaching of pressure-oxidized refractory gold concentrate. Hydrometallurgy 194:105325. https://doi.org/10.1016/j.hydromet.2020.105325
10. Matsuura H, Tsukihashi F (2005) Chlorination and evaporation behaviors of PbO-$PbCl_2$ system in Ar-Cl_2-O_2 atmosphere. ISIJ Int 45(12):1804–1812. https://doi.org/10.2355/isijinternational.45.1804
11. Huang J, Li G, Yang X (2023) Chlorination of $ZnFe_2O_4$ by Molten $MgCl_2$: effect of adding $CaCl_2$. J Sustain Metall. https://doi.org/10.1007/s40831-023-00727-9
12. Wang Y-C et al (2015) The chlorination of La_2O_3 by $MgCl_2$ in the LiCl-NaCl melts. Nucl Sci Technol 26(1):112–116

13. Vieira EA, de Oliveira JR, Alves GF et al (2012) Use of chlorine to remove magnesium from molten aluminum. Mater Trans 53(3):477–482. https://doi.org/10.2320/matertrans.M2011256
14. Molony OW, Hughes D (2007) The refining of benzole by chlorine treatment. J Appl Chem 8(10):690–700. https://doi.org/10.1002/jctb.5010081012
15. Wang H, Feng Y, Li H et al (2020) Simultaneous extraction of gold and zinc from refractory carbonaceous gold ore by chlorination roasting process. Trans Nonferrous Met Soc China 30(4):1111–1123. https://doi.org/10.1016/S1003-6326(20)65282-7
16. Kononova UN, Patrushev VV, Kononov YS (2014) Recovery of noble metals from refractory sulfide black-shale ores. Hydrometallurgy 144:156–162. https://doi.org/10.1016/j.hydromet.2014.02.008
17. Wu H, Wang H, Duan S et al (2022) Full-process analysis on volatilizing gold, zinc by chlorination roasting and synchronous recovery vanadium by water leaching of carbonaceous gold ore. Miner Eng 185:107682. https://doi.org/10.1016/j.mineng.2022.107682
18. Xiong X et al (2021) A novel approach for metal extraction from metal sulfide ores with NH4Cl: a combined DFT and experimental studies. Sep Purif Technol 267:118626. https://doi.org/10.1016/j.seppur.2021.118626
19. Martirosyan VA, Sasuntsyan ME, Savich VV (2018) Preparation of superconcentrate and chromium powder from chromite ore. Metallurgist 62(3–4):355–360. https://doi.org/10.1007/s11015-018-0668-0
20. Fan C, Zhai X, Fu Y et al (2010) Extraction of nickel and cobalt from reduced limonitic laterite using a selective chlorination-water leaching process. Hydrometallurgy 105(1–2):191–194. https://doi.org/10.1016/j.hydromet.2010.08.003
21. Park S-H, Lee S-Y, Ring R et al (2023) Removal of Fe from ilmenite ore powders through selective chlorination using CO and Cl-2 gas mixture at 1073–1173 K in a static bed. J Sustain Metall 9(1):160–171. https://doi.org/10.1007/s40831-022-00628-3
22. Xu B, Yang Y, Li Q et al (2015) Stage leaching of a complex polymetallic sulfide concentrate: focus on the extraction of Ag and Au, Hydrometallurgy. JOM 159:87–94. https://doi.org/10.1016/j.hydromet.2015.10.008
23. Yang C et al (2010) Bioleaching of a low grade nickel–copper–cobalt sulfide ore. Hydrometallurgy 106(1):32–37. https://doi.org/10.1016/j.hydromet.2010.11.013
24. Mu W, Cui F, Xin H et al (2019) A novel process for simultaneously extracting Ni and Cu from mixed oxide-sulfide copper-nickel ore with highly alkaline gangue via $FeCl_3 \bullet 6H_2O$ chlorination and water leaching. Hydrometallurgy 191:105187. https://doi.org/10.1016/j.hydromet.2019.105187
25. Xu X et al (2022) Direct extraction of nickel and copper from low-grade nickel sulfide ore by chlorination roasting with mixed $MgCl_2 \cdot 6H_2O$ and NaCl. JOM 74(5):1989–1999. https://doi.org/10.1007/s11837-021-05122-x
26. Zhu G, Chi R, Shi W et al (2003) Chlorination kinetics of fluorine-fixed rare earth concentrate. Miner Eng 16(7):671–674. https://doi.org/10.1016/S0892-6875(03)00129-8
27. Yu X-L, Bai L, Wang Q-C et al (2012) Recovery of rare earths, niobium, and thorium from the tailings of giant Bayan Obo ore in China. Metall Mater Trans B 43(3):485–493. https://doi.org/10.1007/s11663-012-9638-2

A Review of the Extraction of Gallium from Bauxite Ores

Yutong Hua, Ting-an Zhang, and Long Wang

Abstract In recent years, gallium has garnered significant attention in the semiconductor industry, which constitutes over 80% of the total demand. Gallium is widely dispersed in the Earth's crust, while only two distinct deposits of this precious metal have been discovered—Gallite ($CuGaS_2$) and Soehngeite ($Ga(OH)_3$). Based on the current investigation, it is estimated that approximately 90% of gallium is extracted from the aluminum industry. Therefore, it is imperative for us to explore the synergistic extraction of aluminum and gallium from bauxite, which has been extensively studied by numerous researchers. This paper introduces the trend of gallium in the smelting process of bauxite, summarizing a comprehensive overview of the latest trends in the extraction method of gallium from the bauxite process such as ion exchange method, extraction method, fractional precipitation method, and electrolysis, comparing the advantages and disadvantages of each extraction method, which will guide the efficient extraction of valuable components from bauxite.

Keywords Gallium recovery · Loose metal · Bauxite · Alumina production

Introduction

Gallium is widely used in the manufacture of optical materials, aerospace fields, and solar cell materials, and is the backbone of the electronics industry [1]. With the rapid development of electronics industry and related industries, the market of gallium has been in short supply. Gallium is a kind of dispersed metal, which rarely exists in nature as a single deposit with industrial mining value, and usually enters the lattice of some rock-forming elements in the form of isomorphism. In the early crystallization process of magmas, Ga^{3+} replaces Al^{3+} and partially replaces Fe^{3+} in

Y. Hua · T. Zhang (✉) · L. Wang
Key Laboratory of Ecological Metallurgy of Multi-metal Intergrown Ores of Ministry of Education, Special Metallurgy and Process Engineering Institute, Northeastern University, Shenyang 110819, China
e-mail: zta2000@163.net

© The Minerals, Metals & Materials Society 2024

C. Iloeje et al. (eds.), *Energy Technology 2024*, The Minerals, Metals & Materials Series, https://doi.org/10.1007/978-3-031-50244-6_11

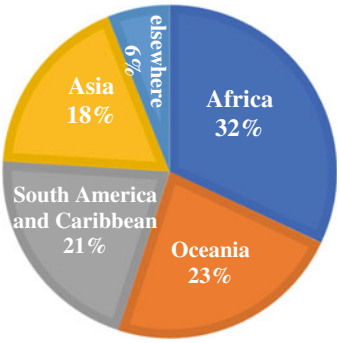

Fig. 1 Global bauxite resource distribution in 2022 [3]

various magmas, especially silicates and silicoaluminates. Ga^{3+} is closely associated with Al^{3+} and Fe^{3+} under the conditions of superbiotic oxidation. 90% of the world's gallium is derived from the by-product of the aluminum industrial production process, 10% from zinc smelting residue, and a very small amount of soot [2]. According to the report "Mineral Commodity Summaries 2023" [3] released by USGS, it is estimated that the global bauxite resources range from 55 to 75 billion tons, and the specific distribution of countries is shown in Figs. 1 and 2. The main deposits in China are ancient weathering crust sedimentary bauxite, often associated with useful elements such as gallium and vanadium, whose proven reserves account for 78% of China's total reserves, followed by accumulative type and lateritic type [4]. Therefore, the abundant bauxite is an important raw material for the production of gallium metal. However, in the traditional bauxite treatment process, gallium is often enriched in the circulating mother liquor or discharged with red mud, resulting in the waste of gallium resources. How to synergistically extract gallium from bauxite has become a research hotspot.

The Trend of Gallium in the Smelting Process of Bauxite

In industrial production, Bayer process is commonly used to treat diaspore or diaspore facies with aluminum-Si ratio greater than 6–7. High silicon and low grade bauxite were treated by sintering. It is more economical to produce medium grade bauxite by Bayer-sintering process. Bauxite generally contains 0.003–0.008% gallium, gallium can be enriched and extracted in the smelting process. The main reactions of gallium in Bayer process and sintering process and the trend distribution of gallium in smelting process will be introduced below.

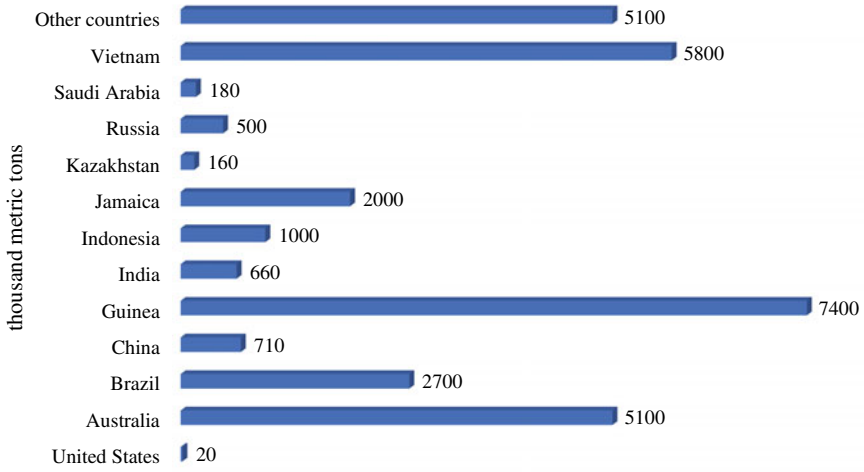

Fig. 2 World bauxite reserves in 2022 [3]

Bayer Method

In industrial-scale production, simultaneous recovery of gallium and production of alumina from Bayer solution are the main process. In the dissolution stage, Ga_2O_3 reacts with the lye to enter the solution in the form of sodium gallite.

$$Ga_2O_3 + 2NaOH = 2NaGaO_2 + H_2O \quad (1)$$

Since the pH values of Al^{3+} and Ga^{3+} precipitated in $Me(OH)_3$ form are 10.6 and 9.7, the solubility of Ga_2O_3 is greater. The sodium aluminate in the solution was decomposed into crystal seeds to produce aluminum hydroxide, and 80–85% of sodium gallite was enriched in the seed mother liquor. The trend and distribution of gallium in the process of bauxite treatment by Bayer process are shown in Fig. 3.

Sintering Process

When the sinter is dissolved by water or dilute lye, about 83.5% gallium in the bauxite remains in the sodium aluminate solution, and the rest is removed with the red mud. The main chemical reactions of gallium in this process are shown in Eq. (2):

$$Ga_2O_3 + Na_2CO_3 = 2NaGaO_2 + CO_2 \uparrow \quad (2)$$

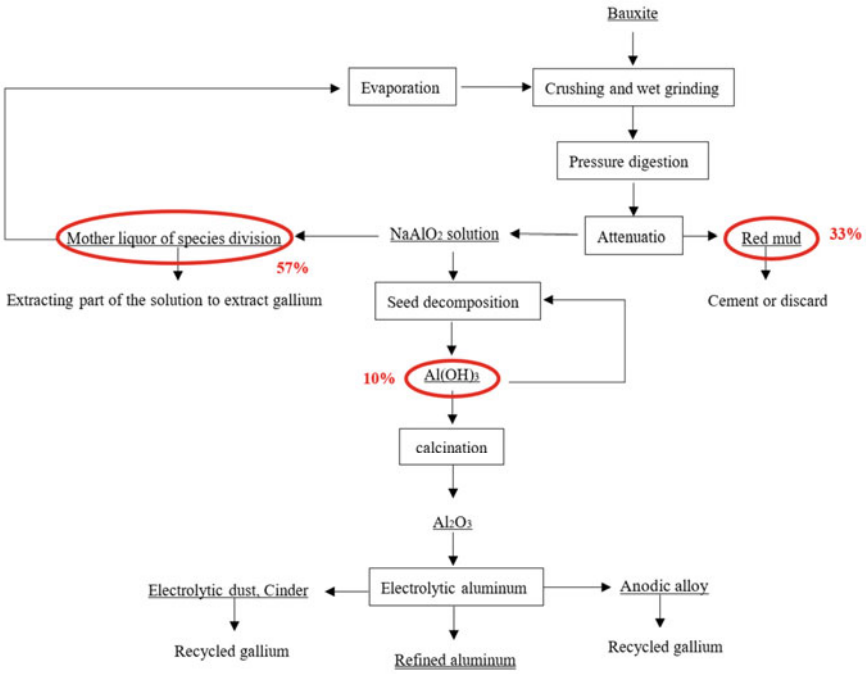

Fig. 3 Trend and distribution of gallium in Bayer process

The calcium aluminate formed in the desilication process contains about 23.8% gallium, and the remaining gallium occurs in sodium aluminate semen for carbonation and decomposition process. The carbon separation process is the process of separating aluminum and enriching gallium. Control of temperature, seed and ventilation rate is conducive to reducing gallium loss.

Extraction Method of Gallium Associated with Bauxite

Ion Exchange Method

The most widely used method for extracting gallium from Bayer's solution is ion exchange [5]. The ion exchange process includes adsorption, leaching of saturated resin and transformation of lean resin with dilute lye [6]. The seed mother liquid was first clarified by a storage tank, the temperature was lowered to 40 °C, and the adsorption stock liquid was carried through the adsorption tower. The adsorption flow rate was maintained at 3 m/h, and the resin was gradually saturated from the bottom of the tower to the top. The discharged saturated resin is added to the

washing tower manually from the top of the washing tower. The saturated resin was washed with NaOH dilute solution, and then washed with alkaline complexing eluent. Gallium metal was obtained by electrolysis after treatment with qualified eluent. There is no waste water in the whole process and all the solution can be recycled. In 1984, Kataoka found that some chelating resins composed of one –NOH group and another active group, such as $–NH_2$ and –OH, showed special extraction ability for gallium [7]. Feng et al. developed a new resin DHG586 with this structure on this basis and applied it in industry [8]. Lu et al. developed an acid leaching-ion exchange method (ALIEP) to recover gallium from Bayer red mud. In this method, the red mud was dissolved with acid, Fe^{3+} was removed by purified leach solution, gallium was enriched by circulating purified solution, and gallium was absorbed by LSC-500S resin by ion exchange method [9]. Sagdiev et al. studied the adsorption thermodynamics of gallium anion complexes on D-403 weakly basic resin and calculated the parameters of a continuously working ion exchange device with a fluidized layer [10].

Extraction Method

In 1967, Bhat and Sundararajan used 3 M hydrochloric acid to precipitate 0.6% gallium-containing gallium produced by the dissolved lime method, taking advantage of the easy dissolution of gallium from a strong acidic chloride solution, and then extracted gallium with 20%TBP solvent [11]. The disadvantage of this method is that it does not directly treat Bayer solution, but obtains gallium-containing precipitation by lime method and then dissolves extraction. In 1974, Helgorsky and Leveque first applied Kelex-100 in Bayer circulation solution to directly extract gallium from the solution [12].

Kelex-100 extraction system uses 8–10% Kelex-100, Vo:Va = 1, decanol as an additive and kerosene as a diluent. The reaction process is Eq. (3). The organic phase containing gallium was washed with 0.2–0.5 mol/L hydrochloric acid solution to remove impurities such as sodium and aluminum, and then extracted with 1.6–1.8 mol/L hydrochloric acid solution. Although sodium and aluminum can also be extracted by Kelex-100 in a small amount, the stability of the complexes formed by sodium and aluminum and extractants is low under alkaline conditions. Decyl alcohol can effectively control the formation of the third phase, but the increase of its concentration will increase the amount of sodium extraction, resulting in difficult separation of aluminum gallium. The extraction process is carried out at 50–60 °C, and increasing the extraction temperature is conducive to accelerating the extraction. Abdollahy et al. used 10% ethanol as modifier to recover gallium from alkaline aqueous solution of Jajarm alumina plant, and studied the influence of different contact time and different concentration of backextract HCl, H_2SO_4, or NaOH on the extraction effect [13]. Under the conditions of Vo:Va = 1 and room temperature, the recovery rate of gallium was 93.39% within 1 h. The co-extracted aluminum was

washed into the organic phase with 5.0 M HCl, and then the gallium was reverted with 1.5 M HCl. The total recovery rate of gallium in the reverted extract was 87.02%.

The problems of this method are high price of extractant, easy oxidation in lye, long extraction equilibrium time, and volatile dilution kerosene. In order to solve the above problems, many scholars have done a lot of research to improve the extraction efficiency. Kekesi studied the extraction kinetics based on pure kerosene and Kelex-100 system, and investigated the selectivity and efficiency of Ga/Al extraction and reextraction process by reagent dosage and stirring intensity [14]. Bauer et al. changed the position of the branch chain and substituted 5-hydroxyquinoline solution for 8-hydroxyquinoline solution [15]. Puvvada et al. used 7-alkyl instead of 8-hydroxyquinoline to extract gallium from Bayer process liquid [16]. Selecting extractants such as Kermac470b or cyclohexane can improve extraction kinetics in solution [17]. The addition of organic matter can adjust the viscosity, density, and surface tension of the liquid to improve the mass transfer rate [18] and effectively prevent the formation of the third phase.

$$Ga(OH)^{-}_{4(\text{aqueous phase})} + 3HL_{(\text{organic phase})} = GaL_{3(\text{organic phase})} + OH^{-} + 3H_2O \quad (3)$$

Direct extraction method is easy to lose extractant due to insufficient contact between solution and extractant. Resin impregnated with adsorbent can be used as a fixed bed for adsorption [19]. The sodium aluminate solution flows through the resin, gallium is adsorbed on the resin, and the solution returns to the original alumina production process to eluate the saturated resin after adsorption to achieve resin regeneration. Nakayama et al. studied ion exchange resins with different chemical and physical properties as polymer matrix to load Kelex-100, and the gallium recovery rate of ATP202 loaded with Kelex-100 was about 43 mg/g Kelex-100. The extraction rate of gallium with 10% Kelex-100 in kerosene is 2.5 mg/g [20]. The physical pore structure and cation exchange groups of the resin matrix help to recover gallium from strong alkaline solution by supported Kelex-100 resin.

The latest development in solvent extraction is the extraction of metal ions using a new class of extractants called ionic liquids, which have the advantage of low volatility. Sumitra et al. verified the feasibility of extracting gallium with Cyphos 1L 104 extractive agent and applied it to red mud samples [21]. The red mud was dissolved in 5 M HCl, the iron was removed by TBP diluent in toluene, and then gallium was extracted by 0.002 M extractant. Almost all gallium is obtained by vanadium co-extraction, and the recovery rate of gallium is 96.4%. Stijn et al. studied the extraction of gallium from Bayer waste liquid by diluting Kelex-100 with two 1,2,3-triazole ionic liquids [22]. Among them, the hydrophobic ionic liquid with low water content can directly direct the untreated Bayer liquid, and the hydrophilic ionic liquid shows good selectivity for gallium ($\alpha_{Ga/Al} \approx 20$). Azza et al. first used 5-nonyl-2-hydroxyacetophenone oxime (NHAO) as an extractant to extract the reference material (NIM-L) and black mica raw materials from the leach liquid [23]. After extraction at room temperature for 7 min with 0.5 M NHAO as solvent, compared to 1, the selectivity or separation factor of all interfering ions in the leach solution was (Ga/M) > 63, and Ga was selectively removed from the add-ons using 0.5 M H_2SO_4.

Fractional Precipitation Method

Lime Method

In 1952, the American Aluminum Company (Alcoa) first proposed the use of lime to achieve aluminum-gallium separation [24]. When the circulating liquid is fully carbonized, about 10% of gallium remains in the solution due to the high solubility of gallium in Na_2CO_3 and $NaHCO_3$. The precipitation is mainly $Al(OH)_3$ and Daocene ($Na_2O{\cdot}Al_2O_3{\cdot}2CO_2{\cdot}nH_2O$), and gallium is isomorphic to Daocene instead of aluminum. Because aluminum and calcium oxide react to produce insoluble calcium aluminate solid slag, gallium does not react with calcium oxide into the liquid phase, and gallium and aluminum can be separated. The main chemical reactions that occur during this process are as follows:

$$Na_2O{\cdot}Ga_2O_3{\cdot}2CO_2{\cdot}nH_2O + 2Ca(OH)_2 \rightarrow 2NaGaO_2 + 2CaCO_3 \downarrow + (n+2)H_2O \quad (4)$$

$$Na_2O{\cdot}Al_2O_3{\cdot}2CO_2{\cdot}nH_2O + 3Ca(OH)_2 \rightarrow 3CaO{\cdot}Al_2O_3{\cdot}6H_2O \downarrow \quad (5)$$

The process takes place in two steps, first the milk of lime reacts with sodium carbonate to fully dissolve gallium and aluminum in Eq. (6). The second step is to precipitate most of the aluminum in the form of $3CaO{\cdot}Al_2O_3{\cdot}6H_2O$.

$$Ca(OH)_2 + Na_2CO_3 = CaCO_3 \downarrow + 2NaOH \quad (6)$$

In general, every 1 kg of gallium produced will produce 10t of calcium aluminate, and a large number of residues are difficult to dispose of [25]. In addition, in the full carbonization process, the circulating liquid contains about 60 g/L of $NaHCO_3$, which requires further treatment to enter the alumina production process. The lime process has been phased out in industrial production.

Carbonization Process

In 1947, the French company Pechiney Compagnie filed a patent for the partial carbonization of CO_2 gas in Bayer's aluminate solution [26]. Figure 4 shows a typical carbonization process chain. After the bauxite is digested with caustic soda, the impurities are removed to obtain an unstable aluminate solution (the ratio of Al_2O_3 to Na_2O in the solution is higher than the equilibrium value), which is then decomposed by Bayer to remove the additional alumina to obtain a stable solution. By bubbling carbon dioxide gas, the liquid is partially carbonated until the ratio of Al_2O_3 to Na_2O is 4:5, at which time an unstable solution is obtained again, and the solution contains only 10% alumina after removal of precipitation. By using this method, the ratio of

Fig. 4 Process chain of enrichment of gallium in bauxite by carbonization [26]

Ga_2O_3 to Al_2O_3 in the precipitated product obtained after complete carbonization is 150–200 times higher than the original, and the enrichment of gallium oxide is realized, which provides a basis for the subsequent recovery of gallium.

Xu et al. proposed a three-stage carbonation process to produce gallium metal [27]. The method uses the precipitation acidity of Ga_2O_3 and Al_2O_3 in alkaline solution (the precipitation pH value of $Al(OH)_3$ is 10.6, and the precipitation pH of $Ga(OH)_3$ is 9.4–9.7 in alkaline solution) to achieve the separation of aluminum gallium in carbon mother liquor. The sodium gallite obtained from the three times of decomposition is precipitated and dissolved in an alkaline solution, and the metal gallium is recovered by electrolysis of this solution. Process flowchart and reaction equation of carbonation process are in Fig. 5.

Font et al. carried out carbonation treatment of concentrated gallium leachate when recovering gallium from IGCC fly ash, and found that 91% of aluminum precipitated at pH = 10.5, while more than 98% gallium remained in the solution [28]. Wen et al. studied the recovery of gallium from corundum flue dust and proposed that the improvement of alkali ore mass ratio and leaching temperature is conducive to the leaching of gallium (the most suitable alkali ore mass ratio is 1.2 and leaching temperature is 80 °C). Gallium was then deposited by carbonation process, and the recovery rate of gallium was more than 99% during carbonization [29].

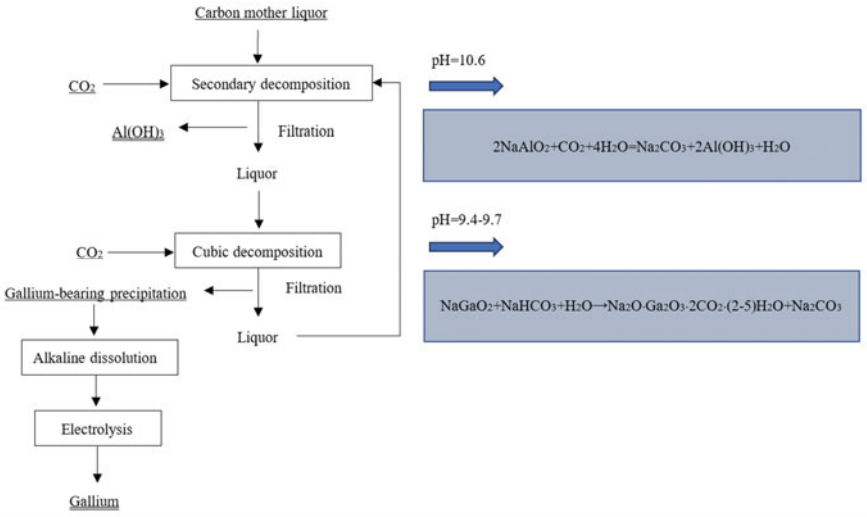

Fig. 5 Process flowchart for the production of gallium metal by three-stage carbonation [27]

Compared with the lime process, the process of recycling gallium by carbonization is short, easy to operate, and the amount of lime and carbon dioxide is greatly reduced, which saves the production cost and effectively avoids the loss of alumina in the form of calcium aluminate in the production process. The problem of this method is that it is difficult to control the slow carbonization of aluminum alone in actual production. It is calculated that the production of 1 kg of gallium will produce about 1.5 t of poor quality aluminum hydroxide [30]. Lilia et al. studied aluminate carbonization behavior and also confirmed co-precipitation of gallium hydroxide, sodium carbonate, and aluminum compounds in the treatment of an aluminate-gallate with sodium bicarbonate [31]. When extracting gallium and vanadium from the red mud of an aluminum refinery, Abdulvaliyev et al. adopted the calcium hydroaluminate precipitation carbonization method. In the first stage of carbonization, $Al(OH)_3$ precipitates and 15% Ga and V_2O_5 precipitates [32].

Electrolysis

In 1934, Hoffma used the potential difference between impurity elements and gallium for the first time to apply electrolysis to the extraction and refining of gallium [33]. In 1955, Bereteque proposed the amalgam process for the extraction of gallium. The homogenization of gallium and mercury greatly reduced the precipitation potential of gallium, and the overvoltage of hydrogen on the mercury cathode was larger [34]. This method can be used to precipitate gallium in mercury cathodes even if the concentration of gallium in the solution is low. In an electrolytic cell with a mercury cathode area of 12 m^2, gallium amalgam was obtained by electrolysis for 24 h under current density of 5000 A/m^2, cell voltage of 4 V, and electrolyte temperature of 40–50 °C, as shown in Eq. (7). When the amalgam obtained by electrolysis contains 0.3–1% gallium, the gallium amalgam is transferred to a closed container, and NaOH is added to boil to near boiling, so that Ga–Hg is decomposed and gallium-rich solution is obtained. The separated mercury is reused for electrolysis, which periodically requires purification to remove iron and other accumulated impurities. Using stainless steel as anode, the free gallium was recovered by electrolysis again at current density of 8000 A/m^2 and tank voltage of 10 V.

$$GaO_2^- + 2H_2O + 3e \xrightarrow{Hg} Ga(-Hg) + 4OH^- \quad (7)$$

The problem with this method is that the solubility of gallium in mercury is low (1.3% at room temperature [35]) and a large amount of mercury is consumed (2–3 t of mercury are required to produce 1 kg of gallium). Mercury will also be transferred into $NaAlO_2$ liquid (containing mercury up to 0.02–0.1 g/L), affecting the alumina production process. Some scholars have improved the amalgam method on this basis. Large area cathode is obtained by rotating cathode and improving electrolytic cell. Graphite blocks and 10%NaOH solution were added to gallium amalgam, heated to

100 °C, and stirred strongly for 0.5 h to form galvanic cells with gallium amalgam and graphite, and electrolyte containing gallium more than 20 g/L was obtained [36]. The electrolysis method can effectively remove micro-inclusions and can be used for deep purification of gallium [37].

Conclusions

Gallium plays an increasingly important role in the electronics industry and the world demand is increasing year by year. Bauxite is widely concerned as an important source of gallium production. In the traditional production process, gallium is usually enriched in the circulating mother liquor or discharged through red mud, resulting in resource waste. In order to meet the market demand for gallium and improve the comprehensive utilization of valuable elements in bauxite, this paper summarizes the research of some experts and scholars on the extraction of gallium from bauxite, and summarizes the main extraction methods such as ion exchange method, extraction method, precipitation method, and electrolysis method and the existing problems. It lays a foundation for the subsequent, efficient, and environmentally friendly collaborative extraction of major elements such as aluminum and gallium from bauxite.

References

1. Moskalyk RR (2003) Gallium: the backbone of the electronics industry. Miner Eng 16(10):921–929. https://doi.org/10.1016/j.mineng.2003.08.003
2. China Institute of Geology and Mineral Information (1992) Minerals of China. China Building Materials Industry Press, Beijing, pp 210–211
3. Reston (2023) Bauxite and alumina. In: Mineral commodity summaries. U.S. Geological Survey. https://pubs.usgs.gov/periodicals/mcs2023/mcs2023.pdf. Accessed 19 Sept 2023
4. Gao L, Li J, Wang D (2015) Outline of metallogenic regularity of bauxite deposits in China. Acta Geol Sinica—Engl Ed 89(6):2072–2084. https://doi.org/10.1111/1755-6724.12618
5. Flerus B, Friedrich B (2020) Recovery of gallium from smartphones—Part II: Oxidative alkaline pressure leaching of gallium from pyrolysis residue. Metals 10(12). https://doi.org/10.3390/met10121565
6. Li YJ, Lei T, Zou YM (2018) Thin metal metallurgy. Metallurgical Industry Press, Beijing, pp 392–393
7. Kataoka Y, Matsuda M, Yoshitake H (1984) Method for recovery of gallium. US Patent
8. Feng F, Li Y (2006) Effect of Bayer process solution composite on adsorbing gallium by resin. Hydrometall China 25:30–32
9. Lu FH, Xiao TF, Lin J (2018) Recovery of gallium from Bayer red mud through acidic-leaching-ion-exchange process under normal atmospheric pressure. Hydrometallurgy 175:124–132. https://doi.org/10.1016/j.hydromet.2017.10.032
10. Sagdiev VN, Cheremisina OV, Ponomareva MA (2019) Process of extraction of gallium from technological solutions with the use of ion exchange resins. Metallurgist 63(1–2):206–214. https://doi.org/10.1007/s11015-019-00811-0

11. Bhat TR, Sundararajan S (1967) The extraction of gallium chloride by tributyl phosphate and the recovery of gallium from Bayer liquor. Less Common Met 12(3):231–238
12. Helgorsky J, Leveque A (1974) Procédé de récupération du gallium de solutions très basiques par extraction liquide/liquide. French Patent
13. Abdollahy M, Naderi H (2007) Liquid–liquid extraction of gallium from Jajarm Bayer process liquor using Kelex 100. Iran J Chem Chem Eng—Int Engl Ed 26(4):109–113
14. Kekesi T (2007) Gallium extraction from synthetic Bayer liquors using Kelex 100-kerosene, the effect of loading and stripping conditions on selectivity. Hydrometallurgy 88(1–4):170–179. https://doi.org/10.1016/j.hydromet.2007.04.006
15. Bauer D, Pescher Cluzeau Y (1987) Liquid–liquid extraction of aluminium and gallium with 5-substituted 8-hydroxyquinolines. Hydrometallurgy 18:243–253
16. Puvvada GVK, Yedavalli BVS, Rao AS (1998) Solvent extraction of gallium from Bayer process liquor (Indal, Muri) using 7-alkyl-substituted-8-hydroxyquinoline (Kelex-100). Trans Indian Inst Met 51(4):223–225
17. Zhou T, Pesic B (1989) Solvent extraction of gallium with Kelex 100 from artificial sodium aluminate solutions. Trans Inst Min Metall C 98:C147–C152
18. Fourre D, Bauer G (1983) Enhancement of the extraction rate of gallium by the 7-(1-vinyl-3,3,5,5-teramethylhexyl)-8-quinolinol using micro-emulsion as organic phase. Solvent Extr Ion Exchange 1:465–483
19. Chen Y, Zhang TA, Lv GZ (2022) Extraction and utilization of valuable elements from bauxite and bauxite residue: a review. Bull Environ Contam Toxicol 109(1):228–237. https://doi.org/10.1007/s00128-022-03502-w
20. Nakayama M, Egawa H (1997) Recovery of gallium(III) from strongly alkaline media using a Kelex-100-loaded ion-exchange resin. Ind Eng Chem Res 36(10):4365–4368. https://doi.org/10.1021/ie9700270
21. Nayak S, Devi N (2017) Studies on extraction of gallium (III) from chloride solution using Cyphos IL 104 and its removal from photodiodes and red mud. Hydrometallurgy 171:191–197. https://doi.org/10.1016/j.hydromet.2017.04.016
22. Raiguel S, Dehaen W, Binnemans K (2020) Extraction of gallium from simulated Bayer process liquor by Kelex 100 dissolved in ionic liquids. Dalton Trans 49(11):3532–3544. https://doi.org/10.1039/c9dt04623b
23. El Wakil AF, Zaki SA, Ismaiel DA (2023) Extraction and separation of gallium by solvent extraction with 5-non-yl-2-hydroxyacetophenone oxime: fundamentals and a case study. Hydrometallurgy 216
24. Frary FC, Oakmont P (1952) Process of producing gallium. US Patent
25. Lu X, Wang L, Wang X (2008) Research progress in gallium recovery technology. Nonferrous Met 60(04):105–108
26. Beja M (1951) Method of extracting gallium oxide from luminous substances. US Patent 2,574,008, 6 Nov 1951
27. Xu F, Xu N (2002) Gallium production of three stage carbonization process. Henan Chem Ind 10:21–24
28. Font O, Querol X, Juan R (2007) Recovery of gallium and vanadium from gasification fly ash. J Hazard Mater 139(3):413–423. https://doi.org/10.1016/j.jhazmat.2006.02.041
29. Wen K, Jiang F, Zhou XY (2018) Recovery of gallium from corundum flue dust by two-stage alkali leaching, carbonation, acid leaching and solvent extraction process. Metals 8(7). https://doi.org/10.3390/met8070545
30. Zhao Z, Yang YX, Xiao YP (2012) Recovery of gallium from Bayer liquor: a review. Hydrometallurgy 125:115–124. https://doi.org/10.1016/j.hydromet.2012.06.002
31. Lilia A, Pasechnik S, Yatsenko P (2004) Study of the behaviour of gallium during reagent carbonozation of aluminate and zinate solutions. Chem Sustain 12:239–241
32. Abdulvaliyev RA, Akcil A, Gladyshev SV (2015) Gallium and vanadium extraction from red mud of Turkish alumina refinery plant: hydrogarnet process. Hydrometallurgy 157:72–77. https://doi.org/10.1016/j.hydromet.2015.07.007

33. Kudermann G, Blaufuß KH (1977) Characterization of high purity gallium. Microchimica Acta 91(1–6):269–274
34. La Breteque Pierre D (1955) Method of recovering gallium from an alkali aluminate lye. US Patent 59050356A
35. Miyake S (1969) Method for directly electrochemically extracting gallium from circulating aluminate solution in the Bayer process by eliminating impurities. US Patent
36. Zhai XJ, Lv ZJ (2010) Gallium metallurgy. Metallurgical Industry Press, Beijing, pp 81–82
37. Mochalov L, Logunov A, Vorotyntsev V (2021) Preparation of gallium of the special purity for semiconductors and optoelectronics. Sep Purif Technol 258(1). https://doi.org/10.1016/j.seppur.2020.118001

Technoeconomic Analysis of Supercritical Fluid Extraction Process for Recycling Rare Earth Elements from Neodymium Iron Boron Magnet

Gisele Azimi and Maziar E. Sauber

Abstract This study is focused on technoeconomics of supercritical fluid extraction (SCFE) technology as applied to the recovery of rare earth elements (REEs) from end-of-life neodymium iron boron magnets. The REEs are in increasingly high demand and due to their limited supply, their recovery from electronic waste is highly promoted. The supercritical fluid extraction (SCFE) process is recognized as a green alternative to hydro and pyrometallurgy to recover REEs from secondary resources. The technical feasibility of SCFE for recycling of REEs from end-of-life neodymium iron boron magnets has been proven in the past. Using a wide range of data sources including laboratory results, literature data, scaling models, scenario analysis, and sensitivity analysis, this study performs a sound economic analysis of the SCFE process at an industrial scale. A detailed estimation of the costs and revenues associated with the process is conducted and the primary factors that affect its profitability are identified. The findings demonstrate that the SCFE of REEs from neodymium iron boron magnets can be economically viable under certain circumstances, with the efficiency of extracting dysprosium and neodymium and the price of their respective oxides being the main drivers of profitability. By providing valuable insights into the technoeconomic feasibility of the SCFE process for REEs recovery, this study informs future research and development activities in the field.

Keywords Supercritical fluid extraction (SCFE) · Rare earth elements · Neodymium iron boron magnet

G. Azimi (✉)
Laboratory for Strategic Materials, Department of Chemical Engineering and Applied Chemistry, University of Toronto, 200 College Street, Toronto, ON M5S 3E5, Canada
e-mail: g.azimi@utoronto.ca

M. E. Sauber
CanmetMINING, Natural Resources Canada, 555 Booth Street, Ottawa, ON K1A 0G1, Canada

© The Minerals, Metals & Materials Society 2024

C. Iloeje et al. (eds.), *Energy Technology 2024*, The Minerals, Metals & Materials Series, https://doi.org/10.1007/978-3-031-50244-6_12

Introduction

The rising demand for wind turbines and electric vehicles has led to a significant increase in the need for permanent magnets like neodymium iron boron (NdFeB) magnets and the associated rare earth elements (REEs). Properly managing waste NdFeB magnets not only reduces landfill waste but also allows for the recovery of critical REEs like neodymium (Nd), dysprosium (Dy), and praseodymium (Pr), which are in high demand and facing supply challenges. NdFeB magnets contain more than 20% of REEs, making them 10 times richer in REEs compared to the minimum industrial grade primary ores (1–2 wt%) [1]. Recycling REEs from end-of-life products also helps address the balance problem where less valuable REEs such as cerium and lanthanum constitute the majority of REEs in primary ore resources. Additionally, recycling helps avoid dealing with radioactive elements like uranium and thorium often present in primary REEs resources [2].

The strategic importance of rare earth elements (REEs) is acknowledged worldwide, but their global supply is concentrated in a few countries, leading to supply insecurities. However, recycling REEs presents an opportunity to address these challenges and mitigate supply uncertainties. Recycling REEs from various products could make a substantial contribution to the global supply. Specifically, recycling NdFeB magnets, which are abundantly available, could provide a valuable supplement to geological stocks. The quantity of NdFeB magnets available for recycling is approximately four times the annual extraction rate of the individual elements in 2007, indicating their significant potential to play a larger role in the future and contribute significantly to the global REE supply [3].

In a typical NdFeB magnet manufacturing facility, around 20–30% of the magnets are discarded as scrap, resulting in approximately 1500–2500 tonnes of waste per year. GéoMégA is constructing a plant designed to produce more than 2000 tonnes of sintered neo magnets annually, meeting about 17% of the current demand for neo magnets in the United States [4]. During the manufacturing and machining process of neo magnet blocks, up to 30% of the material is generated as swarf and scrap, totaling 600 tonnes, which needs to be recycled. This recycling effort is essential for minimizing waste and maximizing the utilization of valuable materials.

Traditional recycling methods for rare earth elements (REEs) commonly rely on pyrometallurgy and hydrometallurgy. In pyrometallurgy, a mixture of reducing and fluxing agents is used during calcination to separate and extract REEs from the raw materials. Hydrometallurgy, on the other hand, employs chemical solutions to dissolve and extract REEs from the raw materials. These techniques are chosen based on the specific properties of the materials to be recycled and the intended final products. Hydrometallurgy has some significant drawbacks, including the consumption of large amounts of reagents such as strong acids, bases, and organic solvents, resulting in the production of hazardous waste streams and acidic wastewater [5].

However, in recent years, an alternative process called supercritical fluid extraction (SCFE) has been developed for recovering metals, especially REEs, from end-of-life products like nickel metal hydride batteries [6], NdFeB magnets [1], and fluorescent

lamp phosphors [7]. In the SCFE process, a solvent is pressurized and heated beyond its critical points and used as the leaching agent. Supercritical carbon dioxide (sc-CO_2) has gained attention as a chosen solvent for REE extraction due to its beneficial properties, including moderate critical points ($T_c = 31.06$ °C, $P_c = 7.37$ MPa, and $\rho_c = 469$ kg/m^3), inertness, low cost, abundance, and ease of separation and recycling through pressure change [8]. Sc-CO_2 is considered an ideal solvent for REEs because of its unique combination of favorable properties, such as high diffusivity, low viscosity, and high solvability, enabling efficient extraction of solutes from solid and liquid matrices [7].

The technical feasibility of using SCFE for recovering REEs from end-of-life NdFeB magnets has been explored by our group in recent years [1]. However, there is a significant knowledge gap regarding the economic feasibility of these processes. To address this gap, the present study offers a technoeconomic analysis (TEA) of the SCFE process for REEs recovery. This novel attempt systematically evaluates the economic viability of SCFE for REEs recovery, filling a crucial gap in the current understanding of this field. The study's findings will serve as a valuable foundation for future research and development in the utilization of SCFE for metal recovery.

In this study, TEA is used to assess the economic feasibility of the SCFE process for recycling REEs from NdFeB magnets. The mass and energy balance are calculated based on the proposed processing conditions found in the literature [1]. Project economics are evaluated, along with scenario analysis and sensitivity studies. The study's results identify key process variables that affect the process economics, providing valuable insights for decision-making regarding research and development investments by companies and governments in this field.

Process Modeling Approach

In this study, a simplified process modeling approach is employed using Microsoft Excel spreadsheets to obtain a high-level mass and energy balance. The process modeling is based on the proposed process configuration illustrated in the block flow diagram shown in Fig. 1. The diagram encompasses all inputs and outputs, including material and energy, for the entire process. The SCFE extraction process is represented on the left side, and the separation process is depicted on the right side, with a dashed line separating the two. Each box in the diagram represents the battery limit (ISBL) considered for each processing unit, indicating the scope of analysis for each stage of the process. This approach provides a comprehensive overview of the mass and energy flows throughout the entire SCFE and separation process, enabling a thorough evaluation of the proposed REEs recovery technique.

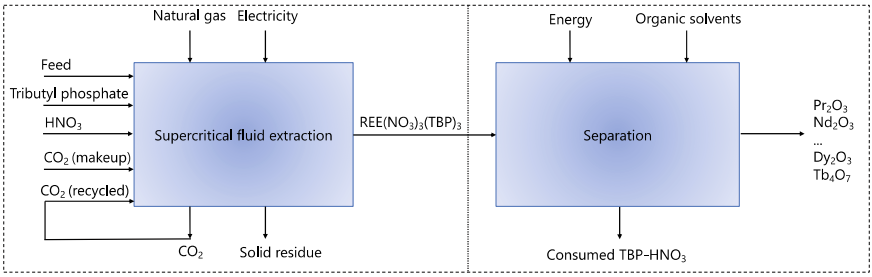

Fig. 1 Block flow diagram presenting the SCFE and separation (based on solvent extraction) processes

Economic Modeling and Analysis

The economic modeling and analysis of the SCFE process were conducted to assess its profitability based on estimated material and energy consumption at the industrial scale. The cost model considered fixed and variable costs, which were further categorized into capital, reagent, energy, and labor costs. The capital cost estimation was derived from a scaling model using empirical data from industrial-scale vessels. Reagent cost estimation utilized a bottom-up approach, where the cost was calculated by multiplying the quantity of materials with their respective prices, focusing on the SCFE process (shown in the left segment with a dashed line in Fig. 1).

Regarding the separation process after SCFE, a black box approach was adopted for economic analysis since no study has reported the direct separation of the product obtained after SCFE for metals. This approach assumes that the final products after SCFE are in the form of $REE(NO_3)_3(TBP)_3$, and individual metal oxides are obtained as the final saleable product after separation using solvent extraction. The cost of separating REEs on an industrial scale using solvent extraction was estimated based on personal communications with REEs industrial refineries. According to these communications, the separation cost for La, Ce, Pr, and Nd was proposed to be 10 USD/kg, while for other REEs, it was 20 USD/kg.

In this study, the discounted cash flow (DCF) method is used for financial modeling of the proposed SCFE process, and all cost figures and analysis results are presented in 2023 USD. If cost inputs used in the analysis are not in USD, they were converted to USD using exchange rates as of July 2023. The evaluation focuses on the SCFE process taking place in Ontario, Canada. The project development and construction periods are assumed to be 24 months each, with a total project life cycle of 48 months. The project starts with a 24-month development period for permitting, design, contracting, and procurement of long lead items, followed by another 24 months of construction before the plant reaches commercial operation. Considering the high-pressure operating conditions and batch operation process, an annual availability of 85% is assumed to account for both scheduled and unscheduled downtimes. Additionally, during the first three months following the start of commercial operation (ramp-up period), the plant operates at 80% of its nominal

capacity, as defined for each scenario. The project's operating lifetime is assumed to be 40 years. For simplicity, the financial analysis assumes that the entire capital cost of the project is funded from equity, with no debt involved. The reported net present values (NPVs) are based on an annual discount rate of 7.5%. The entire financial analysis is conducted on a pre-tax basis, and no depreciation assumptions are made. Furthermore, the project salvage value and the remediation costs of the facility at the end of its lifetime are assumed to be the same, meaning the project salvage value covers the remediation costs.

Scenario Analyses

In the scenario analysis, the economics of the SCFE process for REEs recycling from magnets were evaluated using two key variables: reagent consumption, mainly the adduct to feed ratio, and the REE concentration in the feed. The lower and upper levels for each variable were determined based on information from the literature and laboratory-scale studies on these feeds. The design matrix, as shown in Table 1, uses "MG" to represent the magnet, "Ad" denotes the adduct consumption, and "C" represents the feed composition. "H" and "L" indicate the high and low levels of each variable, respectively.

The REE extraction efficiency for each scenario was selected based on laboratory-scale experiments conducted under specific operating conditions [1]. It was assumed that the extraction efficiency remains constant and independent of the feed composition under the same operating conditions. By analyzing the various scenarios, the study identifies the combinations of variables that yield economic feasibility for the SCFE process. Additionally, it helps prioritize process development based on the outcomes, enabling informed decision-making regarding further research and investment directions.

Results and Discussion

Mass and Energy Balance

Table 2 illustrates the mass and energy flows for the various scenarios investigated. It is shown that tributyl phosphate (TBP), HNO_3, and the feed are the top three streams in terms of flowrate. For the magnet case, the main product is Nd_2O_3, owing to the high concentrations of Nd in the feeds. TBP consumption in this study is calculated based on the stoichiometry of the adduct, which is determined to be $TBP(HNO_3)_{1.9}(H_2O)_{0.6}$. This consideration takes into account the water solubility of TBP, which can result in certain losses during the process, leading to a more accurate estimation of TBP consumption.

Table 1 Scenario analysis matrix for evaluating the economics of REE recycling from NdFeB magnet (MG) using SCFE process

Scenario name	UoM	1. MG, Ad:H, C:L	2. MG, Ad:H, C:H	3. MG, Ad: L, C:L	4. MG, Ad: L, C:H
Feed composition					
Nd	wt%	18.5	23.0	18.5	23.0
Pr	wt%	3.6	6.8	3.6	6.8
Dy	wt%	0.1	6.8	0.1	6.8
Extraction yield					
Fe	%	57.0	57.0	51.0	51.0
Nd	%	95.0	95.0	71.0	71.0
Pr	%	94.0	94.0	76.0	76.0
Dy	%	100.0	100.0	68.0	68.0
Temperature	°C	55.0	55.0	55.0	55.0
Pressure	MPa	20.7	20.7	20.7	20.7
Duration	h	1.0	1.0	1.0	1.0
Feed mass	kg	164.9	164.9	304.3	304.3
Feed density	kg/L	7.0	7.0	7.0	7.0
Adduct to feed ratio	L/kg	10.0	10.0	5.0	5.0
Reactor volume	L	4000.0	4000.0	4000.0	4000.0
CO_2 loss rate	%	2.5	2.5	2.5	2.5

Ad: adduct, C: feed concentration, H: high, L: low

Table 2 Mass and energy flows for the studied four scenarios. The total plant volume is 4000 L

Mass and energy flows	Scenario 1	Scenario 2	Scenario 3	Scenario 4
Feed (tonne/year)	1228	1228	2266	2266
HNO_3 solution (tonne/year)	2260	2485	5052	5442
TBP (tonne/year)	6686	7351	10677	11501
CO_2 (tonne/year)	331	331	346	346
Electricity (MWh/year)	2592	2592	2592	2592
Natural gas (m^3/year)	898,560	898,560	898,560	898,560
Nd_2O_3 (equivalent) (tonne/year)	252	313	347	432
Pr_2O_3 (equivalent) (tonne/year)	49	92	73	137
Dy_2O_3 (equivalent) (tonne/year)	1	96	2	120
Residue (tonne/year)	602	448	1299	1096

During the SCFE process, REEs in the NdFeB magnets react with the TBP-HNO_3 adduct, forming $REE(NO_3)_3(TBP)_3$ organometallic complexes that are soluble in sc-CO_2 [9]. After the reaction is complete, and depressurization occurs, the CO_2 is separated from the complexes and can be captured and recycled for the next batch. However, some CO_2 may be lost due to leakage, and the leakage is assumed to be 2.5% based on previous studies [10]. The $REE(NO_3)_3(TBP)_3$ complexes are collected for subsequent separation and purification processes.

Operating Expenditure

In this technoeconomic study evaluating the proposed SCFE process in Ontario, Canada, the operational expenditure (Opex) consists of material costs (feed and reagents), energy and utility costs (electricity and natural gas), maintenance costs, and indirect costs such as professional services, stakeholder engagement, property tax, and insurance. The combined indirect costs were assumed to be 300,000 USD and indexed at an annual rate of 2%.

A factor of 65% of fixed capital investment (FCI) has been allocated for maintenance and repairs, considering the potential need for adaptations and optimization during the implementation of SCFE as a novel process. Processes involving higher operating pressures typically necessitate increased maintenance and repair costs. To account for major maintenance, overhaul, or replacement of process equipment, a major maintenance and reserve account (MMRA) is considered. This account is funded from project revenues during the first half of the project's operational lifetime, and the balance will be used during a two-year period in the middle of the project's lifetime for necessary maintenance, overhaul, or equipment replacement.

The study assumes a 24 × 7 operation schedule with three 8-h shifts, and each batch takes 1 h from start to finish. Plant availability is assumed to be 85% on an annual basis, meaning the process will be operational for 20 h every day, 360 days a year. A 15% downtime on an annual basis is considered in the cost estimation to account for scheduled and unscheduled maintenance activities.

In summary, this study provides a comprehensive analysis of the economic feasibility of the proposed SCFE process, taking into account various direct and indirect operating costs, maintenance considerations, and downtime estimates to ensure an accurate evaluation of the process's profitability and potential challenges.

Table 3 provides a summary of the material (reagent) and utility costs considered in the study. To prepare the end-of-life NdFeB magnet scrap for the SCFE process, it undergoes pre-processing called preferential degradation. This process involves separating malleable metal components like nickel or other coatings, iron, stainless steel, aluminum, and printed circuit boards. The pre-processing steps may include shredding, crushing, magnetic separation, ball milling, and screening. After pre-processing, the material goes through size reduction to achieve the particle size required for the SCFE process. To account for the costs associated with the pre-processing of magnet scrap, the analysis assumes a nominal value of 1500 USD per

Table 3 Materials cost used in the SCFE process

Item	Cost	Unit	Source
Nitric acid	$268	USD/tonne	[12]
TBP	$860	USD/tonne	[a]
Liquid CO_2	$460	USD/tonne	[13]
NdFeB magnet scrap	$2430	USD/tonne	[b]
Electricity	$0.12	USD/kWh	[14]
Natural gas	$0.28	USD/m^3	[14]

[a] The price of TBP is quoted from Beijing Dongke United Technologies Co. Ltd.
[b] The price of NdFeB magnet scrap is 2.43 USD/kg according to the industrial supplier (Tradewell Ferromet Private Limited)
[c] The price of waste fluorescent lamp phosphors is 0.4 USD/kg according to an industrial recycler (Ontario Lamp Recyclers Inc.)

tonne of processed feed, based on communications with the industry. Additionally, a waste (solid residue) disposal rate of 36 USD per tonne is assumed for the proper management of solid residues generated during the process [11]. This cost is factored into the overall economic analysis to account for waste handling and disposal.

Figure 2 illustrates the percentage contribution of each Opex item to the overall Opex for each scenario reflecting the costs during the first year of operation. For subsequent years, each cost item will escalate at its corresponding escalation rate. In all scenarios, the cost of TBP stands out as the most significant item. For the magnet case, the cost of feed is also substantial. Additionally, labor and HNO_3 costs are significant across all scenarios. These findings highlight the key cost drivers in the SCFE process for REEs recycling from NdFeB magnets, emphasizing the importance of optimizing and managing TBP consumption, feed costs, and labor and HNO_3 expenses to enhance the economic viability of the process. By identifying these major cost components, the study provides valuable insights for process optimization and financial planning to ensure cost-effective and sustainable REEs recovery.

Capital Expenditure

In the capital expenditure (Capex) estimate, the financial analysis focuses on the fixed capital investment (FCI) within the inside battery limit (ISBL). A contingency of 10% has been added to the ISBL part of the Capex estimate to account for potential unforeseen costs and uncertainties. Although a higher contingency might be warranted for this class of cost estimation, other components of the total project costs are considered elsewhere in the analysis, justifying the 10% contingency. The capital equipment cost was estimated using a scaling model based on empirical data from existing industrial-scale SCFE plants. Previous studies have reported the cost of SCFE plants containing reactors in various sizes, ranging from 5 $\times$ 290 to 4 $\times$

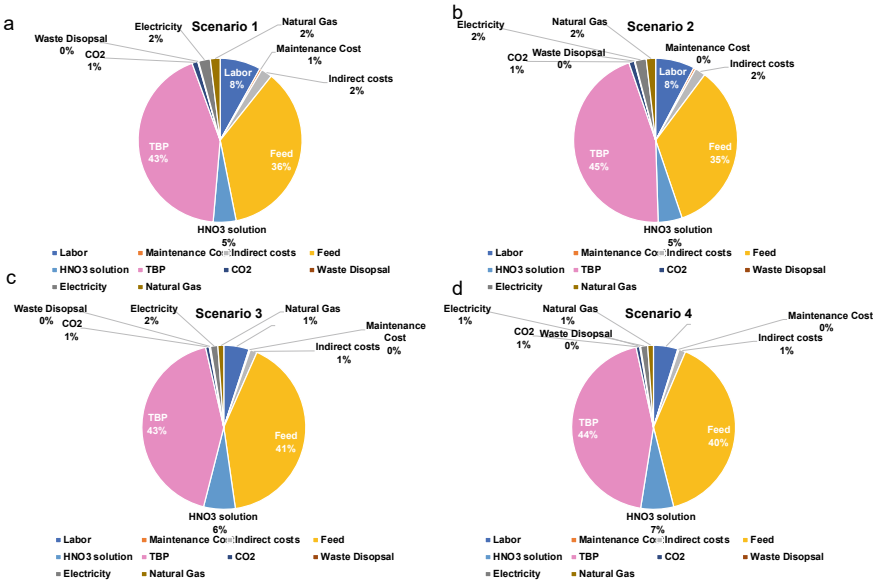

Fig. 2 Distribution of Opex for the SCFE of the NdFeB magnet: **a** adduct to feed ratio: high, feed composition: low, **b** adduct to feed ratio: high, feed composition: high, **c** adduct to feed ratio: low, feed composition: low, **d** adduct to feed ratio: low, feed composition: high

2000 L [13]. To estimate the capital cost of the plant, a high-level approach was taken. The equipment cost data from literature were plotted against the total reactor volume after being adjusted for process operating pressure and change in cost over time using the chemical engineering plant cost index (CEPCI). The CEPCI values were taken from the "Chemical Engineering Plant Cost Index" for 2023 and used to convert the cost data points from the literature to 2023 USD figures [15].

In this study, a plant with 2 × 2000 L reactors is selected for the SCFE process, with a maximum operating pressure of 310 bar. Using the previously described calculations, the equipment cost for this plant is estimated to be 6323.33 million USD in 2023. To calculate the total engineering, procurement, and construction management (EPC) costs, several items are considered. These include equipment cost, spare parts (4% of equipment cost), installation, piping, and electrical costs (30% of equipment cost), resulting in the installed equipment cost. The next components are engineering, procurement, and construction management costs (20% of the installed equipment cost), construction costs (8% of the installed equipment cost), and freight costs for equipment and construction materials (10% of the installed equipment cost). A contingency cost of 10% of the total mentioned costs is also added to obtain the total EPC costs.

To calculate the total capital expenditure (Capex), development costs (including environmental studies and acquiring licenses), land purchase price, owner's project management, owner's engineer, and construction insurance costs are also included in

Table 4 Capex summary for nominal 2 × 2000 L capacity SCFE plant

Capex, '000 USD	Scenario 1	Scenario 2	Scenario 3	Scenario 4
Land cost	1500	1500	1500	1500
Development cost	1000	1000	1000	1000
Other owner's cost	500	500	500	500
Total EPC, including	10,884	10,884	10,884	10,884
Equipment cost	5383	5383	5383	5383
Spare parts	215	215	215	215
Installation cost	1615	1615	1615	1615
EPC management	1400	1400	1400	1400
Construction	560	560	560	560
Freight	721	721	721	721
Contingency	989	989	989	989
Total	13,884	13,884	13,884	13,884

addition to the total EPC costs. Table 4 presents the total Capex for the four studied scenarios, providing an overview of the overall investment required for each scenario. This comprehensive analysis allows for a detailed evaluation of the capital costs associated with implementing the SCFE process for REEs recycling from NdFeB magnets. It enables informed decision-making and financial planning for potential investors and stakeholders interested in the project.

Profitability and Scenario Analysis

The study considers two types of profitability indicators: static and dynamic. The static profit (P_{stat}) is calculated using Eq. (1) and takes into account the project lifetime (n), annual market sales volume (V), product value (Π_{p}), and operating expenses (Π_{op}) [16].

$$P_{\text{stat}} = nV\left(\Pi_{\text{p}} - \Pi_{\text{op}} - \frac{\text{CapEx}}{nV}\right) \tag{1}$$

For dynamic profitability calculations, two indicators are used: net present value (NPV) and internal rate of return (IRR). Both indicators are calculated using the discounted cash flow method (DCF). The IRR represents the return on investment for each scenario, considering the time value of money and accounting for all revenues and costs over the project's lifetime, including capital costs and operating expenses.

The NPV values for all scenarios are calculated using a constant discount rate of 7.5% per annum, showing the size of profit (if any) for each scenario. If the IRR of a scenario is less than 7.5%, the calculated NPV using a discount rate of 7.5% yields

a negative profit (indicating a loss). In other words, the IRR is the discount rate at which the NPV becomes zero.

Figure 3a and b presents the results for static profit (P_{stat}) and NPV (in million USD) and IRR (%) for the four scenarios investigated in this study. The static profits for scenarios involving NdFeB magnet with high feed concentration are 1.4 and 1.7 billion USD over the entire project lifetime. The difference between the two numbers for this feed is due to the consumption of the adduct based on the adduct to feed ratio. In the case of NdFeB magnet, the NPV and IRR are higher for the high feed concentration scenarios. The most profitable scenario for the NdFeB magnet is #4, which contains high feed concentration with a low adduct to feed ratio. These findings provide valuable insights into the economic viability and profitability of different scenarios for REEs recycling using SCFE.

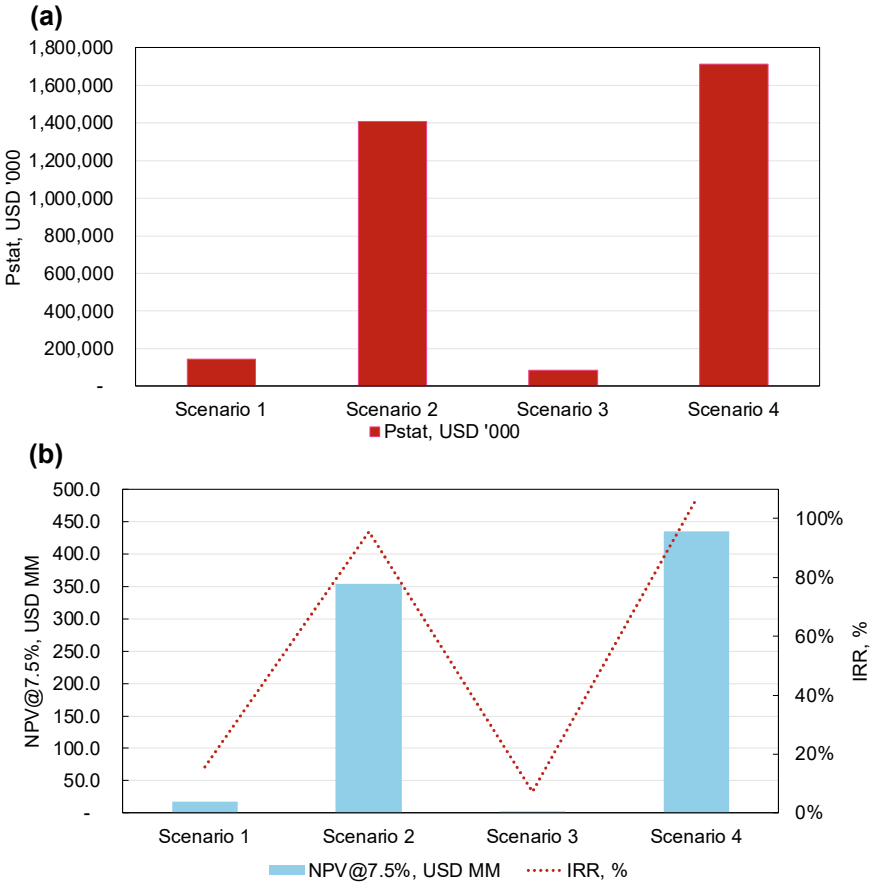

Fig. 3 **a** Static profit (in 1000 USD) and **b** NPV (in million USD) and IRR (%) results for the four scenarios investigated in this study (shown in Table 1)

Conclusions

The study suggests that supercritical fluid extraction (SCFE) using CO_2 as the solvent and TBP-HNO_3 adduct as the chelating agent could be an economically feasible technology for extracting REEs from end-of-life NdFeB magnets, given specific criteria. The analysis provides a systematic approach to evaluate the economic viability of SCFE for REEs recovery, including scenario analysis using available data from similar industries and laboratories.

The scope of the study focuses on 2 × 2000 L reactors operating in Ontario, Canada, with four scenarios based on REEs concentration in the feed and adduct to feed ratio being studied. The operational and capital expenditure estimates indicate that the Opex of the plant in the first year ranges between 13 and 22 million USD for the magnet. The total Capex of the plant is 13.8 million USD.

The total revenue of the plant in the first year varies between 17 and 65 million USD. The static profit is highest for scenario 4 (low adduct to feed ratio, high concentration feed). This scenario also has the highest NPV and IRR, with a payback period of around 0.5 years. Therefore, the concentration of REEs in the feed and adduct to feed ratio are critical variables affecting the process's profitability. The material cost, particularly the amount of adduct used, is a crucial driver for improving the economic performance of the process. Future research and development activities should focus on minimizing the TBP amount to enhance the process's economic feasibility.

It is important to note that the conducted technoeconomic analysis (TEA) is based on a technology readiness level (TRL) of 4 and a cost estimate class of 5 (Rough Order of Magnitude—ROM cost estimate). The TRL level indicates that the technology has undergone validation in a laboratory environment, while the ROM cost estimate is used in the early stages of a project when information is limited. As the project progresses, the accuracy of the cost estimate should improve with more information and relevant testing. Regular reviews and updates of the cost estimate are necessary to ensure its accuracy and reflect any potential changes in the project's status.

Acknowledgements The authors acknowledge the financial support provided by the Government of Canada, Canada Research Chair Tier.

References

1. Zhang J, Anawati J, Yao Y, Azimi G (2018) Aeriometallurgical extraction of rare earth elements from a NdFeB magnet utilizing supercritical fluids. ACS Sustain Chem Eng 6:16713–16725
2. Binnemans K, Jones PT, Müller T, Yurramendi L (2018) Rare Earths and the Balance Problem: How to Deal with Changing Markets? J Sustain Metall 4:126–146
3. Yang Y et al (2017) REE recovery from end-of-life NdFeB permanent magnet scrap: a critical review. J Sustain Metall 3:122–149
4. GEOMEGA (2022) Geomega to recycle rare earths from USA rare earth's anticipated neo magnet production in the United States

5. Tunsu C, Petranikova M, Gergorić M, Ekberg C, Retegan T (2015) Reclaiming rare earth elements from end-of-life products: a review of the perspectives for urban mining using hydrometallurgical unit operations. Hydrometallurgy 156:239–258
6. Yao Y, Farac N, Azimi G (2018) Supercritical fluid extraction of rare earth elements from nickel metal hydride battery. ACS Sustain Chem Eng 6:1417–1426
7. Zhang J, Anawati J, Azimi G (2022) Urban mining of terbium, europium, and yttrium from real fluorescent lamp waste using supercritical fluid extraction: process development and mechanistic investigation. Waste Manag 139:168–178
8. Sinclair LK, Baek DL, Thompson J, Tester JW, Fox RV (2017) Rare earth element extraction from pretreated Bastnäsite in supercritical carbon dioxide. J Supercrit Fluids 124:20–29
9. Zhang J, Chen N, Morozova V, Voznyy O, Azimi G (2023) Investigating metal-tributyl phosphate complexes during supercritical fluid extraction of the NdFeB magnet using density functional theory and X-ray absorption spectroscopy. Inorg Chem 62:7689–7702
10. Osorio-Tobón JF, Carvalho PIN, Rostagno MA, Meireles MAA (2016) Process integration for turmeric products extraction using supercritical fluids and pressurized liquids: economic evaluation. Food Bioprod Process 98:227–235
11. Turton R, Bailie RC, Whiting WB, Shaeiwitz JA (2008) Analysis, synthesis and design of chemical processes. Pearson Education
12. EChemi.com (2023)
13. Del Valle JM, De La Fuente JC, Cardarelli DA (2005) Contributions to supercritical extraction of vegetable substrates in Latin America. J Food Eng 67:35–57
14. Ontario Energy Board (2023)
15. The Chemical Engineering Plant Cost Index (2023)
16. Buchner GA, Zimmermann AW, Hohgräve AE, Schomäcker R (2018) Techno-economic assessment framework for the chemical industry—based on technology readiness levels. Ind Eng Chem Res 57:8502–8517

Life Cycle Assessment for the Mining and Metallurgical Industries: Issues and Challenges

Nawshad Haque

Abstract Environmental, Social and Governance (ESG) rating is a key topic of attention by the industries, particularly for the companies trading in the stock exchanges. There is a lack of reliable, robust, and credible ESG rating tools. Mining, mineral processing, and metallurgical technologies are required to be evaluated by consistent and standard methodology to be used by the industries to claim their environmental performances. Life cycle assessment is one such methodology that can be integral to the environmental part of the ESG rating. However, there are several issues that needs attention by the practitioners specific to the mining and metallurgical products and processes. There are several factors such as defining boundary, data inputs, and allocation where multiple metals are produced with significantly different prices, dynamic nature of the changes of the energy sources, particularly, electricity and impact method selection. These make LCA studies challenging which need careful attention by the mining industry experts. Energy, carbon, water, and waste (ECWW) footprint of metals can be a generic simple score card for evaluating the environmental performance of metals, practically in many cases. These indicator results can be fed into the ESG rating tools for company performances in the stock market.

Keywords LCA · Allocation · Energy carbon water waste · ESG · Sustainability

Introduction

Recently the evolution and awareness about Environment, Social, and Governance (ESG) rating have got attention in the business community. This awareness is growing exponentially in the stock markets for company rating and performances. ESG rating tools are under development although reliable and high-quality rating tools are still lacking in the industry. There is a risk of so-called greenwashing which is claiming a

N. Haque (✉)
CSIRO Energy, Private Bag 10, Clayton South, VIC 3169, Australia
e-mail: Nawshad.Haque@csiro.au

© The Minerals, Metals & Materials Society 2024

C. Iloeje et al. (eds.), *Energy Technology 2024*, The Minerals,
Metals & Materials Series, https://doi.org/10.1007/978-3-031-50244-6_13

product environmentally friendly without quantified evidence and indicators. Thus, the regulatory bodies in the stock exchanges are monitoring the company declaration and consistency of the ESG performance of the companies.

Topics such as 'reducing environmental impacts' and 'improving community relations' have consistently been the top two issues for mining industry stakeholders over the past decade in many surveys. Social license to operate (SLO) is one of the important of ten key risks faced by the mining industry. Life cycle assessment (LCA) is one such tool that can be further developed, improved, and used for sustainability evaluation in the mining industry and can form part of the ESG rating although there are mixed opinions among the LCA community about this aspect. It can be applied to operating mine sites, processing plants, and metal production refineries to improve their operations. The functional unit can be mineral commodities or metals such as a final identifiable product or co-product, within the specified boundary, or by-products (e.g., products produced but used outside the boundary). The evaluation target can be a current or new technology or technology mix that can be compared on a similar basis at the same scale. LCA reports can provide information on how much energy is used (direct and indirect), where and when it is used, greenhouse emissions associated with energy use and other site emissions, and overall environmental impacts including water consumption and waste generation.

However, there are number of issues that need to be resolved before undertaking LCA studies to produce consistent results irrespective of the practitioners undertaking such studies. The issues can primarily be managed under several categories. One is related to data collection and quality, which is related to temporal and spatial aspects. Despite the existence of an International Standard [1], there is a lack of uniform methodology that can specify boundary, technology, and representativeness specific to mining and metals industries. Another major issue is related to the allocation of impact to a specific mineral or metal product where multiple metals or minerals are produced. Although, there are mines producing a single product, in many instances the issue of co-products makes LCA difficult without an understanding at the processing level of the production of this specific functional unit.

A co-ordinated review [2] was undertaken, in collaboration with international metal associations (copper, aluminium, cobalt, lead, zinc, manganese, molybdenum, stainless steel, and nickel), that offered recommendations on a harmonized approach to LCA methodologies within the metals and minerals industry. Except few reviews in the last decades [3], actual LCA studies and methodology papers in the public domain are still limited. The purpose of this paper is to bring these LCA issues together and describe challenges specific to mining, mineral processing, and metal production. The main objective is to state how uniform methodology can be developed in the context of undertaking LCA for the mining industry.

Overview of Life Cycle Assessment

LCA has been a recognized method for measuring the environmental impacts of products, processes, technology, and services. It provides a scientifically sound method for comparing products, processes, and technology on common grounds. LCA originated in the early 1990 with initiatives from the Society of Environmental Toxicology and Chemistry (SETAC) and United Nations Environment Program (UNEP). LCA evaluates the total environmental burdens and benefits over the entire life cycle for a product from 'cradle' to 'grave' including material and energy used during extraction and processing of raw materials, manufacturing, transportation, use, recycling, and end-of-life fate. Depending on the scope of a study, the life cycle sometimes is bounded between 'cradle to gate' or 'gate to gate', or 'cradle to grave'. In a commercial sense, LCA assists environmental assessment such as eco-labelling, environmental product declarations (EPD), and so-called carbon or water footprints. In practice, the lack of industrial data, skills, and resources presents a significant challenge to undertaking LCA.

There are initiatives in various countries to collect such data or develop databases (often referred to as Life Cycle Inventory (LCI)) for LCA, which are sometimes co-ordinated under the leadership of government, private organizations, or learned societies. One such initiative in Australia is called Australian Life Cycle Inventory Database Initiative (AusLCI), led by the Australian Life Cycle Assessment Society [4]. There has been significant LCI data development for several thousand industrial processes in Europe. There was also an attempt to make datasets of 'world average' technology for a particular process and customizing these data sources for various regions of the world, including North America. One such database set is called 'Ecoinvent' [5]. With some scrutiny, modification, and customization by LCA experts, these databases have been packaged in recently developed standard LCA software such as SimaPro developed by the Dutch company, PRé Consultants Ltd [6]. Ecoinvent Centre owns, maintains, and updates the Ecoinvent database and sells licenses as part of LCA software sales. Another LCA software, GaBi, now called LCA for Experts [7], also contains similar datasets (called 'system process' rather than so-called 'unit process'), which are maintained and owned by that company. Given that LCA is an evolutionary process, any study can be updated once precise data sources become available for a specific technology or geographical location. There is other similar software such as OpenLCA with databases available that one can explore further [8].

Furthermore, international standards series [9–12] provide principles and framework for undertaking LCA including water footprints. According to these standards, LCA should include definition of goal and scope, inventory analysis, impact assessment, and interpretation of results, as its phases as illustrated in ISO [1]. These international standards series [9–12] provide further details on each of these steps and stages. Publications covering LCA studies have appeared in established scientific journals, predominantly in the International Journal of Life Cycle Assessment, the Journal of Cleaner Production, and the Journal of Industrial Ecology.

Applications of LCA in the Mining Industry

The Mining, Minerals and Sustainable Development (MMSD) project highlighted the application of LCA for the mining industry sector in its landmark document in 2002 [13]. An updated document, prepared in 2012, briefly reported the progress and challenges [14]. Few mining companies undertake LCAs and there are few successful product stewardship initiatives that act across the entire value chain of the mining industry [14]. There are various reasons for this slow LCA development and reluctant acceptance of LCA in mining sector. A key one is that the mining industry sits upstream in the value chain and is not under the scrutiny of the consumers who use their products in daily lives. Although a large of number of metals are used in mobile phones, few consumers appreciate the link between their phones and the mines in Australia, South Africa, and elsewhere where the metals come from. Although some attempts have been made by metal associations (e.g., steel, aluminium, copper, and gold) towards the application of LCA for developing sustainability score cards for metals, the aggregation of LCI data at a global level has lost the main purpose of a LCA for understanding plant- or site-wide improvements. The objective has been to focus on the specific environmental impacts of a single metal to compare it with other metals and materials. This is necessary from a marketing advantage point of view but mine site-wide, mill, or plant-wide improvements will not occur through these types of LCAs based on aggregated data, even on a regional level. Challenges reported highlighting the complexity of situations at mine sites means implementation of LCA studies across the mining sector is highly variable [15]. LCA can be used by companies for efficiency improvement of production processes, waste management, innovation, and green marketing. However, studies of that nature are extremely limited in literature.

The challenges of LCA for mining were reported [16] when developing a tool called Life Cycle Environmental Impact in Mining (LICYMIN) in the context of bauxite. The LICYMIN tool has evolved over time not only for academic research purposes but also has been used in practical applications including LCA of aggregates extraction, while the Waste and Resources Action Program (WRAP) made these tools available to the UK aggregates community [16]. Despite the increasing application of LCA for engineering evaluation of systems and products, the application of LCA in the mining industry is limited [17]. They recommended that future research should focus on the development of a mining specific LCA framework, data uncertainty characterization, and software development to increase the application of LCA in mining. This study also reported that publicly available sustainability reports rarely provide data for a whole mine being more often for an entire company since they are corporate reports by companies such as BHP and Rio Tinto. This makes it difficult for LCA methods to be applied by mining professionals in their everyday work and decision making. Based on the evaluation of a large volume of sustainability reports, company sustainability reports should clearly specify the fuel used by type of vehicles, heat or electrical energy, sources of electricity and their mix (including

GHG emissions factors), and the boundaries of the operation to allow more meaningful use of the data in LCAs [18]. Sustainability reports should be published at regular intervals so that improvements towards more sustainable performance can be measured, and LCAs of mining activities for primary metal production can be carried out readily. A new guideline document has been published for Organisational LCA (O-LCA) by the UNEP SETAC Life Cycle Initiative that provides details on how to conduct an LCA for an organisation [19].

Some companies report greenhouse gas emissions using the World Resources Institute/World Business Council for Sustainable Development Greenhouse Gas Protocol which reports both for Scope 1 (on-site use of material and energy input) and Scope 2 (purchased electricity from outside the site) GHG but no emissions are reported under Scope 3 (e.g., upstream transport, emission by their suppliers of materials and energy and similar downstream activities). Table 1 shows various stages and key items to be considered for mining and minerals LCA.

Table 1 Stages, unit processes, and inputs for LCA of primary metal production

Stages	Unit processes	Equipment and plant	Potential materials, energy, fuel, chemicals
Mining (underground, open-cut, in-situ)	Blasting Loading Hauling Ventilation Dewatering Run-of-mine (ROM) ore Waste rock dump operation	LHD vehicles, pumps, conveyors, dozers, water tankers, stackers, reclaimers	Diesel, electricity, ANFO explosives
Mineral processing	Size reduction, comminution (crushing, grinding), screening, flotation, filtering, physical separation, dense media separation	Flotation plant, filter plant, cyclones, ball mill, crushing plants, screening plants, conveyors, thickeners, pumps	Electricity, steel ball consumables, ball mill liners, flotation reagents (frother, collectors, modifier)
Metal production (pyrometallurgy)	Pre-treatment (roasting), reduction, fire-refining, electro-refining	Smelting furnaces, refining plants, rotary kilns, and furnaces	Electricity, diesel, fuel oil, natural gas, coal, fluxes, limestone
Metal production (hydrometallurgy)	Leaching, solution purification, reduction of metal, precipitation of compounds	Leaching tanks, electro-winning plants, solvent extraction plants	Sulphuric acid, salts and electrolytes, kerosene, electricity

CSIRO has undertaken and published LCA studies in the mineral's domain including ferro-metals, base-metals, and some light metals, covering both hydrometallurgical and pyro-metallurgical processing routes. Although greenhouse gas emissions from mining activities are generally low compared with other life cycle stages for current ore grades, a recent LCA study was undertaken to look more closely at the mining of iron ore, copper, and bauxite [20]. LCA results have also been published on the uranium nuclear fuel cycle [21] and the production of gold [22], ferroalloys [23], manganese, and magnesium. The main selected environmental impact categories were gross energy requirement (GER), which was used to estimate global warming potential (GWP) or greenhouse gas emissions in CO_2 equivalent units, solid waste burden, and water usage [24]. CSIRO has extensively studied the LCA of iron production and steel making in Australia [25].

Weakness of Previous LCA Studies for the Mining Industry

Many of these above studies undertaken by CSIRO and other authors suffer several weaknesses from data aggregation and robust uniform methodology. Some of the key issues for application of LCA in the minerals industry sector are reported [26]. During this process of aggregation, the variability across the data set is lost [27]. Aggregation significantly dilutes the value of the data set and the usefulness of the LCA. In particular:

- The loss of information on regional supply chains is significant and hinders more detailed study of the actual impact of products and the options available to mitigate this.
- The underlying representativeness of much of this data is often also poor as it is comprised of site-based data for a limited number of operations that in many cases has been extrapolated to represent whole regions.
- Environmental impacts associated with the primary production of metal products are highly variable between regions and even individual sites within a region.
- The current aggregation of data limits the ability to properly assess and select materials based upon their point of origin.
- Improvements to the regionalisation of LCA data are important for certain types of impact assessment studies, such as those that consider water scarcity or changes to water quality.

Issues and Challenges

Issues noted above are discussed further here. Those related to data collection and data quality related to the specification of boundary conditions, the technology applied, the variability of processing conditions and the allocation of impact to a specific mineral or metal product where multiple metals or minerals are produced. There

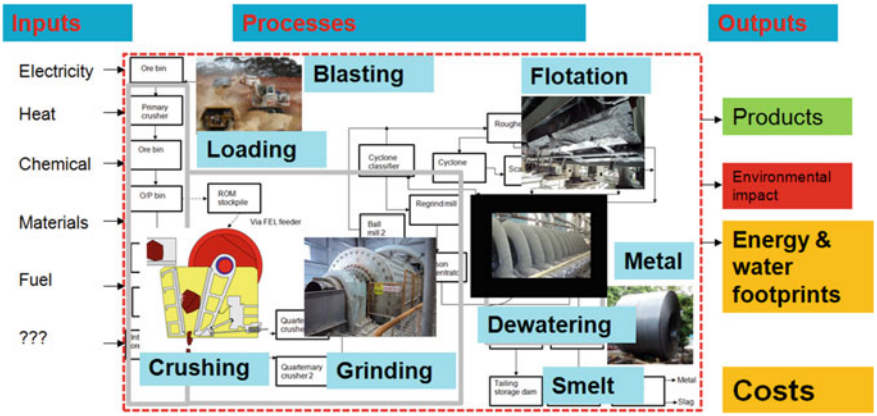

Fig. 1 Example system boundary for a mining and metal production LCA

are several weaknesses and drawbacks in the use of commercial LCA software for mining LCAs. However, currently this is the most popular and available approach for undertaking LCA. Some of the limitations will be discussed.

System Boundary Issues

The system boundary is chosen to reflect which unit processes are to be included in the LCA study. Example is given in Fig. 1. In the LCA of primary metals, a specific system boundary should cover three specific stages. These are mining, mineral processing, or milling and metal production. Each stage will have several unit processes. There are various types and methods of mining. For example, mining includes exploration, blasting, ventilation, dewatering, loading, and hauling to a run-of-mine stockpile or waste rock dump for typical underground mining. Mineral processing typically will include crushing, screening, and grinding, beneficiation by flotation and filtering and producing intermediate product such as concentrate. Then metal making includes roasting, smelting, refining and further downstream product manufacturing. These unit processes will vary depending on metals.

Functional Unit Issues

There are several minerals and metals that can be evaluated using LCA. A comprehensive list is shown in Table 2. A comparison of approaches is shown for metals LCA, and other studies are shown in Table 3. The product and process of an LCA study can be described either as a physical product (e.g., gold, copper, aluminium,

and car) or as a processing technology, service, or function (e.g., dewatering, beneficiation, smelting technologies, electricity generation, and drying). Functional unit must be described not only in the sense of quality of the product but also in relation to its actual use or application. LCA is undertaken per 'functional unit' since equal functions are compared. This may not necessarily be equal volumes or weights, particularly if the LCA is undertaken for comparison. LCA indicator results for primary metal production are generally presented per tonne of metal produced [24].

Input LCI Data Issues

LCI data sources can be from industry-average data from plant or site measurements, literature or scientific papers, life cycle inventory databases, other databases from governments, international governmental organizations, associations, industry association reports, and government statistics. Data quality can be evaluated using Pedigree Matrix analysis (time, location, technology, precision, completeness, reproducibility, and reliability) used in LCA.

Allocation Related Issues

A product or process system is used for LCA within a specified boundary. An LCA model or a system is connected by unit processes for energy and material inputs to make this product or to offer this service which has been chosen as a 'functional unit' for LCA study. The unit process is the smallest part of this system for which the data has been collected. A unit process often produces more than one product which is common for the mining industry. An example is Olympic Dam Operations owned by BHP Ltd in South Australia. The Olympic Dam mine site is located near Roxby Downs in South Australia and is an iron oxide copper gold (IOCG) type deposit. The primary products from the site are copper, uranium oxide, gold, and silver. A large proportion of copper producers also produce co-products such as gold, silver, nickel, lead, zinc, and molybdenum. Therefore, a method for allocating a proportion of the energy consumed and GWP at the site to individual products is required.

If two products are produced from a unit process using the same material and energy inputs, they are co-products. However, if one product is investigated in the immediate next step, this is termed the main product. Co-products that are used outside the scope of the boundary are termed as by-product. It would be questionable if all the environmental burdens are attributed to the main product when other co- or by-products are produced from the same process unit. In those circumstances, it is required to decide how this allocation will be made. The LCA standards provide guidelines for allocation. The environmental impact can be allocated on a mass basis or an economic basis. The standard advises that allocation should be avoided by expansion of the system boundaries. However, where this is not possible

Table 2 Metals and commodities and LCA issues

Names	Groups	Element/ compound	Main LCA issues and challenges							
			Geography	Ore grade	Technology	Chemical input sources	Energy input sources	Allocation	Mining method	Nature of coal or gas
Minerals	Iron ore	Fe	√	√	√		√		√	
	Bauxite	Al	√	√	√	√	√			
	Copper concentrate	Cu	√	√	√	√	√	√	√	
	Other mineral concentrates	Base metals	√	√	√	√	√	√	√	
	Ferro-metals (iron)	Iron, steel, stainless steel	√	√	√	√	√			
	Ferroalloys	Ferroalloys	√	√	√	√	√			
	Light metals	Al, Mg, Ti	√	√	√	√	√			
Metals	Base metals	Cu, Ni, Pb, Zn, Ni	√	√	√	√	√	√	√	
	Precious metals	Au, Ag, Pt	√	√	√	√	√	√	√	
	Speciality metals	Sn, Cd	√	√	√	√	√	√		
	Rare earth metals	15 REE, Sc, Y	√	√	√	√	√	√	√	
Fuel	Solid fuel	Coal	√	√	√	√	√		√	√
	Liquid fuel	Oil	√	√	√	√	√	√	√	√
	Gas	Gas	√	√	√	√	√		√	√

Table 3 Comparison of approaches between standard LCA and minerals and metals LCA

Components of LCA	Standard product LCA	Minerals and metals LCA
Goal and scope of study	Marketing	Process and technology improvement, comparing equipment and process performance
Functional unit	Product of everyday use by downstream consumer	Product is in the upstream for input in the manufacturing
System boundary	Large	Small
Temporal data	Important but often ignored	Important issue, technology changes, ore grade changes
Spatial data	Important but hard to trace	Geographical location of site is important for ore grade and sources of energy
Technology	May not be too much technology dependent and energy-intensive due to use of smaller quantity of material input per functional unit	Bulk metal, highly technology dependent and energy-intensive, metals produced from low grade to high grade
Data variation issues	Possible	High variation due to ore grade and technology and geography
Impact indicators	Carbon, water	Energy use, greenhouse gases, water use, waste production
Interpretation, reporting, and communication	For consumers directly using this product, needs to be clearer to the ordinary people	Consumers cannot see this product in the large quantity, target clients are big manufacturers (auto industry, building industry, government regulators), and then message needs to be simplified for the final consumer

then economic allocation is the preferred method based on the relative prices of each product in the value where they are split. Further sensitivity analysis is recommended in situations where allocation is too confusing. Some cases, precious metals miners are advocating for the use of operating costs as basis for allocation due to the volatility of the price of the PGMs. The allocation of impact based on the avoided environmental impact has been shown [28].

Impact Method Issues

There are various impact methods available in LCA softwares such as SimaPro or GaBi (e.g., Recipe, Ecoindicator, Impact 2002+, Australian Indicator, and USEtox).

Impact method is selected based on the availability in software, geographical location, and the experience of the LCA practitioners. Each method has their own set of assumptions and calculation setup as well as their own midpoint and endpoint impact categories. Midpoint categories provide an estimate of how much environmental burden is produced by a given process. The impact categories provided by several impact methods were reported for an iron ore LCA [26]. Energy, carbon, water, and waste (ECWW) footprint of metals can be a generic simple score card for evaluating the environmental performance of metals practically in many cases. However, toxicity, radioactivity, or other additional impact categories may be selected where relevant depending on the metals (e.g., uranium and rare earth elements).

Conclusions

Environmental, Social, and Governance (ESG) awareness is growing exponentially in the stock exchanges. Reliable, robust, and credible ESG rating tools are required for the industries to demonstrate the performance in the present time and consistently in the future. Mining, mineral processing, and metallurgical technologies have some unique issues that need to be evaluated using a consistent and standard methodology. Life cycle assessment can be an integral part of the ESG rating. Defining boundary, data inputs, and allocation where multiple metals are produced with significantly different prices, dynamic nature of the changes of the energy sources, particularly electricity, impact method selection are important considerations. These factors make LCA studies challenging which need careful attention by the mining industry experts. Energy, carbon, water, and waste (ECWW) footprint of metals can be a generic simple score card for evaluating the environmental performance of metals. These indicator results can be used for ESG rating tools. Industry should invest adequate resources for research and development on the development of high-quality databases and methodology for consistent LCA studies in the mining and metallurgical industries.

References

1. ISO 14044 (2006) Environmental management—life cycle assessment—requirements and guidelines. International Organization for Standardization (ISO), Geneva
2. Santero N, Hendry J (2016) Harmonization of LCA methodologies for the metal and mining industry. Int J Life Cycle Assess 21:1543–1553
3. Segura-Salazar J, Lima FM, Tavares LM (2019) Life Cycle Assessment in the minerals industry: current practice, harmonization efforts, and potential improvement through the integration with process simulation. J Clean Prod 232:174–192. https://doi.org/10.1016/j.jclepro.2019.05.318
4. ALCAS (2023) Australian Life Cycle Assessment Society—Australian Life Cycle Inventory Database Initiative. https://www.alcas.asn.au/auslci. Accessed 16 Sept 2023
5. Ecoinvent (2023) Ecoinvent Database. https://ecoinvent.org. Accessed 16 Sept 2023
6. PRe (2023) PRe sustainability. https://pre-sustainability.com/solutions/tools/simapro. Accessed 16 Sept 2023

7. Sphera (2023) Sphera ESG company. https://sphera.com/life-cycle-assessment-lca-software. Accessed 16 Sept 2023
8. OpenLCA (2023) Open source Life Cycle Assessment software. https://www.openlca.org. Accessed 16 Sept 2023
9. ISO 14040 (1997) Environmental management—life cycle assessment—principles and framework. International Organization for Standardization (ISO), Geneva
10. ISO 14041 (1998) Environmental management—life cycle assessment—goal and scope definition and inventory analysis. International Organization for Standardization (ISO), Geneva
11. ISO 14042 (2000) Environmental management—life cycle assessment—impact assessment. International Organization for Standardization (ISO), Geneva
12. ISO 14043 (2000) Environmental management—life cycle assessment—life cycle interpretation. International Organization for Standardization (ISO), Geneva
13. IIED (2002) Breaking new ground: mining, minerals and sustainable development. International Institute for Environment and Development. https://www.iied.org/sites/default/files/pdfs/migrate/9084IIED.pdf. Accessed 16 Sept 2023
14. Buxton A (2012) MMSD+10: reflecting on a decade. IIE D Discussion Paper. International Institute for Environment and Development, London. https://www.iied.org/sites/default/files/pdfs/migrate/16041IIED.pdf. Accessed 16 Sept 2023
15. Durucan S, Korre A, Munoz-Melendez G (2006) Mining life cycle modelling: a cradle-to-gate approach to environmental management in the minerals industry. J Clean Prod 14:1057–1070. https://doi.org/10.1016/j.jclepro.2004.12.021
16. Korre A, Durucan S (2009) Life cycle assessment of aggregates. EVA025—Final Report: Aggregates Industry Life Cycle Assessment Model: Modelling Tools and Case Studies. Waste and Resources Action Program, Oxon, UK. https://ceramics.org/wp-content/uploads/2017/05/EVA025-MIRO-Life-Cycle-Assessment-of-Aggregates-final-report.pdf. Accessed 16 Sept 2023
17. Awuah-Offei K, Adekpedjou A (2011) Application of life cycle assessment in the mining industry. Int J Life Cycle Assess 16:82–89. https://doi.org/10.1007/s11367-010-0246-6
18. Northey S, Haque N, Mudd G (2013) Using sustainability reporting to assess the environmental footprint of copper mining. J Clean Prod 40:118–128. https://doi.org/10.1016/j.jclepro.2012.09.027
19. Blanco JM, Finkbeiner M, Inaba A (2015) Guidance on organizational life cycle assessment. UNEP SETAC LCI, Berlin 152p
20. Norgate T, Haque N (2010) Energy and greenhouse gas impacts of mining and mineral processing operations. J Clean Prod 18:266–274
21. Norgate T, Haque N, Koltun P (2014) The impact of uranium ore grade on the greenhouse gas footprint of nuclear power. J Clean Prod 84:360–367. https://doi.org/10.1016/j.jclepro.2013.11.034
22. Norgate T, Haque N (2012) Using life cycle assessment to evaluate some environmental impacts of gold production. J Clean Prod 29–30:53–63. https://doi.org/10.1016/j.jclepro.2012.01.042
23. Norgate T, Haque N (2013) Estimation of greenhouse gas emissions from ferroalloy production using life cycle assessment with particular reference to Australia. J Clean Prod 39:220–230. https://doi.org/10.1016/j.jclepro.2012.08.010
24. Norgate T, Jahanshahi S, Rankin WJ (2007) Assessing the environmental impact of metal production processes. J Clean Prod 15:838–848
25. Jahanshahi S, Mathieson JG, Somerville MA, Haque N, Norgate TE, Deev A, Pan Y, Xie D, Ridgeway P, Zulli P (2015) Development of low-emission integrated steelmaking process. J Sustain Metall 1(1):94–114. https://doi.org/10.1007/s40831-015-0008-6
26. Yellishetty M, Haque N, Dubreuil A (2012) Issues and challenges in life cycle assessment in the minerals and metals sector: a chance to improve raw materials efficiency. In: Sinding-Larsen R, Wellmer FW (eds) Non-renewable resource issues: geoscientific and societal challenges. Springer, New York, pp 229–246

27. Northey S, Haque N, Cooksey M (2015) Addressing variability of life cycle based environmental impacts of metal production. Paper presented at the 7th Annual High Temperature Processing Symposium, Swinburne University, Hawthorn, Australia, 2–3 Feb 2015, pp 20–22
28. Weidema B (2001) Avoiding co-product allocation in life-cycle assessment. J Ind Ecol 4(3):11–33

The Synergistic Extraction Kinetics of Aluminum and Silicon from High-Alumina Fly Ash by Carbochlorination

Long Wang, Zi-mu Zhang, Ting-An Zhang, Guo-Zhi Lv, Zhi-He Dou, and Xi-yu Zhang

Abstract In light of the high alumina content (nearly 50%) in the high-alumina fly ash, high-alumina fly ash is considered a significant and promising alternative resource to bauxite. Towards the prevailing issues in the current process of extracting alumina from fly ash, a novel synergistic extraction of aluminum and silicon from high-alumina fly ash was proposed, which features carbochlorination with chlorine and carbon as raw materials. In this paper, the carbochlorination kinetics of aluminum and silicon was investigated. The results indicate that the carbochlorination process of fly ash conforms to the reaction model without generating solid byproducts. The carbochlorination of alumina and silica was governed by chemical reactions at 850–950 °C, with an activation energy of 65.70 kJ/mol and 89.06 kJ/mol, respectively. The reaction series and the kinetic equation, which takes into account the temperature and partial pressure of chlorine gas were successfully determined.

Keywords High-alumina fly ash · Carbochlorination · Synergistic extraction · Kinetics · Activation energy

Introduction

High-alumina fly ash containing 35–50% alumina has been discovered in Inner Mongolia and Shanxi of China, exhibiting comparable alumina content to bauxite [1]. The current total volume has surpassed 300 million tons, demonstrating an annual growth rate of approximately 50 million tons [2]. On the other hand, the shortage of

L. Wang · T.-A. Zhang (✉) · G.-Z. Lv · Z.-H. Dou · X. Zhang
Key Laboratory of Ecological Metallurgy of Multi-metal Intergrown Ores of Ministry of Education, Northeastern University, Shenyang 110819, China
e-mail: zta2000@163.net

Z. Zhang
College of Mechanical Engineering, Shenyang University of Chemical Technology, Shenyang 110142, China

© The Minerals, Metals & Materials Society 2024

C. Iloeje et al. (eds.), *Energy Technology 2024*, The Minerals, Metals & Materials Series, https://doi.org/10.1007/978-3-031-50244-6_14

bauxite reserves in China is significantly inadequate, with annual imports of bauxite resources accounting for over 60% of the total demand [3]. The high-alumina fly ash is expected to present a promising alternative resource for the alumina industry [4].

Due to its cost-effectiveness and streamlined workflow, the Bayer process currently dominates as the primary global method for alumina preparation [5]. The Bayer process cannot treat high-alumina fly ash directly due to its steady mullite phase and low A/S ratio (0.8–1.5). A variety of processes have been developed for the recovery of alumina from high-alumina fly ash, including both the alkali and acid processes [6]. In the alkali method, the pre-desilication process is used for the enrichment of alumina in the high-alumina fly ash [7]. While, the Al/Si ratio can only be increased to approximately 2.6 based on previous findings, as high-alumina fly ash is generated at extremely high temperatures and primarily consists of mullite, corundum, and amorphous silica [8]. The high silica content in the pre-desilicated fly ash also requires more energy and raw materials, leading to higher production costs in the subsequent lime-soda sintering process [9]. Thus, this method was ultimately discontinued due to issues such as substantial energy consumption and secondary contamination.

Considering that silicon dioxide is inert to conventional acids, it is preferable to employ acid methods for the disposal of high-alumina fly ash [10]. The aluminum minerals in high-alumina fly ash, such as mullite and metakaolinite, have limited reactivity with acid under typical conditions [11]. Therefore, the acid method is commonly employed for the treatment of circulating fluid bed fly ash, which primarily comprises amorphous aluminum and silicate phases [12]. The acid method enhances the leaching process of aluminum, silicon, and other associated elements from high-alumina fly ash into solution [13]. This enables the efficient utilization of multiple elements in fly ash [14]. Nevertheless, the energy consumption associated with crystallization and dehydration processes is typically substantial in the acid method, potentially overshadowing the advantage of high extraction efficiency.

The conventional treatments for fly ash are confronted with challenges of high energy consumption and environmental contamination [15]. Therefore, this study proposes a novel process of synergistic extraction of aluminum and silicon from high-alumina fly ash, which comprises two distinct procedures: carbochlorination and purification processes. The carbochlorination process converts aluminum, silicon, and other oxide phases in high-alumina fly ash into their respective chloride phases [16]. The follow-up purification process is a sophisticated technique employed for the refinement of carbochlorination products, such as $AlCl_3$, $SiCl_4$, and other component chlorides, which serve as vital chemical raw materials.

In this study, the carbochlorination kinetics of aluminum and silicon was investigated. The reaction series and the kinetic equation, which takes into account the temperature and partial pressure of chlorine gas were determined. The research findings presented in this study can provide valuable guidance for carbochlorination of natural and secondary resources.

Materials and Methods

The fly ash utilized in this study was obtained from a thermal power plant in Inner Mongolia, China. The high-alumina fly ash was subjected to ICP analysis (Optima 8300DV, PE, USA), and the content of alumina and silica is 48.39% and 38.73%, respectively (Table 1). The mixed gas was achieved through the application of chlorine gas (Cl_2, > 99.8%) and nitrogen gas (N_2, > 99.9%) with a certain proportion.

The details of the carbochlorination process are presented as follows: high-alumina fly ash and carbon in a specific mass ratio were homogeneously mixed, followed by pelletization into pellets with a diameter ranging from 4 to 6 mm. The fine pellets could be obtained after drying at 90 °C for 24 h. Subsequently, a disk granulating machine carried out the carbochlorination kinetics experiment of the fine pellets. During the carbochlorination process, the products resulting from carbochlorination were gathered in the separation apparatus. After the carbochlorination process, the carbochlorination residues were subjected to leaching in hot water at a temperature of 80 °C with a liquid-to-solid ratio of 10:1 for 30 min. The leaching solution was subsequently separated by a circulating water vacuum pump, and the leaching residues were analyzed by ICP. The carbochlorination efficiency of aluminum and silicon from high-alumina fly ash was calculated using the following formula:

$$C_{\mathrm{Al/Si}}(\%) = [(m_0 - m_1)/m_0] \times 100\%, \tag{1}$$

where m_0 is the content of aluminum and silicon in the pellet before carbochlorination (g) and m_1 is the content of aluminum and silicon in the residues after carbochlorination and leaching (g).

The morphologies and phase composition of fly ash and the carbochlorination residues were examined via SEM (SU-8010, Japan) and XRD (PW3040/60, Philips, Netherlands).

Table 1 Chemical composition of high-alumina fly ash used in this study

Components	Al_2O_3	SiO_2	TiO_2	MgO	CaO	Others
Content (wt%)	48.39	38.73	1.74	0.40	2.65	8.09

Results and Discussion

The Carbochlorination Kinetics of Aluminum in the Fly Ash

The carbochlorination kinetics of aluminum in the fly ash was investigated within the temperature range of 850–900 °C. The remaining experimental conditions included a chlorine gas flow rate of 0.30 L/min, a carbon content of 27.0 wt%, and a chlorine gas partial pressure of 101.3 kPa. The carbochlorination efficiency of aluminum is illustrated in Fig. 1.

Figure 1 demonstrates that aluminum's carbochlorination efficiency continuously increases with time under identical temperature conditions. Similarly, under constant time conditions, the carbochlorination efficiency of aluminum also shows a progressive rise with increasing temperature. To examine the carbochlorination kinetics of aluminum in the fly ash, Eqs. (2) and (3) were used to fit the carbochlorination efficiency [17]:

$$1-(1-x)^{1/3}=bk_rC_{A,b}t/(a\rho_b r_0)=K_1t, \tag{2}$$

$$1-(1-x)^{2/3}=2bD_rC_{A,b}t/\left(a\rho_b r_0^2\right)=K_2t, \tag{3}$$

where a, b is a stoichiometric number, ρ_b is the molar density of the solid phase, mol/cm^3, r_0 is the initial radius of the solid reactant particle, cm, k_r is the chemical reaction rate constant, and $C_{A,b}$ is the concentration of the reactant gas A in the main gas phase, mol/cm^3.

It was assumed that the chemical reaction controlled the alumina carbochlorination reaction as the limiting step. The carbo carbochlorination efficiency under different time conditions was then substituted into the limiting Eq. (2), and a scatter

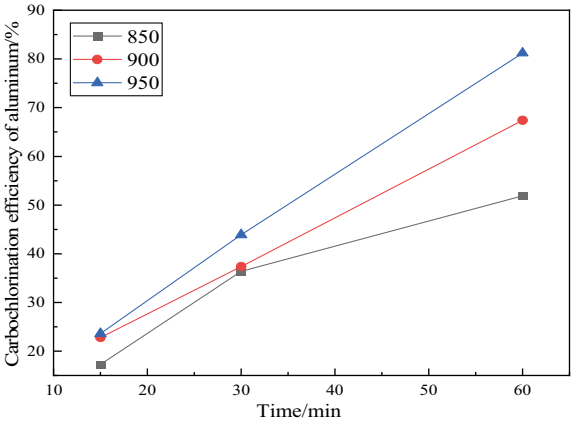

Fig. 1 Carbochlorination efficiency of aluminum at different temperatures

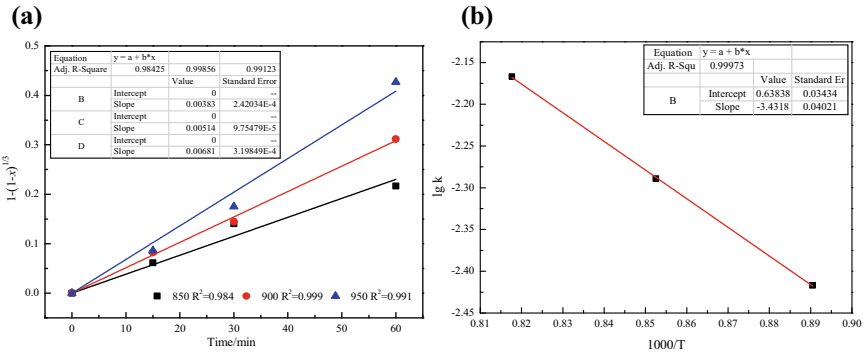

Fig. 2 Relationship between efficiency and time (**a**) and relationship between 1000/T and lg k (**b**)

plot with $1-(1-x)^{1/3}$ against time was generated. The scatter points were subsequently fitted, as depicted in Fig. 2a. The correlation coefficients all exceed 0.98, indicating a high level of fitting. The slopes obtained under three different temperature conditions are utilized in the Arrhenius formula (4). The linear slope at different temperatures can be determined by fitting straight lines, as illustrated in Fig. 2b [18].

$$\lg k = -\mathrm{Ea}/(2.303RT) + A, \tag{4}$$

where k is the apparent rate constant of the reaction, A is a constant, R is the molar gas constant, 8.314 kJ/mol, and Ea is the apparent activation energy, J/mol.

The correlation coefficient is 0.9997, and the apparent activation energy of 65.7 kJ/mol is determined by comparing it with Eq. (5), within the temperature range from 850 to 950 °C. The obtained result is by the characteristics of chemical reaction control kinetics after thorough verification, whereas assuming kinetic conditions under diffusion control yields unsatisfactory fitting results and calculated apparent activation energy that falls outside the characteristic range of diffusion control. Therefore, within this temperature range, chemical reaction control becomes the primary limiting factor for the alumina carbochlorination reaction. Moreover, temperature significantly influences the rate of chemical reactions, which is consistent with the carbochlorination efficiency of aluminum in Fig. 1.

The fitting results in Fig. 2b lead us to the conclusion that Eq. (5) represents the temperature kinetic equation of the carbochlorination reaction of aluminum in the fly ash.

$$\lg k = -3.4318 \times 1000/T + 0.63838 \tag{5}$$

The Carbochlorination Kinetics of Silicon in the Fly Ash

The carbochlorination efficiency of silicon in the fly ash at different temperatures can be determined under identical experimental conditions, as illustrated in Fig. 3.

In Fig. 3, the carbochlorination efficiency of silicon is relatively lower compared to that of alumina. The efficiency of silicon carbochlorination significantly decreases at three temperatures for 15 min, but gradually improves with higher temperatures. From a thermodynamic perspective, the standard Gibbs free energy of the carbochlorination process for silicon is comparatively higher than that of the carbochlorination process for aluminum. Previous research indicates that, during the carbonization process of high-aluminum fly ash, initial degradation primarily occurs within the mullite structure, where aluminum is predominantly chlorinated followed by silicon[19].

The carbochlorination efficiency of silicon was seamlessly integrated into Eq. (2) in the blink of an eye, followed by a meticulous fitting of a scatter plot showcasing the temporal pair $1-(1-x)^{1/3}$. The resulting fitting image is elegantly presented in Fig. 4a. The correlation coefficients all exceed 0.94, indicating a high level of fitting. The slopes obtained under three different temperature conditions are utilized in the Arrhenius formula (4), the linear slope at different temperatures can be determined by fitting straight lines, as illustrated in Fig. 4b.

The scatter plot in Fig. 4b shows a well-fitted line with an impressive correlation coefficient of 0.85. The discernible activation energy of 90.05 kJ/mol exceeds the threshold value of 40 kJ/mol prescribed by the Arrhenius formula. Therefore, it can be concluded that the chlorination process of silicon oxide is primarily influenced by chemical factors within the temperature range from 850 to 950 °C. The fitting results depicted in Fig. 4b lead us to the compelling conclusion that Eq. (6) elegantly represents the temperature kinetic equation of the reaction of silicon in the fly ash.

$$\lg k = -4.70323 \times 1000/T + 1.61356 \tag{6}$$

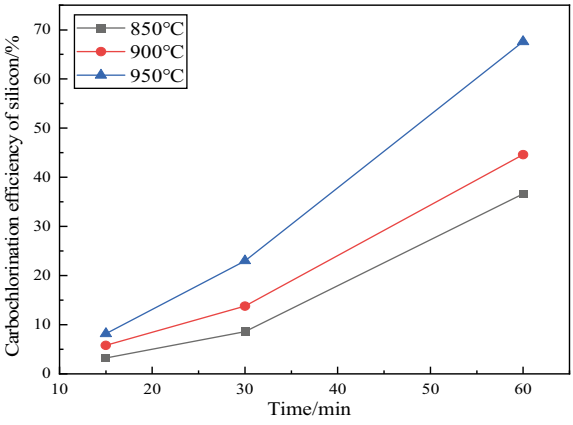

Fig. 3 Carbochlorination efficiency of silicon at different temperatures

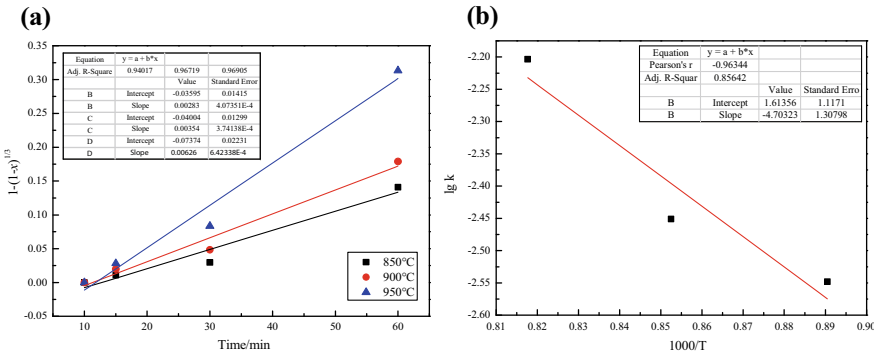

Fig. 4 Relationship between carbochlorination efficiency of silicon and time at different temperatures (**a**) and relationship between 1000/T and lg k (**b**)

The Carbochlorination Reaction Order of Aluminum in the Fly Ash

To explore the carbochlorination reaction order of aluminum in the fly ash, the experimental conditions were as follows: temperature set at 950 °C, gas flow rate maintained at 0.30 L/min, carbon content at 27.0 wt%, and chlorine gas partial pressures adjusted to 60.8, 81.0, and 101.3 kPa respectively. The experimental results are illustrated in Fig. 5.

The carbochlorination efficiency of aluminum exhibited a gradual increase in Fig. 5 as both the partial pressure and time increased. The carbochlorination efficiency of aluminum in Fig. 5 was modeled as $1 - (1 - x)^{1/3}$, and a scatter plot illustrating the relationship between carbochlorination efficiency and time under

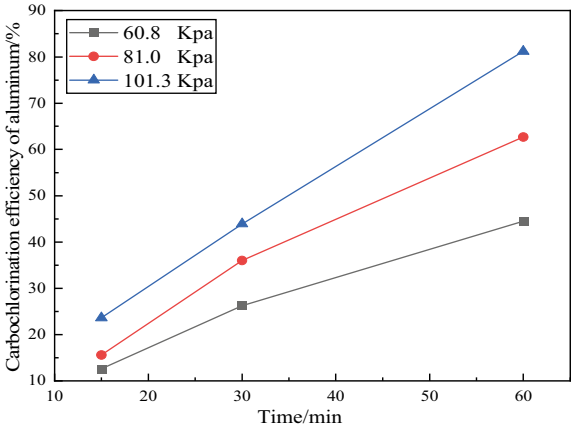

Fig. 5 Carbochlorination efficiency of aluminum at different partial pressures

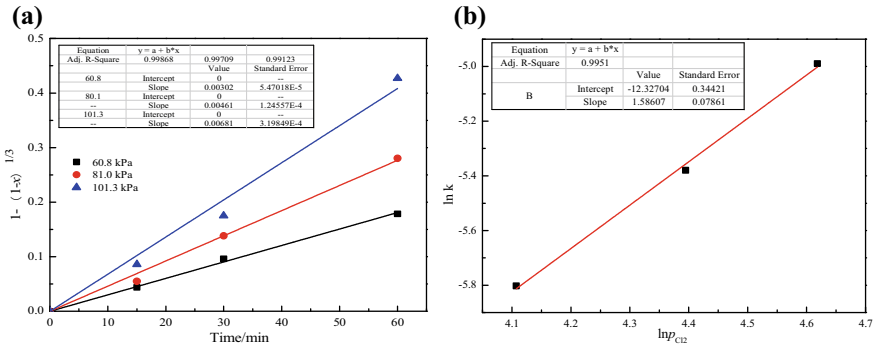

Fig. 6 Relationship between efficiency and time (**a**) and relationship between ln $p\mathrm{Cl}_2$ and ln k (**b**)

different chlorine partial pressures was generated and fitted, as shown in Fig. 6a. The correlation coefficients of reaction time to the fitting line were all above 0.99 under three different chlorine partial pressures, indicating a strong fit. The linear slope at different various partial pressures of chlorine gas can be determined by fitting straight lines, as illustrated in Fig. 6b. A direct correlation is established between the chemical reaction rate constant (k) and the partial pressure of chlorine gas. The reaction order for the alumina chlorination process is found to be 1.59.

The Carbochlorination Reaction Order of Silicon in the Fly Ash

The carbochlorination efficiency of silicon in the fly ash can be determined at various partial pressures, using identical experimental conditions in Sect. 3.3 and illustrated in Fig. 7.

The observation from Fig. 7 indicates that, at a chlorine gas partial pressure of 60.8 kPa and a reaction time of 15 min, the aluminum in the fly ash undergoes a reaction before silicon in the carbochlorination process [20], resulting in a relatively lower carbochlorination efficiency of silicon. The carbochlorination efficiency of silicon in the fly ash increases proportionally with an increase in the partial pressure of chlorine gas and reaction time. The reaction reaches its maximum efficiency at 67.6% when the partial pressure of chlorine gas reaches 101.3 kPa and the duration is set to 60 min.

The chlorination reaction of silicon is chemically controlled within the temperature range from 850 to 950 °C. Therefore, the carbochlorination efficiency of silicon in Fig. 7 can be mathematically expressed as $1-(1-x)^{1/3}$. The relationship between carbochlorination efficiency and time under various chlorine partial pressures is visualized using a scatter plot, which is generated and fitted in Fig. 8a.

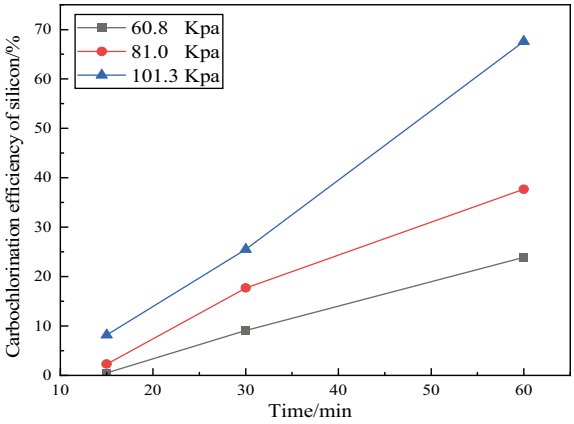

Fig. 7 Carbochlorination efficiency of silicon at different partial pressures

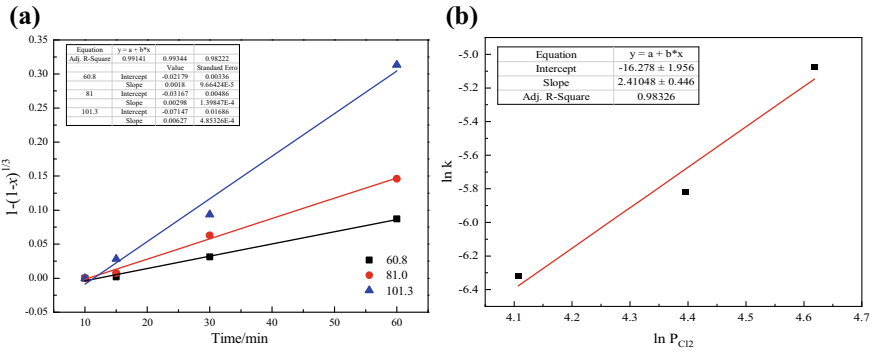

Fig. 8 Relationship between efficiency and time (**a**) and relationship between ln pCl_2 and ln k (**b**)

The relationship between carbochlorination efficiency and time under different chlorine partial pressures is demonstrated in Fig. 8a with correlation coefficients of 0.99, 0.99, and 0.98, indicating a high level of conformity. The linear slope at different various partial pressures of chlorine gas can be determined by fitting straight lines, as illustrated in Fig. 8b. By conducting a comprehensive analysis in Fig. 8b, a direct correlation can be subsequently established between the chemical reaction rate constant (k) and the partial pressure of chlorine gas, indicating a determined reaction order of 2.41 for the alumina chlorination process.

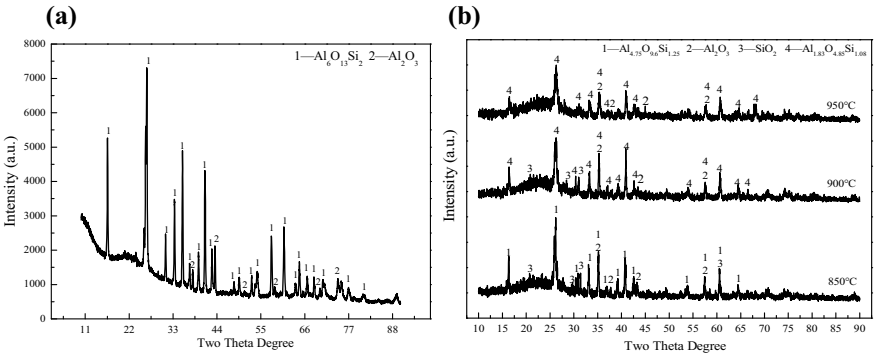

Fig. 9 XRD patterns under various temperatures **a** fly ash; **b** carbochlorination residues

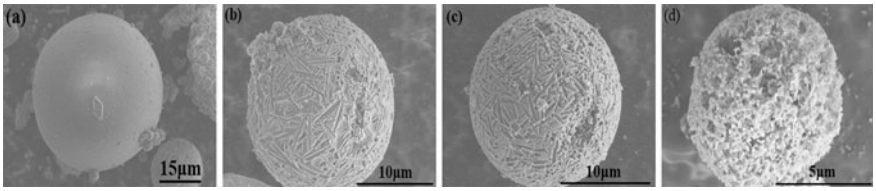

Fig. 10 Morphology characterization of the samples **a** fly ash; **b** 850 °C; **c** 900 °C; **d** 950 °C

Characterization of Fly Ash and Carbochlorination Residues

To further elucidate the carbochlorination process of fly ash, X-ray diffraction (XRD) and scanning electron microscopy (SEM) analysis were performed on both the fly ash and carbochlorination residues obtained at different temperatures, as depicted in Figs. 9 and 10.

The phase composition of fly ash residue at various reaction temperatures is illustrated in Fig. 9. The peak strength of mullite and alumina undergoes a substantial decline as the temperature rises, concomitant with an augmentation in their half-width and height. The statement implies that the crystallization degree of the phase deteriorates as temperature changes, ultimately resulting in the carbonization-induced destruction of mullite's crystal structure. The intermediate phases $Al_{4.75}O_{9.63}Si_{1.25}$ and $Al_{1.83}O_{4.85}Si_{1.08}$ are formed from $Al_6O_{13}Si_2$ during the mullite formation. Furthermore, the reduction in the Al and Si content within the chemical formula suggests that elevated temperatures can enhance the carbochlorination process of high-alumina fly ash.

The fly ash and carbochlorination residues were subjected to scanning electron microscopy (SEM) analysis at various temperatures, with the results presented in Fig. 10. The high-alumina fly ash exhibits a sleek and spherical particle morphology, as depicted in Fig. 10a. The surface gradually undergoes corrosion by chlorine gas

as the temperature increases, resulting in a progressively rougher texture characterized by numerous gullies, as illustrated in Fig. 10b, c. The occurrence of surface erosion and hollow-out phenomenon in Fig. 10d at a temperature of 950 °C highlights the critical role that temperature plays as a limiting factor in the carbothermal chlorination effect of high-alumina fly ash. From an intuitive perspective, it has been experimentally confirmed that as the temperature increases, there is a corresponding increase in the carbochlorination efficiency. Furthermore, the SEM results demonstrate that the progressive temperature increase leads to mullite's structural integrity degradation.

Conclusions

In this study, a novel process of synergistic extraction of aluminum and silicon from high-alumina fly ash was proposed, which features carbochlorination with chlorine and carbon as raw materials. The results indicate that the carbochlorination process of fly ash conforms to the reaction model without generating solid byproducts. The carbochlorination of alumina and silica was governed by chemical reactions at 850–950 °C, with an activation energy of 65.70 kJ/mol and 90.05 kJ/mol, respectively. The reaction order for the chlorination process of aluminum in the fly ash has been determined to be 1.59. The reaction order for the chlorination process of silicon in the fly ash has been determined to be 2.41. The SEM results demonstrate that the progressive temperature increase leads to mullite's structural integrity degradation. The research findings in this paper provide valuable guidance for carbochlorination of natural and secondary resources using a carbochlorination system.

Acknowledgements The authors gratefully acknowledge the National Natural Science Foundation of China (No. 52304364) and the financial support of the National Key Research and Development Program (No. 2022YFB3504502).

References

1. Ahmaruzzaman M (2010) A review on the utilization of fly ash. Prog Energy Combust 36:327–363
2. Yan S, Zhang TA, Chu C, Zhang X, Sun J, Lv G, Yang H (2015) Preparation of zeolite 4A by using high-alumina coal fly ash. In: Light metals 2015, 147–151
3. Cao PX, Li G, Jiang H, Zhang X, Luo J, Rao M, Jiang T (2021) Extraction and value-added utilization of alumina from coal fly ash via one-step hydrothermal process followed by carbonation. J Clean Prod 323:129174
4. Gao Y, Liang K, Gou Y, Wei S, Cheng F (2020) Aluminum extraction technologies from high aluminum fly ash. Rev Chem Eng 37:885–906
5. Ma ZB, Zhang S, Zhang HR, Cheng FQ (2019) Novel extraction of value metals from circulating fluidized bed-derived high-alumina fly ash by acid-alkali-based alternate method. J Clean Prod 230:302–313

6. Bai G, Qiao YH, Shen B, Chen SL (2011) Thermal decomposition of coal fly ash by concentrated sulfuric acid and alumina extraction process based on it. Fuel Process Technol 92:1213–1219
7. Li D, Jiang KX, Jiang XX, Zhao F, Wang SD, Feng LY, Zhang DG (2022) Improving the A/S ratio of pretreated coal fly ash by a two-stage roasting for Bayer alumina production. Fuel 310:122478
8. Guo Y, Li J, Yan K, Cao L, Cheng F (2019) A prospective process for alumina extraction via the co-treatment of coal fly ash and bauxite red mud: investigation of the process. Hydrometallurgy 186:98–104
9. Guo Y, Zhao Z, Zhao Q, Cheng F (2017) Novel process of alumina extraction from coal fly ash by pre-desilicating-Na_2CO_3 activation—acid leaching technique. Hydrometallurgy 169:418–425
10. Rui H, Zhang L, Li L, Zhu L (2021) Solvent extraction of lithium from hydrochloric acid leaching solution of high-alumina coal fly ash. Chem Phys Lett 771(2):138510
11. Sangita S, Nayak N, Panda CR (2017) Extraction of aluminum as aluminum sulfate from thermal power plant fly ashes. Trans Nonferrous Met Soc 27(9):2082–2089
12. Wang RC, Zhai YC, Wu XW, Ning ZQ, Ma PH (2014) Extraction of alumina from fly ash by ammonium hydrogen sulfate roasting technology. Trans Nonferrous Met Soc 24(5):1596–1603
13. Sahayam AC, Venkateswarlu G, Thangavel S, Spectroscopy A (2021) Leaching of gallium from coal fly ash, alumina and sediment samples with an acid mixture for its determination by ICP-OES. Atom Spectrosc 42:32–35
14. Rampou M, Ndlovu S, Shemi A (2017) Purification of coal fly ash leach liquor for alumina recovery using an integrated precipitation and solvent extraction process. J Sustain Metall 3:1–11
15. Adelman DJ, Burnet G (2010) Carbochlorination of metal oxides with phosgene. Aiche J 33:64–69
16. Wang L, Zhang TA, Lv GZ, Dou ZH, Zhang WG, Niu LP (2019) Carbochlorination kinetics of high-alumina fly ash. JOM 71:492–498
17. Hua YY (2004) Introduction to the kinetics of metallurgical processes. Metallurgical Industry Press, Beijing, pp 144–147 (in Chinese)
18. Kanari N, Gaballah I, Allain E (1999) A study of chromite carbochlorination kinetics. Metall Mater Trans B 30:577–587
19. Wang L, Zhang TA, Lv GZ, Dou ZH, Zhang WG, Zhang JZ, Niu LP, Liu Y (2019) Carbochlorination of alumina and silica from high-alumina fly ash. Miner Eng 130:85–91
20. Wang L, Zhang TA, Lv GZ, Zhang JJ, Dou ZH, Zhang WG, Niu LP, Liu Y (2018) Investigation of the carbochlorination mechanism of mullite from fly ash. Metall Mater Trans B 49:2835–2845

Part IV
Renewable Energy, Combustion and Material Efficiency

Fused Alumina Production from Non-metallic Residue of Aluminum White Dross

Selçuk Kan, Hasan Güney, Kağan Benzeşik, and Onuralp Yücel

Abstract Aluminum dross occurs while production of aluminum. Depending on the aluminum process such as primer or seconder, chemical composition varies. White dross occurs from primer aluminum production and it contains 20–80 wt% Al. Black dross occurs from seconder aluminum production and it contains 5–25 wt% Al. White dross is ground, so metallic part and non-metallic residue (NMR) can be separated. Since oxides are brittle and aluminum is ductile, they can be separated from each other due to their particle size. Metallic part is used to produce aluminum ingots and NMR is landfilled and when it reacts with groundwater or humidity, it has several hazardous effects to nature. In this study NMR was used to produce fused alumina in an electrical arc furnace. Direct smelting and calcination of dross conditions before smelting are investigated. Products were investigated with XRF and XRD techniques. 90–95 wt% Al_2O_3 containing fused alumina was produced.

Keywords Aluminum · Environmental effects · Recycling and secondary recovery

Introduction

Aluminum production is increasing every year around the world. Aluminum can be produced with two different production methods, primary and secondary production. While primary aluminum production is based on refining bauxite ore to obtain aluminum oxide, secondary aluminum production aims to reuse the wastes generated in primary aluminum production by various methods or to recycle aluminum products.

In addition, secondary aluminum production amounts are increasing every year due to problems such as energy consumption during primary aluminum production, the formation of wastes in the production processes, and the formation of

S. Kan · H. Güney · K. Benzeşik · O. Yücel (✉)
Department of Metallurgical and Materials Engineering, Faculty of Chemical and Metallurgical Engineering, Istanbul Technical University, 34469 Maslak, Istanbul, Turkey
e-mail: yucel@itu.edu.tr

© The Minerals, Metals & Materials Society 2024

C. Iloeje et al. (eds.), *Energy Technology 2024*, The Minerals, Metals & Materials Series, https://doi.org/10.1007/978-3-031-50244-6_15

serious environmental problems for living things and the environment during storage. Unlike primary production, secondary aluminum production has advantages such as low energy consumption and low amount of waste generation. By using secondary aluminum production methods, significant advantages can be obtained in terms of CO_2 consumption, solid waste, energy consumption, atmospheric emissions, and investment costs [1, 2].

Dross is a waste material that generated during melting or heat treatment processes in primary smelting plants, foundries and recycling facilities. Dross contains high amount of metallic aluminum and aluminum oxide and some other components such as salts and minor oxides. There are 3 types of dross; white dross (15–70 wt% Al, 23–30% Al_2O_3), black dross (12–20 wt% Al, 30–50 wt% Al_2O_3), and salt cake (wt% 4–10 Al, 50–70% Al_2O_3). The white drosses collected at the facilities are ground using a ball mill. Due to its hardness, alumina becomes fine powder, while aluminum pieces with a ductile structure become flattened rather than ground. Using a vacuum system by utilizing the difference between particle sizes, fine alumina powders are collected in bag filters and this part is called non-metallic residue (NMR). The metallic aluminum-rich part remaining in the mill is passed through a magnetic separator in order to remove the iron coming from the ball mill, and the obtained metallic part is melted under salt and turned into ingot. The non-metallic part is disposed of by landfilling [3].

Various risks arise when the non-metallic parts of aluminum white drosses are disposed of by landfilling. Various gases and liquids such as ammonia, phosphine, and methane can mix with the soil and cause the pH value of groundwater to increase. This increase in pH not only pollutes the groundwater, but also affects the vitality negatively by disrupting the ecological balance. Some reactions that occur in this process [4, 5]:

$$AlN + 3H_2O \rightarrow Al(OH)_3 + NH_3 \tag{1}$$

$$2Al_5O_6N + 3H_2O \rightarrow 5Al_2O_3 + 2NH_3 \tag{2}$$

$$AlP + 3H_2O \rightarrow Al(OH)_3 + PH_3 \tag{3}$$

$$Al_2S_3 + 6H_2O \rightarrow 2Al(OH)_3 + 3H_2S \tag{4}$$

$$Al_4C_3 + 12H_2O \rightarrow 4Al(OH)_3 + 3CH_4 \tag{5}$$

$$2Al + 3H_2O \rightarrow Al_2O_3 + 3H_2 + \text{heat} \tag{6}$$

In this study, the non-metallic parts of the white drosses produced in primary aluminum production were used as raw materials. The production conditions of fused alumina in the electric arc furnace were investigated. A 270 kVA DC electric arc

furnace was used in melting experiments. The products formed as a result of melting were characterized by XRF and XRD methods, and their hardness and density values were measured.

Experimental

The process flow diagram is shown in Fig. 1. Chemical analysis results of NMR are shown in Table 1. Non-metallic residue (NMR) of aluminum white dross was smelted in EAF with and without calcination. Schematic view of the EAF was given in Fig. 2. Calcination was done in a rotary kiln at 850 and 1150 °C. Three preliminary experiments were conducted using smelter grade alumina (SGA) to optimize EAF conditions such as electrode and crucible diameter. Calcination wasn't applied in the experiment which coded EAF 4. Calcination was applied at 850 °C in EAF 5–6 experiments and at 1150 °C in EAF 7. All experiment parameters are given in Table 2.

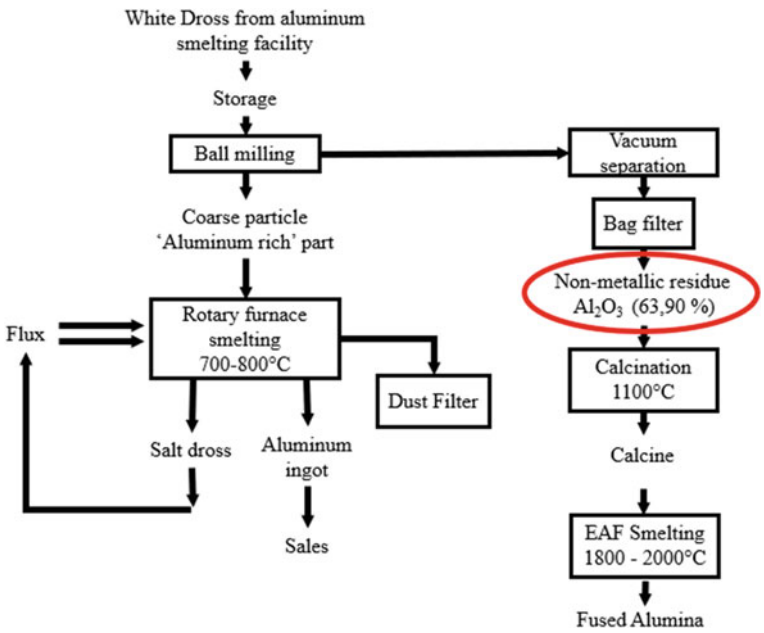

Fig. 1 Flow diagram of the process

Table 1 Chemical analysis of non-metallic residue

Al_2O_3	Fe_2O_3	SiO_2	Na_2O	CaO	Cl	MgO	F	SO_3
63.90	0.18	2.43	11.1	1.49	4.81	0.01	1.86	1.53

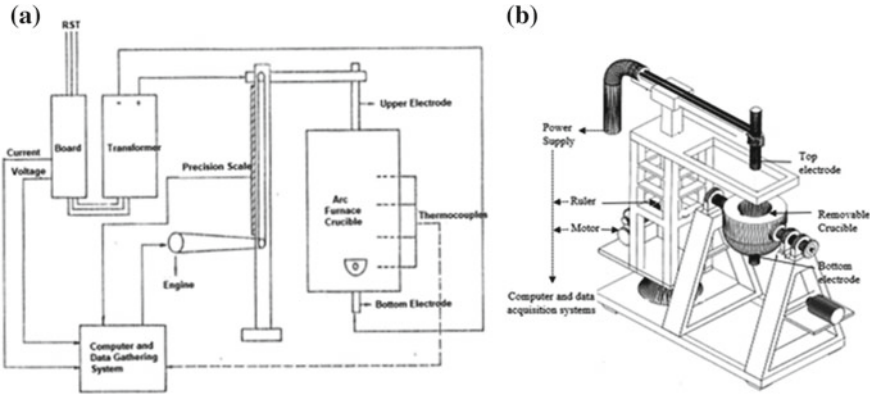

Fig. 2 Schematic view of the EAF

Table 2 Experiment's parameters

Experiment	Time (min)	Charge amount (kg)	Smelting product (kg)	Energy consumption (kW)	Electrode consumption (g)	Temperature (°C)	Details
EAF 4	45	20	18.45	35	161	1880	No calcination
EAF 5	35	15	11.73	40	250	1950	850 °C Calcination + EAF
EAF 6	50	16	13.73	40	298	1920	850 °C Calcination + EAF 5 Sinter + EAF
EAF 7	43	17.8	15.48	45	478	1895	1150 °C Calcination + EAF

NMR was fed to the pre-heated furnace. EAF was left for cooling for 1 day after each experiment. Three samples were taken from each experiment for characterization. One sample was taken from the surface of the product, 1 sample was taken from the inside, and 1 sample was taken from the part close to the bottom electrode. They are named 1-2-3 from top to bottom (e.g. 4.1, 4.2, and 4.3). Chemical analysis and XRD analysis were applied to all samples. Density and hardness measurements were performed to 4.2, 5.2, 6.2, and 7.2. Archimedes' principle was used for density measurements. Vickers was used for the hardness. $500 \times g$ force was applied for 10 s.

Table 3 Chemical analysis results of experiments

Sample	Al_2O_3	SiO_2	Na_2O	CaO	MgO	Cl
EAF 4.2	95.71	1.24	0.4	1.37	–	–
EAF 5.2	92.1	2.09	–	1.83	1.13	–
EAF 6.2	92.8	0.61	–	2.63	1.08	0.005
EAF 7.2	90.7	1.67	–	1.39	5.31	–

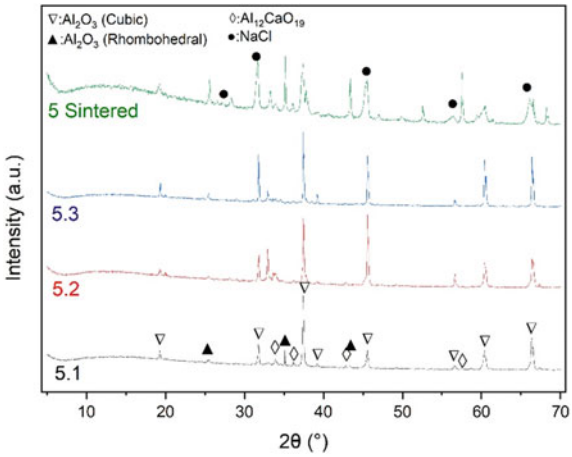

Fig. 3 XRD results of EAF 5

Results and Discussion

Sintered parts were observed in EAF 5 and 6 experiments. High amount of Na was observed in the EAF 5 and EAF 6 sintered parts. The calcination temperature was increased to 1150 °C because of this situation. Al_2O_3 content was increased to 81% after calcination. Chemical analysis results of selected samples are given in Table 3. A high amount of MgO was observed in some samples, this is because of the inhomogeneity of the NMR. Al_2O_3 content was increased to 90–95% after smelting in EAF.

XRD results of EAF 5, 6, and 7 are given in Figs. 3, 4 and 5, respectively. NaCl peaks were observed in sintered parts of EAF 5 and 6. Rest of the peaks mostly belong to Al_2O_3. Ca or Mg containing oxides were observed in some samples. Alumina phases were transformed into cubic structure after smelting. Rhombohedral alumina was observed in calcined and sintered parts.

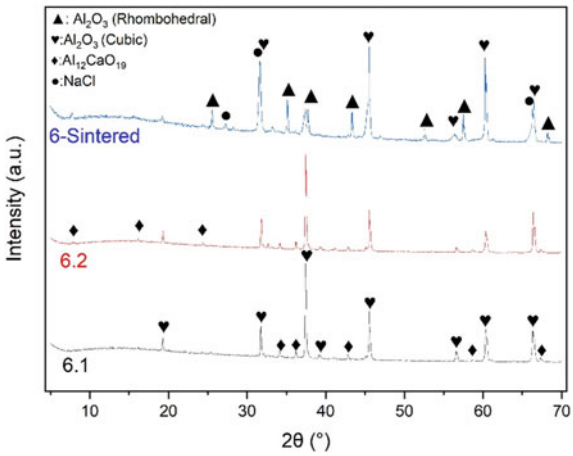

Fig. 4 XRD results of EAF 6

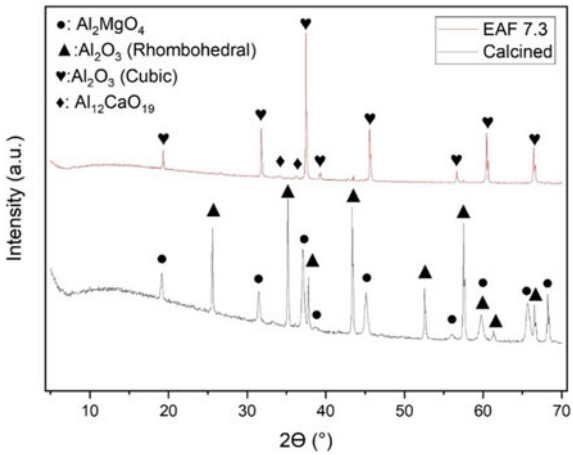

Fig. 5 XRD results of EAF 7

Conclusion

In this study, non-metallic part of the aluminum white dross was used as a raw material to produce fused alumina in an EAF. Alumina content of the non-metallic residue was 63.90%. It was increased to 86% after calcination. Furthermore, it was increased to 90–95% after smelting in EAF. XRD results show that smelted products are in cubic alumina phase, some minor peaks were also observed which belong to Ca or Mg containing phases. This process shows that it is possible to use NMR, which has no usage area, as a raw material in the production of fused alumina.

Acknowledgements This study was carried out within the scope of the project numbered 122N040, "The Production of Aluminum Metal, Other Metals and Compounds" supported by TUBİTAK. The authors sincerely thank ETİ Aluminyum for chemical analysis.

References

1. Gil A (2005) Management of the salt cake from secondary aluminum fusion processes. Ind Eng Chem Res 44(23):8852–8857. https://doi.org/10.1021/ie050835o
2. Mahinroosta M, Allahverdi A (2018) Hazardous aluminum dross characterization and recycling strategies: a critical review. J Environ Manag 223:452–468. https://doi.org/10.1016/j.jenvman.2018.06.068
3. Polat BT, Öner İE, Kan S, Benzeşik K, Yücel O (2022) Fused calcium aluminate production from aluminum white dross residue. J Sustain Metall 8:851–862. https://doi.org/10.1007/s40831-022-00532-w
4. Tsakiridis PE (2012) Aluminium salt slag characterization and utilization—a review. J Hazard Mater 217–218:1–10. https://doi.org/10.1016/j.jhazmat.2012.03.052
5. David E, Kopac J (2019) The assessment of the recycling process of aluminum hazardous waste and a new route of development. Mater Today: Proc 10:340–347. https://doi.org/10.1016/j.matpr.2018.10.415

Numerical Investigation on H_2 Reduction Characteristics of Fe_3O_4 in Drop Tube Furnace

Zhenfeng Zhou, Zukang Wan, and Guang Wang

Abstract The flash iron-making process is expected to be a new iron-making technology due to its nonuse of coke, pellets, sintered ore, and extremely high production efficiency. Hydrogen is an excellent reducing agent for flash iron-making with fast reduction rate and none CO_2 emission. In this study, the effect of hydrogen concentration and reduction temperature on reduction characteristics of Fe_3O_4 in a drop tube furnace was investigated using the computational fluid dynamics method. The results show that the Fe_3O_4 particles can be reduced in seconds. The reduction degree gradually increases with increase of hydrogen concentration and reduction temperature. The maximum metallization ratio can reach 88.95%.

Keywords Flash iron-making · Fe_3O_4 · Hydrogen · Reduction

Introduction

A large amount of coke, sintered ore, and pellet ore will be consumed during blast furnace production process. Much energy will be consumed and much pollution will be produced during the sintering and coking processes [1–3]. Under the multiple pressures of resources and environment, the blast furnace is faced with great challenges. It is urgently necessary to develop an economical and environmentally friendly iron-making technology. The flash iron-making process directly utilizes iron ore powder without coking and sintering processes. The iron-making process is greatly simplified, and the emissions of CO_2 and pollutants will be greatly reduced [4, 5]. In

Z. Zhou (✉) · Z. Wan
College of Mechanical and Electronic Engineering, Shandong University of Science and Technology, Qingdao 266590, China
e-mail: zhouzhenfeng@sdust.edu.cn

G. Wang
State Key Laboratory of Advanced Metallurgy, University of Science and Technology Beijing, Beijing 100083, China
e-mail: wangguang@ustb.edu.cn

© The Minerals, Metals & Materials Society 2024

C. Iloeje et al. (eds.), *Energy Technology 2024*, The Minerals, Metals & Materials Series, https://doi.org/10.1007/978-3-031-50244-6_16

addition, the flash iron-making process has high production efficiency, and iron ore powder can be fully reduced in seconds [6, 7].

The diffusion rate of H_2 is five times that of CO, and the reduction rate is eleven times that of CO. The reduction product of H_2 is water without any pollution [8]. Therefore, H_2 is the most ideal reducing agent for flash iron-making process. A large amount of research has been conducted on the reduction process of iron ore powder in H_2 atmosphere. Chen et al. [6, 9] investigated the reduction characteristics of Fe_3O_4 under different conditions using a drop tube furnace and achieved a high reduction degree. However, the reduction temperature is higher and the reduction characteristic at lower reduction temperature was not investigated. In industrial process, the lower temperature reduction characteristics are more important. Wang et al. [8, 10] simulated the reduction characteristics of iron ore powder using the computational fluid dynamic (CFD) method. The effect of pressure on reduction was discussed. However, the reduction characteristics at lower reduction temperature are also not studied. Therefore, the lower reduction temperature reduction characteristic of iron ore powder is needed to be investigated.

The micron-sized Fe_3O_4 particles can be reduced completely by H_2 in seconds at the 1273 K temperature [8]. The temperature condition of 1273 K can be achieved easily in the industrial process. Furthermore, the bonding of iron ore powder can be effectively avoided at the temperature [11]. Therefore, it is more important to investigate the reduction characteristics of iron ore powder near 1273 K. In real process, the iron ore powder is injected into the furnace. Therefore, the flow and reaction characteristic of Fe_3O_4 plumes was investigated using CFD method. The effect of H_2 concentration and reaction temperature was investigated. It was found that the metallization rate gradually increases with the increase of hydrogen concentration. The metallization rate at 100% H_2 concentration and 1273 K temperature is 88.95%. This study has important guiding significance for the development of flash iron-making technology.

Geometric Model and Simulation Conditions

A real drop tube furnace was simulated. The heating section of the drop tube furnace is 1000 mm long with a diameter of 80 mm. Figure 1a shows the schematic diagram of the geometric model, and Fig. 1b shows the grid of the model. The structured grids were used in the simulation process.

Table 1 shows the main simulation conditions. The particle feeding rate is 5 g/min. For case 1–4, the reaction temperature is 1273 K, and the H_2 concentration is 30%, 50%, 70% and 100%, respectively. The H_2 concentration for case 5 and case 6 is 100%, and the reaction temperature is 1073 K and 1173 K, respectively. The diameter of Fe_3O_4 particles is 50 μm.

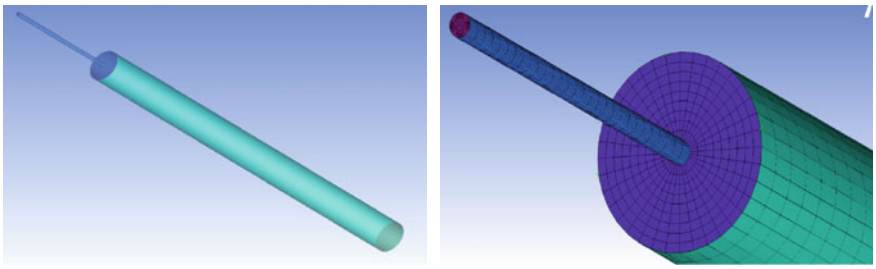

(a) (b)

Fig. 1 Geometric model and mesh

Table 1 Simulation conditions

Case	Temperature (K)	H_2 content (vol.%)	Particle feeding rate (g/min)
1	1273	30	5
2	1273	50	
3	1273	70	
4	1273	100	
5	1073	100	
6	1173	100	

Model Description

The gas-particle flow and reaction in the drop tube furnace were calculated based on the framework of the software package ANSYS-FLUENT. In this model, the gas phase is treated with an Eulerian frame and described by the steady-state Reynolds-averaged Navier–Stokes equations closed by the k–ε turbulence model [12]. The governing equations for the gas phase include mass, momentum, energy, gas species, turbulent kinetic energy, and turbulent dissipation rate [13–15].

Particles of Fe_3O_4 are treated as discrete phase, modeled using the Lagrange method, where the trajectories of the discrete particles are determined by integrating Newton's second law of motion. The drag force (f_D) and turbulent dispersion are included. Full coupling of mass, momentum, and energy of particles with the gas phase is implemented. The change of particle temperature is governed by three physical processes: convective heat transfer, latent heat transfer associated with mass transfer, and radiant heat transfer. The governing equations for the particle phase are summarized in Table 2 [13, 14].

Where m_p is the mass of particles; d_p is the diameter of particles; T_g and T_p are the temperatures of gas and particle phases.

The following reactions are considered during the reduction process:

$$Fe_3O_4 + H_2 = 3FeO + H_2O$$

Table 2 Governing equations for the particle phase

Mass	$\frac{\mathrm{d}m_p}{\mathrm{d}t} = -\dot{m}$
Momentum	$m_p \frac{\mathrm{d}u_p}{\mathrm{d}t} = -f_D$ $-f_D = \frac{1}{8}\pi d_p^2 \rho C_D \lvert U - U_p \rvert (U - U_p)$
Energy	$m_p C_p \frac{\mathrm{d}T_P}{\mathrm{d}t} = -q$ $\pi d_p \lambda N_\mu (T_g - T_p) + \sum \frac{\mathrm{d}m_p}{\mathrm{d}t} H_{\mathrm{reac}} + A_p \varepsilon_p \left(\pi I - \sigma_B T_p^4\right)$

$$\mathrm{FeO} + \mathrm{H_2} = \mathrm{Fe} + \mathrm{H_2O}$$

The heterogeneous surface reaction model is used. The expression of reaction rate is as follows [16–18]:

$$R = A_{\mathrm{ore}} \frac{\rho_g}{W} \sum_{m=4,6} a_{n,m} \left(K \frac{\omega_{\mathrm{H_2},g}}{M_{\mathrm{H_2}}} - \frac{\omega_{\mathrm{H_2O},g}}{M_{\mathrm{H_2O}}} \right)$$

where A_{ore} is the specific surface area of particles; ρ_g is the density of gas phase; K is the reaction equilibrium constant; $\omega_{\mathrm{H_2}}$ and $\omega_{\mathrm{H_2O}}$ are the mass fraction of $\mathrm{H_2}$ and $\mathrm{H_2O}$; W and $a_{n,m}$ are the resistance factors.

Results and Discussion

Effect of H_2 Concentration

Figure 2 shows the effect of $\mathrm{H_2}$ concentration on final metallization rate. The metallization rate increases greatly with increase of $\mathrm{H_2}$ concentration. When the $\mathrm{H_2}$ concentration is 30%, the metallization rate is only 21.49%. When the $\mathrm{H_2}$ concentration is 50%, the metallization rate is increased to 44.83% with an increase of 23.43%. The metallization rate reaches 88.95% at 100% $\mathrm{H_2}$ concentration and has an increase of 23.55% compared with that of 70% $\mathrm{H_2}$ concentration. This is because that the reaction rate is closely related with $\mathrm{H_2}$ concentration. The reaction rate will increase linearly with $\mathrm{H_2}$ concentration, while other conditions unchanged. However, the increase rate of metallization rate decreases with the increase of hydrogen concentration. When $\mathrm{H_2}$ concentration is from 30 to 50%, the average increasing rate of metallization rate is about 10.75% for every 10% increase in $\mathrm{H_2}$ concentration. However, the average increasing rate of metallization rate is only 7.85% for every 10% increase at 70–100% $\mathrm{H_2}$ concentration. The gas flow rate decreases with increase of $\mathrm{H_2}$ concentration, and the particles flow rate decreases accordingly. This is unfavorable for the dispersion of particles, and the reaction rate will be limited. Moreover, the $\mathrm{H_2O}$ concentration

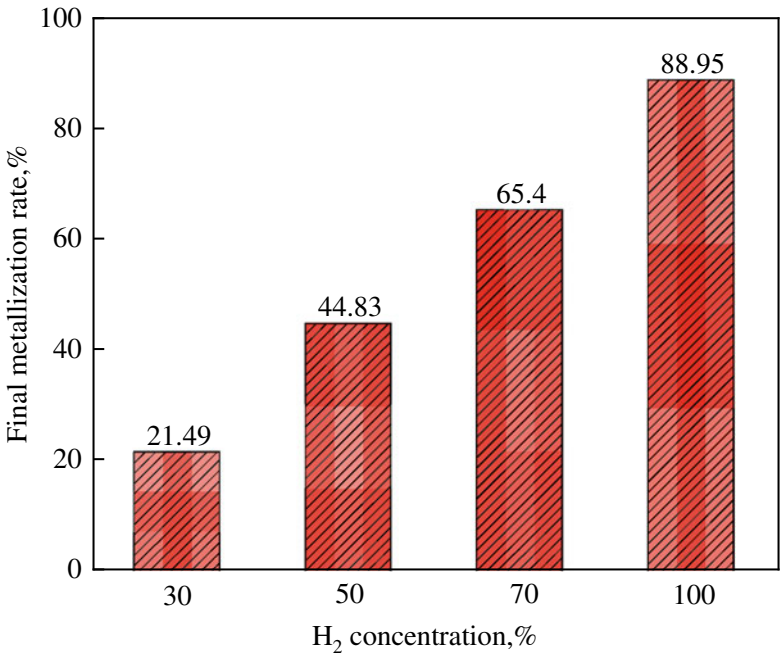

Fig. 2 Effect of H_2 concentration on final metallization rate

will increase more significantly during the reaction process, which is detrimental to the reaction rate.

To further under the effect of H_2 concentration on reaction characteristics of Fe_3O_4 particles' stream, the average metallization rate of different positions was analyzed, as shown in Fig. 3. The starting position of reduction is advanced with increase of H_2 concentration. When the H_2 concentration is 30%, some iron is reduced till the 0.4 m distance from the lance tip. Some iron is reduced at the 0.3 m distance, when the H_2 concentration is 50%. However, some iron is found only at the 0.1 m distance, when the H_2 concentration is 100%. This is because the reduction rate increases with increase of H_2 concentration. Furthermore, the flow velocity of particles decreases, which means that the particles will remain longer in the same distance. The entire reaction rate during the flow process obviously increases with increase of H_2 concentration. The reduction rate at 30, 50, and 70% H_2 concentration remains basically throughout the entire movement process. When H_2 concentration is 100%, the reaction rate first increases and then slows down. This is because the reaction rate at 30, 50, and 70% H_2 concentration is lower, and H_2 is relatively sufficient throughout the entire process. However, the reaction rate at 100% H_2 concentration is higher, and much H_2 is consumed. The reaction is limited at the end of the furnace due to the lack of H_2.

In order to further reveal the effect of H_2 concentration on reduction characteristics, the residence time of particles at different hydrogen concentrations was

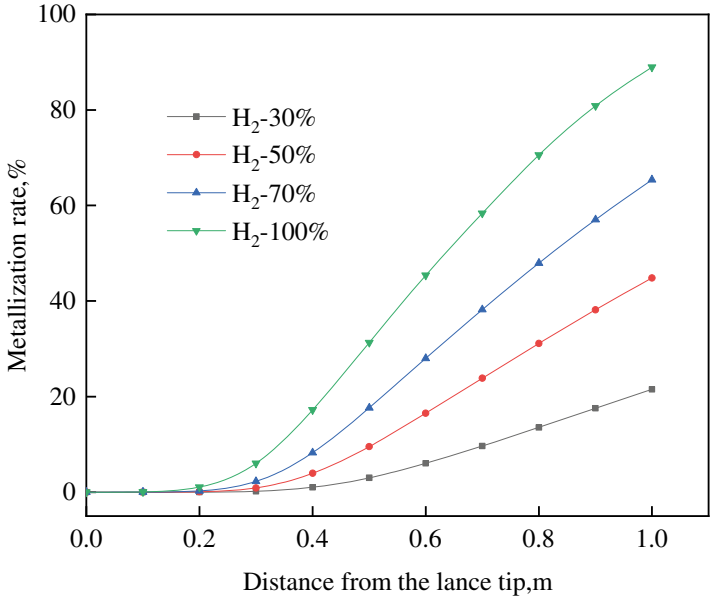

Fig. 3 Effect of H_2 concentration on metallization rate at different positions

analyzed, as shown in Fig. 4. As hydrogen concentration increases, the residence time of particles increases. When the hydrogen concentration is 30%, the average residence time of particles is 1.08 s. The residence time is 1.36 s as the H_2 concentration increases to 50%. When the hydrogen concentration is 100%, the residence time is 1.69 s, which is 1.56 times as many as that of 30% H_2 concentration. Base on theoretical calculation of unreacted shrinking core model, the reduction time of 50 μm Fe_3O_4 is approximately 2.07 s at 1273 K temperature and 30% H_2 concentration. It means that most particles fail to fully react due to insufficient reaction time. The theoretical reaction time at 100% H_2 concentration is about 0.84 s. It indicates that the residence times can satisfy full reaction of Fe_3O_4 particles. Therefore, it is vitally important to increase reaction times for the reactions, especially at the lower H_2 concentration.

To further understand the characteristics of particles stream, the flow and reduction characteristic at different H_2 concentration was analyzed, as shown in Fig. 5. As the concentration of hydrogen increases, the width of particle stream increases overall. The starting position of dispersion is advanced, and the particles are more dispersed. This is because the flow rate of particles increases as the concentration of H_2 decreases, and therefore, the particles will have less time to disperse. In addition, due to the increase in gas flow rate, it is more difficult for particles inside the stream to move outside. This is also a main reason for lower metallization rate. The particles' flow rate will decrease with increase of H_2 concentration and has more time to fully disperse. Furthermore, the particles around the stream have higher metallization rate. This is because most particles are concentrated in the internal area of the stream, and

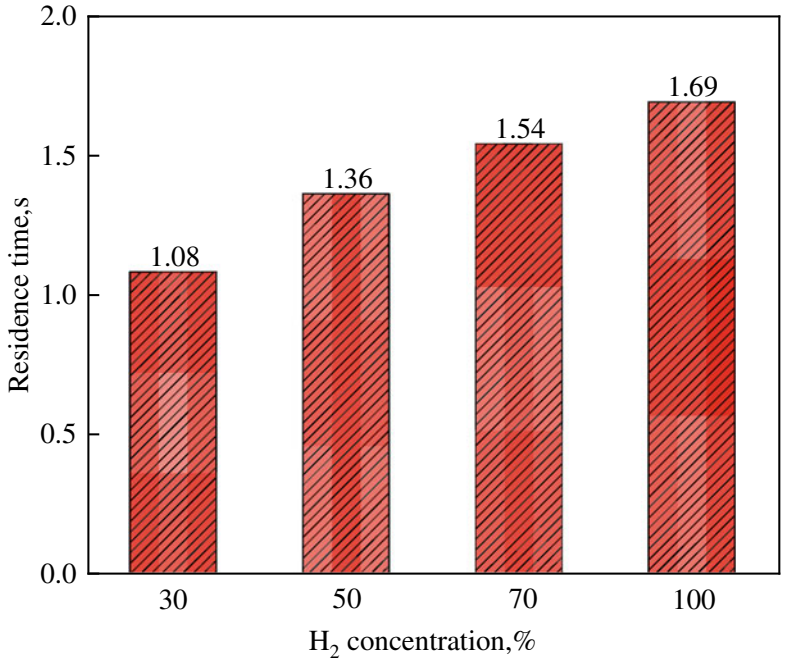

Fig. 4 Effect of H_2 concentration on residence time

the metallization rate is lower due to the lack of H_2. The particles' concentration around the stream is lower, and the H_2 is sufficient for reaction.

Effect of Reduction Temperature

In order to further explore the ideal conditions for Fe_3O_4 reduction, the effect of reaction temperature on the metallization rate was studied at a 100% H_2 concentration, as shown in Fig. 6. The metallization rate increases with increase of reduction temperature. When the temperature is 1073 K, the metallization rate is 45.11%; when the temperature is 1173 K, the metallization rate is 67.18%, an increase of 22.07%. The metallization rate at 1273 K increases to 88.95% and has an increase of 21.77% compared to that of 1173 K. The temperature has a significant impact on the metallization rate, as the chemical reaction rate is closely related with the temperature. In addition, as the reaction temperature increases, the diffusion rate of H_2 increases, which is beneficial for reduction. Moreover, as the temperature increases, the equilibrium constant of FeO reduction decreases, which is more conducive to the reaction. In the actual process, a high metallization rate can be achieved by maintaining the reaction temperature at around 1273 K.

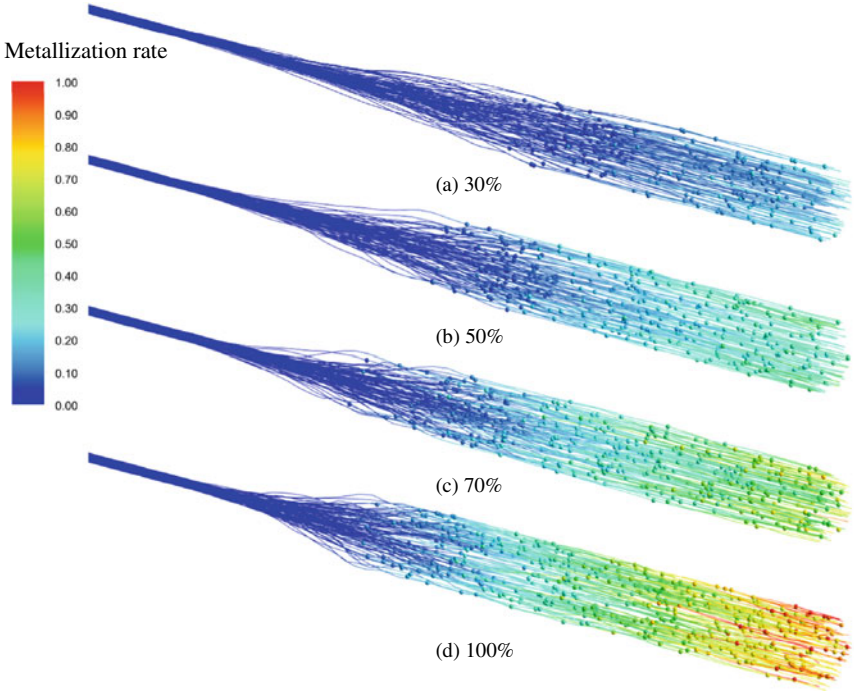

Fig. 5 Effect of H_2 concentration on flow and reduction characteristics of particles

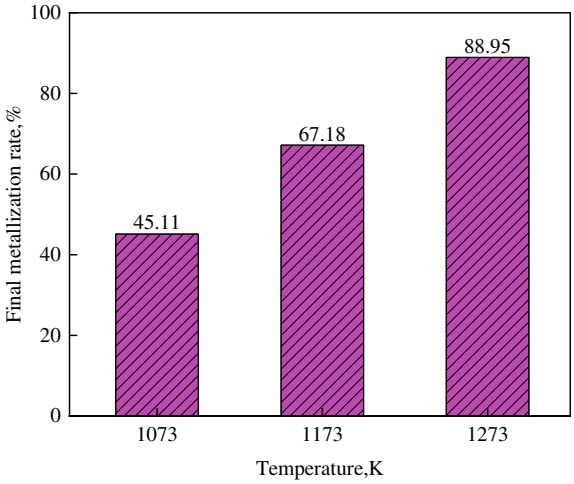

Fig. 6 Effect of reaction temperature on final metallization rate

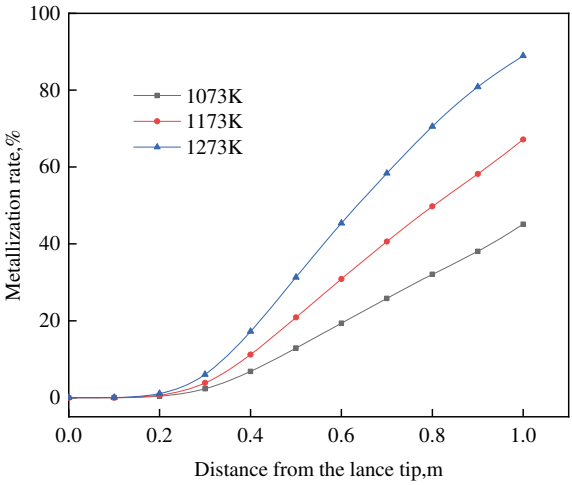

Fig. 7 Effect of reaction temperature on metallization at different positions

Furthermore, the metallization rate at different positions was investigated, as shown in Fig. 7. The starting point of reduction at different temperatures is basically the same, because the change in reaction temperature has a small impact on gas flow rate, and the residence time of particles in the furnace does not change much. As the reaction temperature increases, the reduction rate rapidly increases, and the difference in metallization rate at different temperatures also gradually increases. When the reaction temperature is 1073 and 1173 K, the overall growth rate of metallization rate remains unchanged. When the reaction temperature is 1273 K, the growth rate of metallization rate shows a slight trend of first increasing and then decreasing. This is mainly because when the reaction temperature is lower, the overall metallization rate is lower, and the reduction atmosphere during the entire process does not change much, and the particles can maintain a relatively stable reduction rate. When the reaction temperature is higher, the initial reaction rate is faster and a large amount of H_2 is consumed, while in the later stage of the reaction, the reduction rate decreases due to the lack of H_2.

Conclusions

In this study, the reduction characteristic of Fe_3O_4 particles in a drop tube furnace was investigated using the CFD method. The main conclusions are as follows:

(1) The Fe_3O_4 particles can be completely reduced by H_2 in seconds. H_2 is an ideal reducing agent for flash iron-making. The metallization rate can reach 88.95% at 100% H_2 concentration and 1273 K reaction temperature.

(2) As the reaction temperature increases, the metallization rate gradually increases, and the effect of reaction temperature on the metallization rate is more obvious. The metallization rate increases by 43.84%, when the reaction temperature increases from 1073 to 1273 K.
(3) Fe_3O_4 particles are more significantly affected by reaction temperature, and the relatively lower H_2 concentration and higher reaction temperature can be chosen in the actual process.

References

1. Suopajarvi H, Pongracz E, Fabritius T (2014) Bioreducer use in Finnish blast furnace ironmaking—analysis of CO_2 emission reduction potential and mitigation cost. Appl Energy 124:82–93
2. Wang H-t, Zhao W, Chu M-s, Feng C, Liu Z-g, Tang J (2017) Current status and development trends of innovative blast furnace ironmaking technologies aimed to environmental harmony and operation intellectualization. J Iron Steel Res Int 8(24):751–769
3. Kushnir D, Hansen T, Vogl V, Åhman M (2020) Adopting hydrogen direct reduction for the Swedish steel industry: a technological innovation system (TIS) study. J Clean Prod 242:118185
4. Yang Y, Shen Z, Wen X, Liu H (2022) Energy and emission analysis of flash ironmaking-powder generation coupling processes with various fuels. Appl Therm Eng 217:119280
5. Yang Y, Shen Z, Xu J, Liu H (2022) Numerical analysis of the dust control performance of a counter-current swirling configuration in the flash ironmaking reactor. ISIJ Int 11(62):2225–2235
6. Chen F, Mohassab Y, Zhang S, Sohn HY (2015) Kinetics of the reduction of hematite concentrate particles by carbon monoxide relevant to a novel flash ironmaking process. Metall Mater Trans B 46:1716–1728
7. Chen F, Mohassab Y, Jiang T, Sohn HY (2015) Hydrogen reduction kinetics of hematite concentrate particles relevant to a novel flash ironmaking process. Metall Mater Trans B 46:1133–1145
8. Wang X, Fu G, Li W, Zhu M (2019) Numerical simulation of effect of operating conditions on flash reduction behaviour of magnetite under H_2 atmosphere. Int J Hydrogen Energy 48(44):26261–26270
9. Wang H, Sohn H (2013) Hydrogen reduction kinetics of magnetite concentrate particles relevant to a novel flash ironmaking process. Metall Mater Trans B 44:133–145
10. Wang X, Fu G, Li W, Zhu M (2019) Numerical analysis of effect of water gas shift reaction on flash reduction behavior of hematite with syngas. ISIJ Int 12(59):2193–2204
11. Guo L, Bao Q, Gao J, Zhu Q, Guo Z (2020) A review on prevention of sticking during fluidized bed reduction of fine iron ore. ISIJ Int 1(60):1–17
12. Launder BE, Spalding DB (1972) Lectures in mathematical models of turbulence
13. Wu D, Zhou P, Yan H, Shi P, Zhou CQ (2019) Numerical investigation of the effects of size segregation on pulverized coal combustion in a blast furnace. Powder Technol 342:41–53
14. Zhou Z, Huo H, Wang G, Xue Q, She X, Wang J (2017) Effect of oxygen-coal lance configurations on coal combustion behavior. Steel Res Int 1(88):1600197
15. Shen Y, Shiozawa T, Austin P, Yu A (2014) Model study of the effect of bird's nest on transport phenomena in the raceway of an ironmaking blast furnace. Miner Eng 63:91–99
16. Austin PR, Nogami H, Yagi J-i (1997) A mathematical model for blast furnace reaction analysis based on the four fluid model. ISIJ Int 8(37):748–755

17. Cheng B, Xiong J, Li M, Feng Y, Hou W, Li H (2020) Numerical investigation into gas-particle inter-phase combustion and reduction in the flash ironmaking process. Metals 6(10):711
18. Yang Y, Li D, Guo L, Wang Z, Guo Z (2020) Numerical simulation of the gasification-reduction coupling process in the innovative multi-generation system. Appl Therm Eng 168:114899

Use of Over-Stoichiometric Flame for Post-Combustion, Burning VOC and Solid Fuel, Improving Its Efficiency, and Reducing the Carbon Footprint in Regular Process of Lead Recovery in Rotary Furnaces

B. Ferreira, J. von Scheele, E. Isihara, E. Breciani, and A. Dupond

Abstract The lead recovery process for automotive batteries is known to be not only a smelting process but also a chemical recovery process, including several reactions to have it done as pure metal (Pb). The traditional technology route includes shredded batteries, iron chips, and coal to reduce lead oxides into metallic lead. Although the market understands it as a usual process of direct reduction, therefore aiming reductant atmospheres and under-stoichiometric flames, SK Metais, through gas analyses, mass balances, and evaluation of the entire production stream, understood its process, chemical needs, and reactions, changing the standard process to become one of the most efficient facilities toward low emissions, and at meantime improving their throughputs.

Keywords Pyrometallurgy · Recycling · Sustainability · Lead · Recovery · Automotive · Batteries

B. Ferreira (✉)
Linde Technology, 175 East Park Drive, Tonawanda, NY 14150, USA
e-mail: brenno.ferreira@linde.com

J. von Scheele
Linde Technology, Carl-von-Linde-Strasse 25, 85716 Unterschleissheim, Germany
e-mail: Joachim.von.scheele@linde.com

E. Isihara
White Martins Gases Industriais (Linde plc), Diadema, SP 09961-350, Brazil
e-mail: edson.isihara@linde.com

E. Breciani · A. Dupond
SK Metais, Modelo, SC 89872-000, Brazil
e-mail: gerencia@skmetais.com

© The Minerals, Metals & Materials Society 2024

C. Iloeje et al. (eds.), *Energy Technology 2024*, The Minerals,
Metals & Materials Series, https://doi.org/10.1007/978-3-031-50244-6_17

Introduction

Used lead-acid batteries, also known as used automotive batteries, are considered primary sources of lead for secondary lead recovery plants, making them a vital material for the economy's circulation. Each automotive battery is composed of lead grids and lead oxide paste to form the cells, with polymeric involucres used to insulate the cells, sulfuric acid employed as an electrolyte, and a plastic box (Fig. 1). Each kilogram (kg) of automotive battery can yield up to 50% in mass of lead bullion, although only 30–45% of it is metallic lead (Pb). Other common lead carriers include lead oxide I (PbO), lead oxide II or lead dioxide (PbO_2), lead sulfate ($PbSO_4$), and lead paste slurries [1].

The primary process aiming to recover the lead content from scrap (shredded used batteries) is the pyrometallurgical process using short rotary smelters [1, 3]. Even though lead melts at 327 °C, therefore having a low energy requirement, that process occurs around 1.200 °C. Solid carbon, as charcoal or coke, is added as a reducing agent, and iron chips to promote the desulfuration and a flux agent (soda ash) to support slag formation and sulfur capture are loaded to complete all reactions to yield metallic lead at the end of the smelting process. The main reactions toward reducing the Pb oxides and sulfides are described in Eqs. 1–12 [1]:

$$Na_2CO_3 \rightarrow Na_2O + CO_2 \tag{1}$$

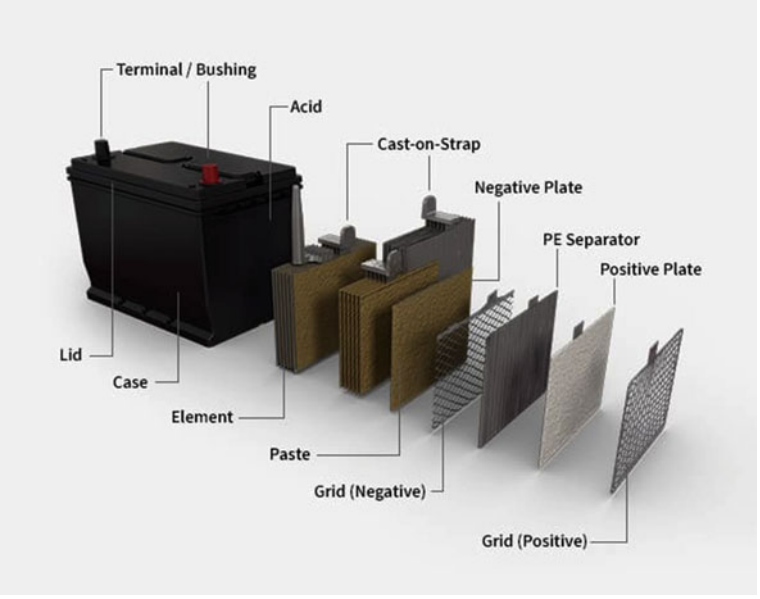

Fig. 1 Anatomy of an automotive battery [2]

$$PbSO_4 \rightarrow Pb + SO_2 + O_2 \quad (2)$$

$$PbSO_4 + 2C \rightarrow PbS + 2CO_2 \quad (3)$$

$$2PbO + C \rightarrow 2Pb + CO_2 \quad (4)$$

$$PbO_2 + C \rightarrow Pb + CO_2 \quad (5)$$

$$PbS + Na_2O + C \rightarrow Pb + Na_2S + CO \quad (6)$$

$$PbS + FeO + C \rightarrow Pb + FeS + CO \quad (7)$$

$$PbS + Fe \rightarrow Pb + FeS \quad (8)$$

$$PbS + 2PbO \rightarrow 3Pb + SO_2 \quad (9)$$

$$PbS + PbO_2 \rightarrow 2Pb + SO_2 \quad (10)$$

$$PbS + O_2 \rightarrow Pb + SO_2 \quad (11)$$

$$Fe + {}^1/_2O_2 \rightarrow FeO \quad (12)$$

Almost all those reactions are endothermic and need minimum energy to start at room temperature. The primary energy source is a burner running usually with liquid or gas fuel and air or pure oxygen as comburent (oxidant). The combustion energy required for a typical lead-acid battery recovery is 500–1000 kWh/ton Pb depending on the burner technology, furnace lining, scrubbers, filters for flue gas, and process operations. Considering propane and liquefied petrol gas (LPG) as fuel, it means about 220 kg of CO_2 per MWh (kg CO_2/MWh), and at the end, only combustion emissions of 100–220 kg of CO_2 per ton of PB bullion (kg CO_2/ton Pb); therefore, efforts to reduce energy consumptions mean a straight-forwardly reduction in CO_2 emissions.

SK Metais

The SK Metais company is located in the western region of Santa Catarina state, Brazil (Fig. 2), funded in 1998 to supply batteries internal components, improving its facilities and production since then. It commits to the environment and local society. The company raised its production, reaching more than 15 thousand metric tons (kton) of lead production yearly using continuous investments and new machinery, equipment, technologies, and training. It is the most efficient lead company in Brazil.

SK has a reverse logistic to remove used batteries and lead scrap from the market and return it as lead alloys in ingots and manufactured lead products as metallic grids and battery poles.

SK Metais Process

SK Metais has its own engineering team developing new process equipment and designing its facilities layout toward a more efficient process and state-of-the-art technology. Recovering batteries starts with logistics and selection, going to a well-developed shredded machine that separates plastic, acid, and high-density lead materials. Plastic and sulfur acid are recovered as by-products and distributed to other industries; meanwhile, the shredded battery goes to the smelter to be recovered. The mechanical design to the smelter is shown in Fig. 3.

SK has different stalls for shredded materials, coal sizes, and iron chips. After being shredded and segregated, the lead-bearing material goes to a specific stall

Fig. 2 SK Metais facilities in Modelo, SC, Brazil [4]

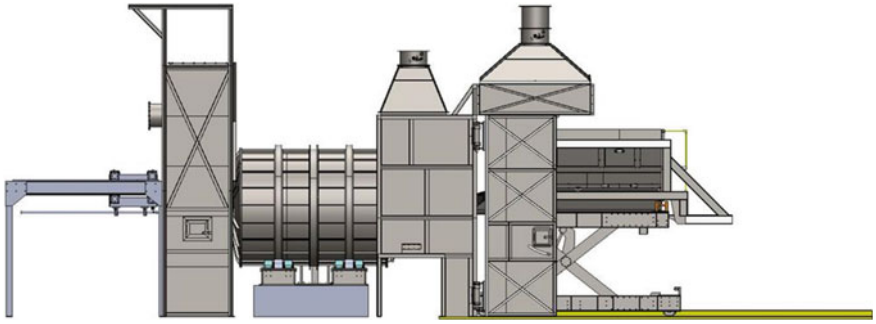

Fig. 3 SK Metais pyrometallurgical equipment design: loader, rotary furnace, post-combustion chamber, burner, and hoods

where each batch will be prepared adding specific amounts of scrap, coal, and iron chips. SK developed a process to use any flux agents.

A heavy-loader machine transports the material and loads it into an automatic loader, equipped with a built-in scale, that loads the rotary furnace by its front door. The furnace has a touch-screen panel where the operator will command the load step. In the meantime, production assistants open the front door and follow the process in case of manual operations requirements. All hoods are set to draft small particles, smoke, and gas during the entire process. This time usually is set in 15 min, and mass fed around 10 tons of lead scrap.

The scale shows the actual mass loaded, and after that, the operator closes the furnace door and automatically sets to start the first smelting, automatically setting the exhaustion system to increase the fan rotation speed, therefore drafting a large mass of particles during the first rotations while the material is not entirely settled to the furnace. In the clock, the pilot burner ignites, sending a flame signal through the flame sensor, and the main burner is allowed to start, still out of the furnace chamber. Once it releases LPG and pure oxygen, together with the pilot flame, the main burner has the flame ignited and monitored by a second back mounted ultra-violet (UV) flame sensor that keeps monitoring the flame through the 3.5 m long oxygen pipe inside the burner. The combustion energy heats the furnace to start the metallic lead melting and have the temperature rising. The time frame for this step is 50 min.

When reaching the specified time, new additions of coal and iron chips are made to start the chemical reactions to recover the lead from the lead oxides and sulfides, completing 12 tons fed into the furnace. That keeps raising its temperature with an oxygen-LPG burner running 800 kW and over-stoichiometric ratio defined by the fuel, CO, and volatile organic compounds' (VOCs) rates (usually Lambda = 1.8). The furnace includes an attached post-combustion chamber designed to settle heavy particles before it goes carried by the flue gas downstream to a vortex and the filter system. Once the burner is mounted outside and inserted through the flue gas ends, it means a double-pass furnace, where the flue gas goes oppositely to the visible flame, aspirating hot gases inside the furnace and exchanging heat with the cold gases near

the flame root, promoting better combustion. The step duration is 150 min, enough residence time to promote all reduction reactions and smelt the lead content.

The next step is to open the tap-hole manually and tap all 7.0–7.7 tons of lead followed by slag in a ladle car. It lasts 10 min and an additional 15 min to remove the solid slag over the molten lead and set the furnace for the next batch, completing an entire process with a TAP-to-TAP time of 240 min.

Combustion Technology

Back to the beginning of SK operation, the main burner system was a typical burner operating with Heavy Fuel Oil (HFO) and blast air. Improvements were made, replacing that with a new LPG and combustion air, including measurement and temperature control. In 2015, SK started to enrich its combustion air using pure oxygen to change the O_2 balance from 20.9% up to 30%. The benefits reached were the reduction of batch time and improvement of the overall production.

In 2016, SK decided to invest, hiring the White Martins company (Linde group), the oxygen supplier, to design a new burner for fuel savings and process improvements. In January 2017, the system was deployed using a customized water-cooled burner, built as a pipe-in-pipe with LPG pipe, including a replaceable nozzle, O_2 pipe, and water jacket (Fig. 4).

The flow control train follows international safety standards, including flow control valves, orifice plate, and pressure transmitter to control the flow rate, block valves, leakage self-test, individual temperature, and pressure transmitter to compensate for the flow rate and all sorts of gauges, control and safety equipment, as well a built-in electrical panel with operation knobs and touch-screen interface. Improvements were made afterward, including the second flame sensor and the external pilot burner with electrical ignition.

The new system was designed to operate with 4.5 MW, foreseeing to heat a furnace with a capacity as big as 40 tons of scrap (10 m^3) and aiming to achieve a monthly

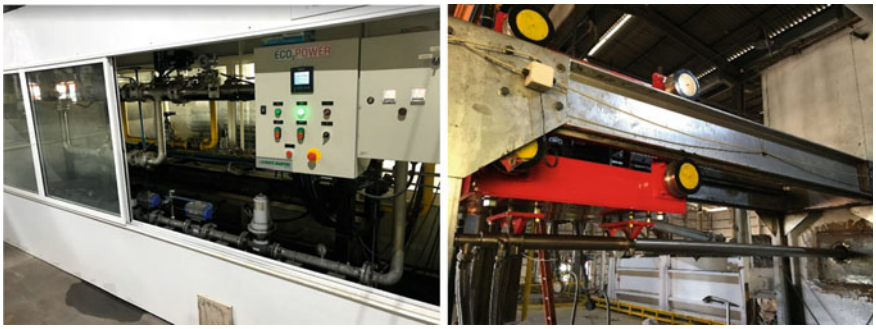

Fig. 4 White Martins (Linde group) combustion system customized to SK Metais

production of 1.500 tons of lead. At that moment, SK had a furnace with a body for 10 tons of scrap (2 m^3).

Quickly the system reached good performance indicators, reducing the batch-to-batch time from 8 to 6 h. Meanwhile, the specific fuel consumption decreased to 600 kWh/t Pb (previously oxygen enriched was 960 kWh/t Pb), performing 37.5% of fuel reduction and 35% in production boost.

Process Analyses

Back in the startup time in early 2016, some improvements were made to leverage better results with the new combustion system, including new scrubbers and sleeve filters system and new lining closing the gas ends from 800 to 600 mm once the total flue gas volume was reduced from 1.500 to 350 Nm^3/h (more than 75% of reduction in the flue gas flow rate).

The actual result was a better process, reducing the TAP-to-TAP time from 6 to 5 h even more, but some issues happened with a high-intensity flame outside the furnace. In a partnership with the White Martins teams (Linde group), the oxygen and combustion technology supplier, changes on the flame profile aiming to change the flame momentum were realized. Despite those flames showing outside the furnace and flowing through the post-combustion chamber, inside, the flame was not large enough to reflect on the front door and go to the flue gas ends.

A visible flame outside means enough fuel, comburent, temperature, and mix. Even though the lead recovery process requires a reductant atmosphere, it does not mean the burner needs to be under-stoichiometric to provide the reductant atmosphere. All plastic and Sulphur contents, VOCs, and carbon fed to the furnace are enough to create a reductant zone inside the furnace. In addition to burners running under-stoichiometric (Lambda = 0.9), additional CO is yielded to the furnace's inside atmosphere.

A manual tune had been set to supply more oxygen to burn all remaining fuel inside the furnace, and straightforwardly, the visible flame disappeared, meaning that all CO, S, and VOCs were burning inside. The same tune has been set throughout the subsequent batches to confirm the lack of oxygen and remaining fuel flowing outside the furnace. The empirical test brought an outstanding performance, reducing the batch time to less than 4 h with no additional changes.

The White Martins team decided to perform a gas analysis for one week (30 batches) to check the flue gas and confirm the empirical assumptions. The SK Metais provided a sample point behind the furnace (post-combustion) with a 2-m stainless steel probe to get samples inside the furnace neck before it reacts with the drawn air. At the most draft point, a second sample point was provided downstream on the post-combustion chamber connection to the exhaustion system as shown in Fig. 5.

White Martins used a Siemens ULTRAMAT 23 analyzer rack with sample pump, particle filter, and moisture filter using Silica Gel as moisture absorber to analyze the gas. The analyzer was able to get CO_2 concentrations in a range of 0–65%, CO:

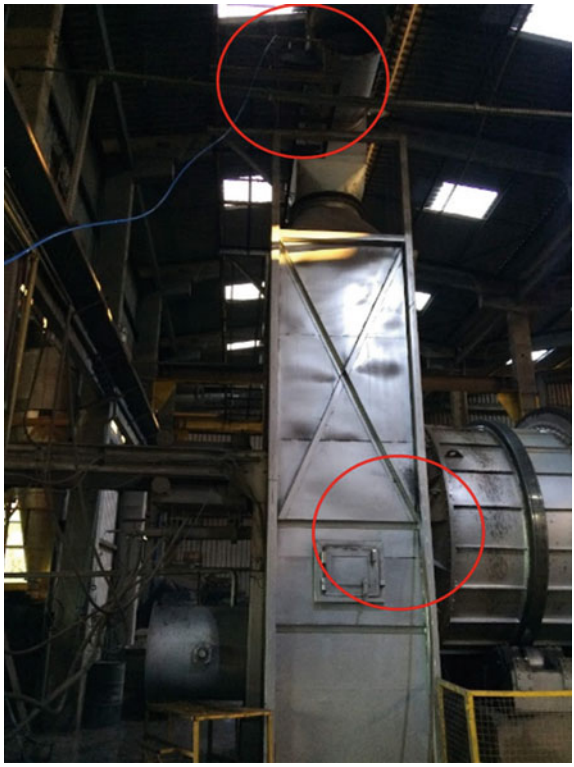

Fig. 5 Sample points where the gas analyses were performed

0–2.500 ppm, and O_2: 0–25%. Additional Siemens Analyzer, also ULTRAMAT 23 model tuned to get high CO, low CO_2, and CH_4, was installed in series to get high volumes of CO in ranges of CO: 0–40%, CO_2: 0–2.6%, and CH_4: 0–4.5%. A bias was performed every 60 min with fresh air: O_2: 20.9%, CO_2, CO, and CH_4: 0 (Fig. 6).

Different tests were made using over-stoichiometric and under-stoichiometric ratios in the burner set. The feed rate remained the same, and the reductant agent (charcoal) was in a ratio of 50 kg/ton of lead scrap. As an example, the following chart in Fig. 7 shows the results from gas analyses in two different batches.

It was technically confirmed that a large amount of CO was flowing downstream the furnace and burning inside the post-combustion chamber. Volumes as high as 28% with peaks of 40% of CO were obtained during the gas analyses running with stoichiometric flame (5 Nm^3 O_2: 1 Nm^3 of GLP, or 2.45 Nm^3 O_2: 1 kg LPG). The exhaustion fan draft was under the same pressure for both cases.

It is also possible to see the blue columns representing the CO, mainly during the beginning of the batch, with peaks after the coal charge, decreasing at the end of the process during the slag tap. It shows that there is a lot of CO yield by coal as it burns and reacts with lead (Pb) oxides. CH_4 shows a short peak during the beginning of the process, related to high plastic and VOCs during the shredded scrap load. O_2 is almost nil due to a high presence of CO and, therefore, a complete combustion reaction, yielding CO_2. Minor changes are due to slight infiltration and air dilution.

Fig. 6 Gas analyzer and combustion system's electrical panel

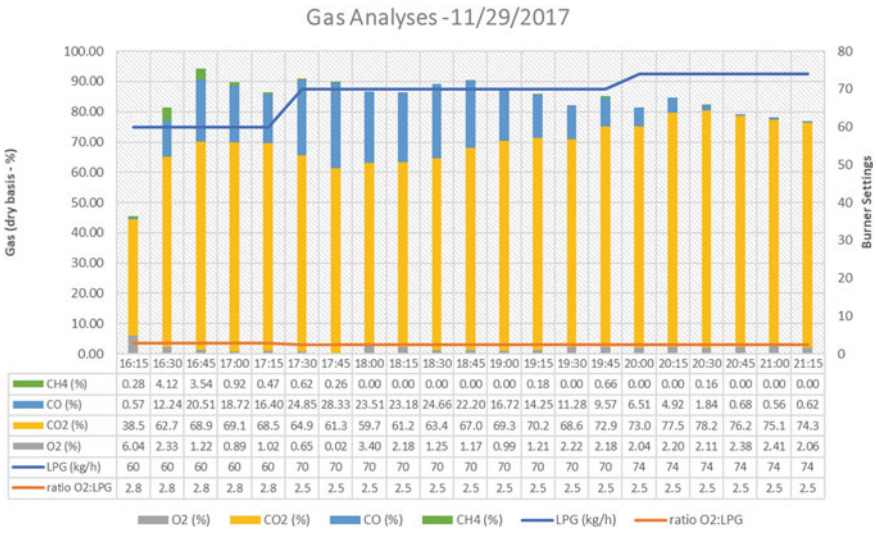

	16:15	16:30	16:45	17:00	17:15	17:30	17:45	18:00	18:15	18:30	18:45	19:00	19:15	19:30	19:45	20:00	20:15	20:30	20:45	21:00	21:15
CH4 (%)	0.28	4.12	3.54	0.92	0.47	0.62	0.26	0.00	0.00	0.00	0.00	0.00	0.18	0.00	0.66	0.00	0.00	0.16	0.00	0.00	0.00
CO (%)	0.57	12.24	20.51	18.72	16.40	24.85	28.33	23.51	23.18	24.66	22.20	16.72	14.25	11.28	9.57	6.51	4.92	1.84	0.68	0.56	0.62
CO2 (%)	38.5	62.7	68.9	69.1	68.5	64.9	61.3	59.7	61.2	63.4	67.0	69.3	70.2	68.6	72.9	73.0	77.5	78.2	76.2	75.1	74.3
O2 (%)	6.04	2.33	1.22	0.89	1.02	0.65	0.02	3.40	2.18	1.25	1.17	0.99	1.21	2.22	2.18	2.04	2.20	2.11	2.38	2.41	2.06
LPG (kg/h)	60	60	60	60	60	70	70	70	70	70	70	70	70	70	70	74	74	74	74	74	74
ratio O2:LPG	2.8	2.8	2.8	2.8	2.8	2.5	2.5	2.5	2.5	2.5	2.5	2.5	2.5	2.5	2.5	2.5	2.5	2.5	2.5	2.5	2.5

Fig. 7 Analyses showing the CO, CO_2, O_2, and CH_4 volumes throughout a batch on November 29, 2017, using stoichiometric ratio O_2:fuel

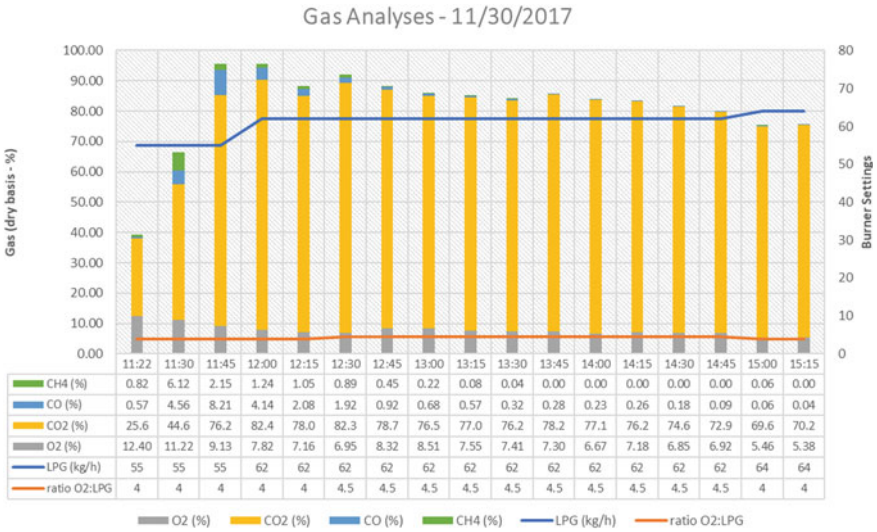

Fig. 8 Analyses showing the CO, CO_2, O_2, and CH_4 volumes throughout a batch on November 30 2017, using over-stoichiometric ratio O_2:fuel

Despite all practical tests followed by gas analyzers, the CO amount could not reach 0%, using oxygen excess of at most 8%. On the other hand, the system was tuned to run with a low oxygen excess (0–1%). In the meantime, the CO at the flue gas ends in a range of 30–4000 ppm (peaks of 8%), being burned downstream by the leakage air (Fig. 8).

For the over-stoichiometric example, it is possible to see lower amounts of CO (blue column), as mentioned above, and a higher and steady oxygen excess volume (grey column) to provide enough reaction with CO yield CO_2. There is room for improvement, depending on lance techniques to leverage more mix reacting O_2 to CO flowing downstream in a short time frame and chamber space. Small peaks of CH_4 (green column) happen at the beginning of the batch, upon the furnace load, related to residual plastics and VOCs.

SK Metais redefined all process parameters (recipes), working with a 4 to 4.5 Nm^3 O_2 ratio for each 1 kg of LPG, which means a Lambda of 1.6–1.8. The process parameters have been changing slightly around the original sets defined during the practical tests in 2016.

In 2018, a new test to confirm the results showed equivalent results from SK Metais, keeping the same parameters. Back in those days, SK Metais improved the scrap recovery system, changed the furnace body from 10 to 12 tons of Scrap (April 2018), reduced the diameter/length ratio, and increased the lead surface to take advantage of high radiation heat transfer inside the furnace. The key performance indicators are steady throughout seven years after analyses with an average of 4 h per batch (TAP-to-TAP time), 300 kWh/ton of Pb bullion, Lambda 1.8, and O_2 consumption of 100 Nm^3/ton of Pb bullion.

In 2019, SK Metais decided to invest in a new technology to tune the burner automatically, regarding the CO and VOCs' volumes remaining from the chamber reaction. White Martins (Linde) supported this application, supplying the lead OPTIVIEW™, which has been under evaluation since then.

Conclusions

The process of recovering lead from used automotive lead-acid batteries typically involves pyrometallurgical techniques. However, it is imperative that we establish a circular economy for these batteries, as it presents a sustainable solution for obtaining pure lead from scrap while minimizing the environmental impact of primary processes and reducing reliance on non-renewable resources like lead ores. With the world's automotive fleet continuing to grow and drive demand for automotive batteries and lead, this approach is more critical than ever.

Pyrometallurgical plants emit greenhouse gases, with a carbon footprint ranging from 100 to 220 kg CO_2 per 1000 kg of lead bullion produced through combustion. Nevertheless, initiatives are underway worldwide to lower these figures, and proper methods of landfilling and utilizing plastic and sulfuric acid as by-products are being adopted. Additionally, SK Metais has devised a process that uses minimal amounts of fuel and oxygen, resulting in reduced CO_2 emissions.

Based on empirical tests and gas analyses, it has been proven that the atmosphere inside the lead furnace has a high reducing potential, primarily due to the carbon content fed into the furnace as a reductant agent, along with VOCs and Sulphur from the scrap of shredded batteries. SK Metais has been able to leverage these remaining fuels and achieve better results by using customized oxy-fuel burners and over-stoichiometric flames. As a result, they have been able to achieve one of the lowest specific consumptions in the market, consuming only 300 kWh per ton of Pb bullion, while producing crude lead with equivalent CO_2 emissions of just 66 kg CO_2.

New technologies have been continuously tested in SK Metais, aiming for additional improvements and repeatability of process parameters and performance.

References

1. Santin BO Thesis (D.Sc.) (2013) Estudo de reacoes solido/liquido e solido/gas em altas temperaturas: o caso das reacoes do $PbSO_4$ e PbO no processo pirometalurgico de reciclagem de Pb a partir de baterias chumbo-acido. Universidade Federal de Sao Carlos—UFSCar
2. Clarios (2023). Homepage: https://www.autobatteries.com/how-batteries-work/anatomy-of-car
3. Lopes PP, Stamenkovic VR (2020) Past, present, and future of Lead-acid batteries. Science 369:923
4. SK Metais (2023). Digital Folder and Homepage: https://skacumuladores.com.br/site/empresa

Part V
Poster Session

A Multi-objective Scheduling Model for a Gas-Steam-Electricity Coupling System in the Steelwork Based on Time-of-Use Electricity Pricing

Weijian Tian, Haifei An, Xiancong Zhao, and Hao Bai

Abstract By-product gas, steam, and electricity coupling system plays an important role in providing stable energy supply for steelworks. In this paper, a multi-period GSECS scheduling model with the objectives of economics and in-plant grid reliability was constructed. Economics is reflected in the reduction of gasholder penalty cost, electricity interaction cost, and carbon emission cost while the reliability is shown as the variance of the electric load. In GPC, a new method of defining gasholder penalty factor was designed to distinguish different types and operating intervals of gasholders. The NSGA-II was used to obtain the multi-objective Pareto solution set, and the optimal solution was filtered based on the improved AHP—entropy weight method. With a calculated example, compared to manual operations, the gasholder penalty cost was reduced by − 51.37% after optimization, as well as a reduction of 25.23% in the deviation of the gasholder, enhancing its stability. In addition, the variance of the in-plant grid was improved by 45.15%.

Keywords Steel production process · Multi-energy coupling system · On-site power plants · Time-of-use electricity pricing · NSGA-II

Introduction

By-product gases, steam, and electricity are crucial secondary energy sources in the typical steel producing process, accounting for 50–60% of the total energy consumption of iron and steel plants (ISPs) [1]. The production and consumption of by-product gas often fluctuate due to changes in production process conditions or production abnormalities. By-product gas systems typically employ various types of gasholders

W. Tian · H. An · X. Zhao · H. Bai (✉)
State Key Laboratory of Advanced Metallurgy, University of Science and Technology Beijing, 30# Xueyuan Road, Beijing 100083, China
e-mail: baihao@metall.ustb.edu.cn

School of Metallurgical and Ecological Engineering, University of Science and Technology Beijing, 30# Xueyuan Road, Beijing 100083, China

© The Minerals, Metals & Materials Society 2024

C. Iloeje et al. (eds.), *Energy Technology 2024*, The Minerals, Metals & Materials Series, https://doi.org/10.1007/978-3-031-50244-6_18

and the on-site power plant (OPP) to maintain a balanced regulation of by-product gas. A gasholder serves as a storage device for by-product gases, mitigating to some extent the imbalance between gas production and consumption, thereby ensuring stable operation of the gas system. OPP is one of the important gas consumers which can produce steam and electricity from the gases in the gasholders, to keep balance of the gas system, fully utilize the surplus by-product gases, and reduce the high purchasing cost of external energy sources. The OPP establishes a mutually dependent and supportive relationship among by-product gases, steam, and electricity, forming a tightly coupled system. The stability of the by-product gas, steam, and electricity coupling system (GSECS) is crucial for the steel production. To ensure stable gas supply during the production processes, the gasholder level often experiences significant fluctuations, resulting in increased operational costs. Moreover, considering the application of time-of-use (TOU) electricity tariff, the electricity generation units in OPP have advantages to effectively reduce the cost of purchasing electricity through strong peak load regulation capabilities [2]. However, ensuring the stable operation of the power grid in ISPs remains a primary concern for the electric power system. Peak load regulation through OPPs can lead to frequent fluctuations in peak and off-peak periods, which is unfavorable for grid stability. Consequently, achieving the optimized allocation of by-product gas, steam, and electricity in GSECS necessitates the development of a comprehensive and rational scheduling model to enhance energy efficiency and reduce production costs.

Previous studies on the scheduling model of the GSECS differs in terms of objective function, constraint conditions, optimization scope, and algorithms. Furthermore, most studies primarily focus on optimizing economic objectives or converting other objectives into costs through penalties or rewards. Zeng et al. [3] established a short-term dispatch model of GSECS considering TOU tariff with the objective of minimizing fuel cost, equipment maintenance cost, and electricity purchasing cost and obtained the optimal operation scheme of waste heat boiler, turbine, and other devices in each time period. Hu et al. [4] introduced the relationship between thermal efficiency and operating load in the boiler and optimized the load setting and start-stop state of the energy conversion equipment in different periods within the GSECS to achieve a reasonable distribution of surplus gas among the gasholder and the OPP. Wei et al. [5] established the GSECS model based on the operating characteristic curves of boilers and steam turbines and determined the penalty factors for the other two types of gasholders based on the capacity of blast furnace gasholders, and the results showed that both electricity trading prices and coal purchase prices would affect the power generation in the OPP.

Electrical reliability is vital to steel production, as a substantial amount of electrical equipment is employed throughout the process. Considering the important role of the gasholders in maintaining the stability of energy systems, higher requirements for the reasonable distribution of gases in the gasholders should be put forward. In the steel industry, it is imperative to propose a novel model to ensure the electrical reliability of the power system. Lu et al. [6] considered the scenario of electric vehicle random connection in a microgrid, taking into account three different

scheduling objectives: operational cost, pollutant treatment cost, and load variation. These objectives were combined into a single objective using cost weighting. However, the significance of electrical reliability is often disregarded in the realm of energy management within the steel industry.

Previous studies have lacked clarity on the energy management aspects of GSECS in ISPs, as it overlooks electrical reliability while considering the stability of gasholders. This paper proposes an energy management strategy for GSECS that takes into account factors such as grid interaction and gas refilling/discharging, with the optimization objectives of both economic and reliability aspects. Subsequently, a quantitative analysis is conducted on the multi-criteria optimal solution to provide decision-makers with reference options.

Model

This section presents a scheduling model established for the GSECS of a specific ISP. The ISP possesses seven gasholders, including two blast furnace gasholders, three converter gasholders, and two coke oven gasholders. Moreover, an OPP, consisting of two CCPP (Gas-Steam Combined Cycle Power Plant) units and one CHP (combined heat and power generation) unit, utilizes the by-product gas from the gasholders to provide steam and electricity for steel production. Based on pressure and temperature, the steam is classified into three grades. The simplified CHP model generates S1-grade steam by consuming by-product gas. After undergoing pressure reduction and temperature adjustment, the S1-grade steam is transformed into S2-grade and S3-grade steam for use in production processes, while the remaining thermal load is utilized for electricity generation. The GSECS is able to interact with the external power grid to obtain electricity in case of insufficient supply, and surplus gas can be stored in gasholders and discharged through the combustion tower when the gas volume reaches the maximum capacity of the gasholder. The 24-h operating data of the ISP was selected as the optimization period and was divided into 96 periods. Tables 1 and 2 represent the parameters of gas and steam, respectively. Figure 1a, b represent the surplus gas supply and production energy requirements, respectively.

Table 1 Relevant parameters of by-product gas

Gas	Price (yuan/m^3)	Calorific value (kJ/m^3)	Carbon emission factor (kg/m^3)
BFG	0.213	3200	0.439
LDG	0.553	8300	0.581
COG	1.168	17,520	1.118

Table 2 Enthalpy of steam

Steam type	S1	S2	S3
Enthalpy (kJ/kg)	3475	2920	2796
Temperature (°C)	435	240	170
Pressure (MPa)	3.5	1	0.4

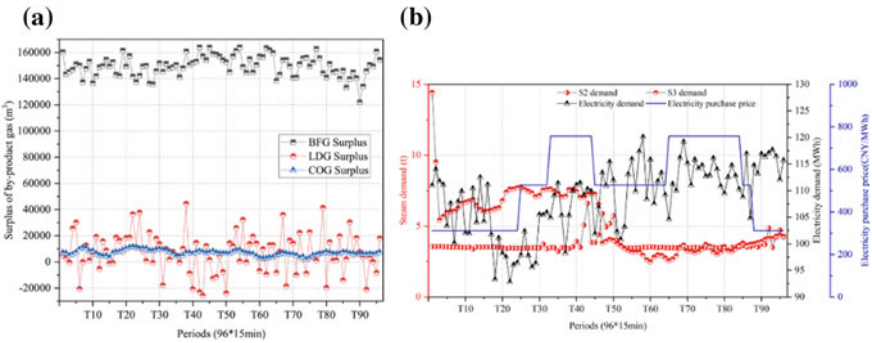

Fig. 1 By-product gas surplus, production energy demand, and electricity prices of the case ISP

Penalty Factors of Gasholders

When the by-product gas exceeds the maximum capacity (HH) in the gasholder, it will be released, resulting in economic losses and environmental pollution. Conversely, if the gas quantity falls below the minimum capacity (LL), it would lead to severe mechanical accidents. The gasholder level should ideally vary within the range of HH and LL, which is referred to as the controllable range (CR), as shown in Eq. (1). Furthermore, reference levels (R) are established to evaluate the stability of the gasholders, aiming to minimize fluctuations around these reference levels. Additionally, there are two intermediate levels set around the reference level, namely the high level (H) and low level (L). The region between these two levels is defined as the safety range, and it is preferable to maintain the gasholder level within this range. Table 3 shows the range of the gasholder.

$$\mathrm{CR}_{g,i} = V_{g,i}^{HH} - V_{g,i}^{LL} \tag{1}$$

where $\mathrm{CR}_{g,i}$ is the controllable space of the i-th g gasholder, m^3, g including BFG, COG, and LDG. $V_{g,i}^{HH}$ and B, respectively, represent the level of the i-th g gasholder; $V_{g,i}^{HH}$ and $V_{g,i}^{LL}$ represent the HH and LL, respectively, of the i-th g gasholder.

This article has proposed a new penalty factor formulation, which is composed of controllable range, by-product gas price, and by-product gas calorific value. The factor can reflect the type and size of the gasholder:

Table 3 Range of gasholders in the case ISP

Volume (m^3)	V_{LL}	V_L	V_R	V_H	V_{HH}	CR
BFG1#	30,000	97,500	151,500	205,500	300,000	270,000
BFG2#	20,000	65,000	101,000	137,000	200,000	180,000
LDG1#	8000	26,000	40,400	54,800	80,000	72,000
LDG2#	8000	26,000	40,400	54,800	80,000	72,000
LDG3#	15,000	48,750	75,750	102,750	150,000	135,000
COG1#	15,000	48,750	75,750	102,750	150,000	135,000
COG2#	15,000	48,750	75,750	102,750	150,000	135,000

$$w_{HH-H}^{g,i} = P_g \cdot \frac{\left(V_{g,i}^{HH} - V_{g,i}^{H}\right) \cdot \mathrm{Ca}_g}{\sum_i \sum_g^3 \mathrm{CR}_{g,i} \cdot \mathrm{Ca}_g} \tag{2}$$

$$w_{H-N}^{g,i} = P_g \cdot \frac{\left(V_{g,i}^{H} - V_{g,i}^{N}\right) \cdot \mathrm{Ca}_g}{\sum_i \sum_g^3 \mathrm{CR}_{g,i} \cdot \mathrm{Ca}_g} \tag{3}$$

$$w_{N-L}^{g,i} = P_g \cdot \frac{\left(V_{g,i}^{N} - V_{g,i}^{L}\right) \cdot \mathrm{Ca}_g}{\sum_i \sum_g^3 \mathrm{CR}_{g,i} \cdot \mathrm{Ca}_g} \tag{4}$$

$$w_{L-LL}^{g,i} = P_g \cdot \frac{\left(V_{g,i}^{L} - V_{g,i}^{LL}\right) \cdot \mathrm{Ca}_g}{\sum_i \sum_g^3 \left(\mathrm{CR}_{g,i} \cdot \mathrm{Ca}_g\right)} \tag{5}$$

where $w_{HH-H}^{g,i}$ represents the penalty factor for the i-th g gasholder, CNY/m^3, and range represents a certain range of the gasholder. P_g is the price of gas g, CNY/m^3; Ca_g is the calorific value of gas g, kJ/m^3. The penalty factors for the gasholder are shown in Table 4.

The stability of the gasholders can be evaluated by the deviation volume (DV), which indicates the difference between the gasholder level and the reference level

Table 4 Penalty factors for gasholders in case ISP

Volume (CNY/m^3)	w_{LL-L}	w_{L-R}	w_{R-H}	w_{H-HH}
BFG1#	0.004879	0.003904	0.003904	0.006831
BFG2#	0.003253	0.002602	0.002602	0.004554
LDG1#	0.008762	0.00701	0.00701	0.012267
LDG2#	0.008762	0.00701	0.00701	0.012267
LDG3#	0.016429	0.013143	0.013143	0.023001
COG1#	0.073246	0.058597	0.058597	0.102545
COG2#	0.073246	0.058597	0.058597	0.102545

over the entire dispatch period:

$$\mathrm{SDV} = \sum_{j=1}^{J} \mathrm{DV}_j = \sum_{j=1}^{J} \sqrt{\frac{1}{T} \sum_{t=1}^{T} \left(V_{j,t} - V_{j,R}\right)^2} \tag{6}$$

Optimization Objectives

Economic Objective

The economic objective consists of three costs, represented by the symbol f_1:

$$f_1 = \mathrm{GPC} + \mathrm{EIC} + \mathrm{CEC} \tag{7}$$

where GPC is the gasholder penalty cost, EIC is the electricity interaction cost, and CEC is the carbon emission cost.

The GPC is related to the capacity and penalty factor of the gasholder:

$$\mathrm{GPC} = \sum_{t=1}^{T} \sum_{\mathrm{range}=1}^{4} \sum_{g} \sum_{i=1}^{I} w_{\mathrm{range}}^{g,i} \cdot D_{\mathrm{range},t}^{g,i} \tag{8}$$

when

$$V_{HH}^{g,j} < V_t^{g,j},\ V_{\mathrm{flar},t}^{g,j} = V_t^{g,j} - V_{HH}^{g,j} \tag{9}$$

where $D_{\mathrm{range},t}^{g,j}$ is the deviation in the range of the ith g gasholder in period t, and range refers to the four regions of LL-L, L-N, N-H, and H-HH.

The EIC is related to the amount of electricity sold/purchased and price:

$$\mathrm{EIC} = \begin{cases} \sum_{t=1}^{T} P_{P_e,t} \cdot E_{\mathrm{pur},t} \\ \sum_{t=1}^{T} P_{S_e,t} \cdot E_{\mathrm{sale},t} \end{cases} \tag{10}$$

where $P_{S_e,t}$ and $P_{P_e,t}$ are the sold/purchased prices of electricity in period t, respectively; $E_{\mathrm{sale},t}$ and $E_{\mathrm{pur},t}$ are the amount of electricity sold/purchased in period t, respectively.

The CEC is shown in Eq. (11):

$$\mathrm{CEC} = C_{\mathrm{tax}} \cdot \sum_{t=1}^{T}\left[\sum_{g}\sum_{i=1}^{I}\left(\sum_{B}\mathrm{GF}_{t,B}^{g,j}\cdot \mathrm{CEF}_{g} + V_{\mathrm{flar},t}^{G,i}\cdot \mathrm{CEF}_{\mathrm{flar}}\right) + E_{\mathrm{pur},t}\cdot \mathrm{PEF}\right] \tag{11}$$

where C_{tax} is the carbon tax, CNY/$t\mathrm{CO_2}$, with a value of 50; $\mathrm{GF}_{t,B}^{g,j}$ is the consumption of the ith g gasholder by equipment B during period t, m^3; CEF_g is the $\mathrm{CO_2}$ emission factor of gas g, $t\mathrm{CO_2}/\mathrm{m}^3$; $\mathrm{CEF}_{\mathrm{flar}}$ is the average $\mathrm{CO_2}$ emission factor of by-product gas, with a value of 1.176, $t\mathrm{CO_2}/\mathrm{m}^3$; PEF is the electricity purchase emission factor, with a value of 0.7937, $t\mathrm{CO_2}$/MWh.

Stability Objective

Currently, load variance of grid is used to reflect electric reliability [7]. Reducing load variance on the power generation side to enhance the security and stability of the GSECS is also a significant objective:

$$f_2 = v_{\mathrm{CP1}} + v_{\mathrm{CP2}} + v_{\mathrm{CHP}} \tag{12}$$

$$v_B = \frac{1}{T}\sum_{t=1}^{T}\left[E_{B,t} - \frac{1}{T}\sum_{t=1}^{T}\left(E_{B,t}\right)\right]^2 \tag{13}$$

Power Generation Model

Electricity Generation Units of the OPP

There are three generating units present in the OPP of this ISP, and the heat load of each generating unit and its upper and lower limits are shown in Eqs. (14) and (15), respectively.

$$H_{B,t} = \sum_{G}\sum_{j=1}^{J}\left(q_G \cdot \mathrm{GF}_{t,B}^{g,j}\right) \tag{14}$$

$$H_{B,t}^{\min} \le H_{B,t} \le H_{B,t}^{\max} \tag{15}$$

where $H_{\mathrm{CHP},t}^{\min}$ is equal to 175, GJ; $H_{\mathrm{CHP},t}^{\max}$ is equal to 320, GJ; $H_{\mathrm{CP1},t}^{\min}$ is equal to 200, GJ; $H_{\mathrm{CP1},t}^{\max}$ is equal to 310, GJ; $H_{\mathrm{CP2},t}^{\min}$ is equal to 70, GJ; $H_{\mathrm{CP2},t}^{\max}$ is equal to 110, GJ.

Where $H_{B,t}$ is the thermal load of equipment B during period t, MJ; and $\mathrm{GF}_{t,B}^{g,j}$ is the amount of gas consumed by equipment B from the ith g gasholder during period t, m^3; $H_{B,t}^{\min}$ and $H_{B,t}^{\max}$ are the minimum and maximum heat loads of equipment B during period t, respectively, m^3.

There is a limit on the amount of gas sent from the gasholder to the generating unit, as shown in Eq. (16).

$$\left| \sum_{j=1}^{J} \mathrm{GF}_{t,B}^{g,j} - \sum_{j=1}^{J} \mathrm{GF}_{t-1,B}^{g,j} \right| \leq \Delta \mathrm{GF}_{B}^{g,j} \tag{16}$$

where $\Delta \mathrm{GF}_{\mathrm{CHP}}^{\mathrm{BFG}}$ is equal to 20,000, m^3; $\Delta \mathrm{GF}_{\mathrm{CHP}}^{\mathrm{LDG}}$ is equal to 8000, m^3; $\Delta \mathrm{GF}_{\mathrm{CHP}}^{\mathrm{COG}}$ is equal to 4000, m^3; $\Delta \mathrm{GF}_{\mathrm{CP1}}^{\mathrm{BFG}}$ is equal to 15,000, m^3; $\Delta \mathrm{GF}_{\mathrm{CP1}}^{\mathrm{COG}}$ is equal to 2500, m^3; $\Delta \mathrm{GF}_{\mathrm{CP2}}^{\mathrm{BFG}}$ is equal to 10,000, m^3; and $\Delta \mathrm{GF}_{\mathrm{CP2}}^{\mathrm{COG}}$ is equal to 2500, m^3.

Equation (17) is the general expression for the nonlinear fitting curve of the heat load of CHP and the extraction of S1-grade steam. $\mathrm{S1}_t$ is the amount of S1-grade steam generated by CHP during period t, t.

$$\mathrm{S1}_t = A_0 \cdot \left(H_{\mathrm{CHP},t}\right)^2 + A_1 \cdot H_{\mathrm{CHP},t} + A_2 \tag{17}$$

where A_0 is equal to -0.00112, A_1 is equal to 0.68599, and A_2 is equal to -41.33008.

$H_{\mathrm{CHP},t}^{\mathrm{sur}}$ is the remaining heat load after meeting the steam demand of S2-grade and S3-grade, MJ:

$$H_{\mathrm{CHP},t}^{\mathrm{sur}} = \mathrm{S1}_t \cdot \Delta H_{s1} - \mathrm{S2}_t \cdot \Delta H_{s2} - \mathrm{S3}_t \cdot \Delta H_{s3} \tag{18}$$

Equation (19) is the limit on $H_{\mathrm{CHP},t}^{\mathrm{sur}}$, which can effectively regulate the generation of S1-grade steam and the heat load of CHP, thereby affecting the power generation of CHP.

$$H_{\mathrm{CHP},t}^{\mathrm{sur,min}} \leq H_{\mathrm{CHP},t}^{\mathrm{sur}} \leq H_{\mathrm{CHP},t}^{\mathrm{sur,max}} \tag{19}$$

where $H_{\mathrm{CHP},t}^{\mathrm{sur,min}}$ is equal to 75, GJ; $H_{\mathrm{CHP},t}^{\mathrm{sur,max}}$ is equal to 200, GJ.

The general expression of the linear fitting curve for the CHP generation capacity and heat load is displayed in Eq. (20):

$$E_{\mathrm{CHP},t} = B_0 \cdot \left(H_{\mathrm{CHP},t}^{\mathrm{sur}}\right)^2 + B_1 \cdot Q_{t,\mathrm{sur}}^{\mathrm{CHP}} + B_2 \tag{20}$$

where B_0 is equal to $-\ 1.48887 \cdot 10^{-4}$, B_1 is equal to 0.07981, and B_2 is equal to 2.08903.

The theoretical power generation model of CCPP is relatively complex and needs to be simplified by extracting characteristic curves of heat load and power output, where C_0 is equal to 0.14458, C_1 is equal to $-\ 5.10295$, D_0 is equal to 0.17047, and D_1 is equal to $-\ 6.57066$.

$$E_{\mathrm{CP1},t} = C_0 \cdot H_{\mathrm{CP1},t} + C_1 \tag{21}$$

$$E_{\mathrm{CP2},t} = D_0 \cdot H_{\mathrm{CP2},t} + D_1 \tag{22}$$

Energy Balance

The balance of by-product gas can be expressed as:

$$F^{g}_{\mathrm{sur},t} + \sum_{i=1}^{I} V^{g,i}_{t-1} = \sum_{i=1}^{I} \sum_{B} \mathrm{GF}^{g,i}_{t,B} + \sum_{i} V^{g,i}_{t} + \sum_{i=1}^{I} V^{g,i}_{\mathrm{flar},t} \tag{23}$$

where $F^{g}_{\mathrm{sur},t}$ represents the excess amount of g gas during the t period; $V^{g,i}_{t-1}$ and $V^{g,i}_{t}$ are the levels of the ith g gasholder during the $t-1$ and t periods, respectively, and $V^{g,i}_{\mathrm{flar},t}$ is the emission amount of the ith g gasholder during the t period.

The total electricity generation is the sum of the three power generation units of the OPP:

$$E_{\mathrm{prod},t} = \sum_{B} E_{B,t} = E_{\mathrm{CHP},t} + E_{\mathrm{CP1},t} + E_{\mathrm{CP2},t} \tag{24}$$

When the electricity demand exceeds the total electricity generation, electricity is purchased from the external power grid. Conversely, when the electricity demand is lower than the total power generation, it is sold:

$$E_{\mathrm{dem},t} - E_{\mathrm{prod},t} = \begin{cases} E_{\mathrm{pur},t},\ E_{\mathrm{dem},t} \geq E_{\mathrm{prod},t},\ E_{\mathrm{sale},t} = 0 \\ E_{\mathrm{sale},t},\ E_{\mathrm{dem},t} \leq E_{\mathrm{prod},t},\ E_{\mathrm{pur},t} = 0 \end{cases} \tag{25}$$

There is a limit to the amount of electricity purchased during adjacent periods:

$$\left| E_{\mathrm{pur},t} - E_{\mathrm{pur},t-1} \right| \leq E^{\max}_{\mathrm{pur}} \tag{26}$$

where $E^{\max}_{\mathrm{pur}}$ is equal to 20, MWh.

Decision Strategy

Optimization Method

The GSECS constructed in this study is a multi-objective optimization problem, where the objectives of economic efficiency and reliability cannot be simultaneously optimized. Typically, as the value of one objective function increases, the values of other objectives decrease. Therefore, it is necessary to find a compromise method for the optimal solution. Non-dominated Sorting Genetic Algorithm II (NSGA-II), a genetic algorithm based on the concept of Pareto optimality, has been proven effective for energy scheduling problems [8].

Determination of Weight

The two optimization objectives in this study involve subjective judgments regarding the practicality of engineering operations, which require considering the influence of subjective factors. Therefore, it is necessary to subjectively assess the importance of optimization objectives using expert scoring and analytic hierarchy process (AHP). The entropy weight method is regarded objective since the weights of indicators are determined based on data variability [9]. However, using objective weighting methods blindly may lead to inaccurate results and deviation from actual requirements. Game theory synthesis weight method can combine the characteristics of multiple evaluation indicator weights and find the optimal solution among them. The comprehensive weights are shown in Table 5. The comprehensive weights of EIC, CEC, GPC, V_{CP1}, V_{CP2}, and V_{CHP} are 18.93%, 13.43%, 20.19%, 16.28%, 18.50%, and 12.67%, respectively.

Table 5 Comparison of each objective between manual operation and optimization

Criteria	Manual operation	After optimization	Percent change%
f_1	3,470,330.67 CNY	3,235,839.54 CNY	− 6.76
EIC	2,615,023.40 CNY	2,540,707.37 CNY	− 2.84
CEC	560,064.13 CNY	550,107.83 CNY	− 1.78
GPC	298,205.16 CNY	145,024.34 CNY	− 51.37
f_2	15.27	8.37	− 45.15
v_{CP1}	7.50	2.62	− 65.02
v_{CP2}	6.94	5.61	− 19.09
v_{CHP}	0.82	0.14	− 83.60

Ideal Point

F_1 and f_2 form a concave curve in the Pareto solution set, signifying the mutual exclusivity between high cost-effectiveness and high reliability, making it arduous to simultaneously attain the optimal solution. The underlying principle behind this is that the improvement in the stability of the gasholder will lead to a reduction in the controllable gas volume of the OPP, thereby increasing the power exchange with the power grid. Hence, striking a balance between economic efficiency and grid interaction is imperative for making more judicious decisions. The TOPSIS method 0 is a multi-attribute decision analysis approach that ranks alternatives based on their proximity to the ideal solution, considering a finite set of evaluation criteria. The comparison of each objective between manual operation and optimization is shown in Table 5.

Results and Analysis

Gasholder Stability

The level of gasholder in manual operation and algorithm optimization is shown in Fig. 2. The levels of all gasholders tend to be around the reference level after optimization. Specifically, the BFG1# gasholder level shown minimal fluctuations compared to before optimization, which can be attributed to its larger capacity compensating for the fluctuations in other gasholders. The BFG2# gasholder level significantly reduces in the HH-H range, with most of the fluctuations occurring within the safe zone. As for the LDG holders, especially LDG3#, their levels become remarkably stable. In the manual operation, both COG 1# and COG 2# mostly stayed in the HH-H range throughout the entire period. After optimization, their levels gradually approach the reference level, indicating that more COG was utilized by OPP. This is one of the reasons why other gasholders are becoming more stable as well. Figure 3a shows the DV of the gasholders during manual operation and optimization results. The 25.23% reduction in the SDV indicated an improvement in the stability of the gasholders, particularly for the COG 1#, COG 2#, BFG 2#, and LDG 3#. Due to the limited CS of LDG 1# and 2#, their reduction in the DV was not significant.

Carbon Emissions

Figure 3b shows the carbon emissions of the power generation units and purchased electricity before and after optimization. The carbon emissions of the three power

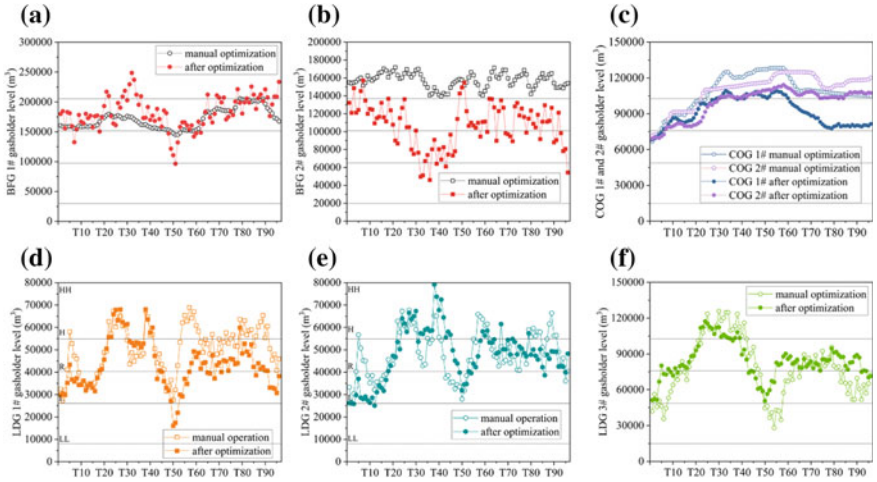

Fig. 2 Comparison of manual operation and optimal calculation results for the holder level of by-product gases under each time period

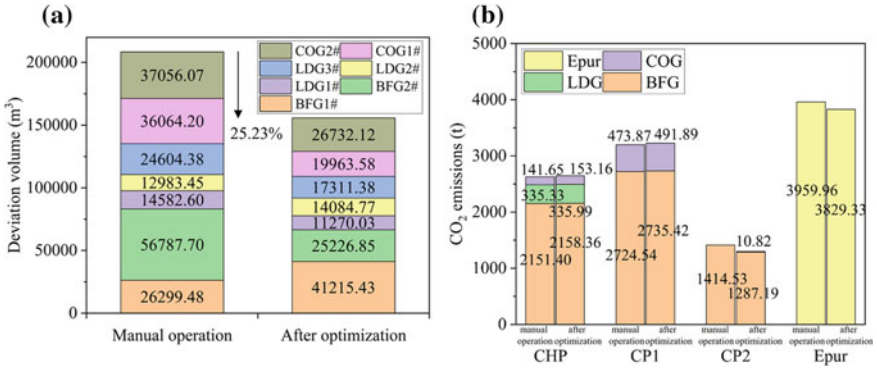

Fig. 3 **a** Comparison of the DV of gasholder after manual operation and optimization; **b** manual operation and optimization results of CO_2 emissions

generation units increased after optimization, while the indirect emissions from purchased electricity decreased. This indicated that the power generation units utilized more by-product gas to generate electricity, thereby reducing the need for purchasing electricity. Overall, there was a 0.95% reduction in total CO_2 emissions from the power generation units, a 3.30% decrease in indirect power-related emissions, and an overall reduction of 1.78% in carbon emissions. It is evident that optimizing scheduling can enhance power generation efficiency and achieve CO_2 emissions reduction by adjusting the gas composition at the power generation end.

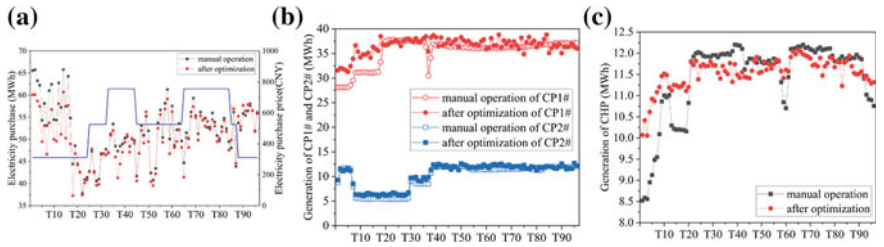

Fig. 4 Generator sets and purchased electricity for each period

However, it does not alter the energy consumption structure of the GSECS significantly. The reduction in CO_2 emissions is limited without increasing clean energy sources such as wind and solar energy.

Electrical Reliability

The purchased electricity and power generation of each period are shown in Fig. 4. The optimized cost of EIC decreased by 2.84%. Compared to manual operations, all three units exhibited an increase in electricity generation throughout the scheduling period, particularly during off-peak hours. However, due to the balancing effect of objective f_2, the reduction in purchased electricity cost was limited, ensuring stability on the power generation side. CP1 not only possessed high generating capacity but also exhibited remarkable efficiency, prioritizing gas supply during optimization and resulting in a significant increase in electricity generation. The reliability of CHP units increased by 83.60%.

Conclusions

The study aimed to construct a gas-steam-electricity coupled system for a steel plant, incorporating gasholders and on-site power plant, with the objectives of economic efficiency and power reliability. A new penalty factor for gasholder fluctuations was established, taking into account the controllable range of gasholders, gas prices, and heating values. This factor fully reflected the characteristics of different types and sizes of gasholders. The NSGA-II algorithm was used to solve the model, and an energy management strategy for the coupled system was designed based on the optimization results. The expected solution was selected using the TOPSIS method with comprehensive weights. The results showed that compared to manual operations, the total cost decreased by 234,491.13 CNY after optimization. As a whole, the GSECS sacrificed the stability of BFG1# in order to compensate for the stability of

other gasholders, resulting in a 25.23% decrease in the SDV. Due to an increase in electricity generation during off-peak hours after optimization, the EIC decreased by − 2.84%. Meanwhile, electric reliability improved significantly, especially for CHP units with an 83.60% reduction in load variance. However, without introducing new clean power sources such as solar and wind power, the potential for carbon emission reduction through optimization scheduling is limited.

References

1. He DF, Liu PZ, Feng K (2019) Collaborative optimization of rolling plan and energy dispatching in steel plants. China Metall 29(04):75–80. https://doi.org/10.13228/j.boyuan.issn1006-9356.20180306
2. Chen HD, Meng F, Wang Q (2023) Influence of installed capacity of energy storage system and renewable energy power generation on power system performance. Energ Storage Sci Technol 12(02):477–485. https://doi.org/10.19799/j.cnki.2095-4239.2022.0439
3. Zeng YJ, Sun YG (2015) Short-term scheduling of steam power system in iron and steel industry under time-of-use power price. J Iron Steel Res Int 22(9):795–803. https://doi.org/10.1016/S1006-706X(15)30073-X
4. Hu ZB, He DF (2022) Operation scheduling optimization of gas-steam-power conversion systems in iron and steel enterprises. Appl Therm Eng 206. https://doi.org/10.1016/j.applthermaleng.2022.118121
5. Wei ZQ, Zhai XQ, Zhang Q (2020) A MINLP model for multi-period optimization considering couple of gas-steam-electricity and time of use electricity price in steel plant. Appl Therm Eng 168. https://doi.org/10.1016/j.applthermaleng.2019.114834
6. Lu XH, Zhou KL, Yang SL (2018) Multi-objective optimal load dispatch of microgrid with stochastic access of electric vehicles. J Clean Prod 195:187–199. https://doi.org/10.1016/j.jclepro.2018.05.190
7. Zhang XZ, Wang ZY, Lu ZY (2021) Multi-objective load dispatch for microgrid with electric vehicles using modified gravitational search and particle swarm optimization algorithm. Appl Energ 306. https://doi.org/10.1016/j.apenergy.2021.118018
8. Wang HQ, Xie ZS, Pu L (2022) Energy management strategy of hybrid energy storage based on Pareto optimality. Appl Energ 327. https://doi.org/10.1016/j.apenergy.2022.120095
9. Jin ZS, Liu HC, Kou W (2021) Selection of purification technology for small and medium-sized biogas projects based on AHP and entropy weight method. Renew Energ Resour 39(10):1294–1300. https://doi.org/10.13941/j.cnki.21-1469/tk.2021.10.003
10. Hu YJ, Wu LZ, Shi C (2020) Research on optimal decision-making of cloud manufacturing service provider based on grey correlation analysis and TOPSIS. Int J Prod Res 58(3):748–757. https://doi.org/10.1080/00207543.2019.1600760

Design and Research of Three-Stage Reactor of Carbonation Process of Calcified Residue

Li Xiang, Liu Yan, Zhang Tingan, Xiao Yadong, Li Xiaolong, Wang Kun, and Liu Guanting

Abstract A three-stage cross-flow Venturi jet reactor was innovatively designed in this study to conduct an experimental study on the physical simulation of the carbonization process of calcified slag. The pH changes during CO_2 absorption by NaOH were measured by a pH meter. The influence law of superficial gas velocity, superficial liquid velocity, and inlet pressure on CO_2 absorption rate and utilization rate were investigated. The results show that the volumetric mass transfer coefficient with the increase of superficial gas velocity first remains unchanged and then increases, decreases with the increase of superficial liquid velocity, and increases with the increase of inlet pressure, and the latter stage is greater than the previous stage. The CO_2 utilization rate does not change with the increase of superficial gas velocity and inlet liquid velocity but increases with the increase of inlet pressure and remains unchanged afterwards. This result provides support for the design and industrial application of carbonization reactors.

Keywords Carbonization · Jet flow · Venturi · Absorption rate · Utilization rate · Physical simulation

Introduction

The aluminium oxide industry in China is developing rapidly and has greatly accelerated the consumption of high-quality bauxite with a high aluminium–silicon ratio. The aluminium metallurgical enterprises are facing a severe test [1, 2]. In the Bayer method process of producing aluminium oxide, the equilibrium solid phase of red mud is hydrated aluminosilicate. The consumption of aluminium oxide and caustic alkali increases with the increase of silicon oxide content, and the loss of aluminium

L. Xiang · L. Yan (✉) · Z. Tingan · X. Yadong · L. Xiaolong · W. Kun · L. Guanting
School of Metallurgy, Northeastern University, Shenyang 110819, China
e-mail: liuyan@smm.neu.edu.cn

Z. Tingan
e-mail: zta2000@163.net

© The Minerals, Metals & Materials Society 2024

C. Iloeje et al. (eds.), *Energy Technology 2024*, The Minerals,
Metals & Materials Series, https://doi.org/10.1007/978-3-031-50244-6_19

oxide is more than that of silicon oxide. As the ore grade decreases year by year, the economic advantages of the Bayer method become less obvious, and the amount of red mud produced also increases [3–5].

In order to break through the key technical bottlenecks in the utilization of low-grade bauxite resources or red mud, Northeastern University has proposed a method of treating low-grade bauxite (red mud) with calcification-carbonization method to produce aluminium oxide after years of research [6–10], achieving efficient utilization of valuable elements in low-grade bauxite [11] and zero discharge of solid waste. The carbonization reaction of calcium transformation slag is the key in this method, and the mass transfer coefficient during the carbonization process is an essential parameter for measuring the mass transfer characteristics between gas–liquid phases and designing reactors. Stapurewicz et al. [12] studied the influence of different bottom jet elements on the mass transfer rate between CO_2 and NaOH solution, and the study showed that at low gas speeds, the interface area of the multihole plug injection was larger and the gas absorption rate was higher. Based on the study of three-phase flow, Kaiyue et al. [13] investigated the effects of superficial gas velocity and superficial liquid velocity on the gas–liquid volume mass transfer coefficient of three-phase micro fluidized beds. The results indicate that increasing the superficial gas velocity and the superficial liquid velocity increases the gas–liquid volume mass transfer coefficient. The gas–liquid mass transfer coefficient is the basic parameter for studying the gas–liquid absorption process. Optimizing the reactor configuration and operating parameters to improve the mass transfer rate is particularly important for further improving the mass transfer efficiency and strengthening the carbonization process.

Therefore, based on the single-stage Venturi reactor, this paper designed a three-stage cross-flow Venturi jet reactor and investigated the influence of operating conditions on the CO_2 absorption rate of all stages of reactors in the NaOH aqueous solution-CO_2 system by physical simulation close to the working conditions. The volume mass transfer coefficient and CO_2 utilization rate were quantitatively calculated to explore their influence on the process of carbonization decomposition [14]. The study of mass transfer rate in the reactor can further achieve efficient multiphase reactions, achieve good economic and environmental benefits, and provide a theoretical and experimental basis for improving the calcification-carbonization method of low-grade ore.

Experiment

Experimental Device

The experimental setup is illustrated in Fig. 1. The main reactor uses organic glass instead of stainless steel material and establishes a physical model based on geometric and dynamic similarity [15]. Its inner diameter is 290 mm, effective height is 700 mm,

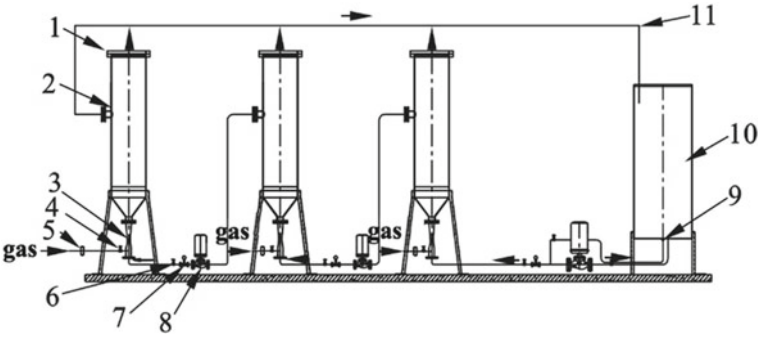

Fig. 1 Picture of the experimental equipment

and it is fixed with carbon steel brackets. The inner diameter of the nozzle at the diameter change point is 26 mm, and the effective volume of the liquid storage tank is 0.244 m^3. The liquid flows through various stages of reactors at a stable flow rate from the storage tank by the action of a pump to complete circulation. The gas flows through a Venturi jet device and is sprayed into the reactor from below each stage to achieve gas–liquid mixing. Gas velocity and liquid velocity are controlled by intake and ball valves, respectively, and measured by gas rotameters and electromagnetic flowmeters.

Measuring Method

In this experiment, CO_2 was blown into the NaOH solution. The pH value of the solution at any time at 50 cm from the bottom of the first stage reactor was detected using a pH meter, and the CO_2 concentration at that time was calculated. The relationship between pH value and CO_2 concentration in the solution has been derived by Shuangyi et al. [16]:

$$Y = \left[(\mathrm{H}^+) + X - \frac{K_{\mathrm{H_2O}}}{(\mathrm{H}^+)}\right] \frac{K_1K_2 + K_1(\mathrm{H}^+) + (\mathrm{H}^+)^2}{2K_1K_2 + K_1(\mathrm{H}^+)} \tag{1}$$

$$K_1 = \frac{(\mathrm{HCO_3^-})(\mathrm{H}^+)}{\mathrm{H_2CO_3}} = 10^{-6.352} \quad K_2 = \frac{(\mathrm{CO_3^{2-}})(\mathrm{H}^+)}{\mathrm{HCO_3^-}} = 10^{-10.329}$$

$$K_{\mathrm{H_2O}} = \frac{(\mathrm{H}^+)(\mathrm{OH}^-)}{1} = 10^{-14} \quad (\mathrm{H}^+) = 10^{-\mathrm{pH}} \tag{2}$$

In the equation: X is the concentration of NaOH, mol/L; Y is the concentration of CO_2, mol/L; K_1, K_2, K_{H_2O} are the ionization equilibrium constants of HCO_3^-, CO_3^{2-}, H_2O.

Volume mass transfer coefficient AK/V:

$$\ln[(Ce - Ct)/(Ce - C_0)] = -(AK/V)t \tag{3}$$

In the equation: A is reaction surface area, cm^2; V is volume of NaOH solution, cm^3; t is reaction time, s; K is mass transfer coefficient of CO_2, cm/s; Ce, Ct, C_0 is equilibrium concentration of CO_2, absorption concentration of CO_2 after t seconds, initial concentration of O_2, mol/L.

CO_2 utilization rate η [17]:

$$\eta = [V(C_{CO_2II} - C_{CO_2I})/t]/[\rho_{CO_2} Q/M] \tag{4}$$

In the equation: V is the volume of the solution, cm^3; C_{CO_2II} is CO_2 concentration in the solution at t_{II}, mol/L; C_{CO_2I} is CO_2 concentration in solution at $t_I$mol/L; ρ_{CO_2} is CO_2 gas density, 1.977×10^{-3} g/cm^3; Q is CO_2 gas flow rate, L/min; M is molecular weight of CO_2, g.

Experimental Results and Discussion

Research on CO_2 Absorption Rate

Effect of Superficial Gas Velocity on CO_2 Absorption Rate

Experimental conditions: superficial liquid velocity 1.658 m s^{-1}, intake pressure 0.2 MPa. The pH value of the reactor over time is measured by changing the superficial gas velocity.

It can be seen from Fig. 2 that when the superficial gas velocity is high, the rate of pH decrease in the early stage is greater than in the later stage. When the superficial gas velocity is small at 3.539 m s^{-1}, the pH first slowly and then rapidly decreases. After CO_2 enters the reactor at high speed through the Venturi nozzle, the gas–liquid is fully mixed and rapidly reacts with OH^- ions in the solution, causing a rapid decrease in the pH of the solution. As the OH^- concentration continues to decrease, the trend of pH decrease slows down. When the superficial gas velocity is small, the pH value decreases slowly due to the low CO_2 content in the initial stage, and the pH decline speed accelerates with the increase of the superficial gas velocity.

Figure 3 shows that as the superficial gas velocity increases, the volumetric mass transfer coefficient slowly increases and then suddenly increases in the early stage. This is because as the superficial gas velocity increases, the amount of CO_2 injected per unit time increases, the gas–liquid agitation is strengthened, the contact area is enlarged, and the mass transfer coefficient of the solution is increased as the reaction is accelerated. The concentration of OH^- ions in the later stage of the reaction is relatively low, and the volumetric mass transfer coefficient slowly increases with the superficial gas velocity of CO_2.

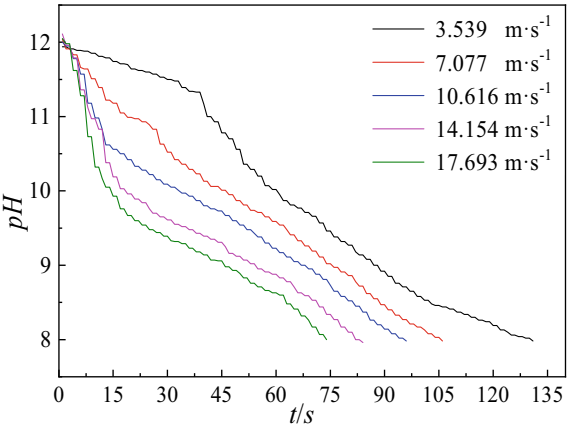

Fig. 2 Curves of pH-time under different superficial gas velocities

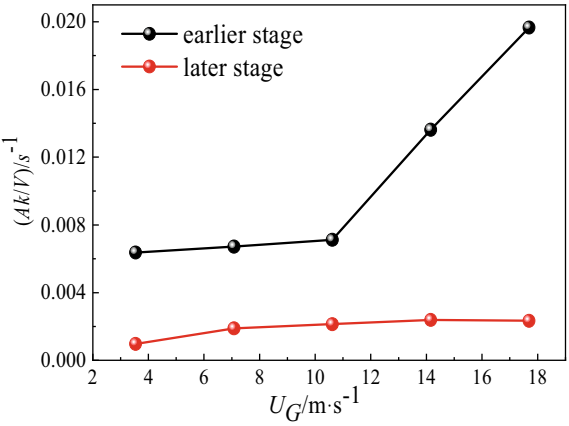

Fig. 3 Relation between volumetric transfer coefficient and superficial gas velocity under different periods

Effect of Superficial Liquid Velocity on CO_2 Absorption Rate

Experimental conditions: The superficial gas velocity is 7.077 m s^{-1}, and the inlet pressure is 0.2 MPa. The pH value of the reactor over time is measured by changing the superficial liquid velocity.

As shown in Fig. 4, as the superficial liquid velocity increases, the pH value decreases linearly with time, and the rate of decrease is constant. When the superficial liquid velocity increases, the degree of fluid turbulence intensifies, and the gas–liquid contact time decreases, resulting in a slower decrease in pH. But at the same time, the rising speed of the fluid in the reactor increases, the frequency of gas–liquid contact increases, and the reaction rate increases, leading to a faster decrease in pH. The rate of decrease in pH value remains unchanged under comprehensive action.

It can be seen from Fig. 5 that the mass transfer coefficient by volume in the early stage gradually decreases with the increase of the superficial liquid velocity, which

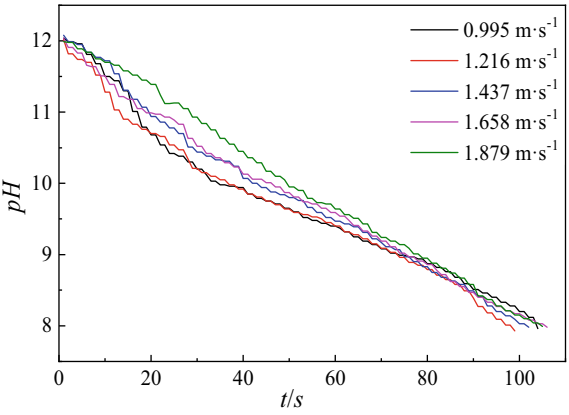

Fig. 4 Curves of pH-time under different superficial liquid velocities

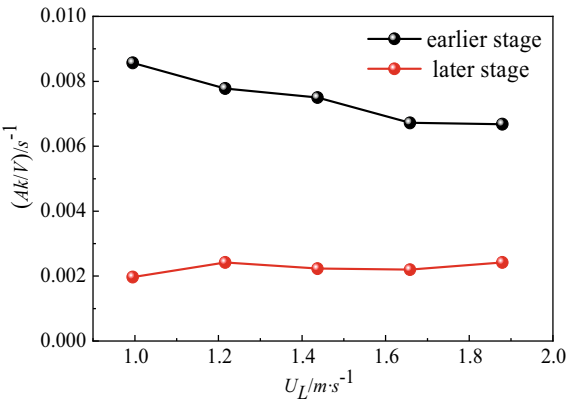

Fig. 5 Relation between volumetric transfer coefficient and superficial liquid velocity under different periods

is because the superficial liquid velocity is positively correlated with the degree of turbulence, and the combined effect of the increased fluid rising velocity gradually reduces the volumetric mass transfer coefficient. At the late stage of the reaction, the concentration of OH^- ions is low, and CO_2 is saturated, resulting in a small rate of change in the volumetric mass transfer coefficient.

Effect of Intake Pressure on CO_2 Absorption Rate

Experimental conditions: the superficial liquid velocity is 1.658 m s^{-1}. When the superficial gas velocities are 7.077 m s^{-1} and 14.154 m s^{-1}, respectively, the pH value of the reactor over time is measured by changing the inlet pressure.

As shown in Fig. 6, the rate of pH value decrease gradually accelerates as the intake pressure increases. The pH value decreases slowly at low superficial gas velocity (Fig. 6a). At high superficial gas velocity (Fig. 6b), the rate of pH value decreases

fast at first and then slowly. With increased intake pressure, the speed of gas entering the reactor increases, agitating the solution more effectively, improving gas–liquid contact, speeding up the reaction rate, and causing the pH to fall more quickly.

As shown in Fig. 7, with the increase of inlet pressure, the volumetric mass transfer coefficient under different superficial gas velocities in the early stage continuously increases. In contrast, the volumetric mass transfer coefficient is almost unchanged in the later stage. In the early stage, the concentration of OH^- ions was relatively high, and the intake speed increased with the increase of inlet pressure, resulting in sufficient gas–liquid contact and a higher volumetric mass transfer coefficient. In the later stage of the reaction, the concentration of OH^- ions is low and CO_2 is excessive. The concentration of OH^- ions limits the reaction, making the volumetric mass transfer coefficient almost constant.

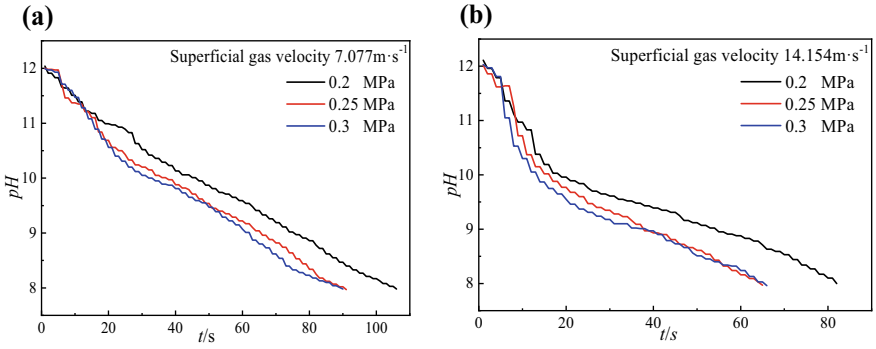

Fig. 6 Curves of pH-time under different intake pressures

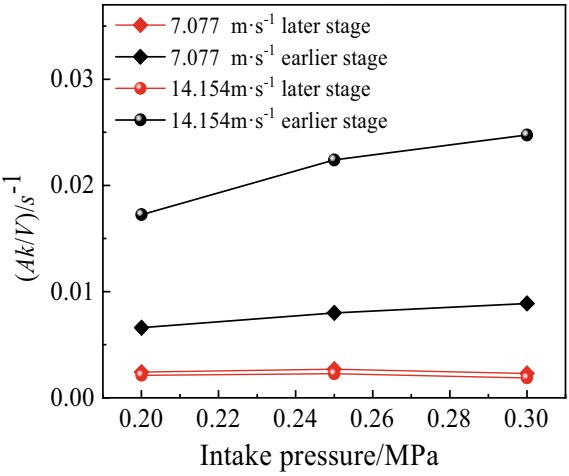

Fig. 7 Relation between volumetric transfer coefficient and intake pressure under different periods

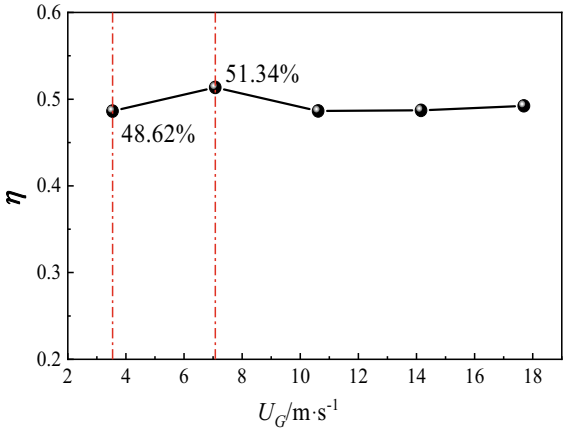

Fig. 8 Efficiency of CO_2 under different superficial gas velocities

Research on CO_2 Utilization Rate

Effect of Superficial Gas Velocity on CO_2 Utilization Rate

From Fig. 8, it can be observed that at a superficial gas velocity of 7.077 m s^{-1}, the maximum CO_2 utilization rate is 51.34%; at a superficial gas velocity of 3.539 m s^{-1}, the minimum CO_2 utilization rate is 48.62%. As the superficial gas velocity increases, the intake of CO_2 increases. At the same time, the gas enters the reactor at high speed due to the action of the Venturi tube, and the gas–liquid is fully stirred and in contact. The CO_2 fully reacts, shortening the reaction time, ultimately resulting in an almost unchanged CO_2 utilization rate.

Effect of Superficial Liquid Velocity on CO_2 Utilization Rate

As indicated in Fig. 9, when the superficial liquid velocity is 1.216 m s^{-1}, the maximum CO_2 utilization rate is 54.90%, and when the superficial liquid velocity is 1.658 m s^{-1}, the minimum CO_2 utilization rate is 51.34%. The increase in superficial liquid velocity intensifies fluid turbulence and reduces the residence time of the gas in the reactor, and CO_2 overflows from the liquid surface before it can react, thereby reducing gas utilization efficiency. But at the same time, the rising speed of the fluid increases, the frequency of gas–liquid contact increases, and the gas utilization rate is improved. Under the comprehensive effect, the CO_2 utilization rate remains almost unchanged.

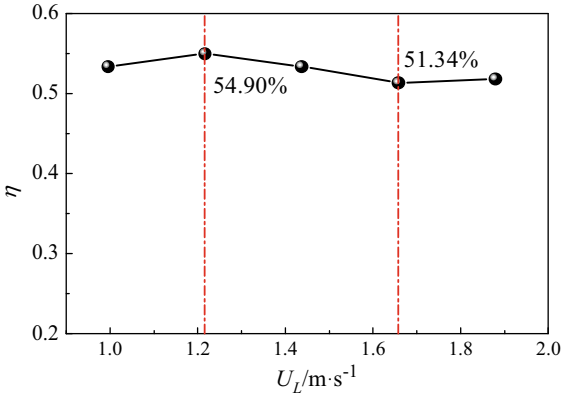

Fig. 9 Efficiency of CO_2 under different superficial liquid velocities

Effect of Intake Pressure on CO_2 Utilization Rate

As shown in Fig. 10, CO_2 utilization first increases and then remains unchanged as the inlet pressure increases. The superficial gas velocity is 7.077 m s^{-1}. The utilization rate is the lowest at 51.34% when the inlet pressure is 0.2 MPa. The maximum utilization rate is 60.56% at an inlet pressure of 0.3 MPa. The superficial gas velocity is 14.154 m s^{-1}, with the lowest utilization rate of 48.71% at an inlet pressure of 0.2 MPa, and the highest utilization rate of 63.17% at an inlet pressure of 0.25 MPa. When the intake pressure is low, the intake speed increases with the increase of intake pressure, the gas–liquid agitation increases, the degree of fluid turbulence increases, and the gas–liquid contact is sufficient, leading to an increase in CO_2 utilization rate. When the intake pressure is high, due to the fast intake speed, some gases do not fully react and flow out of the upper end of the reactor, resulting in a small change in utilization rate.

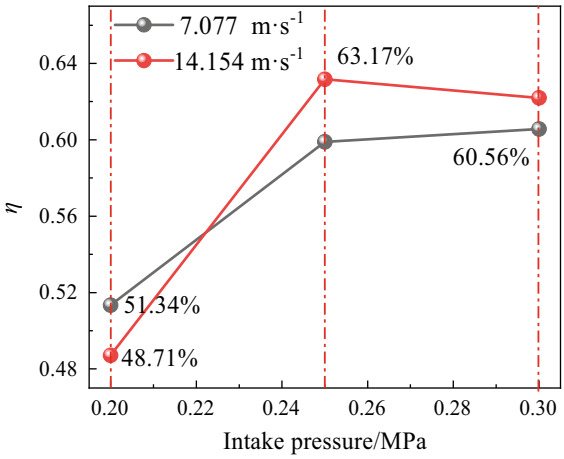

Fig. 10 Efficiency of CO_2 under different intake pressure

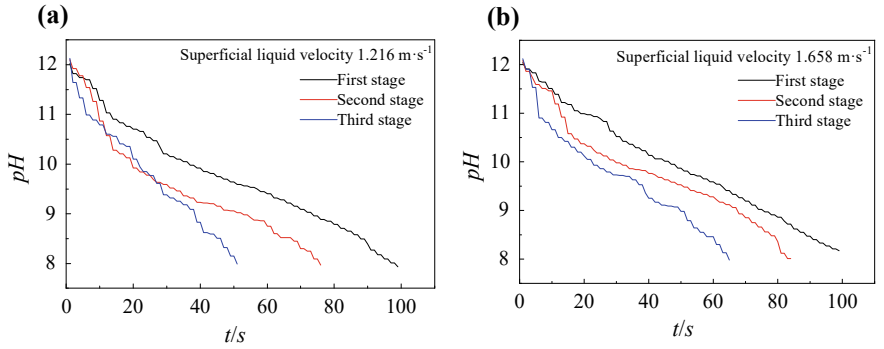

Fig. 11 Curves of pH-time in different stages

Absorption Rate in Each Stage of Reactor

Experimental conditions: the superficial gas velocity is 7.077 m s^{-1}, the inlet pressure is 0.2 MPa, and the superficial liquid velocities are 1.216 m s^{-1} and 1.658 m s^{-1}, respectively. The pH values of each stage are measured over time.

As shown in Fig. 11, the pH value gradually decreases with time. In each stage of the reactor, the pH value decreases at the Third stage > Second stage > First stage. When the superficial gas velocity of CO_2 is the same, the solution acts as a diluent when the fluid flows from the first stage to the second and third stages, resulting in a faster decrease in pH in the latter stage reactor than in the previous stage.

From Fig. 12, the relationship between the volumetric mass transfer coefficients of each stage in the early stage is Third stage > Second stage > First stage, while in the later stages, the mass transfer coefficients of the volume are small and almost unchanged. In the early stage of the reaction, the solution continuously enters the subsequent reactor as the reaction progresses, resulting in a decrease in the concentration of OH^- ions, an acceleration of the reaction speed, and an increase in the volumetric mass transfer coefficient. In the later stage of the reaction, the concentration of OH^- ions in each stage reactor all are low, so the volumetric mass transfer coefficient is very small and almost unchanged.

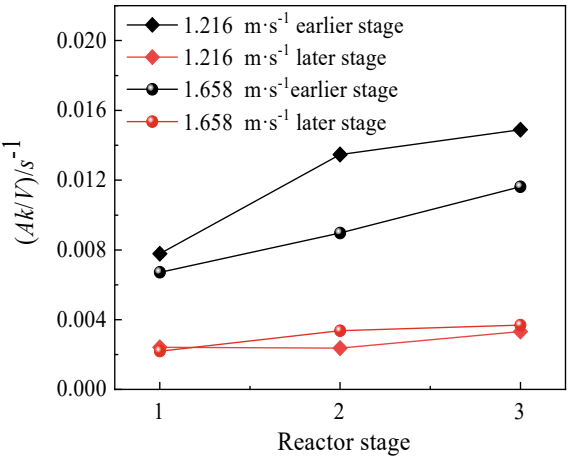

Fig. 12 Volume mass transfer coefficient in various reactors at different periods

Conclusion

In this paper, the effects of different operating conditions on the CO_2 absorption rate and utilization rate in the carbonization process were studied, and the following conclusions were obtained:

(1) With the increase of superficial gas velocity, the mass transfer coefficient by volume first does not change, then rapidly increases, and the CO_2 utilization rate almost unchanged.
(2) With the increase of superficial liquid velocity, the mass transfer coefficient decreases, and the CO_2 utilization rate is almost unchanged.
(3) With the increase of intake pressure, the mass transfer coefficient of volume increases, and the utilization of CO_2 increases first and then remains unchanged.
(4) In each reactor stage, the volumetric mass transfer coefficient of the latter stage is greater than that of the previous stage.

Acknowledgements This work was supported by the special support from the China Postdoctoral Science Foundation (in station) (grant number 2023T1600880) and National Natural Science Foundation Youth Science Foundation Project (grant number 52304324).

References

1. Jiang YJ, Wan M (2021) Study on alumina production process. World Nonferrous Metals 17:175–176
2. Dmitry Z, Liliya P, Mikhail F (2021) Extraction of valuable elements from red mud with a focus on using liquid media—a review. Recycling 6(2):38–38

3. Pan XL, Lv ZY, Wu HF (2023) Research status and prospects of red mud recycling technology for iron and aluminum resources. Chin J Nonferrous Metals 1–32
4. Agrawal S, Dhawan N (2021) Evaluation of red mud as a polymetallic source—a review. Miner Eng 171:107084
5. Steve H (2022) Sustainable bauxite residue management guidance. International Aluminium Institute, London
6. Zhang TA, Lv GZ, Liu Y (2014) Method for dissolving aluminum oxide from medium and low-grade bauxite based on calcification carbonization transformation. CN102757073B
7. Lv GZ, Zhang TA, Guo FF (2019) Clean and efficient utilization of low-grade high-iron sedimentary bauxite via calcification-carbonation method. Hydrometallurgy 187
8. Lv GZ, Zhang TA (2019) Utilization of Bayer red mud by a calcification–carbonation method using calcium aluminate hydrate as a calcium source. Hydrometallurgy 188:248–255
9. Li RB, Zhang TA, Liu Y (2016) Calcification-carbonation method for red mud processing. J Hazard Mater 316(5):94–101
10. Zhu XF, Zhang TA, Wang YX (2016) Recovery of alkali and alumina from Bayer red mud by the calcification-carbonation method. Int J Miner Metall Mater 23(3):257–261
11. Wang Y, Zhang TA (2018) Recovery of alkali and alumina from bauxite residue (red mud) and complete reuse of the treated residue. J Cleaner Prod 188:456–465
12. Stapurewicz T, Themelis NJ (1987) Mixing and mass transfer phenomena in bottom-injected gas-liquid reactors. Can Metall Q 26(2):123–128
13. Wang KY, Ma YL, Li C (2022) Gas-liquid mass transfer coefficient of gas-liquid solid micro fluidized beds. J Chem Ind Eng 73(08):3529–354
14. Wang DX (2017) Simulation study on fluid flow behavior in oxygen bottom blown smelting furnace. Northeastern University
15. Pucciarelli A, Ambrosini W (2020) A successful general fluid-to-fluid similarity theory for heat transfer at supercritical pressure. Int J Heat Mass Transfer 159:120152
16. Inada S, Watanabe Z (1976) The effect of gas properties on the rate of CO_2 absorption into NaOH aqueous solution. Toki and Ben 62(7):807–816
17. Liu H, Zeng H, Liu WP (2004) Simulation experimental study on refining aluminum liquid by rotating powder (flux) spraying. Light Alloy Process Technol 32(4):14–15

Effect of Fe_2O_3 on Blast Furnace Coal Combustion Under Local Oxygen Enrichment

Zhenfeng Zhou and Zukang Wan

Abstract The use of coke will be greatly reduced by much pulverized coal injection. The pulverized coal injection rate of blast furnace can be greatly increased by local oxygen-enrichment method. However, the cooling effect of room-temperature oxygen delays the devolatilization process and the entire coal combustion process will be delayed. To increase the pyrolysis rate will weaken the cooling effect of room-temperature oxygen on coal combustion. The pyrolysis rate increases and activating energy decreases with Fe_2O_3 addition. In this study, the effect of Fe_2O_3 on coal combustion in the blast furnace was simulated. The effect of Fe_2O_3 without oxygen enrichment on coal burnout is unobvious. For local oxygen enrichment, the coal burnout greatly increases and has a maximum increase of 22.03%.

Keywords Blast furnace · Oxygen enrichment · Fe_2O_3 · Coal burnout

Introduction

The blast furnace is still a main ironmaking process due to its high production efficiency and energy utilization rate [1, 2]. However, high amount of coke is consumed during blast furnace production process. The price of coke continues to rise due to shortage of coking coal resources, which leads to increase of blast furnace production costs. In addition, much energy will be consumed and a large amount of pollutants will be generated in the coking process. Under the pressure of economy and environment, the use of coke must be reduced in the blast furnace production process. The consumption of coke can be effectively reduced by much coal injection. However, to achieve above goals, the most important issue is the full combustion of coal in the raceway region.

Z. Zhou (✉) · Z. Wan
College of Mechanical and Electronic Engineering, Shandong University of Science and Technology, Qingdao 266590, China
e-mail: zhouzhenfeng@sdust.edu.cn

Z. Wan
e-mail: m17302290180@163.com

© The Minerals, Metals & Materials Society 2024

C. Iloeje et al. (eds.), *Energy Technology 2024*, The Minerals, Metals & Materials Series, https://doi.org/10.1007/978-3-031-50244-6_20

There are many factors that affect the combustion of coal, such as blast temperature, coal type, coal particle size, and oxygen concentration. Shen et al. [3, 4] investigated the effect of blast temperature on coal combustion and found that the coal burnout has an increase of about 1.5% for every increase of 100 °C. However, the blast temperature of advanced blast furnace has widely reached 1200 °C. It is difficult to achieve a higher blast temperature. Zhou et al. [5, 6] investigated the effect of coal type on coal combustion and found that high volatile coal has a higher burnout rate. But its heat value is lower, which cannot meet the heat requirements of the blast furnace. Liu et al. [7] investigated the effect of oxygen concentration in hot blast on coal combustion and found that the coal burnout only has an increase of about 1.5% for every increase of 1% oxygen content. The traditional oxygen enrichment method have cannot meet the requirement of higher coal injection rate. Zhou et al. [8] found that the oxygen concentration around coal particles can be greatly increased by the local oxygen enrichment method. However, the cooling effect of room-temperature oxygen delays the coal combustion process. The effect of oxygen enrichment will be weaker and even be invalid. Fu et al. [9] investigated the effect of different catalysts on coal pyrolysis and found that the devolatilization process is accelerated. Wu et al. [10] investigated the effect of Fe_2O_3 on coal pyrolysis and found that the activation energy of pyrolysis process is reduced.

In order to overcome the problems of previous research on blast furnace coal injection, in this paper, the effect of Fe_2O_3 on coal combustion in the blast furnace is investigated using the computational fluid dynamics (CFD) method. In other study, the activation energy of pyrolysis process is reduced by adding Fe_2O_3. The effect of Fe_2O_3 on coal combustion process is simulated. It found that the coal combustion process of traditional condition is greatly advanced, but the change of final burnout is not obvious. Furthermore, the effect of Fe_2O_3 on coal combustion process under local oxygen enrichment was investigated. When the addition amount of Fe_2O_3 is 5 and 10%, the coal burnout is greatly increased. The coal burnout has an increase of 21.59% and 22.03%, respectively. This study has important guiding significance for the development of coal injection technology in blast furnaces.

Geometric Model and Simulation Conditions

Figure 1 is the schematic diagram of geometric model. The model simulated the lance, blowpipe, tuyere, and raceway region of a blast furnace. The depth of the raceway region is 700 mm. The raceway region was simplifying designed considering flow and combustion characteristics of the coal plume. The structure of base case is used to simulate the coal combustion without oxygen enrichment, and the structure of local oxygen enrichment is used to simulate the coal combustion with oxygen enrichment. The blast temperature is 1200 °C and the oxygen content in hot blast is 21%. For local oxygen enrichment, the total oxygen concentration is 24%, and the remaining oxygen is injected into the blowpipe by the oxygen lance.

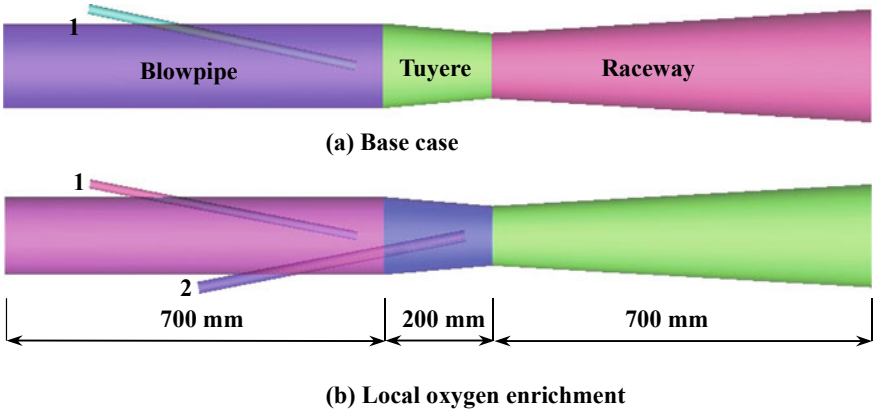

Fig. 1 Schematic diagram of geometric model

Model Description

The gas-particle flow and reaction in the drop tube furnace were calculated based on the framework of the software package ANSYS-FLUENT. In this model, the gas phase is treated with an Eulerian frame and described by the steady-state Reynolds-averaged Navier–Stokes equations closed by the k–ε turbulence model [11]. The governing equations for the gas phase includes mass, momentum, energy, gas species, turbulent kinetic energy, turbulent dissipation rate [12–14].

Particles of pulverized coal are treated as discrete phase, modelled using the Lagrangian method, where the trajectories of the discrete particles are determined by integrating Newton's second law of motion. The drag force (f_D) and turbulent dispersion are included. Full coupling of mass, momentum, and energy of particles with the gas phase is implemented. The change of particle temperature is governed by three physical processes: convective heat transfer, latent heat transfer associated with mass transfer, and radiative heat transfer. The governing equations for the particle phase are summarized in Table 1.

The devolatilization process releases volatiles ($C_\alpha H_\beta O_\gamma N_\delta$) and char (C(s)). The coal devolatilization process is simulated using the single-rate devolatilization model

Table 1 Governing equations for the particle phase

Mass	$\frac{dm_p}{dt} = -\dot{m}$
Momentum	$m_p \frac{du_p}{dt} = -f_D$ $-f_D = \frac{1}{8}\pi d_p^2 \rho C_D \lvert U - U_p \rvert (U - U_p)$
Energy	$m_p C_p \frac{dT_P}{dt} = -q$ $\pi d_p \lambda N_\mu (T_g - T_p) + \sum \frac{dm_p}{dt} H_{\text{reac}} + A_p \varepsilon_p \left(\pi I - \sigma_B T_p^4\right)$

[15].

$$\text{Raw coal} = \alpha VM + (1 - \alpha)C$$

The rate constants k are expressed in the Arrhenius format [16]. The activating energy of pyrolysis with 0%, 5%, and 10% Fe_2O_3 addition amount is 65.6 kJ/mol, 51.3 kJ/mol, and 40.7 kJ/mol, respectively.

$$k = A \exp(-E/T)$$

For the char reactions, the heterogeneous surface reaction model is used. The following reactions are considered during the coal combustion process:

$$C + 0.5O_2 = CO$$

$$C + CO_2 = 2CO$$

$$C + H_2O = CO + H_2$$

The reaction rate for char is expressed as follows [17]:

$$R_{j,r} = A_p \eta_r Y_j P \frac{k_r D_{0,r}}{D_{0,r} + k_r}$$

Results and Discussion

Effect of Fe_2O_3 Addition on Coal Combustion

Figure 2 shows the effect of Fe_2O_3 addition amount on final coal burnout. The final coal burnout does not gradually increase with increase of Fe_2O_3 addition amount. The coal burnout is 74.83% without Fe_2O_3 addition. When the Fe_2O_3 addition amount is 5%, the coal burnout is 80.91% with an increase of 6.08%. But the coal burnout of 10% Fe_2O_3 addition amount is 78.91% decreased by 2% than that of 5% Fe_2O_3 addition. The activation energy of pyrolysis process decreases with the increase of Fe_2O_3 addition amount. The pyrolysis rate will increase and the combustion process will be advanced. Therefore, the char will have longer distance to combust. However, the oxygen around the coal particles is limited. The coal combustion process is enhanced in the early stage and will be delayed in the late stage due to the lack of oxygen. Finally, the total coal burnout changes little.

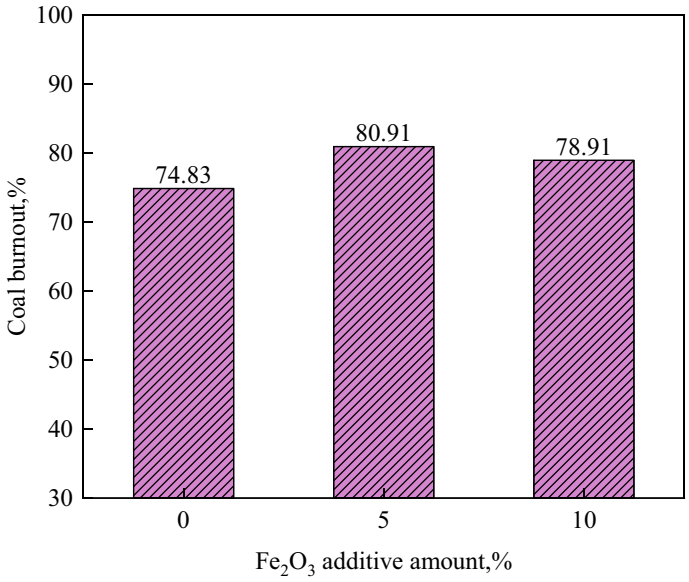

Fig. 2 Effect of Fe_2O_3 addition amount on final coal burnout

To further understand the effect of Fe_2O_3 on coal combustion, the coal burnout at different positions was investigated, as shown in Fig. 3. The coal combustion process is greatly advanced with increase of Fe_2O_3 addition amount, and the combustion rate rapidly increases in the early stage. The coal burnout slowly increases in the early stage without Fe_2O_3 addition and begins to rapidly increase at the distance of 0.4 m from the coal lance tips. The coal burnout begins to rapidly increase at 0.2 m distance under 5% Fe_2O_3 addition amount. The distance is only 0.1 m under 10% Fe_2O_3 addition amount. The coal burnout still remains rapid increase at the later stage of raceway region without Fe_2O_3 addition. However, the combustion process slows at the later stage of raceway region with Fe_2O_3 addition. Finally, the gap in coal burnout gradually decreases at the end of raceway region. The reasons causing aforementioned phenomenon are as follows. The activation energy of pyrolysis process decreases with the increase of Fe_2O_3 addition amount, and the coal rapidly combusts in the early stage. However, the combustion process greatly weakens due to the lack of oxygen in the later stage. In general, the main reasons causing the little change of final coal burnout are the lack of oxygen.

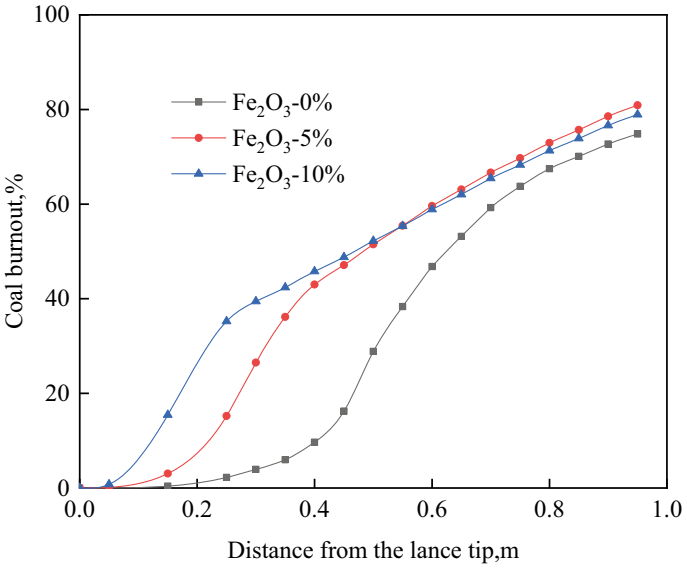

Fig. 3 Effect of Fe_2O_3 addition addition amount on coal burnout at different positions

Effect of Fe_2O_3 on Coal Combustion Under Local Oxygen Enrichment

The oxygen concentration around coal particles will be greatly increased by local oxygen enrichment, and the coal burnout will significantly increase. Therefore, the effect of Fe_2O_3 addition on coal combustion under local oxygen enrichment was investigated. The effect of Fe_2O_3 addition amount on coal burnout under local oxygen enrichment is shown in Fig. 4. The coal burnout significantly increases under local oxygen enrichment. The coal burnout without Fe_2O_3 addition under local oxygen enrichment is 91.06% with an increase of 16.23% than that of base case. The coal burnout of 5% Fe_2O_3 addition amount is 96.42% with an increase of 21.59% than base case. The coal burnout of 10% Fe_2O_3 addition amount is 96.86% and most coal particles have full combusted.

To further reveal the effect of Fe_2O_3 on coal combustion under local oxygen enrichment, the coal burnout at different positions is investigated, as shown in Fig. 5. The coal combustion process is delayed without Fe_2O_3 addition due to the cooling effect of room temperature. However, the coal burnout rapidly increases at the 0.6 m distance from the coal lance tips. This is because the room-temperature oxygen competes for heat with coal particles, and the devolatilization process is mainly affected by temperature. The char rapidly combusts at the later stage under rich oxygen concentration. The coal combustion process is not delayed with Fe_2O_3 addition and is greatly advanced with increase of Fe_2O_3 addition amount. This is because

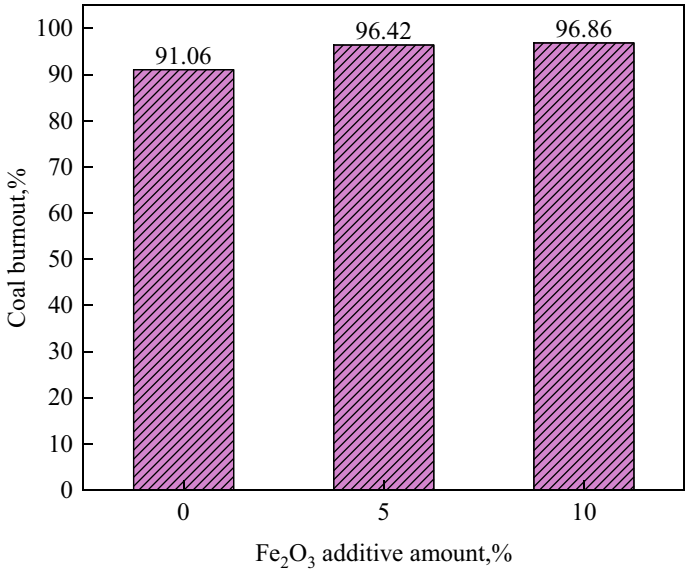

Fig. 4 Effect of Fe_2O_3 addition amount on final coal burnout under local oxygen enrichment

the pyrolysis rate increases with Fe_2O_3 addition, which makes up the cooling effect of room temperature.

Figure 6 shows the flow and combustion characteristics of coal plume. In general, the coal particles are more dispersed under local oxygen enrichment. The oxygen stream flows into the inner region of coal plume, and the coal particles in the center region are pushed toward surroundings. More coal particles will contact with oxygen, which is beneficial for coal combustion. The coal burnout without Fe_2O_3 addition in the early stage is lower. Much coal particles of higher burnout can be found in the early stage of the raceway region under Fe_2O_3 addition. Furthermore, the particles' concentration in the center region of coal plume is higher and the burnout is lower. This is because large amount of coal particles are concentrated in the center region of coal plume, and the oxygen surrounding the particles cannot meet the combustion of whole particles. For local oxygen enrichment, the coal burnout in the center region is high, but the burnout around coal plume is lower. This is because the oxygen flows into the center region of coal plume, and the oxygen concentration greatly increases.

Conclusions

The effect of Fe_2O_3 on coal flow and combustion characteristics in the blast furnace was investigated using the CFD method. The main conclusions are as follows:

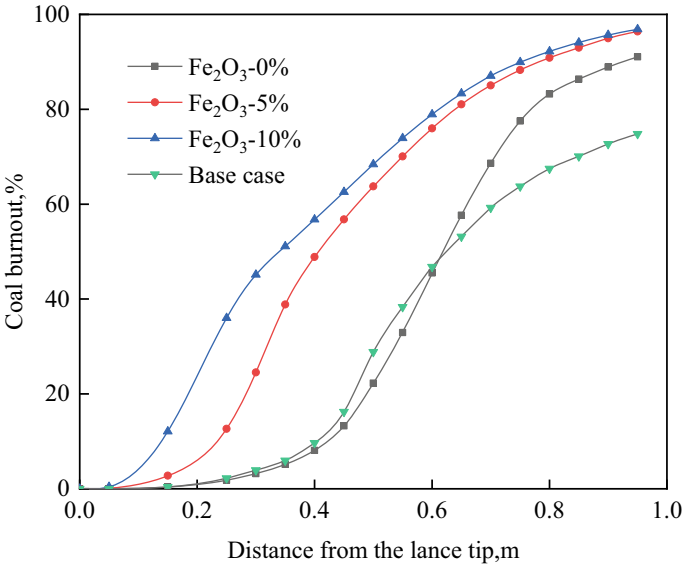

Fig. 5 Effect of Fe_2O_3 on coal burnout at different positions under local oxygen enrichment

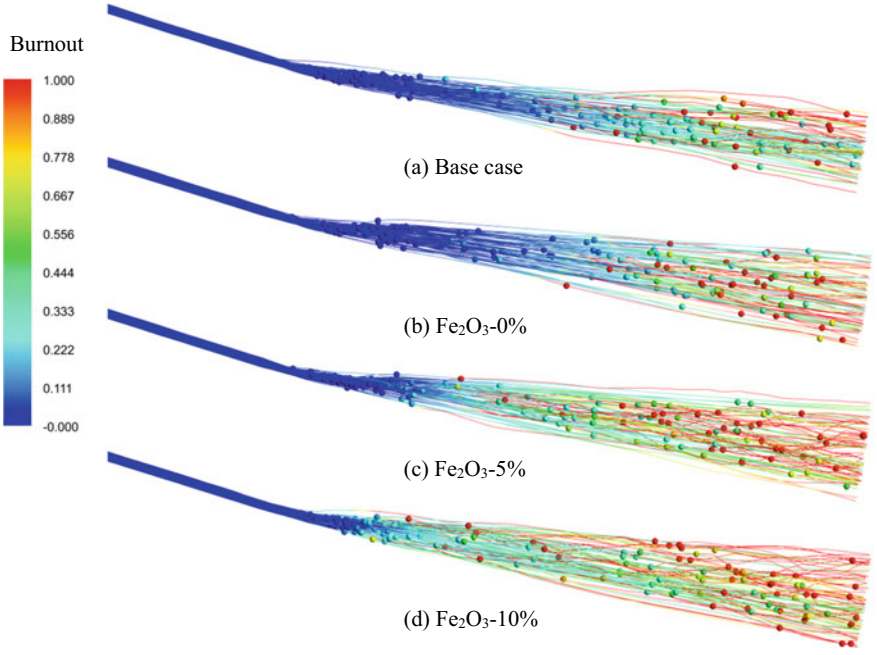

Fig. 6 Coal flow and combustion characteristics under local oxygen enrichment

(1) The effect of Fe_2O_3 on coal burnout is unobvious without oxygen enrichment, but the coal combustion process is advanced. The main reasons are that the activation energy of pyrolysis process is reduced, but the further combustion is limited by oxygen.
(2) For local oxygen enrichment, the coal burnout greatly increases with Fe_2O_3 addition. The coal burnout is 96.86% with the addition of 10% Fe_2O_3, which is an increase of 22.03% than base case.
(3) The coal combustion process is delayed due to the cooling effect of room-temperature oxygen. However, the cooling effect is offset by the addition of Fe_2O_3. This is because of the significant increase of pyrolysis rate that ensures the full utilization of oxygen.

References

1. Suopajarvi H, Pongracz E, Fabritius T (2014) Bioreducer use in Finnish blast furnace ironmaking—analysis of CO_2 emission reduction potential and mitigation cost. Appl Energ 124:82–93
2. Wang H, Zhao W, Chu M, Feng C, Liu Z, Tang J (2017) Current status and development trends of innovative blast furnace ironmaking technologies aimed to environmental harmony and operation intellectualization. J Iron Steel Res Int 8(24):751–769
3. Shen Y, Guo B, Yu A, Zulli P (2009) Model study of the effects of coal properties and blast conditions on pulverized coal combustion. ISIJ Int 6(49):819–826
4. Shen Y, Maldonado D, Guo B, Yu A, Austin P, Zulli P (2009) Computational fluid dynamics study of pulverized coal combustion in blast furnace raceway. Ind Eng Chem Res 23(48):10314–10323
5. Zhou C, Liu G, Wang X, Qi C (2016) Co-combustion of bituminous coal and biomass fuel blends: thermochemical characterization, potential utilization and environmental advantage. Bioresour Technol 218:418–427
6. Tiwari H, Das A, Singh U (2018) Novel technique for assessing the burnout potential of pulverized coals/coal blends for blast furnace injection. Appl Therm Eng 130:1279–1289
7. Liu Y, Shen Y (2019) CFD study of charcoal combustion in a simulated ironmaking blast furnace. Fuel Process Technol 191:152–167
8. Zhou Z, Xue Q, Li C, Wang G, She X, Wang J (2017) Coal flow and combustion characteristics under oxygen enrichment way of oxygen-coal double lance. Appl Therm Eng 123:1096–1105
9. Fu Y, Guo Y, Zhang K (2016) Effect of three different catalysts (KCl, CaO, and Fe_2O_3) on the reactivity and mechanism of low-rank coal pyrolysis. Energ Fuels 3(30):2428–2433
10. Wu L, Zhou J, Yang R, Tian W, Song Y, Zhang Q et al (2021) Enhanced catalytic microwave pyrolysis of low-rank coal using Fe_2O_3@ bluecoke absorber prepared by a simple mechanical ball milling. J Energ Inst 95:193–205
11. Launder BE, Spalding DB (1972) Lectures in mathematical models of turbulence
12. Wu D, Zhou P, Yan H, Shi P, Zhou CQ (2019) Numerical investigation of the effects of size segregation on pulverized coal combustion in a blast furnace. Powder Technol 342:41–53
13. Zhou Z, Huo H, Wang G, Xue Q, She X, Wang J (2017) Effect of oxygen-coal lance configurations on coal combustion behavior. Steel Res Int 1(88):1600197
14. Shen Y, Shiozawa T, Austin P, Yu A (2014) Model study of the effect of bird's nest on transport phenomena in the raceway of an ironmaking blast furnace. Miner Eng 63:91–99
15. Ubhayakar SK, Stickler DB, Von Rosenberg CW, Gannon RE (1977) Rapid devolatilization of pulverized coal in hot combustion gases. In: Symposium (international) on combustion. Elsevier, pp 427–436

16. Shen YS, Guo BY, Yu AB, Maldonado D, Austin P, Zulli P (2008) Three-dimensional modelling of coal combustion in blast furnace. ISIJ Int 6(48):777–786
17. Wijayanta AT, Alam MS, Nakaso K, Fukai J, Kunitomo K, Shimizu M (2014) Numerical study on pulverized biochar injection in blast furnace. ISIJ Int 7(54):1521–1529

Modeling Carbon Composite Briquette Reaction Under H_2-H_2O-CO-CO_2-N_2 Atmosphere

Siyuan Cheng and Huiqing Tang

Abstract Charge carbon composite briquette (CCB) is an effective method to reduce CO_2 emissions and save energy in blast furnace (BF) ironmaking. Presently with the hydrogen-bearing gas being injected in the BF, the content of H_2 and H_2O in the BF gas is comparable to those of CO and CO_2, and they could not be ignored in analyzing the CCB reaction behavior in the BF shaft. In this research, a mathematical model was developed for analyzing the reaction behavior of CCB under the H_2-H_2O-CO-CO_2-N_2 atmosphere. The model was one-dimensional. Chemical reactions, internal gas diffusion, and mass transfer between the CCB and the atmosphere were considered in the model. Using the model, the influence of gas composition and temperature on CCB reaction was discussed and the reaction progress was investigated. The simulation results showed that increasing temperature or increasing hydrogen in the atmosphere can prompt the reduction of iron oxide and the gasification of carbon in CCB. In the investigated temperature range, iron oxide reduction by hydrogen and carbon gasification by water vapor played important roles in the CCB reaction process.

Keywords Carbon composite briquette · Model · Reaction behavior · Blast furnace · Hydrogen

Introduction

Steel materials play an important role in the world's economy, and at present, the demand for steel materials is still increasing. The blast furnace (BF) ironmaking has the advantages such as simple process and high production efficiency, so the BF-BOF (basic oxygen converter) process is the predominant route for producing iron and steel all over the world [1]. However, BF ironmaking is responsible for most of

S. Cheng · H. Tang (✉)
State Key Laboratory of Advanced Metallurgy, University of Science and Technology Beijing, 30 Xueyuan Rd., Beijing 100083, China
e-mail: hqtang@ustb.edu.cn

© The Minerals, Metals & Materials Society 2024

C. Iloeje et al. (eds.), *Energy Technology 2024*, The Minerals, Metals & Materials Series, https://doi.org/10.1007/978-3-031-50244-6_21

the CO_2 emissions in the BF-BOF process and occupies more than 70% of the total energy consumption. In recent years, to prevent global warming, many countries have paid attention to CO_2 emissions reduction. For example, China launched its policies to realize the goal of "carbon peak" by 2030 and "carbon neutral" by 2060 [2]. Therefore, reducing CO_2 emissions and energy consumption is the main development direction in BF ironmaking in the future.

Charging carbon composite briquette (CCB) in BF is considered to be a promising technology for efficient BF operations and has been demonstrated by several industrial practices [3, 4]. CCB represents a class of materials produced by agglomerating fine powders of carbonaceous materials with iron ore fines. On the other hand, considering that hydrogen energy has the advantages of diverse sources and low carbon emissions, the injection of hydrogen-rich gases (natural gas, coke oven gas, and so on) into the BF has set off an upsurge [5–7]. It is considered that a combination of these two technologies may even improve the operation efficiency of the BF. Hydrogen and water vapor are insignificant components in BF gas in traditional BF operations; therefore, previous studies on CCB reaction behavior were mainly carried out under a CO-CO_2-N_2 atmosphere. However, in the case of BF operations with enhanced hydrogen reduction, hydrogen and water vapor in BF gas could not be ignored and their influence on CCB reaction behavior has to be considered. Thus, its reaction kinetics and reaction development under an H_2-H_2O-CO-CO_2-N_2 atmosphere need studies for a better combination of the technologies of CCB charging and BF hydrogen-rich metallurgy.

In this study, a mathematical model has been developed for CCB reaction under the H_2-H_2O-CO-CO_2-N_2 atmosphere. Afterward, the influences of reaction temperature and gas composition on CCB reaction behavior were investigated, and the reaction development in the CCB under specific conditions was elucidated.

Numerical Investigation

Simulation Conditions

The CCB employed in the present simulation was prepared using cold briquetting followed by heat treatment [8]. The CCB had a diameter (d) of 0.015 m and a mass of 5.0 g. Its properties are given in Table 1. The CCB was prepared using cold briquetting followed by heat treatment; therefore, volatile in the CCB was negligible. The gangue in CCB mainly included SiO_2 and Al_2O_3.

To understand the CCB reaction behavior under CO-CO_2-H_2-H_2O-N_2 atmosphere (BF gas atmosphere), six cases were investigated. The conditions of simulation for each case are listed in Table 2. As under high temperature, the reaction (R1) can reach thermodynamic equilibrium quickly; therefore, in Table 2, the volume fractions of CO, CO_2, H_2, and H_2O satisfy the thermodynamic equilibrium of reaction (R1) under the corresponding temperature. The reaction time of each case was fixed at 1800 s.

Table 1 Properties of CCB

Mass/g	Diameter/m	Porosity/–	Chemical composition			
			Carbon/wt.%	FeO/wt.%	Metallic iron/ wt.%	Gangue/wt.%
5.0	0.015	0.4	14.33	66.14	6.87	12.66

Table 2 Conditions of simulation cases

Case No	Temperature/K	Atmosphere (BF gas)				
		CO/vol.%	CO_2/vol.%	H_2/vol.%	H_2O/vol.%	N_2/vol.%
I	973	20	6.2	20	3.8	50
II	1073	20	4.8	20	5.2	50
III	1173	20	3.4	20	5.6	50
IV	1273	20	3.8	20	6.2	50
V	1173	30	7.0	10	3.0	50
VI	1173	10	2.1	30	7.9	50

$$\begin{gathered} \mathrm{CO(g)} + \mathrm{H_2O(g)} = \mathrm{CO_2(g)} + \mathrm{H_2(g)} \\ \Delta G^0 = 0.031T - 33.64 \ \mathrm{(kJ)} \end{gathered} \tag{R1}$$

Reaction Model

The model is established for the reaction of a single CCB in the BF upper part and is one-dimensional in the radial direction. The model includes reactions that occurred in the CCB, the internal gas diffusion, and the mass transfer between CCB and BF gas. The concept of the model is shown in Fig. 1. Both the gas phase and the solid phase are considered in the model. The gas phase is an ideal gas and includes CO, CO_2, H_2, H_2O, and N_2. As the CCB was partially reduced in the preparing stage, the solid phase only includes FeO, Fe, and C. Assumptions in the model are (1) CCB volume is constant throughout the reaction process, (2) mass transfer by convection is not considered, and (3) the involved reactions are the reactions given in Table 3.

The general governing equation of the gas phase is built based on the mass conservation of the gas species in the CCB. It is Eq. (1).

$$\frac{\partial(\alpha P_i)}{\partial t} = \frac{1}{r^2}\frac{\partial}{\partial r}\left(r^2(\alpha^2 D_{\mathrm{i-N_2}}/\sqrt{3})\frac{\partial P_{\mathrm{i}}}{\partial r}\right) + S_i \tag{1}$$

where i = CO, CO_2, H_2, and H_2O; P: pressure, pa; t: time, s; r: radial direction, m; D_{i-N_2}: gas diffusivity, $m^2\ s^{-1}$; α: porosity,–; $S_{CO} = RT(R_4 + 2.0R_3 - R_1)$; $S_{CO_2} = RT(R_1 - R_3)$; $S_{H_2} = RT(R_4 - R_2)$; and $S_{H_2O} = RT(R_2 - R_4)$.

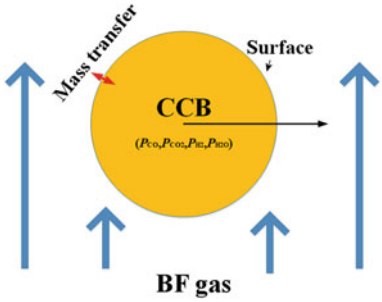

Fig. 1 Illustration of the model

Table 3 Reactions involved in the model

No	Reaction	Reaction rate/(mol m^{-3} s^{-1})	References
1	FeO (s) + CO (g) = Fe (s) + CO_2(g)	$R_1 = \frac{(P_{CO}-P_{CO_2}/K_1)/(8.314T)}{(K_1/(k_1(1+K_1))}(1-f_O)^{2/3})a_{gs}$ $k_1 = \exp(0.805 - 7385/T)$, $K_1 = \exp(-2.946 + 2744.63/T)$	[8, 9]
2	FeO (s)+H_2(g) = Fe (s) + H_2O (g)	$R_2 = \frac{(P_{H_2}-P_{H_2O}/K_2)/(8.314T)}{(K_2/(k_2(1+K_2))}(1-f_O)^{2/3})a_{gs}$ $k_2 = \exp(7.96 - 14096/T)$, $K_2 = \exp(0.9387 - 1586.9/T)$	
3	C (s) + CO_2(g) = 2CO (g)	$R_3 = \rho_{C,0}k_3(1-f_C)^{2/3}(P_{CO_2}/1.01\times10^5)/M_C$, $k_3 = 1600\exp(-138000/RT)$	
4	C (s) + H_2O (g) = CO (g) + H_2(g)	$R_4=\rho_{C,0}k_4(1-f_C)^{2/3}(P_{H_2O}/1.01\times10^5)/M_C$, $k_4 = 1400\exp(-130000/RT)$	

where R_i (i = 1–4): reaction rate of reaction i, mol m^{-3} s^{-1}; K_i: equilibrium constant; k_i: rate constant; T is temperature, K; f_o: reduction fraction of iron oxide, –; f_c: gasification fraction of carbon, –; P: partial pressures of gas species, pa. α_{gs}: specific area, m^2 m^{-3}, and is 1600 m^2/m^3. ρ: density, kg m^{-3}. M: molar weight, kg mol^{-1}

For Eq. (1), the boundary conditions are Eqs. (2, 3), and the initial conditions are Eq. (4).

$$r = 0 : \frac{\partial P_i}{\partial r} = 0 \tag{2}$$

$$r = d/2 : P_i = P_{i,e} \tag{3}$$

$$t = 0,\ r \in (0, d/2) : P_i = P_{i,\,e} \tag{4}$$

where $P_{i,e}$ represents the partial pressure of species i in the atmosphere, Pa.

The general governing equation of the solid phase is constructed based on the mass conservation of the solid phase species. They are Eq. (5).

$$\partial \rho_j / \partial t = S_j \tag{5}$$

where j = FeO, Fe, and C; ρ_j is the density of species j. $S_{\mathrm{FeO}} = M_{\mathrm{FeO}}(-R_1 - R_2)$, $S_{\mathrm{Fe}} = M_{\mathrm{Fe}}(R_1 + R_2)$, and $S_{\mathrm{C}} = -M_{\mathrm{C}}(R_3 + R_4)$.

The initial conditions for Eq. (5) are Eq. (6).

$$t = 0, r \in (0, d/2); \rho_j = \rho_{j,0} \tag{6}$$

Equation (1) is spatially and temporally discretized using an explicit scheme. Equation (5) is solved using an explicit time integration method. Equations (1) and (5) are solved simultaneously.

Results and Discussion

Influence of Temperature

Simulation results of cases I–IV are shown in Figs. 2 and 3. Figure 2 shows the influence of reaction temperature on the iron oxide reduction in CCB. It could be seen that, in case I, the CCB reaches a reduction fraction of 0.68 at 1800 s; in case II, it reaches a reduction fraction of 0.95 at 1800 s; in case III, it reaches a full iron oxide reduction at approximately 700 s; and in case IV, it reaches an iron oxide full reduction by 280 s. Therefore, increasing the temperature is beneficial to the reduction of iron oxide in the CCB. Figure 3 shows the influence of reaction temperature on carbon gasification in CCB. By the end of the reaction, the gasification fraction of carbon in CCB is 0.08 in case I, 0.40 in case II, 0.70 in case III, and 0.85 in case IV, indicating that increasing temperature also prompts the gasification of carbon in the CCB.

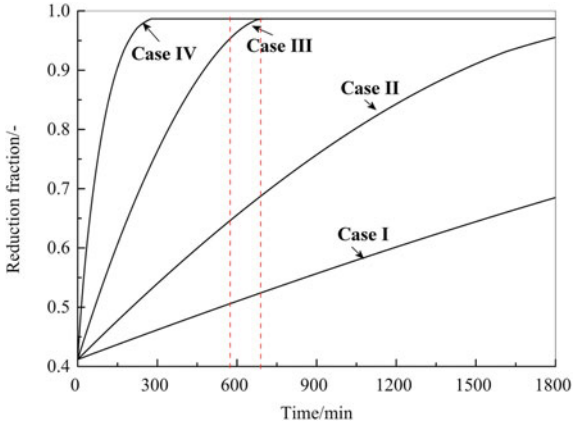

Fig. 2 Influence of temperature on iron oxide reduction in CCB

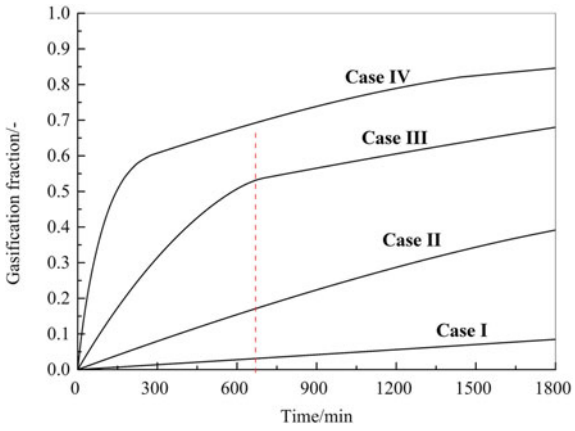

Fig. 3 Influence of temperature on carbon gasification in CCB

Influence of BF Gas Composition

Simulation results of cases III, V, and VI are shown in Figs. 4 and 5. Figure 4 shows the influence of gas composition on the reduction of iron oxide in CCB. It could be seen that the iron oxide in CCB reaches a full reduction at 1100 s in case V, at 700 s in case III and, at 500 s in case VI. Figure 5 shows the influence of gas composition on the carbon gasification in CCB. It is observed that, by the end of the CCB reaction, the gasification fraction of carbon reaches 0.58 in case V, 0.68 in case III, and 0.75 in case VI. Therefore, increasing hydrogen in BF gas can accelerate the reduction of iron oxide and the gasification of carbon in CCB.

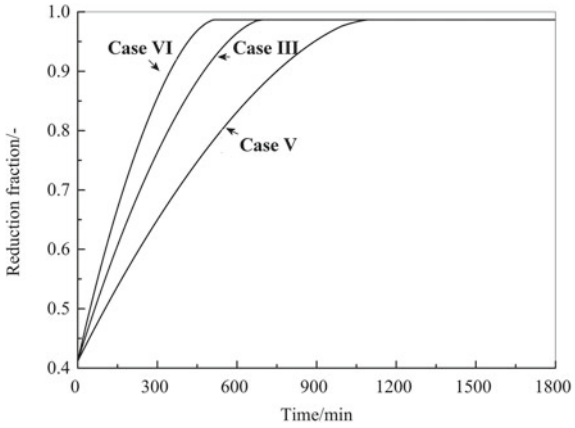

Fig. 4 Influence of BF gas composition on iron oxide reduction in CCB

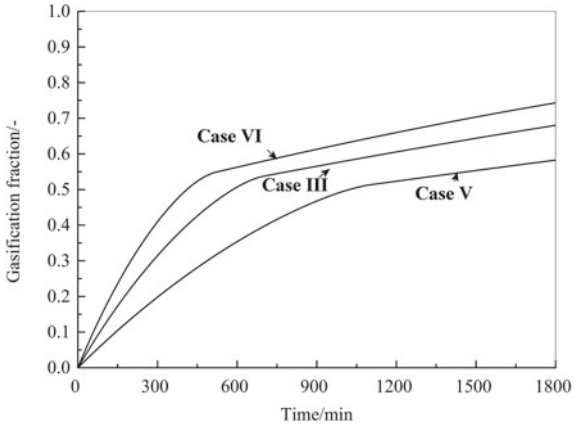

Fig. 5 Influence of BF gas composition on carbon gasification in CCB

Reaction Development in CCB

Case III was selected for analyzing the reaction development in CCB. The results are shown in Fig. 6a–d. From Fig. 6, the reaction development is assumed to be the following. Initially, the rate of Reaction (2) is high. Therefore, the CCB consumed hydrogen from the atmosphere and produced H_2O to the atmosphere. With the development of reaction time, the rate of Reaction (2) decreased. At 600 s, Reaction (4) proceeded faster than Reaction (2). Therefore, the CCB consumed H_2O from the atmosphere and produced hydrogen to the atmosphere. Before the end of iron oxide reduction, the CCB produced CO and CO_2 to the atmosphere. At 600 s, the reduction of iron oxide in CCB was completed. Thereafter, only Reactions (3) and (4) remained. The CCB consumed CO_2 and H_2O from the atmosphere and produced CO and H_2 to the atmosphere; moreover, the pattern of carbon gasification is altered. From the above analysis, it is known that in a hydrogen-rich atmosphere, Reactions (2) and (4) played more important roles in the CCB reaction development than Reactions (1) and (3).

Conclusions

In this study, using the CCB containing carbon: 14.33 wt%, FeO: 66.14 wt%, metallic iron: 6.87 wt%, and gangue: 18.23 wt%, reaction behavior under hydrogen-rich BF gas (H_2-H_2O-CO-CO_2-N_2) was numerically investigated. Some conclusions could be drawn and are the following.

(1) Increasing temperature was beneficial to the reduction of iron oxide and the gasification of carbon in CCB.
(2) Increasing hydrogen in BF gas prompted the reduction of iron oxide and the gasification of carbon in CCB.

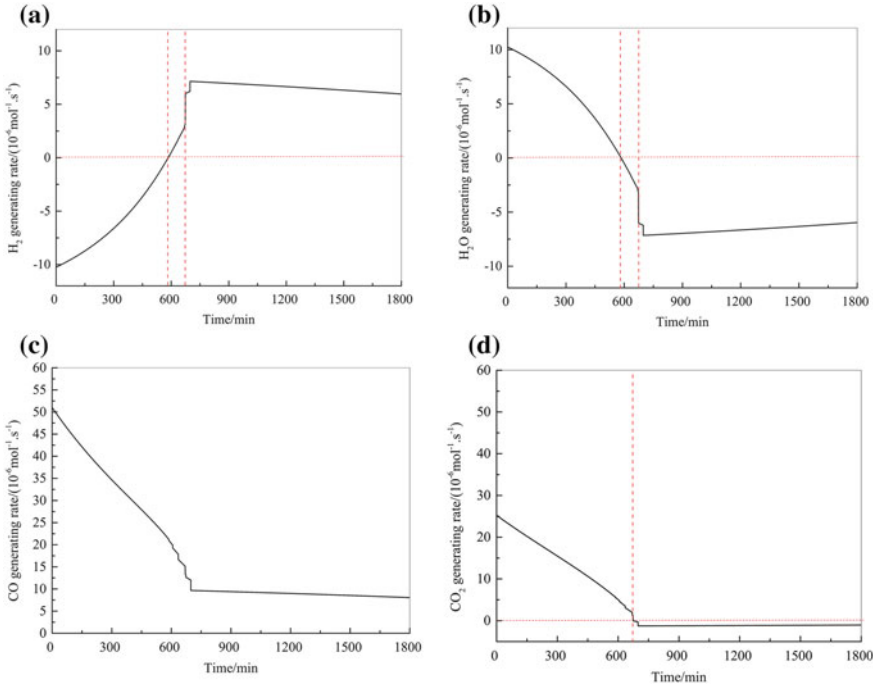

Fig. 6 Gas generating rate: **a** H_2, **b** H_2O, **c** CO, and **d** CO_2

(3) In the reaction of CCB, the CCB initially consumed H_2 from the atmosphere, and it consumed H_2O by the end of iron oxide reduction and consumed CO_2 and H_2O after the iron oxide reduction was completed. Iron oxide reduction by hydrogen and carbon gasification by water vapor played important roles in the reaction process.

Acknowledgements The authors thank the National Natural Science Foundation of China (No. U1960205), and the State Key Laboratory of Advanced Metallurgy USTB for the financial support of this work.

References

1. Naito M, Takeda K, Matsui Y (2015) Ironmaking technology for the last 100 years: deployment to advanced technologies from introduction of technological know-how, and evolution to next-generation process. ISIJ Int 55(1):7–35
2. Zhang C, Vladislav L, Xu R, Sergey G, Jiao K, Zhang J, Li T, Aleksei T, Wang C, Wang G (2022) Blast furnace hydrogen-rich metallurgy-research on efficiency injection of natural gas and pulverized coal. Fuel 311:122412

3. Kasai A, Toyota H, Nozawa K, Kitayama S (2011) Reduction of reducing agent rate in blast furnace operation by carbon composite iron ore hot briquette. ISIJ Int 51(8):1333–1335
4. Yokoyama H, Higuchi K, Ito T, Oshino A (2012) Decrease in carbon consumption of a commercial blast furnace by using carbon composite iron ore. ISIJ Int 52(11):2000–2006
5. Okosun T, Nielson S, Zhou C (2022) Blast furnace hydrogen injection: investigating impacts and feasibility with computational fluid dynamics. JOM 74(4):1521–1532
6. Ren M, Liu W, Zhao J, Zou C, Ren L, Wu H, Zhao J (2023) Effects of hydrogen fraction in co-injection gas on combustion characteristics of the raceway in low carbon emission blast furnace. Int J Hydrogen Energ 48(30):11530–11540
7. Bernasowski M (2014) Theoretical study of the hydrogen influence on iron oxides reduction at the blast furnace process. Steel Res Int 85(4):670–678
8. Tang H, Sun Y, Rong T, Guo Z (2021) Reaction model and reaction behavior of carbon composite briquettein blast furnace. Powder Technol 377:832–842
9. Tang H, Guo Z, Kitagawa K (2012) Simulation study on performance of z-path moving-fluidized bed for gaseous reduction of iron ore fines. ISIJ Int 52(7):1241–1249

Numerical Simulation and Optimization of Local Resistance Characteristics for Energy-Saving Operation in H-Type Ventilation System

Liangzhen Jiao, Xinru Deng, Jiarui Deng, Hang Hu, and Xiusong Duan

Abstract The energy consumption of industrial ventilation systems plays an important role in industry building systems. The resistance of local components accounts for a large part of the total resistance of industrial ventilation systems. Reducing the resistance loss of local components is of great importance for improving the energy efficiency of a ventilation system. In this paper, ANSYS Fluent 18.2 software was used to research the resistance characteristics of the ventilation system with different flow deflectors. The results indicated that adding flow deflectors at the tee could maintain the air volume balance of the ventilation system, reduce the resistance loss, and increase the maximum reduction of resistance rate by 19% in the ventilation system. This study is expected to optimize the low-carbon and energy-saving operation of industrial ventilation systems.

Keywords Numerical simulation · Ventilation system · Local resistance · Energy-saving operation

Introduction

The fan energy consumption caused by ventilation duct resistance accounts for a large proportion of the total power consumption of the building, among which the resistance of local components (tees) accounts for 40–60% of the total resistance of the ventilation and air conditioning duct system [1]. Therefore, optimizing the structure of local components and reducing the resistance loss of local components is of great significance for reducing the energy consumption of the ventilation system.

L. Jiao · X. Deng · J. Deng · X. Duan (✉)
School of Urban Construction, Wuhan University of Science and Technology, Wuhan 430070, China
e-mail: duanxiusong@163.com

H. Hu
School of Minerals Processing and Bioengineering, Central South University, Changsha 410083, China

© The Minerals, Metals & Materials Society 2024

C. Iloeje et al. (eds.), *Energy Technology 2024*, The Minerals, Metals & Materials Series, https://doi.org/10.1007/978-3-031-50244-6_22

Besides, improper design of the ventilation system can lead to severe hydraulic imbalance, resulting in system energy waste, and affecting indoor comfort.

In previous studies on local components, Li, Gong et al. reduced local resistance loss by optimizing the curved surface of the three-way, and Chen, Li, Xie, Wang et al. studied the influence of flow deflectors on local resistance loss. Studies have displayed that adding flow deflectors at the local components of the air duct can improve the flow characteristics of the air stream and reduce the local resistance [1–7]. From the above research status, it can be seen that there have been many studies on the application of flow deflectors in reducing resistance at local components. This paper took the H-type ventilation system as an example to study the reduction of resistance and air volume distribution. By adding flow deflectors in the tee and changing the relative positions of the flow deflectors, the optimal position of the flow deflectors was found from two aspects of the resistance loss and air volume distribution, aiming to reduce resistance loss and maintain air volume balance.

Case Study

Structure of H-Type

H-type ventilation system is one of the commonly used ventilation systems in the design process of ventilation systems and is often applied for end supply in large-scale ventilation systems. The schematic diagram illustrating the structure of the experimental research object in this study is displayed in Fig. 1.

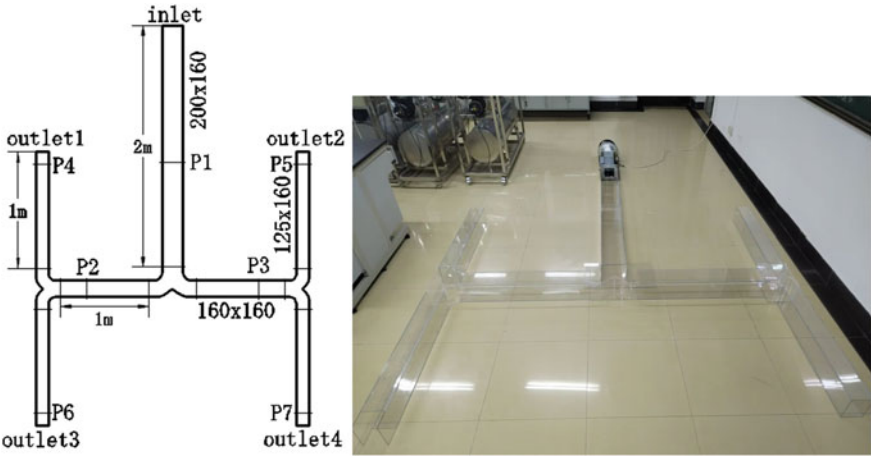

Fig. 1 H-type ventilation system model

Experiment

Acrylic panels were employed as the material for constructing the ventilation system of the experiment (Fig. 1). Sealing treatments were applied to all system connections.

As displayed in Fig. 1, this experiment set up a total of seven measurement sections, including the upstream 5D position of the inlet tee, the upstream 2D position of the outlet tee, and four air supply outlets. Each measurement section consisted of nine measurement points for measuring the air velocity at each location. The average value of the nine measurement points was recorded as the average air velocity of that section.

Governing Equation

This paper primarily studied the airflow organization in the ventilation system and the resistance loss of the ventilation system. Heat exchange between the airflow and the inner surface of the duct was not taken into account. The airflow inside the duct was considered as an incompressible fluid, and the airflow was assumed to be in a steady-state turbulent state. The governing equations were as follows.

(1) Continuity equation

$$\frac{\partial u_x}{\partial x} + \frac{\partial u_y}{\partial y} + \frac{\partial u_z}{\partial z} = 0 \tag{1}$$

(2) Momentum equations

$$\frac{\partial(\rho u_x)}{\partial t} + \nabla \cdot (\rho u_x \vec{u}) = -\frac{\partial \rho}{\partial x} + \frac{\partial \tau_{xx}}{\partial x} + \frac{\partial \tau_{yx}}{\partial y} + \frac{\partial \tau_{zx}}{\partial z} + F_x \tag{2}$$

$$\frac{\partial\left(\rho u_y\right)}{\partial t} + \nabla \cdot \left(\rho u_y \vec{u}\right) = -\frac{\partial \rho}{\partial y} + \frac{\partial \tau_{xy}}{\partial x} + \frac{\partial \tau_{yy}}{\partial y} + \frac{\partial \tau_{zy}}{\partial z} + F_y \tag{3}$$

$$\frac{\partial(\rho u_z)}{\partial t} + \nabla \cdot (\rho u_z \vec{u}) = -\frac{\partial \rho}{\partial z} + \frac{\partial \tau_{xz}}{\partial x} + \frac{\partial \tau_{yz}}{\partial y} + \frac{\partial \tau_{zz}}{\partial z} + F_z \tag{4}$$

where p is the pressure exerted on the fluid elemental volume, N; $\overrightarrow{u}$ is velocity vector, m/s; τ_{xx}, τ_{xy}, τ_{xz} are the surface components of the viscous stress τ on the element body; F_x, F_y, F_z are physical strengths on the micro body.

Table 1 Comparison of experimental and simulated airflow velocities of duct measurement section

	Measured cross-section velocity (m/s)						
	1	2	3	4	5	6	7
Experiment	6.81	4.24	4.15	2.62	2.65	2.59	2.63
Simulation	6.81	4.26	4.26	2.75	2.75	2.83	2.83
Absolute difference	0	0.02	0.11	0.13	0.10	0.24	0.20
Percentage difference	0	0.47%	2.65%	4.96%	3.77%	9.27%	7.60%

Model Selection and Validation

In the simulation of airflow organization, common turbulence models include the standard k–ε model, RNG k–ε model, realize k–ε model, and RSM Reynolds stress model. Among them, the RSM model fully considers the influence of vortex, rotating tension, and streamline deformation on the simulation, which is more reliable for the simulation accuracy of complex flows (such as curved duct lines).

In order to verify the feasibility of the model RSM, the experimental measurement results of the constructed H-type ventilation system were compared with the simulation results. The measured data was the average air speed of each measured section of the ventilation system.

It can be observed from Table 1 that the simulated values and the measured values of the airflow velocity at the measurement points of the air duct were close to the simulated values model and the measured values of the model RSM, with a fitting degree of over 90%. Therefore, the model RSM is reliable, and the model established in this paper can be used to simulate and analyze the airflow organization of the ventilation system.

Results and Discussion

Simulated Conditions

The dimensions of the ventilation system studied in this paper were twice that of the experimental ventilation system. The main duct length of the H-type ventilation system measured 5 m, and the dimensions were 400 mm × 320 mm. The length of the branch ducts on both sides measured 2 m, and the dimensions were 320 mm × 320 mm. The length of the end air duct measured 2 m and the dimensions were 250 mm × 320 mm.

The tee part was modeled as unstructured mesh, and the tee part adopted grid encryption. The straight duct sections were structural grids. After grid independence analysis, the total number of grid cells was 950,000.

The RSM model was adopted. The inlet adopted the velocity inlet, and the inlet speed was set to 7 m/s. The outlet was set to a pressure outlet, and the rough height was set to 0.15 mm. The SIMPLE algorithm was used, and the second-order upwind scheme was used for convective interpolation.

Position of Flow Deflectors

In order to solve the problem of local resistance loss, the method of adding flow deflectors to the tee in the upstream section of the branch ducts was put forward in this paper. The flow deflectors were intended to reduce the resistance loss of the tee. Additionally, this paper has investigated the impact of the flow deflectors on the airflow distribution at the outlets.

The structure of the tee is displayed in Fig. 2. Through the two ends and the midpoint of the deflector in the tee relative position, the relative position of deflectors could be determined. Specifically, the relative position of the starting end was denoted as $2b_1/B_1$; the relative position of the middle end and tail end was denoted as b_2/B_2 and b_3/B_2.

Considering the uniform distribution of air volume in the tee, flow deflectors at the following position were set in the tee to simulate airflow organization (Table 2).

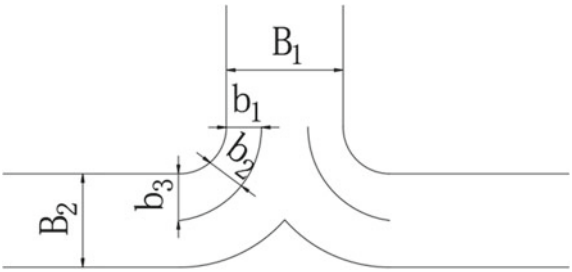

Fig. 2 Structure diagram of the tee

Table 2 Relative position of the deflector

The relative position of deflectors	Parameters of the deflector							
	A	*B*	*C*	*D*	*E*	*F*	*G*	*H*
$2b_1/B_1$	0.5	0.5	0.5	0.6	0.6	0.6	0.6	No deflector
b_2/B_2	0.3	0.3	0.4	0.3	0.4	0.4	0.5	
b_3/B_2	0.4	0.5	0.5	0.4	0.5	0.6	0.6	

(a) No deflector (b) Deflectors C (c) deflectors G

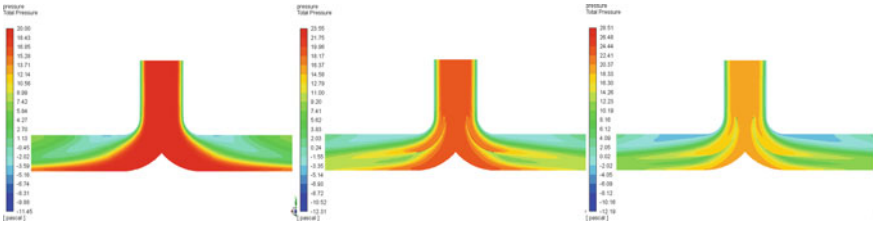

Fig. 3 Pressure contour plots of airflow organization of tee with different flow deflectors

Influence of Deflectors on Local Resistance

Local resistance coefficient:

$$\xi = \frac{\Delta P}{\frac{1}{2}\rho v^2} \tag{5}$$

In Eq. (5), ξ is the local resistance factor; ΔP is the local resistance of the tee, Pa; ρ is the air density, kg/m^3; v is the exit speed of the tee.

Reduction of resistance rate η:

$$\eta = \frac{\xi_n - \xi_0}{\xi_n} \times 100\% \tag{6}$$

In Eq. (6), η is the reduction of the resistance rate of the flow deflectors; ξ_n is the local resistance coefficient of the tee with adding flow deflectors; ξ_0 is the local resistance coefficient of the tee without adding flow deflectors.

The simulation results are displayed in Figs. 3 and 4. Due to the reduction of resistance rate of flow deflector D being $-$ 66%, and in order to visually compare the reduction of resistance rate of other flow deflectors, the flow deflector D was removed. As can be seen from Fig. 4, flow deflectors A and B would increase the local resistance loss of the tee. The flow deflectors C and G had an obvious reduction of resistance effect, and the maximum reduction of resistance rate was 19%.

Influence of Deflector on Air Volume Distribution

The velocity distribution contour plots are displayed in Fig. 5 and the airflow velocity distribution of the outlets is displayed in Table 3. From Fig. 5, it can be observed that the distribution of outlet air volume changed after the flow deflectors were added. Taking the left outlets of the H-type ventilation system as an example, the airflow velocity values of outlet 1 and outlet 3 were 2.85 and 2.74 m/s with flow deflector

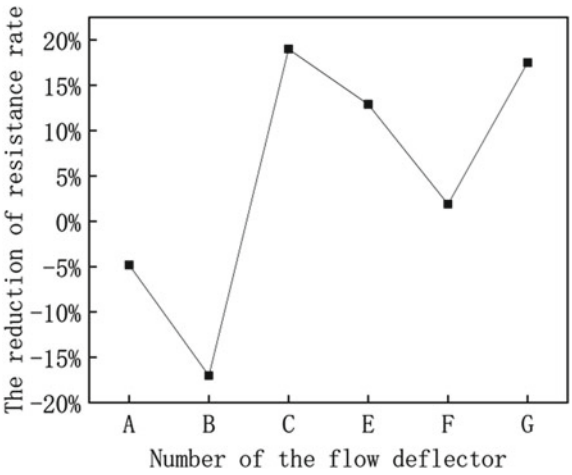

Fig. 4 Reduction of resistance rate of the flow deflectors

C. The air volume distribution trend was the opposite. After adding deflector *G*, the airflow velocity values of outlet 1 and outlet 3 were 2.70 and 2.90 m/s, with the same distribution trend. But the air volume imbalance rate increased.

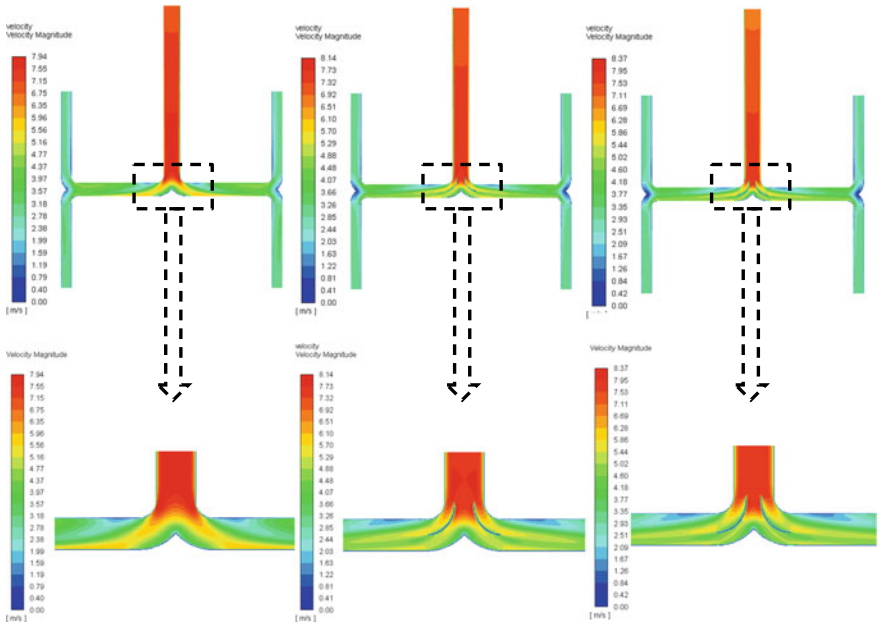

(a) No deflector (b) Deflectors C (c) deflectors G

Fig. 5 H-type ventilation system velocity contour plot

Table 3 Airflow velocity distribution of outlets

	Airflow velocity of outlet under different working conditions (m/s)		
	No deflector	Deflector *C*	Deflector *G*
Outlet1	2.75	2.85	2.70
Outlet3	2.83	2.75	2.90
Absolute difference	0.08	0.10	0.20
Percentage difference	1.43%	1.79%	3.57%

In conclusion, the addition of flow deflectors affected the airflow distribution at the end outlets of the ventilation system. After comparative analysis, it can be observed that flow deflector *C* exhibited better reduction effects with a smaller impact on achieving a uniform airflow distribution. Therefore, the relative position of flow deflector *C* within the tee is considered the optimal location for installing the flow deflectors.

Construction

Adding flow deflectors to the local component is an effective way to reduce the local resistance, which not only reduces the energy consumption of the ventilation system, but also ensures the air volume balance of the ventilation system. In this paper, the model of H-shaped ventilation system was established, and the airflow organization, resistance loss, and air volume distribution in the ventilation system were studied. Relevant conclusions are as follows:

(1) Adding flow deflectors at suitable positions within the tee of the H-type ventilation system can reduce the resistance loss. The results showed that the reduction of the resistance rate of the tee could reach 19% when the flow deflectors were added at the appropriate position, indicating that the reduction of resistance effect was obvious.
(2) The addition of flow deflectors within the tee can impact the distribution of the airflow at the end of the ventilation system. After installing flow deflectors, the air volume at the system outlets would change, and the trend of air volume distribution would also change.
(3) Adding flow deflectors at the appropriate positions can not only reduce the local resistance loss but also ensure the relative balance of the air volume at the ventilation system outlets.

References

1. Li GD, Liu KK (2022) Resistance reduction method for dividing tee of ventilation and air conditioning duct systems. Heat Ventil Air Cond 52(4):160–163
2. Chen SK, Zheng JF, Li AG (2018) Research on resistance reduction of dividing T-type tee junctions in ventilation and air conditioning pipes. Heat Ventil Air Cond 48(11):109–113
3. Li AG, Jing RY, Gao R (2022) Novel low resistance tees for ventilation and air conditioning duct systems. Heat Ventil Air Cond 52(11):118–126
4. Li X, Wang S (2013) Flow field and pressure loss analysis of junction and its structure optimization of aircraft hydraulic pipe system. Chin J Aeronaut 26(4):1080–1092
5. Xie ZH, Zhou YR (2009) Optimization research on guide plate installed in quadrate 90° curved duct. J Basic Sci Eng 17(4):568–571
6. Gong QT, Yang YH, Han K et al (2016) Characteristic analysis on the flow and local resistance in large pipe tees. J Chin Soc Power Eng 36(9):753–758+764
7. Wang ZJ, Li XH, Tang LJ, Duan QS (2019) Optimization research on deflectors installed in right-angle bend tube with rectangular section. Integr Intell Energy 41(8):32–37

Phase Equilibria and Thermodynamic Properties of Selected Compounds in the Ag–Ga–S–AgBr System for Modern Application in Energy Conversion Devices

Mykola Moroz, Fiseha Tesfaye, Pavlo Demchenko, Myroslava Prokhorenko, Bohdan Rudyk, Orest Pereviznyk, Emanuela Mastronardo, Daniel Lindberg, Oleksandr Reshetnyak, and Leena Hupa

Abstract The phase equilibria of the Ag–Ga–S–AgBr system in the part GaS–Ga_2S_5–AgBr–Ag_2S below 600 K were investigated by the modified electromotive force (EMF) method using the Ag^+ catalysts as small nucleation centers of equilibrium phases. Division of the GaS–Ga_2S_5–AgBr–Ag_2S was carried out with the participation of the following compounds Ag_2S, GaS, Ga_2S_3, AgBr, Ag_9GaS_6, $AgGaS_2$, Ag_3SBr, $Ag_3Ga_2S_4Br$, and $Ag_{27}Ga_2S_{12}Br_9$. Reactions were performed by applying electrochemical cells (ECs) with the structure: (−) IE | NE | SSE | R{Ag^+} | PE | IE (+), where IE is the inert electrode (graphite powder), NE is the negative electrode

M. Moroz (✉) · B. Rudyk
Department of Chemistry and Physics, National University of Water and Environmental Engineering, Rivne 33028, Ukraine
e-mail: m.v.moroz@nuwm.edu.ua

F. Tesfaye · L. Hupa
Johan Gadolin Process Chemistry Centre, Åbo Akademi University, 20500 Turku, Finland

P. Demchenko
Department of Inorganic Chemistry, Ivan Franko National University of Lviv, Lviv 79005, Ukraine

M. Prokhorenko
Department of Cartography and Geospatial Modeling, Lviv Polytechnic National University, Lviv 79013, Ukraine

O. Pereviznyk · O. Reshetnyak
Department of Physical and Colloid Chemistry, Ivan Franko National University of Lviv, Lviv 79005, Ukraine

E. Mastronardo
Department of Engineering, University of Messina, 98166 Messina, Italy

D. Lindberg
Department of Chemical and Metallurgical Engineering, Aalto University, Kemistintie 1, 02150 Espoo, Finland

© The Minerals, Metals & Materials Society 2024

C. Iloeje et al. (eds.), *Energy Technology 2024*, The Minerals, Metals & Materials Series, https://doi.org/10.1007/978-3-031-50244-6_23

(silver powder), SSE is the solid-state electrolyte (glassy Ag_3GeS_3Br), PE is the positive electrode, R{Ag^+} is the region of Ag^+ diffusion into PE. The measured EMF and temperature values of ECs were used to determine the standard thermodynamic functions of the compounds $Ag_3Ga_2S_4Br$ and $Ag_{27}Ga_2S_{12}Br$.

Keywords Photovoltaic compounds · Phase equilibria · Thermodynamic properties · EMF method · Gibbs energy

Introduction

To date, establishing the phase composition of the equilibrium *T-x* space of multicomponent inorganic systems at $T \leq 600$ K, when there are kinetic obstacles to achieving a state of thermodynamic equilibrium, remains relevant. The effect on samples of such external factors as long-term annealing during temperature and pressure variations is ineffective in many cases. The possibility of overcoming such kinetic obstacles was established in Refs. [1, 2]. For this purpose, the silver ions Ag^+ were used as catalysts, i.e., small nucleation centers of equilibrium phases.

The concentration tetrahedra of the Ag–Ga–*X*–*Y* (*X* = S, Se, Te; *Y* = Cl, Br, I) in part of the quasi-ternary Ag_2X–Ga_2X_3–Ag*Y* systems are characterized by the presence of semiconductor compounds of the formula composition $AgGa_2X_3Y$ (structure type $CuIn_2Te_3Cl$, space group *I*–4) [3]. Quaternary compounds decompose upon annealing at 600 K [4].

For the case *X* = S and *Y* = Br, the quasi-ternary Ag_2S–Ga_2S_3–AgBr system, in addition to the quaternary compound $AgGa_2S_3Br$, is characterized by the following ternary phases Ag_9GaS_6, $AgGaS_2$ (quasi-binary system Ag_2S–Ga_2S_3) and Ag_3SBr (quasi-binary system Ag_2S–AgBr) [5, 6]. The solid-state phase equilibria in the Ag–Ga–S system and thermodynamic properties of ternary phases were reported in Ref. [7]. The argyrodite family compound Ag_9GaS_6 is a promising thermoelectric material with the figure of merit parameter $ZT \sim 0.6$ and has intrinsic ultralow lattice thermal conductivity [8]. Moreover, Ag_9GaS_6 has a high silver ionic conductivity [9, 10]. The $AgGaS_2$ belongs to the chalcopyrite-structured ternary semiconductor compounds with a direct band gap of (2.48–2.75) eV. This compound has a high transparency in the mid-IR range and can be used as a commercial material for photovoltaic and nonlinear optical applications as well as a promising candidate for X-ray dosimetry [11–13]. The Ag_3SBr compound belongs to the class of superionic materials [14]. Thus, the multi-component compounds and solid solutions based on phases of the Ag–Ga–S system have been considered interesting scientific objects due to the diversity of their crystal structures and physicochemical properties [15–19]. However, these compounds no longer fully meet all the requirements of a new generation of devices for modern applications. For example, the band gap value and weak absorption in the visible light region limit the use of $AgGaS_2$ as absorber material for photovoltaic solar cells. Recently, the photo-electrochemical cells based on the $AgGaS_2$ compound showed an efficiency of 5.85% [20]. Optimization technology

for the synthesis of new materials and improving their technical characteristics is impossible without a comprehensive analysis of the thermodynamic properties of intermediate phases and construction equilibrium phase diagrams.

The points of intersection of the cross-sections $AgGaS_2$–AgBr and Ag_9GaS_6–AgBr of the quasi-ternary system with the tie-line Ga_2S_3–Ag_3SBr are places of potential formation of quaternary compounds $Ag_3Ga_2S_4Br$ and $Ag_{27}Ga_2S_{12}Br_9$. There are no previous reports on quaternary compounds of mentioned composition. The thermodynamic conditions for the formation of quaternary phases likely correspond to the temperature values $T < 600$ K, where there are kinetic obstacles to such a process.

The purpose of this work was to establish by the electromotive force (EMF) method the phase composition of the Ga_2S_3–Ag_3SBr cross-section of the Ag_2S–Ga_2S_3–AgBr system below 600 K and to determine the values of the standard thermodynamic functions of the quaternary compounds in the system. The two-phase equilibrium between compounds of the $AgGaS_2$–$Ag_3Ga_2S_4Br$ and Ag_9GaS_6–$Ag_{27}Ga_2S_{12}Br_9$ cross-sections can be used to vary the nonlinear optical properties of the phases in the way of forming solid solutions on a mutual basis.

Experimental

The high-purity substances Ag (> 99.9 wt%, Alfa Aesar, Germany), Ga, and S (> 99.99 wt%, Alfa Aesar, Germany) were used to synthesize the binary compounds Ag_2S, GaS, and Ga_2S_3. Melts of the Ag_2S, GaS, and Ga_2S_3 compounds in an inert atmosphere were cooled to room temperature, then crushed to a particle size of ~ 1×10^{-6} m for preparation of the positive electrodes (PE) of electrochemical cells (ECs) [21, 22].

The modified EMF method [1, 2] was used both to establish the phase equilibria in the GaS–Ga_2S_5–AgBr–Ag_2S part of the Ag–Ga–S–AgBr concentration tetrahedron below 600 K and to determine the thermodynamic parameters of compounds. For these investigations, a certain number of ECs were assembled:

$$(-)\ \mathrm{IE}|\mathrm{NE}|\mathrm{SSE}|\mathrm{R}\left\{\mathrm{Ag}^+\right\}|\mathrm{PE}|\mathrm{IE}(+),$$

where IE is the inert electrode (graphite powder), NE is the negative electrode (silver powder), SSE is the solid-state electrolyte (glassy Ag_3GeS_3Br [23]), and $R\{Ag^+\}$ is the region of PE that contacts with SSE. At the stage of cell preparation, PE is the non-equilibrium phase mixture of the well-mixed powdered binary compounds Ag_2S, GaS, Ga_2S_3, and AgBr (99.5 wt%, Alfa Aesar, Germany). Compositions of these mixtures covered the entire concentration space of the GaS–Ga_2S_5–AgBr–Ag_2S region. An equilibrium set of phases was formed in the $R\{Ag^+\}$ region at 600 K for 48 h. The Ag^+ ions, displaced for thermodynamic reasons from the NE to the PE electrodes of the ECs, acted as catalysts, i.e., small nucleation centers of equilibrium phases [21, 22].

The experiments were performed in a resistance furnace described in Ref. [24, 25]. To assemble the ECs, a fluoroplastic base with a hole with a diameter of 2 mm was used. The powder components of ECs were pressed at pressure 10^8 Pa into the hole under a load of (2.0 ± 0.1) tons to a density of $\rho = (0.93 \pm 0.02)\ \rho_0$, where ρ_0 is the experimentally determined density of cast samples. The assembled cells were placed in a quartz tube with nozzles for the purging of argon gas [26, 27]. The argon gas had a direction from the NE to PE of ECs at the rate of (10.0 ± 0.2) cm^3 min^{-1}. The temperature of ECs was maintained by an electronic thermostat with ± 0.5 K accuracy. A Picotest M3500A digital voltmeter with an input impedance of > 10^{12} Ohms was used to measure the EMF (E) values of the cells (accuracy ± 0.3 mV) at different temperatures. The reproducibility of the E versus T dependences of ECs in heating–cooling cycles was a criterion for completing the formation of the equilibrium set of phases in the R{Ag^+} region [28].

Results and Discussion

The division of the concentration tetrahedron Ag–Ga–S–AgBr into separate four-phase regions in the GaS–Ga_2S_5–AgBr–Ag_2S part below 600 K is shown in Fig. 1. The division was carried out based on the experimental results of the E versus T relations of the ECs with PE of different phase regions and taking into account the basic rules of the EMF method [29–31]:

(1) within a specific phase region, the EMF value of the cell does not depend on the phase composition of the PE;
(2) ECs with PE of different phase regions are characterized by different EMF values at T = const, Table 1;

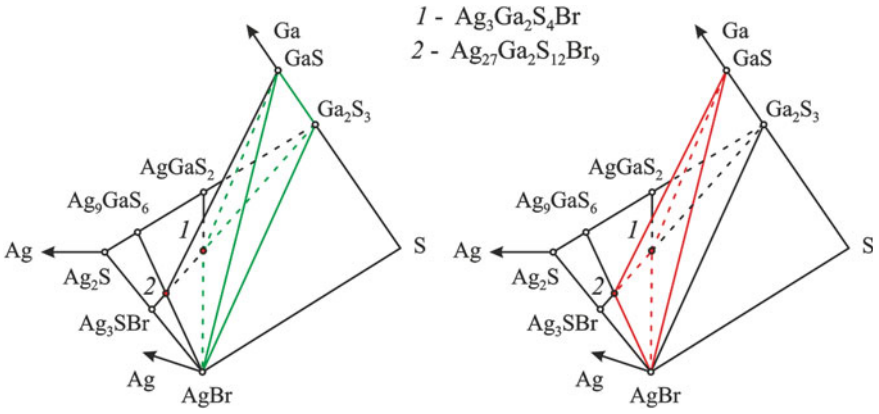

Fig. 1 Spatial position of tetrahedra GaS–Ga_2S_3–AgBr–$Ag_3Ga_2S_4Br$ (left) and GaS–AgBr–$Ag_{27}Ga_2S_{12}Br_9$–$Ag_3Ga_2S_4Br$ (right) in the concentration space of the Ag–Ga–S–AgBr system

Table 1 Measured values of temperature (T) and EMF (E) of the ECs with PE of different phase regions at pressure $P = 10^5$ Pa

T/K	Phase regions		T/K	Phase regions	
	(I)	(II)		(I)	(II)
	E/mV	E/mV		E/mV	E/mV
390.4	211.1	204.1	420.5	224.3	209.4
395.4	213.4	204.9	425.4	226.6	210.2
400.4	215.4	205.9	430.4	228.8	211.2
405.4	217.7	206.8	435.3	231.1	212.1
410.4	219.8	207.6	440.4	233.4	212.9
415.4	222.2	208.5	445.4	235.5	213.7

Standard uncertainties u are $u(T) = 0.5$ K, $u(P) = 10^4$ Pa, and $u(E) = 0.3$ mV

(3) the four-phase region further away from the figurative point of Ag is characterized by a higher EMF value at a specific temperature, Fig. 2.

The spatial position of the established four-phase regions GaS–Ga_2S_3–AgBr–$Ag_3Ga_2S_4Br$ (phase region (I)) and GaS–AgBr–$Ag_{27}Ga_2S_{12}Br_9$–$Ag_3Ga_2S_4Br$ (phase region (II)) relative to the silver point was used to establish the overall potential-determining reactions:

$$2Ag + 2Ga_2S_3 + AgBr = Ag_3Ga_2S_4Br + 2GaS, \quad \text{(R1)}$$

$$8Ag + 5Ag_3Ga_2S_4Br + 4AgBr = Ag_{27}Ga_2S_{12}Br_9 + 8GaS. \quad \text{(R2)}$$

Reactions (R1) and (R2) were carried out in the PE of ECs, and the phase mixtures correspond to phase regions (I) and (II), respectively. According to reactions (R1)

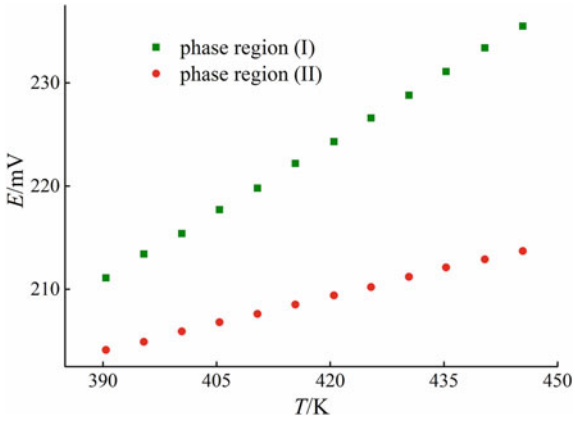

Fig. 2 E versus T dependencies of the ECs with PE of the phase regions (I) and (II)

and (R2), the ratios of binary compounds for assembling the PE of ECs were established. In particular, the compounds $Ag_3Ga_2S_4Br$ and $Ag_{27}Ga_2S_{12}Br_9$ are present in the PE compositions in the following ratios of mixtures of the binary compounds: Ag_2S:Ga_2S_3:AgBr = 1:1:1 and Ag_2S:Ga_2S_3:AgBr = 9:1:9, respectively.

From the data analysis of Fig. 2, it follows that the E versus T dependencies of the ECs in the phase regions (I) and (II) are linear. Therefore, the results of EMF measurements processed by the least squares method [32] can be presented in the form of Eq. (1):

$$E = a + bT \equiv \overline{E} + b\left(T - \overline{T}\right), \tag{1}$$

where $\overline{E} = \frac{\sum E_i}{n}$, $\overline{T} = \frac{\sum T_i}{n}$ (E_i is the EMF of the cell at temperature T_i; n is a number of experimental pairs E_i and T_i).

Coefficients a and b were calculated by the following Eqs. (2) and (3):

$$a = \overline{E} - b\overline{T}, \tag{2}$$

$$b = \frac{\sum\left[\left(E_i - \overline{E}\right)\left(T_i - \overline{T}\right)\right]}{\sum\left(T_i - \overline{T}\right)^2}. \tag{3}$$

The statistical dispersions of the measurement uncertainties consisted of the calculation variances of experimental values of EMF E (u_E^2), coefficients b (u_b^2) and a (u_a^2), as well as dispersions of the calculated by Eq. (1) EMF values $\tilde{E}$ ($u_{\tilde{E}}^2$):

$$u_E^2 = \frac{\sum\left(E_i - \tilde{E}_i\right)^2}{n-2}, \tag{4}$$

$$u_b^2(T) = \frac{u_E^2}{\sum\left(T_i - \overline{T}\right)^2}, \tag{5}$$

$$u_a^2(T) = \frac{u_E^2}{n} + \frac{u_E^2\overline{T}^2}{\sum\left(T_i - \overline{T}\right)^2}, \tag{6}$$

$$u_{\tilde{E}}^2(T) = \frac{u_E^2}{n} + u_b^2\left(T - \overline{T}\right)^2. \tag{7}$$

Uncertainties (Δ_i) of the corresponding quantities can be calculated by the Eq. (8):

$$\Delta_i = k_{St}u_i \tag{8}$$

where k_{St} is the Student's coefficient, and u_i is the standard deviation. At the confidence level of 95% and $n = 12$, the Student's coefficient is equal $k_{St} = 2.179$ [32].

According to [33, 34], the final equation of the E versus T dependences together with the statistical dispersions can be expressed as:

$$E = a + bT \pm k_{St}\sqrt{\left(\frac{u_E^2}{n} + u_b^2\left(T - \overline{T}\right)^2\right)}. \tag{9}$$

An example of calculating the coefficients of Eq. (9) for the phase region (I) is given in Table 2.

Analogously to the phase region (I), coefficients E versus T dependence of the cell with PE of the phase region (II) were calculated. The results of the calculations are listed in Table 3.

The Gibbs energies ($\Delta_r G$), enthalpies ($\Delta_r H$), and entropies ($\Delta_r S$) of the reactions (R1) and (R2) were calculated by the following thermodynamic equations:

$$\Delta_r G = -z\,F E, \tag{10}$$

$$\Delta_r H = -z\,F[E - (\mathrm{d}E/\mathrm{d}T)T], \tag{11}$$

Table 2 Coefficients of the E versus T dependence of the cell with PE of the phase region (I)

T_i	E_i	$(T_i - \overline{T})$	$(T_i - \overline{T})^2$	$\tilde{E}_i$	$\left(E_i - \tilde{E}_i\right)$	$\left(E_i - \tilde{E}_i\right)^2$
K	mV	K	K^2	mV	mV	mV^2
390.4	211.1	− 27.50	756.25	211.04	0.06	0.00
395.4	213.4	− 22.50	506.25	213.26	0.14	0.02
400.4	215.4	− 17.50	306.25	215.49	− 0.09	0.01
405.4	217.7	− 12.50	156.25	217.71	− 0.01	0.00
410.4	219.8	− 7.50	56.25	219.94	− 0.14	0.02
415.4	222.2	− 2.50	6.25	222.17	0.03	0.00
420.5	224.3	2.60	6.76	224.44	− 0.14	0.02
425.4	226.6	7.50	56.25	226.62	− 0.02	0.00
430.4	228.8	12.50	156.25	228.84	− 0.04	0.00
435.3	231.1	17.40	302.76	231.02	0.08	0.01
440.4	233.4	22.50	506.25	233.29	0.11	0.01
445.4	235.5	27.50	756.25	235.52	− 0.02	0.00
$\overline{T}$ = 417.90	$\overline{E}$ = 223.28	–	$\sum (T_i - \overline{T})^2$ = 3572.02	–	–	$\sum \left(E_i - \tilde{E}_i\right)^2$ = 0.09

$\overline{T}$ is the average temperature value, $\tilde{E}$ is the EMF of the cell calculated according to Eq. (1)

Table 3 Coefficients and statistical dispersions of the E versus T dependencies of the ECs in the phase regions (I) and (II)

Phase regions	$E = a + bT \pm k_{St}\sqrt{\left(\frac{u_E^2}{n} + u_b^2(T-\overline{T})^2\right)}$
(I)	$E = 37.25 + 445.15 \times 10^{-3}T \pm 2.179\sqrt{\left(\frac{8.95\times10^{-3}}{12} + 2.51 \times 10^{-6}(T-417.90)^2\right)}$
(II)	$E = 135.35 + 176.09 \times 10^{-3}T \pm 2.179\sqrt{\left(\frac{3.52\times10^{-3}}{12} + 9.86 \times 10^{-7}(T-417.90)^2\right)}$

Table 4 Values of standard thermodynamic function of the reactions (R1) and (R2)

Reactions	$-\Delta_r G^\circ$	$-\Delta_r H^\circ$	$\Delta_r S^\circ$
	kJ mol^{-1}		J (mol K)$^{-1}$
(R1)	32.79 ± 0.08	7.19 ± 0.28	85.90 ± 0.66
(R2)	144.98 ± 0.20	104.47 ± 0.70	135.92 ± 1.67

Uncertainties for $\Delta_r G^\circ$, $\Delta_r H^\circ$, and $\Delta_r S^\circ$ are standard uncertainties

$$\Delta_r S = z\,F(\mathrm{d}E/\mathrm{d}T). \tag{12}$$

where z is the number of electrons involved in the reactions (R1) and (R2), F is the Faraday's constant, and E is the EMF of the ECs.

The values of the thermodynamic functions of reactions (R1) and (R2) in the standard state (T = 298 K and $P = 10^5$ Pa) were calculated according to Eqs. (10)–(12) and are listed in Table 4.

The Gibbs energy, enthalpy, and entropy of the reaction (R1) are related to the Gibbs energy, enthalpy, and entropy of the compounds Ga_2S_3, AgBr, $Ag_3Ga_2S_4Br$, GaS, and pure substance Ag by the following equations:

$$\Delta_{r(R1)}G^\circ = \Delta_f G^\circ_{Ag_3Ga_2S_4Br} + 2\Delta_f G^\circ_{GaS} - 2\Delta_f G^\circ_{Ga_2S_3} - \Delta_f G^\circ_{AgBr}, \tag{13}$$

$$\Delta_{r(R1)}H^\circ = \Delta_f H^\circ_{Ag_3Ga_2S_4Br} + 2\Delta_f H^\circ_{GaS} - 2\Delta_f H^\circ_{Ga_2S_3} - \Delta_f H^\circ_{AgBr}, \tag{14}$$

$$\Delta_{r(R1)}S^\circ = S^\circ_{Ag_3Ga_2S_4Br} + 2S^\circ_{GaS} - 2S^\circ_{Ag} - 2S^\circ_{Ga_2S_3} - S^\circ_{AgBr}. \tag{15}$$

It follows from Eqs. (13)–(15) that:

$$\Delta_f G^\circ_{Ag_3Ga_2S_4Br} = 2\Delta_f G^\circ_{Ga_2S_3} + \Delta_f G^\circ_{AgBr} - 2\Delta_f G^\circ_{GaS} + \Delta_{r(R1)}G^\circ, \tag{16}$$

$$\Delta_f H^\circ_{Ag_3Ga_2S_4Br} = 2\Delta_f H^\circ_{Ga_2S_3} + \Delta_f H^\circ_{AgBr} - 2\Delta_f H^\circ_{GaS} + \Delta_{r(R1)}H^\circ, \tag{17}$$

$$S^{\circ}_{Ag_3Ga_2S_4Br} = 2S^{\circ}_{Ag} + 2S^{\circ}_{Ga_2S_3} + S^{\circ}_{AgBr} - 2S^{\circ}_{GaS} + \Delta_{r(R1)}S^{\circ}. \quad (18)$$

Reactions to determine the standard thermodynamic properties $\Delta_f G^{\circ}$, $\Delta_f H^{\circ}$, and S° of the $Ag_{27}Ga_2S_{12}Br_9$ compound were written in similarity using (R2) with the corresponding stoichiometric numbers.

For the first time, the standard thermodynamic quantities of the quaternary compounds of the Ag–Ga–S–AgBr system were determined using Eqs. (16)–(18) and thermodynamic data of pure substances (Ag, Ga, S, Br_2) and the binary compound GaS, Ga_2S_3, AgBr [35]. The results of the calculations are listed in Table 5.

The temperature dependences of the Gibbs energies of formations of the quaternary compounds of the Ag–Ga–S–AgBr system are described by the following equations:

$$\Delta_f G_{Ag_3Ga_2S_4Br}/\left(\text{kJ mol}^{-1}\right) = -(722.0 \pm 10.2) - (33.4 \pm 0.4) \times 10^{-3}\,\text{T/K}, \quad (19)$$

$$\Delta_f G_{Ag_{27}Ga_2S_{12}Br_9}/\left(\text{kJ mol}^{-1}\right) = -(2443.1 \pm 31.7) - (377.3 \pm 4.9) \times 10^{-3}\,\text{T/K}. \quad (20)$$

Included in Table 5 values of $\Delta_f G^{\circ}_{Ag_3Ga_2S_4Br}$ and $\Delta_f G^{\circ}_{Ag_{27}Ga_2S_{12}Br_9}$ do not contradict the hypothetical reactions of the synthesis of quaternary compounds from binary phases under standard conditions:

$$Ag_2S + Ga_2S_3 + AgBr = Ag_3Ga_2S_4Br, \quad (R3)$$

Table 5 Values of standard ($T = 298$ K and $P = 10^5$ Pa) thermodynamic properties of selected compounds of the Ag–Ga–S–AgBr system

Phases	$-\Delta_f G^{\circ}$	$-\Delta_f H^{\circ}$	S°	References
	kJ mol^{-1}		J (mol K)$^{-1}$	
Ag	0	0	42.677	[35]
Ga	0	0	40.828	[35]
S	0	0	32.056	[35]
Br_2	0	0	152.210	[35]
GaS	204.685	209.200	57.739	[35]
Ga_2S_3	505.702	516.306	142.256	[35]
AgBr	97.095	100.575	107.110	[35]
Ag_3SBr	132.0 ± 0.6	117.0 ± 0.4	50.2 ± 0.6	[36]
$Ag_3Ga_2S_4Br$	731.9 ± 8.9	722.0 ± 10.2	447.4 ± 5.8	Present study
$Ag_{27}Ga_2S_{12}Br_9$	2555.5 ± 28.4	2443.1 ± 31.7	2680.9 ± 34.9	Present study

Uncertainties for $\Delta_f G^{\circ}$, $\Delta_f H^{\circ}$, and S° are standard uncertainties

$$9Ag_2S + Ga_2S_3 + 9AgBr = Ag_{27}Ga_2S_{12}Br_9. \quad \text{(R4)}$$

Calculated values of the Gibbs energies of reactions (R3) and (R4) are equal, respectively: $\Delta_{r(R3)}G^\circ = -40.4$ kJ mol^{-1} and $\Delta_{r(R4)}G^\circ = -811.3$ kJ mol^{-1}.

Conclusions

The phase space of the Ag–Ga–S–AgBr system in the GaS–Ga_2S_5–AgBr–Ag_2S part is characterized by the binary (Ag_2S, GaS, Ga_2S_3, AgBr), ternary (Ag_9GaS_6, $AgGaS_2$, Ag_3SBr), and quaternary ($Ag_3Ga_2S_4Br$, $Ag_{27}Ga_2S_{12}Br_9$) compounds. Quaternary compounds are components of the concentration tetrahedra GaS–Ga_2S_3–AgBr–$Ag_3Ga_2S_4Br$ and GaS–AgBr–$Ag_{27}Ga_2S_{12}Br_9$–$Ag_3Ga_2S_4Br$. The spatial position of the established tetrahedra relative to the silver point was used to establish the overall potential-determining reactions of the synthesis of compounds. The synthesis of quaternary compounds was carried out from the calculated amounts of binary phases in the positive electrodes of the cells with the participation of the Ag^+ catalyst. For the first time, the values of standard thermodynamic functions (Gibbs energies, enthalpies, and entropies) of quaternary compounds were calculated based on the temperature dependences of the EMF of electrochemical cells. The variation of the composition of ternary and quaternary compounds within the homogeneity regions opens wide possibilities for changing their physicochemical properties.

Acknowledgements The present work was financed partially by the grant of the Ministry of Education and Science of Ukraine No 0123U101857 “Physico-chemistry of functional nanomaterials for electrochemical systems”, international projects: #HX-010123 from “Materials Phases Data System, Viznau, Switzerland” and the Simons Foundation (Award Number: 1037973). This work was partly funded by the K.H. Renlund Foundation under the project “Innovative e-waste recycling processes for greener and more efficient recoveries of critical metals and energy” at Åbo Akademi University.

Conflict of Interest
The authors declare that they have no conflict of interest.

References

1. Moroz M, Tesfaye F, Demchenko P, Prokhorenko M, Prokhorenko S, Reshetnyak O (2021) Non-activation synthesis and thermodynamic properties of ternary compounds of the Ag–Te–Br system. Thermochim Acta 698:178862(1)–(7). https://doi.org/10.1016/j.tca.2021.178862
2. Moroz M, Tesfaye F, Demchenko P, Kordan V, Prokhorenko M, Mysina O, Reshetnyak O, Gladyshevskii R (2023) Synthesis, thermodynamic properties, and structural characteristics of multicomponent compounds in the Ag–Ni–Sn–S system. JOM 75:2016–2025. https://doi.org/10.1007/s11837-023-05784-9

3. Ivashchenko I, Kozak V, Gulay L, Olekseyuk I (2022) Crystal structure of $AgGa_2Se_3Cl(Br)$ compounds. Proc Shevchenko Sci Soc Ser Chem Sci LXX:62–68. https://doi.org/10.37827/ntsh.chem.2022.70.062
4. Range K-J, Handrick K (1988) Neue 1320637-Verbindungen/New 1320637 compounds. Z Naturforsch B 43:240–242. https://doi.org/10.1515/znb-1988-0218
5. Brandt G, Krämer V (1976) Phase investigations in the silver-gallium-sulphur system. Mater Res Bull 11:1381–1388. https://doi.org/10.1016/0025-5408(76)90049-0
6. Chbani N, Loireau-Lozac'h A-M, Rivet J, Dugué J (1995) Système pseudo-ternaire Ag_2S-Ga_2S_3-GeS_2: diagramme de phases—domaine vitreux. J Solid State Chem 117:189–200. https://doi.org/10.1006/jssc.1995.1262
7. Ibragimova GI, Shikhiyev YuM, Babanly MB (2006) Solid phase equlibria in Ag-Ga-S (Se, Te) systems and thermodynamic properties of ternary phases. Chem Probl 1:23–28
8. Lin S, Li W, Bu Z, Gao B, Li J, Pei Y (2018) Thermoelectric properties of Ag_9GaS_6 with ultralow lattice thermal conductivity. Mater Today Phys 6:60–67. https://doi.org/10.1016/j.mtphys.2018.09.001
9. Hellstrom E, Schoonman J (1980) Silver ionic and electronic conductivity in Ag_9GaS_6. Solid State Ionics 1:199–210. https://doi.org/10.1016/0167-2738(80)90004-1
10. Lin S, Li W, Pei Y (2021) Thermally insulative thermoelectric argyrodites. Mater Today 48:198–213. https://doi.org/10.1016/j.mattod.2021.01.007
11. Asadov MM, Mustafaeva SN (2015) X-ray dosimetry of an $AgGaS_2$ single crystal. Bull Russ Acad Sci Phys 79:1113–1117. https://doi.org/10.3103/S106287381509004X
12. Laksari S, Chahed A, Abbouni N, Benhelal O, Abbar B (2006) First-principles calculations of the structural, electronic and optical properties of $CuGaS_2$ and $AgGaS_2$. Comput Mater Sci 38:223–230. https://doi.org/10.1016/j.commatsci.2005.12.043
13. Mouacher R, Seddik T, Rezini B, Haq B, Batouche M, Ugur G, Ugur S, Belfedal A (2022) First-principles calculations of electronic and optical properties of $AgGa_{1-x}Tl_xS_2$ alloys: analyses and design for solar cell applications. J Solid State Chem 309:122996. https://doi.org/10.1016/j.jssc.2022.122996
14. Palazon F (2022) Metal chalcohalides: next generation photovoltaic materials? Sol RRL 6:2100829. https://doi.org/10.1002/solr.202100829
15. Piasecki M, Myronchuk GL, Parasyuk OV, Khyzhun OY, Fedorchuk AO, Pavlyuk VV (2017) Synthesis, structural, electronic and linear electro-optical features of new quaternary $Ag_2Ga_2SiS_6$ compound. J Solid State Chem 246:363–371. https://doi.org/10.1016/j.jssc.2016.12.011
16. Kim J-H, Kim B-Y, Jang E-P, Yoon S-Y, Kim K-H (2018) Synthesis of widely emission-tunable Ag–Ga–S and its quaternary derivative quantum dots. Chem Eng J 347:791–797. https://doi.org/10.1016/j.cej.2018.04.167
17. Wei J, Hu Z, Zhou W, Qiu Y, Dai H (2021) Emission tuning of highly efficient quaternary Ag-Cu-Ga-Se/ZnSe quantum dots for white light-emitting diodes. J Colloid Interface Sci 602:307–315. https://doi.org/10.1016/j.jcis.2021.05.110
18. Azhniuk Y, Lopushanska B, Selyshchev O, Havryliuk Y, Pogodin A (2022) Synthesis and optical properties of Ag–Ga–S quantum dots. Phys Status Solidi B 259:2100349. https://doi.org/10.1002/pssb.202100349
19. Valakh M, Litvinchuk AP, Havryliuk Y, Yukhymchuk V, Dzhagan V (2023) Raman- and infrared-active phonons in nonlinear semiconductor $AgGaGeS_4$. Crystals 13:148. https://doi.org/10.3390/cryst13010148
20. Thirumoorthy M, Ramesh K (2021) Characteristics of pulse electrodeposited $AgGaS_2$ thin films for photovoltaic application. Mater Today Proc 47:1847–1854. https://doi.org/10.1016/j.matpr.2021.03.410
21. Moroz MV, Demchenko PYu, Prokhorenko MV, Reshetnyak OV (2017) Thermodynamic properties of saturated solid solutions of the phases Ag_2PbGeS_4, $Ag_{0.5}Pb_{1.75}GeS_4$ and $Ag_{6.72}Pb_{0.16}Ge_{0.84}S_{5.20}$ of the Ag-Pb-Ge-S system determined by EMF method. J Phase Equilibria Diffus 38:426–433. https://doi.org/10.1007/s11669-017-0563-6

22. Moroz MV, Prokhorenko MV, Reshetnyak OV, Demchenko PYu (2017) Electrochemical determination of thermodynamic properties of saturated solid solutions of Hg_2GeSe_3, Hg_2GeSe_4, $Ag_2Hg_3GeSe_6$, and $Ag_{1.4}Hg_{1.3}GeSe_6$ compounds in the Ag–Hg–Ge–Se system. J Solid State Electrochem 21:833–837. https://doi.org/10.1007/s10008-016-3424-z
23. Moroz MV, Demchenko PYu, Mykolaychuk OG, Akselrud LG, Gladyshevskii RE (2013) Synthesis and electrical conductivity of crystalline and glassy alloys in the Ag_3GeS_3Br-GeS_2 system. Inorg Mater 49:867–871. https://doi.org/10.1134/S0020168513090100
24. Moroz MV, Prokhorenko MV (2014) Thermodynamic properties of the intermediate phases of the Ag-Sb-Se system. Russ J Phys Chem A 88:742–746. https://doi.org/10.1134/S0036024414050203
25. Moroz M, Tesfaye F, Demchenko P, Prokhorenko M, Lindberg D, Reshetnyak O, Hupa L (2018) Phase equilibria and thermodynamics of selected compounds in the Ag–Fe–Sn–S system. J Electron Mater 47:5433–5442. https://doi.org/10.1007/s11664-018-6430-3
26. Moroz MV, Prokhorenko MV, Rudyk BP (2014) Thermodynamic properties of phases of the Ag-Ge-Te system. Russ J Electrochem 50:1177–1181. https://doi.org/10.1134/S1023193514120039
27. Prokhorenko MV, Moroz MV, Demchenko PYu (2015) Measuring the thermodynamic properties of saturated solid solutions in the Ag_2Te-Bi-Bi_2Te_3 system by the electromotive force method. Russ J Phys Chem A 89:1330–1334. https://doi.org/10.1134/S0036024415080269
28. Moroz M, Tesfaye F, Demchenko P, Prokhorenko M, Kogut Y, Pereviznyk O, Prokhorenko S, Reshetnyak O (2020) Solid-state electrochemical synthesis and thermodynamic properties of selected compounds in the Ag–Fe–Pb–Se system. Solid State Sci 107:106344(1)–(9). https://doi.org/10.1016/j.solidstatesciences.2020.106344
29. Babanly M, Yusibov Y, Babanly N (2011) The EMF method with solid-state electrolyte in the thermodynamic investigation of ternary copper and silver chalcogenides. In: Kara S (ed). InTech, pp 57–78. https://doi.org/10.5772/28934
30. Mammadov FM, Amiraslanov IR, Imamaliyeva SZ, Babanly MB (2019) Phase relations in the FeSe–$FeGa_2Se_4$–$FeIn_2Se_4$ system: refinement of the crystal structures of $FeIn_2Se_4$ and $FeGaInSe_4$. J Phase Equilibria Diffus 40:787–796. https://doi.org/10.1007/s11669-019-00768-2
31. Hasanova GS, Aghazade AI, Babanly DM, Imamaliyeva SZ, Yusibov YA, Babanly MB (2021) Experimental study of the phase relations and thermodynamic properties of Bi-Se system. J Therm Anal Calorim 147:6403–6414. https://doi.org/10.1007/s10973-021-10975-0
32. Gravetter FJ, Wallnau LB (2017) Statistics for the behavioral sciences, 10th edn. Cengage Learning, Australia and United States
33. Babanly NB, Orujlu EN, Imamaliyeva SZ, Yusibov YA, Babanly MB (2019) Thermodynamic investigation of silver-thallium tellurides by EMF method with solid electrolyte Ag_4RbI_5. J Chem Thermodyn 128:78–86. https://doi.org/10.1016/j.jct.2018.08.012
34. Imamaliyeva SZ, Musayeva SS, Babanly DM, Jafarov YI, Taghiyev DB, Babanly MB (2019) Determination of the thermodynamic functions of bismuth chalcoiodides by EMF method with morpholinium formate as electrolyte. Thermochim Acta 679:178319. https://doi.org/10.1016/j.tca.2019.178319
35. Barin I (1995) Thermochemical data of pure substances. VCH, Weinheim
36. Moroz MV, Prokhorenko MV, Prokhorenko SV (2015) Determination of thermodynamic properties of Ag_3SBr superionic phase using EMF technique. Russ J Electrochem 51:886–889. https://doi.org/10.1134/S1023193515090098

Reaction Behavior of High-Rank Coal with Different Particle Sizes in Coal Gasification and Ironmaking Polygeneration Process

Yaqiang Yuan, Fusong Feng, Wei Wang, and Haibin Zuo

Abstract This study investigates the reaction behavior of high-rank coal with different particle sizes in the coal gasification and ironmaking polygeneration process. The gasification and ironmaking polygeneration process is promising for achieving CO_2 recycling and clean coal utilization. Thus, the CO_2 gasification behavior of two kinds of high-rank coal was investigated by the isothermal thermogravimetric method. The pore structure, chemical structure, and ash composition were also systematically tested. The results show that the particle size significantly influences the CO_2 gasification of high-rank coal. Smaller particle sizes exhibit enhanced reactivity and faster gasification kinetics due to increased surface area and improved accessibility to reactants. The chemical structure and ash can also affect the fuel gasification reactivity. The findings provide valuable insights into optimizing high-rank coal gasification to improve overall process performance and resource efficiency.

Keywords High-rank coal · CO_2 gasification · Different particle sizes · Kinetics

Introduction

Fossil fuels are still the world's main energy source, including coal, coke, oil, and natural gas. Among them, high-rank solid fuels are widely used in the chemical industry, power plants, and metallurgy, for example, anthracite, coke, and bituminous coal [1, 2], which are indispensable in the short term. Their main application path is gasification reaction in the air bed of ironmaking polygeneration process [3, 4]. Therefore, studying their gasification reaction characteristics for energy saving and efficient production is necessary.

Y. Yuan · F. Feng · W. Wang · H. Zuo (✉)
State Key Laboratory of Advanced Metallurgy, University of Science and Technology Beijing, Beijing 100083, China
e-mail: zuohaibin@ustb.edu.cn

© The Minerals, Metals & Materials Society 2024

C. Iloeje et al. (eds.), *Energy Technology 2024*, The Minerals, Metals & Materials Series, https://doi.org/10.1007/978-3-031-50244-6_24

There is much study about the reactivity and kinetics of char gasification [5, 6]. The isothermal thermogravimetric method is commonly applied to analyze the gasification reaction kinetic of different fuels, which is conducted by random pore model (RPM) [7] to obtain the gasification process and kinetic parameters. Li et al. understood the mineral behaviors during anthracite fluidized-bed gasification based on slag characteristics [8]. Wang et al. studied the strength, porosity, and fuel reaction rate change in high-temperature gasification reactions [9]. These works systematically analyze the gasification reaction process for high-rank coals. It is lacking the comparison of gasification characteristics between different particle sizes.

In this study, the char gasification characteristics of two anthracites with different particle sizes were investigated by using the method of isothermal thermogravimetric analysis, which used the RPM model to describe CO_2 gasification kinetics of high-rank coals with different particle sizes and compared with a coke powder. Moreover, various factors, including proximate analysis, elemental analysis, ash composition, microstructure, and carbonaceous structure, were also analyzed systematically.

Experimental

Materials

Sihe (SH) [10] and Chengzhuang (CZ) [11] are typical high-rank anthracites that are very abundant in the Shanxi Province of China. Coke powder (CP) is the main solid fuel for ironmaking production [9]. This study used two anthracites and one coke powder with mixed particle sizes from a steel mill as test samples. Each sample was firstly weighed to 1 kg, crushed to less than 3 mm by a roller crusher, and then screened with four standard test screens of 3 mm, 1 mm, 0.5 mm, and 0.074 mm, respectively. Finally, the screened samples were placed in a 378 K drying oven for 6 h, then placed in sealed plastic bags and stored in a desiccator at room temperature until experiments were carried out. The 1–3, 0.5–1, and 0–0.5 mm of samples were used in thermal analysis tests, and the 0–0.074 mm of samples were characterized by chemical composition and physicochemical structure.

The proximate and ultimate analyses were performed by the standard procedures of Chinese standard (GB/T 212-2001). The elemental analyzer was used for samples to analyze their elements. The weight percent of carbon, hydrogen, nitrogen, and sulfur in samples can be detected accurately, and the weight percent of oxygen was determined in other ways. The testing results of samples are listed in Table 1. The ash of the raw materials was prepared by air oxidation at 1173 K in a muffle furnace according to the Chinese standard (GB/T 212-2008). The ash chemical composition was determined by the X-ray fluorescence (XRF) spectrum analyzer (EDX8000), produced by Shimadzu Corporation, and the results are presented in Table 3.

Different analytical techniques were used to determine the chemical structure and composition of the three high-rank fuels. The morphology of raw materials was

Table 1 Proximate analysis and elemental analysis of SH, CZ, and CP

Sample	Proximate analysis (wt%)				Elemental analysis (wt%)					HHV (kJ/mol)
	FC_{ad}	V_{ad}	A_{ad}	M_{ad}	C_{ad}	H_{ad}	O_{cv}	N_{ad}	S_{ad}	
SH	78.56	7.58	13.33	0.53	76.33	2.30	20.03	1.03	0.31	24.83
CZ	81.18	6.98	11.49	0.35	82.69	2.70	13.11	1.18	0.32	26.88
CP	80.44	3.34	15.91	0.31	80.39	1.12	17.11	0.83	0.55	25.18

Notes FC stands for fixed carbon, V stands for volatiles, A stands for ash, M stands for moisture. Subscript ad stands for air dried basis

observed using Scanning electron microscopy (SEM) (JSM-6701F) at the conditions of 5 kV voltage and amplified 10,000 times. The pore structures of the three coal chars were characterized by a Mercury Injection Apparatus (MIA) at 33 k. The carbon structures of fuel were investigated by a Raman spectrometer. Raman spectra of the samples were measured with a LabRAM HR Evolution high-resolution Raman spectrometer. Each sample was sampled a little and deposited on a rectangular glass slide for the Raman analysis. Raman spectra were obtained in a backscattered configuration with an excitation laser at 532 nm. The Raman spectra at each position give structural information of many carbon micro-crystallites.

Experimental Procedure

The reaction kinetics and mechanism of solid fuel during gasification and combustion are often used in the thermogravimetric analysis (TGA) to investigate such as biomass, coal chars, coke, and other carbon solid waste [12]. The gasification of samples was carried out by using a thermogravimetric analyzer (HCT-4, Henven Scientific Instrument Factory, Beijing) in the default atmosphere. Each raw material was weighed and taken approximately 10 mg for the experiment. The sample was placed in a circular crucible with a height of 6 mm and a diameter of 5 mm. Near the platinum basket, a thermocouple was located to monitor the temperature. According to results in the previous report [13], the temperatures for isothermal experiments were selected to be 1173 K, 1273 K, 1373 K, and 1473 K, respectively. In each experimental plan, the sample was heated at 20 K/min up to the final gasification temperature in the N_2 atmosphere. When the desired temperature was reached, N_2 was replaced by CO_2 with a flow rate of 100 ml/min. The weight loss of the sample was recorded at the final temperature until no weight loss could be observed. To ensure that the experimental results had good reproducibility, each test was repeated at least three times before a result was ascertained. The sample gasification conversion (α) (on an ash-free basis) was calculated according to the following equations:

$$\alpha = \frac{m_0 - m_t}{m_0 - m_\infty} \tag{1}$$

where m_0 denotes the initial mass of the sample; m_t is the mass of the sample at the time t; m_∞ is the final mass of the sample.

Results and Discussion

Physical and Chemical Structure Characteristics

The correlation between the gasification reactivity and raw material properties has been studied by previous investigations [14, 15]. These studies found that gasification reactivity was influenced by volatile content, content and composition of ash, micro-pore, and chemical structure. However, according to Table 1, the volatile content of each sample was very little in this study. So, it was not the main factor that affected the gasification reactivity. The main constituent of the sample was fixed carbon and ash.

Figure 1 shows the SEM photographs of different samples to analyze their morphology differences. At 10,000 times, SH and CZ present block, and CP exist in columnar form generally. By magnifying each sample up to 30,000 times, it can see the compact lamellar structures of SH and CZ inside. However, the correlation between the middle layer and the layer of SH is much closer than CZ, and there are no apparent holes. There are many pores and folds on the surface of SH and CP. The stratified arrangement of carbon would inhibit the gasification reactivity of the fuel, while the presence of pores would increase the adsorption capacity of the sample for CO_2.

The pore characteristic parameters of different samples were summarized in Table 2. For porosity factor and total pore volume, SH is the largest. For median pore diameter obtained from particle volume, CZ is larger than others. It is different from the results calculated by kinetic models. So, the micro-pore structure of samples had a little impact on the gasification rate of fuel particles. From other literatures [16, 17], the physical structure of fuel particle is not critical factor affecting gasification reactivity. The chemical structure related to fixed carbon had a crucial influence on gasification reactivities chars.

The Raman spectra of different samples are shown in Fig. 2a. Two prominent peaks appear in the wavenumber range from 900 to 1800 cm^{-1}. The peak at a shift of 1300–1400 cm^{-1} is the D band, attributed to the stretching vibration mode of amorphous carbon structures. The G band is derived from the peak at the wavenumber of 1550–1600 cm^{-1}, whose relative intensity increases with the number of the graphite C = C bonds [18]. I_D and I_G are represented by the intensities of the D and G bands, respectively. Generally, an amorphous carbon structure could improve the gasification reactivity of char.

It is known that I_{D3}/I_G is one of the most critical Raman parameters for studying the degree of carbon materials in other literature [19, 20]. The value of the Raman parameter I_{D3}/I_G increases with the improvement of the amorphousness degree. Figure 2b–d

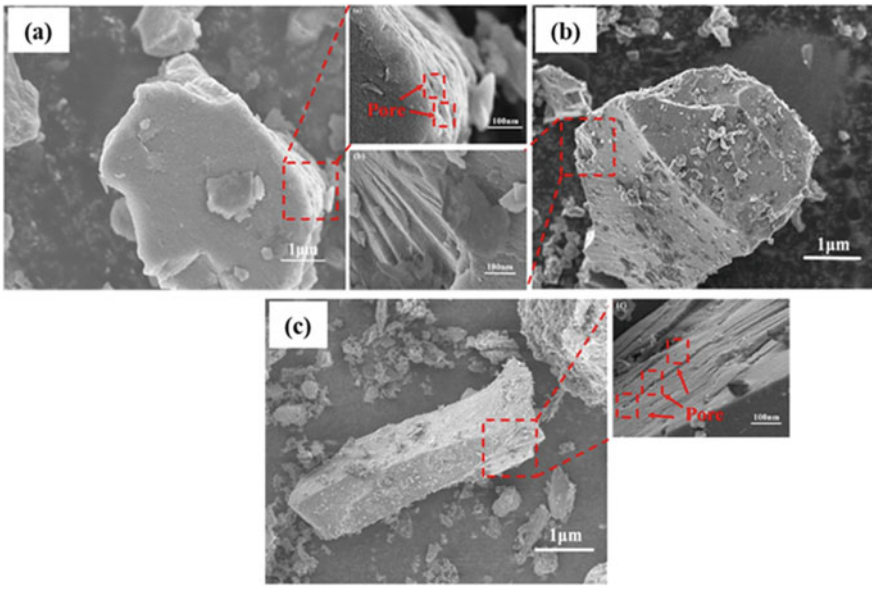

Fig. 1 SEM photographs of different fuels: **a** SH, **b** CZ, **c** CP

Table 2 Pore characteristic parameters of different samples

Sample	P_f (%)	D_v (nm)	V_t (ml/g)
SH	53.1708	1894.20	0.8001
CZ	43.4698	6841.62	0.5465
CP	47.9225	2779.26	0.5422

Notes P_f: porosity factor, D_v: median pore diameter obtained from particle volume, V_t: total pore volume

Table 3 Main components of SH, CZ, and CP ash (wt%)

Sample	CaO	MgO	SiO_2	Fe_2O_3	Al_2O_3	TiO_2	$Na_2O + K_2O$	CI	HI
SH	4.19	0.86	48.46	4.11	38.64	1.63	2.11	12.70	89.06
CZ	4.15	0.87	47.76	3.23	40.30	1.75	1.94	11.35	83.17
CP	4.47	0.89	51.08	7.79	32.41	1.75	1.60	17.32	64.49

shows the dependence of parameter I_{D3}/I_G of different samples, and it could be found that the order of I_{D3}/I_G value sequence for various chars can be ranked as CZ < SH < CP. So, the carbon structure order degree of SH and CZ was bigger than CP.

In the various matters of ash, their catalytic effect can be ranked as $K_2O > Na_2O > CaO > MgO > Fe_2O_3$. However, SiO_2, TiO_2, and Al_2O_3 will hinder the reaction [21]. To evaluate the effects of minerals in ash on fuel gasification, the catalytic index

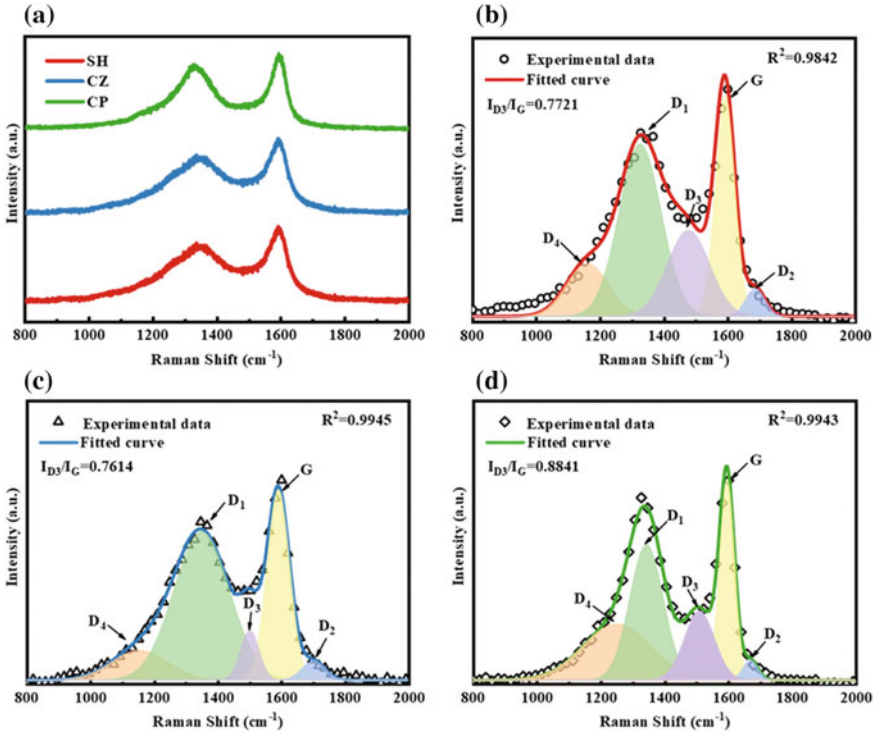

Fig. 2 Raman spectra, the I_{D3}/I_G values of different chars: **a** the Raman spectra of SH, CZ, and CP, **b** the I_{D3}/I_G values of SH, **c** the I_{D3}/I_G values of CZ, **d** the I_{D3}/I_G values of CP

(CI value) and hinder index (HI value) were proposed, which are calculated by the following equations:

$$CI = \frac{CaO + MgO + Fe_2O_3 + Na_2O + K_2O}{SiO_2 + Al_2O_3 + TiO_2} \times 100\% \quad (2)$$

$$HI = \frac{Ash}{CI} \times 100\% \quad (3)$$

As shown in Table 3, the order of the CI value for other samples can be ranked as SH < CZ < CP. The HI value sequence is the opposite of the CI value. Compared with low-rank coal and biomass, high-rank coal has low volatile and high ash content. Therefore, for high-rank coal, the composition and content of ash have a more noticeable effect on the gasification reactivity of the fuel. The CI value of CZ was the smallest, at 11.35%, and the HI value of SH was the biggest, at 89.06%. However, according to the previous study [22], it could be summarized that the carbon structure of the raw material was the main factor affecting the gasification reactivity.

Gasification Behavior of High-Rank Coal with Different Particle Sizes

Figures 3a–c are the conversion curves of SH, CZ, and CP with different particle sizes during the gasification reaction at 1473 K. From the figure that the gasification reaction rates of the three fuels increased first and then decreased with the extension of reaction time and increased with the reduction of particle size. To evaluate the reactivity of different fuels quantitatively, this study employed the reactivity index $R_{0.5}$ proposed by Takayuki et al. [23].

$$R_{0.5} = \frac{0.5}{t_{0.5}} \tag{4}$$

where $t_{0.5}$ represents the time required to reach 0.5 carbon conversion. High $R_{0.5}$ values are associated with high reactivity. The $R_{0.5}$ for each char with different particle sizes are summarized in Fig. 3d. For each char, it is evident that the $R_{0.5}$ decreased with the particle sizes, which mean that the gasification reactivity was

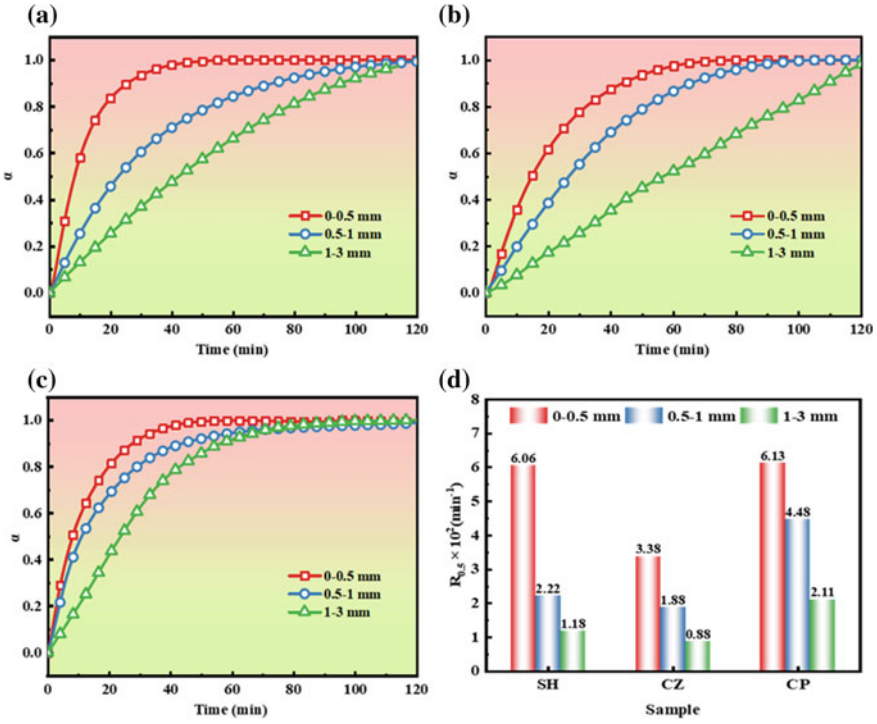

Fig. 3 Gasification reaction characteristics of high-rank coal with different particle sizes: **a** the conversion curves of SH with different particle sizes, **b** the conversion curves of CZ with different particle sizes, **c** the conversion curves of CP with different particle sizes

dramatically influenced by particle sizes. Furthermore, the $R_{0.5}$ of SH, CZ, and CP with different particle sizes of 0–3 mm were 1.18×10^{-2}–6.06×10^{-2} s^{-1}, 0.88×10^{-2}–3.38×10^{-2} s^{-1}, and 2.11×10^{-2}–6.13×10^{-2} s^{-1}, respectively. Therefore, the detailed order of gasification reactivity sequence for various samples can be ranked as CZ < SH < CP with different particle sizes.

Gasification Kinetic Analysis

Kinetic Models

Gasification of the solid fuel is a gas–solid non-catalytic heterogeneous reaction, and the rate of conversion (reactivity or reaction rate) can be expressed as follows:

$$\frac{\mathrm{d}\alpha}{\mathrm{d}t} = k(T) f(\alpha) \tag{5}$$

where t is the reaction time, $k(T)$ is the combustion reaction rate constant, and $f(\alpha)$ is a function of the differential reaction mechanism.

The relationship between apparent reaction rate and temperature can be derived from the Arrhenius equation:

$$k = Ae^{-\frac{E}{RT}} \tag{6}$$

where E is reaction activation energy, A is the pre-exponential factor, R is the universal gas constant, and T is the temperature.

A few models can be used to represent the gasification of high-rank solid fuel particles. This paper applied a gas–solid reaction kinetic model to describe the reactivity of the carbon studied: the random pore model (RPM). The RPM model considers the pore changes of surfaces. It assumes that the interface area will reduce, which is available for reaction. This model also involves the growth of pores during the initial stages of the gasification reaction and the destruction of pores owing to the coalescence of adjacent pores [24]. In this model, the term $f(\alpha)$ was given by different formulations. Their overall reaction rates are expressed by:

$$\frac{\mathrm{d}\alpha}{\mathrm{d}t} = k_{\mathrm{RPM}}(1-\alpha)\sqrt{1-\psi \ln(1-\alpha)} \tag{7}$$

The RPM presents k_{RPM} and φ, which are the apparent gasification reaction rate constant and the pore structure of the non-reacted sample. This study linearizes Eq. (7) to better test this model with the experimental results shown in Eq. (8):

$$\left(\frac{2}{\varphi}\right)\left[(1-\varphi \ln(1-\alpha))^{\frac{1}{2}} - 1\right] = k_{\mathrm{RPM}} t \tag{8}$$

According to Eq. (8), the apparent gasification reaction rate constants (k_{RPM}) were calculated using the isothermal thermogravimetric experimental data. Then, according to plugging these parameters into Eq. (6), the activation energy E and the pre-exponential factor A were calculated using the Arrhenius plot (lnk vs. $1/T$) for each sample and model.

The RPM model can be transformed into expressions for the relationship between conversion and time, as shown in Eq. (9):

$$\alpha = 1 - \exp\left(-k_{\mathrm{RPM}} t\left(1 + \frac{k_{\mathrm{RPM}} t\varphi}{4}\right)\right) \tag{9}$$

The k values were calculated by introducing the estimated E and A values into Eq. (6). A was obtained by introducing the k value into Eq. (9). The kinetic model can be tested and verified by comparing the experimental with calculated α values. The square root error (R^2) is introduced to evaluate the fitting degree of the fitted data and the actual value calculated by the kinetic model:

$$R^2 = \sqrt{\left(\alpha^i_{\mathrm{exp}} - \alpha^i_{\mathrm{cal}}\right)^2} \tag{10}$$

where α^i_{exp} and α^i_{cal} are the experimental and calculated values of the conversion rate at points i = 1, 2, 3, ….

Kinetic Parameters Analysis

In this study, the RPM model was employed to fit the experimental data to assess the validations of selected models and better analyze the reaction behaviors of the studied samples. The gasified reaction rate constants (k_{RPM}) corresponding to the RPM model could be represented by plotting $(2/\varphi)[(1 - \varphi \ln(1 - \alpha))1/2 - 1]$ as a function of time t to obtain the slopes of curves at different reaction temperatures, respectively. In the RPM model, the value of φ was obtained by optimum fitting. It was a constant under different temperatures because φ represented the original pore structure of the carbon particle in the establishment of the RPM model. The RPM model was used to obtain the experimental results from the gasification of high-rank coal at different temperatures, as shown in Fig. 4a–d. This study considered the range of conversion from 0 to 0.9. The activation energy (E) and the pre-exponential factor (A) were calculated by using the Arrhenius plot (lnk vs. $1/T$), based on employing the reaction rate constants calculated at different temperatures [25].

It can be seen from Fig. 4b that the gasified process of the sample at different temperatures was fitted well by the RPM model. The RPM model considered a great deal of column shape of pores that existed in the carbon particles, and the gasified reaction happened on the surface of the inner pores. The original high polymer was destroyed in 1173 and 1273 K, and the reactivity gradually improved. In 1373

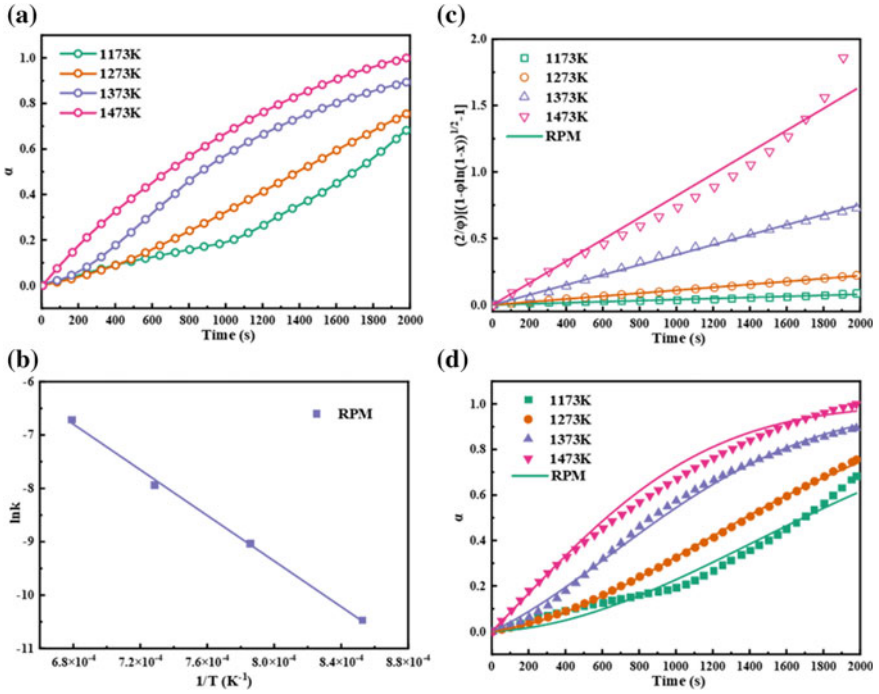

Fig. 4 Calculation process of kinetic parameters: **a** the conversion curves at different temperature, **b** the liner correlation between the experimental data and the simulated line, **c** Arrhenius plots, **d** comparison between experimental data and predicted values by RPM model

and 1473 K, with the reaction proceeding, the increases in column bore diameter and reaction phase lead to an increase in gasification rate. Then, reaction progress brought about the intersection of neighboring pores. Due to pore overlapping, the reaction surface area was reduced, decreasing the reaction rate.

Figure 4c shows the calculation result of the Arrhenius curve by using the reaction rate constants of the RPM model. This method only applies to the chemical reactions as the rate-controlling step. It can be seen in Fig. 4c that there exists a good linear relation between the lnk and $1/T$ under different reaction temperatures of the carbon gasified process, which further shows that the interface chemical reaction is the controlling step during the high-rank fuel gasified process under the different experimental temperatures.

Table 4 shows the pre-exponential factor (A), activation energy (E), and square root error (R^2) obtained by applications of RPM. It can be seen from Table 4 that activation energies of the three kinds of high-rank solid fuels with different grain sizes were distributed in the range of 129.83–198.36 kJ/mol, and the activation energies of fuel with 1–3 mm were higher than fuel with 0.5–1 and 0–0.5 mm. In addition, the pre-exponential factor varied significantly with grain size reduction. For example, the pre-exponential factors of SH decreased from 142.06 s^{-1} of 1–3 mm to 0.26 s^{-1}

Table 4 Kinetic parameters of RPM model by fitting CO_2 gasification data of samples with different grain sizes at 1473 K

Sample	Particle size (mm)	RPM			R^2
		A (s^{-1})	E (kJ/mol)	φ	
SH	1–3	142.06	192.20	0.0822	0.9984
	0.5–1	11.33	175.63	2.6179	0.9975
	0–0.5	0.26	138.17	13.6058	0.9922
CZ	1–3	129.86	198.36	3.6927	0.9987
	0.5–1	17.41	177.10	5.5373	0.9975
	0–0.5	1.70	160.33	3.0024	0.9914
CP	1–3	4.36	148.53	0.4323	0.9977
	0.5–1	1.49	138.30	0.7642	0.9941
	0–0.5	0.31	129.83	4.1000	0.9989

of 0–0.5 mm. However, the trend of changes in each sample's pre-exponential factor and activation energy was the same. By comparing the gasified activation energy parameters of SH, CZ, and CP in Table 4, the activation energies calculated by RPM can be ranked from low to high as CP < SH < CZ, which was consistent with the variation of I_{D3}/I_G and $R_{0.5}$ values.

The experimental conversion was compared with the calculated values at the different temperatures to prove the validation of each model, as shown in Fig. 4d. According to the previous results shown in Fig. 4c, the better the linear relation in calculated results, the higher the overlap ratio between the experimental and model curves in Fig. 4 will be. In this paper, the R^2 value was obtained using Eq. (10) to quantify the fitting degree of the experimental data and the calculated value. The results obtained from the RPM for all samples are summarized in Table 4. The R^2 of SH, CZ, and CP obtained using the RPM model were higher than 0.99, which means that the RPM model is an excellent kinetic model for describing the reactivity of each high-rank coal.

Conclusions

This paper systematically tested the pore structure, chemical structure, and ash components of two high-rank coals and a coke powder. These samples were gasified in a thermal analyzer with a constant flow of CO_2. It is found that the carbon structure order degree of fuel had an essential effect on the gasification reactivity. The gasification reactivity of high-rank coals was worse than that of coke powder. The activation energies of each sample derived from the random pore model lay in the range of 129.83–198.36 kJ/mol. Reducing fuel grain size can improve the gasification reactivity rates and decrease the activation energies of high-rank fuels. The random

pore model could describe the gasification reaction process of the high-rank coal well. The fitting degree of experimental data and calculated value for each sample was higher than 0.99.

Acknowledgements The authors gratefully acknowledge the financial support of the National Natural Science Foundation of China (U1960205), the China Baowu Low Carbon Metallurgy Innovation Foundation (BWLCF202101), and the Minmetals Science and Technology Special Plan (2020ZXA01).

References

1. Li Z, Jiang L, Ouyang J (2018) A kinetic study on char oxidation in mixtures of O_2, CO_2 and H_2O. Fuel Process Technol 179:250–257
2. Hao B, Zhan W (2020) Pore structure evolution during the coke graphitization process in a blast furnace. Int J Miner Metall Mater 9:1226–1233
3. Wang J, Kong L, Bai J et al (2021) Characterization of slag from anthracite gasification in moving bed slagging gasifier. Fuel 292:120390
4. Li K, Khanna R, Zhang J et al (2014) The evolution of structural order, microstructure, and mineral matter of metallurgical coke in a blast furnace: a review. Fuel 133:194–215
5. Wu S, Jing G, Xiao Z (2008) Variation of carbon crystalline structures and CO_2 gasification reactivity of shenfu coal chars at elevated temperatures. Energ Fuels 22:199–206
6. Wang G, Zhang J, Shao J et al (2016) Experimental and modeling studies on CO_2 gasification of biomass chars. Energy 114:143–154
7. Ochoa J, Cassanello MC, Bonelli PR et al (2001) CO_2 gasification of Argentinean coal chars a kinetic characterization. Fuel Process Technol 74:161–176
8. Li F, Zhu Z (2014) Understanding mineral behaviors during anthracite fluidized-bed gasification based on slag characteristics. Appl Energ 131:279–287
9. Wang Z, Pang K, Li K et al (2020) Positive catalytic effect and mechanism of iron on the gasification reactivity of coke using thermogravimetry and density functional theory. ISIJ Int 61:773–781
10. Wang W, Li H, Liu Y et al (2020) Addressing the gas emission problem of the world's largest coal producer and consumer: lessons from the Sihe Coalfield, China. Energ Rep 6:3264–3277
11. Wu Y (2019) Experimental study of the effects of stacking modes on the spontaneous combustion of coal gangue. Process Saf Environ Prot 41:391–399
12. Bao L, Qinghai P, Zhijun H et al (2021) Evaluation on explosibility of pulverized coal in air atmosphere based on functional group structure analysis. Fuel 292:120279
13. Guo W, Xue Q, Liu Y et al (2015) Kinetic analysis of gasification reaction of coke with CO_2 or H_2O. Int J Hydrogen Energ 40:13306–13313
14. Ding L, Wei J, Dai Z et al (2016) Study on rapid pyrolysis and in-situ char gasification characteristics of coal and petroleum coke. Int J Hydrogen Energ 41:16823–16834
15. Hong D, Liu L, Wang C et al (2021) Construction of a coal char model and its combustion and gasification characteristics: molecular dynamic simulations based on ReaxFF. Fuel 300:120972
16. Ad Eyemi I, Janajreh I, Arink T et al (2016) Gasification behavior of coal and woody biomass: validation and parametrical study. Appl Energ 185:1007–1018
17. Hao S, Haiping Y, Chuang Z et al (2022) Co-gasification of petroleum coke with coal at high temperature: effects of blending ratio and the catalyst. Fuel 307:121863
18. He X, Liu X, Nie B et al (2017) FTIR and Raman spectroscopy characterization of functional groups in various rank coals. Fuel 206:555–563
19. Zhao YQ, Zhang YF, Zhang HR et al (2015) Structural characterization of carbonized briquette obtained from anthracite powder. J Anal Appl Pyrol 112:7–12

20. Jy A, Qg A, Lu D et al (2020) Studying effects of solid structure evolution on gasification reactivity of coal chars by in-situ Raman spectroscopy. Fuel 270:117603
21. Ning X, Peng Z, Wang G et al (2020) Experimental study on gasification mechanism of unburned pulverized coal catalyzed by alkali metal vapor. J Energ Inst 93:679–694
22. Mallick D, Mahanta P, Moholkar V (2017) Co-gasification of coal and biomass blends: chemistry and engineering. Fuel 204:106–128. https://doi.org/10.1021/acs.energyfuels.9b03459 https://doi.org/10.2355/isijinternational.isijint-2017-447
23. Takarada T, Tamai Y, Tomita A (1985) Reactivities of 34 coals under steam gasification. Fuel 64:1438–1442
24. Wang Y, Bell D (2017) Competition between H_2O, and CO_2 during the gasification of Powder River Basin coal. Fuel 187:94–102
25. Chao C, Zhang S, Kai X et al (2015) An experimental and modeling study of char gasification with mixtures of CO_2 and H_2O. Energ Fuels 30:1628–1635

Research on Using Carbide Slag to Mineralize the Carbon Dioxide in Electrolytic Aluminum Waste Gas

Xiao Yadong, Liu Yan, Zhang Tingan, Li Xiang, Fang Yu, Li Xiaolong, and Wang Kun

Abstract This study proposes the technology of using waste carbide slag to treat carbon dioxide in the tail gas of electrolytic aluminum and innovatively designs a Venturi gas–liquid–solid three-stage reactor. The ability of $Ca(OH)_2$ slurry to absorb CO_2 under operating conditions was studied. The results show that the residual proportion of CO_2 in the waste gas is below 0.08% through the absorption of the stage reactor. The particle size of calcium carbonate obtained from the third-stage reactor can reach 5.9 um, significantly smaller than the mixing tanks and industrial products. When the gas velocity is greater than 21.231 m/s, the gas holdup and bubbles rising velocity increases rapidly, so the superficial gas velocity should not exceed 21.231 m/s. As the superficial liquid velocity increases, the bubble rising velocity and gas holdup first increase and then decrease. The superficial liquid velocity should exceed 1.504 m/s. As the inlet gas pressure increases, the bubbles rising velocity first increases and then decreases, and the gas holdup first decreases and then increases. Therefore, the gas pressure should be greater than 0.15 MPa.

Keywords Calcium carbide slag · Electrolytic aluminum flue gas · Carbonization reaction · Venturi jet reactor

Introduction

Calcium carbide slag is a difficult industrial waste to treat. Millions of tons of calcium carbide slag are piled up in China yearly, occupying a large amount of land and easily causing secondary pollution [1]. The main component of calcium carbide slag is $Ca(OH)_2$, with 71–95% content [2]. Therefore, the current recycling methods of calcium carbide slag mainly include building and roadbed materials [3], acid wastewater and waste gas treatment, and producing ordinary chemical products such as cement and calcium oxide. However, these products have low added value and poor economic benefits. Therefore, the high-value utilization of calcium carbide

X. Yadong · L. Yan (✉) · Z. Tingan · L. Xiang · F. Yu · L. Xiaolong · W. Kun
School of Metallurgy, Northeastern University, Shenyang 110819, China
e-mail: liuyan@smm.neu.edu.cn

© The Minerals, Metals & Materials Society 2024

C. Iloeje et al. (eds.), *Energy Technology 2024*, The Minerals, Metals & Materials Series, https://doi.org/10.1007/978-3-031-50244-6_25

slag has attracted much attention, and the most important application method is the production of nanocalcium carbonate [4, 5].

Researchers have conducted research on the production process of nanocalcium carbonate from carbide slag using various methods. Yang et al. [6] synthesized rod-shaped $CaCO_3$ with uniform composition through a two-step process of leaching-precipitation using carbide slag. The effects of ethylene glycol addition and reaction temperature on the structure and morphology of $CaCO_3$ products were studied. The formation mechanism of $CaCO_3$ rod bundles was explored using the Muffins-Sekerka theory. Wang et al. [7] used citrate extractants to prepare uniform calcite microspheres/nanorods from calcium carbide slag. The coordination effect of citrate anions with calcium ions can significantly improve the leaching rate of the slag. In addition, citrate solution can be reused. Yan et al. [8] generated food-grade lightweight calcium carbonate through a two-step process of NH_4Cl solution leaching and CO_2 carbonization, achieving high-value utilization of carbide slag. In addition, although many researchers have conducted research on the production of nanocalcium carbonate from carbide slag, due to the presence of various impurities in carbide slag [9], the above methods still easily cause problems such as impure and low whiteness of the synthesized calcium carbonate in the application process.

In addition, the aluminum industry is a pillar industry of the national economy and a high carbon emission industry. The CO_2 emissions from the electrolytic aluminum industry account for 4% of the total carbon emissions in China, putting pressure on the environment and climate. Currently, the chemical absorption method is the most feasible and cost-effective method for directly utilizing CO_2 [11–13]. This method first utilizes the absorption liquid to absorb and separate CO_2 and then regenerates and utilizes CO_2 through thermal desorption. At present, Chikezie et al. [14], Wilke et al. [15], and Li et al. [16, 17] have made certain progress in the research of this method, with the main focus on exploring new solvents to replace existing ethanolamine (MEA) absorbers or solving the problem of high energy consumption by optimizing the process. The above methods have achieved certain results in using CO_2, but there are still problems, such as high prices, high investment costs, and technological constraints.

Therefore, our team [17, 18] proposed a new technology to use carbide slag to generate wastewater rich in $Ca(OH)_2$ and directly capture CO_2 from electrolytic aluminum tail gas to produce nanocalcium carbonate in response to the carbide slag generated in the acetylene industry and the flue gas discharged from industrial production. This technology achieved the dual waste treatment problem of waste slag and exhaust gas and the comprehensive utilization of “waste to waste” among industries. This study will be based on a self-designed Venturi-type three-stage countercurrent gas–liquid–solid reactor and use the carbonization method to investigate the ability and effect of $Ca(OH)_2$ slurry to absorb CO_2 under operating conditions such as superficial gas liquid velocity, gas CO_2 content, and gas pressure.

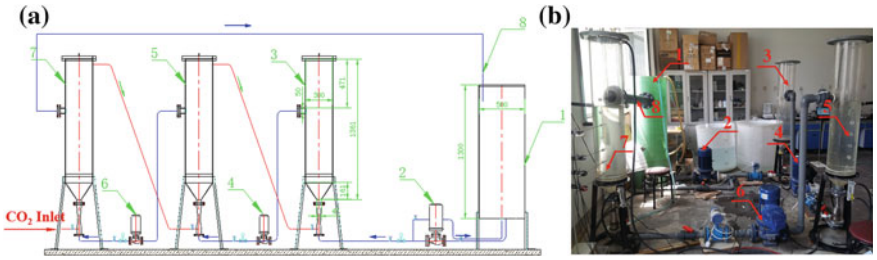

Fig. 1 Experimental setup: **a** design diagram, **b** experimental equipment

Experimental Methods

Experimental Setup

The existing single-stage Venturi jet reactors have drawbacks such as long reaction time and poor gas–liquid–solid mixing effect. Therefore, our team has improved the single-stage equipment using a three-stage countercurrent design and designed an efficient circulating Venturi-type three-stage slurry gas–liquid–solid reactor. This new reactor can improve the driving force of gas–liquid reaction, the absorption rate of CO_2, shorten reaction time, and improve economic benefits.

The experimental setup was used in the CO_2-$Ca(OH)_2$ system, which includes the main reactor, liquid circulation system, and measurement system as a whole, as shown in Fig. 1. The main reactor material is organic glass, with an inner diameter of 300 mm and an effective height of 700 mm, and is fixed by a carbon steel bracket. The inner diameter at the variable diameter of the Venturi jet is 26 mm, and the effective volume of the liquid storage tank is 244 L. During the experiment, CO_2 was sprayed into the reactor through a Venturi jet tube below the first-stage reactor, and the residual gas was discharged from the top and sucked in at the bottom of the second-stage reactor, similar to the third stage. The liquid is pumped into the bottom of the third stage from the storage tank and finally overflows back to the storage tank from the top of the first stage to complete liquid circulation. The gas and liquid velocities are controlled by gas rotary flow meters and electromagnetic flow meters, respectively.

Measurement Method

In this study, bubble characteristics such as bubble rising velocity and local gas holdup are measured by a BVW-2 multi-channel bubble parameter meter developed by the Institute of Process Engineering, Chinese Academy of Sciences. The measurement position is 500 mm from the bottom of the third-stage reactor, which is the middle

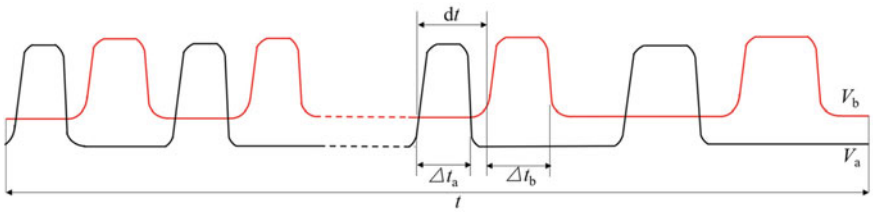

Fig. 2 Schematic of signal from the dual-tip conductivity probe

of the reactor. The measurement principle of this device is that a pair of conductivity probes arranged at a certain distance are used to measure the local conductivity changes between bubbles and water. After detection, amplification, level adjustment, and circuit conversion, a square wave signal, as shown in Fig. 2 [19], is formed and recorded by the computer. Finally, the characteristic parameters of the bubbles can be calculated.

Bubbles rising velocity is defined as the average velocity of local bubbles, calculated by Eqs. (1) and (2).

$$u_b = \frac{1}{I}\sum_{i=1}^{I} u_{b,i} \tag{1}$$

$$u_{b,i} = \frac{l}{I} \tag{2}$$

where u_b is the local bubble mean velocity, m/s; $u_{b,i}$ is the velocity of a single bubble, m/s; l is the distance between the two tips, mm; dt is the bubble lag time, s.

The local gas holdup can be calculated by Eq. (3).

$$\varepsilon = \frac{1}{t}\sum_{i=1}^{i=n_b} \Delta t_i \tag{3}$$

where ε is the local gas holdup; t is the sampling time, s; τ_{1i} is the bubble duration time, s; Δt_i is the number of bubbles counted during the sampling time.

Experimental Parameters

The CO_2 concentration at the top of the reactor is measured by the Leibo 3040 intelligent flue gas comprehensive measurement system, which can calculate the concentration of each gas based on its characteristic absorption spectrum. In this study, different proportions of CO_2 and Ar mixed gas were used to simulate electrolytic aluminum flue gas with different CO_2 contents. $Ca(OH)_2$ saturated solution

Table 1 Experimental parameters

Parameters	Values
Superficial gas velocity, u_g, m/s	10.616, 14.154, 17.693, 21.231, 24.767
Superficial liquid velocity, u_l, m/s	1.062, 1.283, 1.504, 1.725, 1.946
Gas pressure, P_g, MPa	0.1, 0.15, 0.2, 0.25

was used to simulate calcium carbide slag slurry. There conditions were studied to explore the carbonization reaction law in the new three-stage reactor, including superficial gas velocity, superficial liquid velocity, and inlet gas pressure. The experimental parameters are shown in Table 1.

Results and Discussion

Changes of CO_2 Concentration in All Stages of Reactors

The variation of residual CO_2 concentration with gas composition ratio in each stage of the reactor is shown in Fig. 3. The superficial liquid velocity is 1.725 m/s, the superficial gas velocity is 14.154 m/s, and the inlet pressure is 0.1 MPa. As the CO_2 concentration increases, the residual CO_2 concentration in the first-stage reactor gradually increases. The residual CO_2 concentration in the second- and third-stage reactors is very small. Although it slightly increases, the impact can be ignored. After absorption by the first- and second-stage reactors, the CO_2 concentration in the gas has decreased to below 0.3%. After being absorbed by the third-stage reactor, the CO_2 concentration in the residual gas has decreased to below 0.08%, indicating that the CO_2 absorption effect of this new reactor is very significant.

Bubble Characteristics in the Reactor Under Different Experimental Conditions

The gas holdup in the reactor at different superficial gas velocities is shown in Fig. 4. The superficial liquid velocity is fixed at 1.725 m/s, the inlet gas pressure is fixed at 0.1 MPa, and the gas composition is fixed at 100% CO_2. When the gas velocity changes between 10.616 and 21.231 m/s, the gas holdup in the liquid column fluctuates slightly with the increase of gas velocity and is stable at 3–4%. At this time, the CO_2 can be absorbed more completely by the $Ca(OH)_2$ solution, and the change of gas velocity has little effect on the gas holdup of the liquid column. When the superficial gas velocity is greater than 21.231 m/s, CO_2 is relatively excessive, and

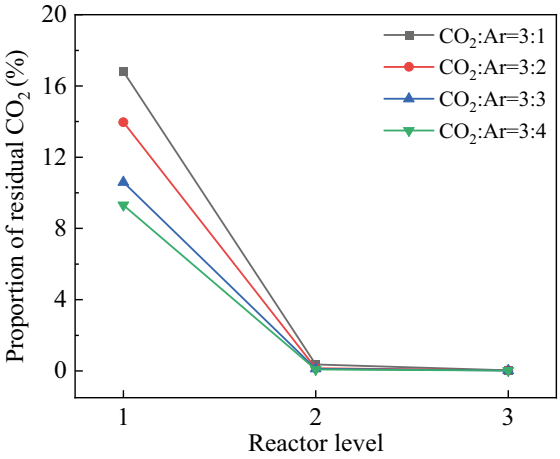

Fig. 3 Residual CO_2 concentration in each stage reactor under different gas composition ratios

the number of bubbles increases, resulting in a rapid increase in gas holdup in the liquid column.

The variation of bubble rising velocity under different superficial gas velocities is shown in Fig. 5. When the superficial gas velocity is between 10.616 and 21.231 m/s, the bubble rising velocity increases first and then decreases, with relatively small fluctuations and stable within 0.5–0.55 m/s. At this point, CO_2 can be fully absorbed by the $Ca(OH)_2$ solution, and the change of gas holdup in the liquid column is relatively small, so the upward resistance of the bubbles remains basically unchanged. When the gas velocity is greater than 21.231 m/s, the bubble rising velocity increases rapidly. At this point, CO_2 is relatively excessive, so the gas holdup in the liquid column increases, the average density decreases, and the upward resistance of the bubbles decreases, thereby increasing the bubble rising velocity. Therefore, the superficial

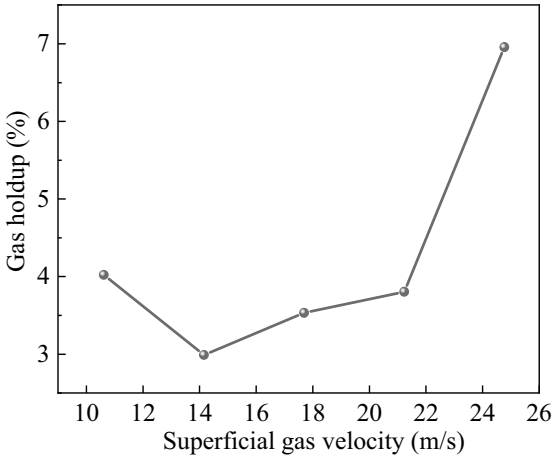

Fig. 4 Gas holdup at different superficial gas velocities

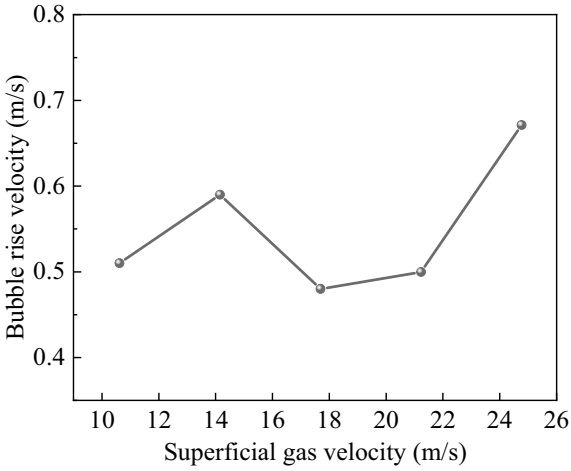

Fig. 5 Bubble rising velocity under different superficial gas velocities

gas velocity should be at most 21.231 m/s to ensure the residence time of bubbles in the reactors and improve reaction efficiency.

The variation of gas holdup in the reactor under different superficial liquid velocities is shown in Fig. 6. The superficial gas velocity is fixed at 14.154 m/s, the inlet gas pressure is fixed at 0.1 MPa, and the gas composition is fixed at 100% CO_2. The gas holdup in the reactor shows a trend of first increasing and then decreasing with the increase of superficial liquid velocity. The maximum gas holdup occurs when the superficial liquid velocity is 1.283 m/s. When the liquid velocity is less than 1.283 m/s, the gas–liquid mixing is not sufficient, and the ability of $Ca(OH)_2$ to absorb CO_2 is weak, so the gas holdup increases with liquid velocity. When the liquid velocity is high, the gas–liquid mixing effect is good, the ability of $Ca(OH)_2$ to absorb CO_2 is enhanced, and the gas holdup decreases with the increase of liquid velocity.

The variation of bubble rising velocity under different superficial liquid velocities is shown in Fig. 7. As the superficial liquid velocity increases, the rising velocity of bubbles shows a trend of first increasing and then decreasing, reaching its maximum velocity of 0.62 m/s at a liquid velocity of 1.504 m/s. When the liquid velocity is low, an increase in liquid velocity will reduce the upward resistance of the bubble and increase its rising velocity. When the liquid velocity is high, the turbulence level inside the reactor intensifies, and the resistance to bubble rise increases, so the bubble rising velocity decreases at this time. Therefore, to ensure sufficient gas–liquid mixing strength and bubble residence time in the reactor, the superficial liquid velocity should be greater than 1.504 m/s based on Figs. 6 and 7.

The variation of gas holdup in the reactor with gas inlet pressure is shown in Fig. 8. The superficial gas velocity is fixed at 14.154 m/s, the superficial liquid velocity is fixed at 1.725 m/s, and the gas composition is fixed at 100% CO_2. As the inlet gas pressure increases, the gas holdup in the reactor shows a trend of first decreasing and then increasing. The gas holdup reaches the minimum value when the inlet pressure is 0.15 MPa. As the inlet pressure increases, the average diameter of bubbles increases,

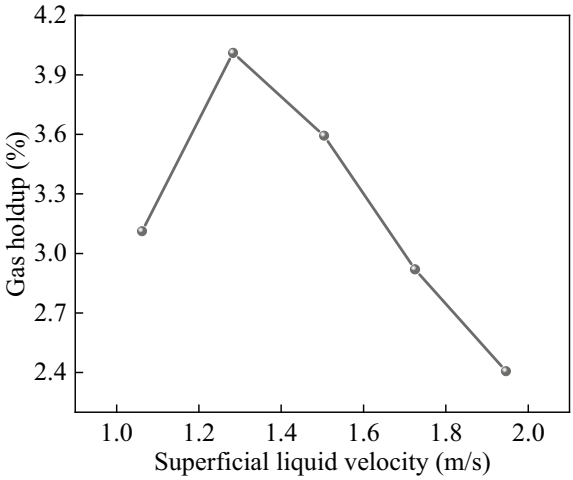

Fig. 6 Variation of gas holdup under different superficial liquid velocities

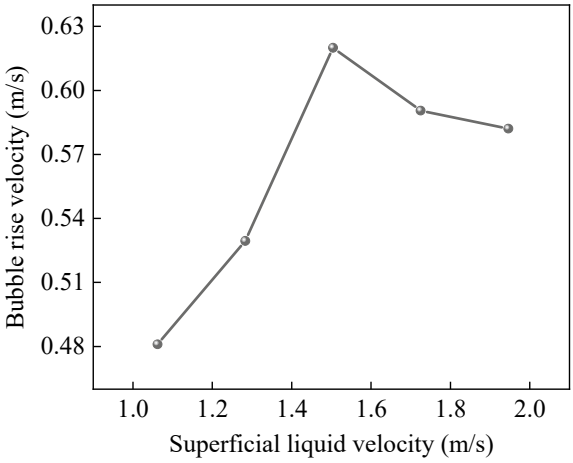

Fig. 7 Bubble rising velocity under different superficial liquid velocity

the number of large bubbles increases, and the gas holdup in the reactor decreases. When the inlet pressure is high, the liquid in the reactor is stirred more violently, the turbulence level intensifies, and the bubbles are easily broken into smaller bubbles. The residence time of the bubbles is prolonged, increasing gas holdup.

The variation of bubble rising speed under different gas pressures is shown in Fig. 9. As the inlet pressure increases, the rising speed of bubbles shows a trend of first increasing and then decreasing. When the inlet pressure is 0.15 MPa, the rising speed of bubbles reaches its maximum value. As the gas pressure increases, the diameter of the bubble increases, the buoyancy increases, and the rising speed increases. When the gas pressure is high, it will cause the liquid to stir more violently, intensify the turbulence, and gradually enhance the ability of $Ca(OH)_2$ to absorb CO_2

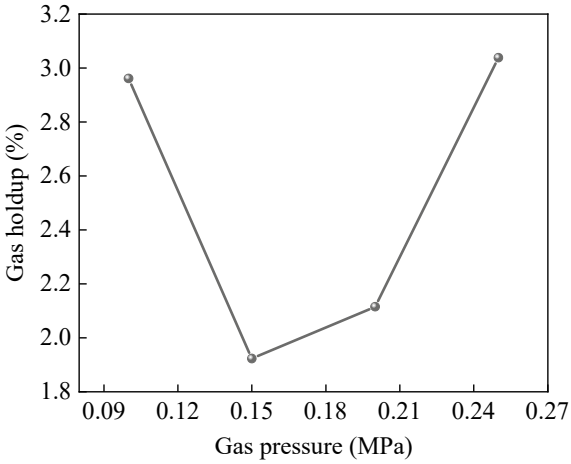

Fig. 8 Gas holdup under different gas inlet pressure

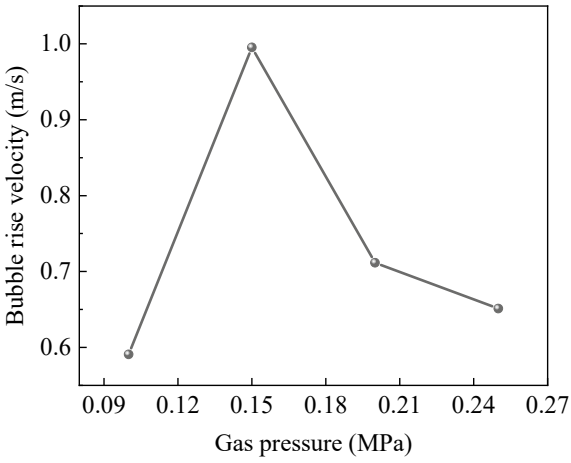

Fig. 9 Bubble rising velocity under different pressure of CO_2

while the rising speed decreases. Therefore, it is determined that the gas pressure should be greater than 0.15 MPa to ensure the gas holdup and gas–liquid mixing strength in the reactor from Figs. 8 and 9.

Particle Size Analysis of Calcium Carbonate Obtained from Different Reactors

The particle size distribution of calcium carbonate obtained from the new three-stage countercurrent reactor, mixing drum, and industrial production is compared in Fig. 10. The experimental conditions in the new three-stage countercurrent reactor are

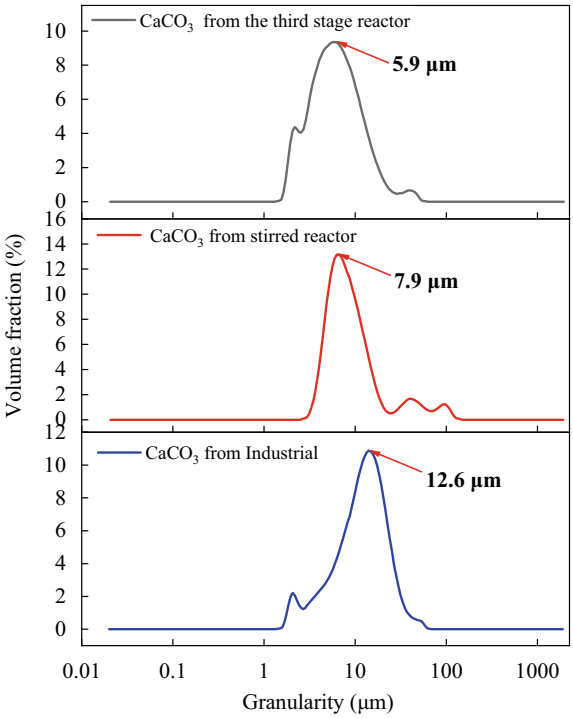

Fig. 10 Particle size distribution of calcium carbonate obtained from different reactors

the superficial liquid velocity of 1.725 m/s, the superficial gas velocity of 14.154 m/s, the inlet pressure of 0.1 MPa, and pure CO_2 gas at room temperature. The experimental conditions in the mixing drum are the superficial gas velocity of 14.154 m/s at room temperature, inlet pressure of 0.1 MPa, pure CO_2 gas, and stirring speed of 200 r/min. The industrial product source is produced by the 50 °C jet reactor of Jiangxi Xinyu Iron and Steel Group. The particle size of calcium carbonate obtained from the third-stage reactor can reach 5.9 μm, significantly smaller than the 7.9 μm obtained from the mixing drum, and 12.6 μm obtained from industrial production. The particle size distribution can demonstrate the superior performance of the new reactor.

Conclusion

This study focuses on experimental research on the carbonization reaction between CO_2 in electrolytic aluminum flue gas and carbide slag based on a self-designed new Venturi-type three-stage countercurrent reactor. The ability and effect of $Ca(OH)_2$ to absorb CO_2 under different operating conditions were investigated, and the following conclusions were obtained:

(1) CO_2 can be fully absorbed by the new Venturi gas–liquid–solid three-stage reactor, greatly improving the utilization rate of CO_2. The CO_2 concentration in the residual gas decreases to below 0.08%, with significant results.
(2) When the gas velocity is greater than 21.231 m/s, the gas holdup and bubbles rising velocity increases rapidly, so the superficial gas velocity should not exceed 21.231 m/s. As the superficial liquid velocity increases, the bubble rising velocity and local gas holdup first increase and then decrease. The superficial liquid velocity should exceed 1.504 m/s. As the inlet gas pressure increases, the bubbles rising velocity first increases and then decreases, and the local gas content first decreases and then increases. Therefore, the gas pressure should be greater than 0.15 MPa.
(3) The particle size of calcium carbonate obtained from the third-stage reactor can reach 5.9 μm, significantly smaller than the 7.9 μm obtained from the mixing drum, and 12.6 μm obtained from industrial production. The particle size distribution can demonstrate the superior performance of the new reactor.

Acknowledgements This work was supported by the special support from the China Postdoctoral Science Foundation (in station) (grant number 2023T1600880) and National Natural Science Foundation Youth Science Foundation Project (grant number 52304324).

References

1. Han F (2019) Industrial solid waste recycling in Western China. Springer
2. Zhao LW, Zhu GY, Li SP (2021) Research progress on characteristics and comprehensive utilization of calcium carbide slag. Clean Coal Technol 27(3):13–26 (in Chinese)
3. Gao X, Yao X, Yang T (2021) Calcium carbide residue as auxiliary activator for one-part sodium carbonate-activated slag cements: compressive strength, phase assemblage and environmental benefits. Constr Build Mater 308:125015
4. Guo LL, Fan XZ, Zhang WY (2017) Research progress on preparation of calcium carbonate with carbide slag. Chem Ind Eng Prog 36(1):364–371 (in Chinese)
5. Zhang C, Li Y, Bian Z (2021) Simultaneous CO_2 capture and thermochemical heat storage by modified carbide slag in coupled calcium looping and $CaO/Ca(OH)_2$ cycles. Chin J Chem Eng 36:76
6. Yang BJ, Shao ZQ, Zhang DX (2021) A mild route for the preparation of calcium carbonate rod bundles in large scale from carbide slag. Micro Nano Lett 16:187
7. Wang Y, Ye B, Hong Z (2020) Uniform calcite mircro/nanorods preparation from carbide slag using recyclable citrate extractant. J Clean Prod 253:119930
8. Yan X, Liu H, Ma Y (2019) A new and green process for producing food grade light calcium carbonate from carbide slag. Mod Chem Ind 39:199
9. Yang H, Cao JW, Wang Z (2014) Discovery of impurities existing state in carbide slag by chemical dissociation. Int J Miner Process 130:66–73
10. Kang MK, Jeon SB, Cho JH (2017) Characterization and comparison of the CO_2 absorption performance into aqueous, quasi-aqueous and non-aqueous MEA solutions. Int J Greenhouse Gas Control 63:281–288
11. Garcia M, Knuutila HK, Gu S (2017) Determination of kinetics of CO_2 absorption in unloaded and loaded DEEA+MAPA blend. Energ Procedia 114:1772–1784

12. Huser N, Schmitz O, Kenig EY (2017) A comparative study of different amine-based solvents for CO_2-capture using the rate-based approach. Chem Eng Sci 157:221–231
13. Chikezie N, Paitoon T, Abdelbaki B (2018) A comparative study of novel activated AMP using 1,5-diamino-2-methylpentane vs MEA solution for CO_2 capture from gas-fired power plant. Fuel 234:1089–1098
14. Wilkes MD, Mukherjee S, Brown S (2021) Transient CO_2 capture for open-cycle gas turbines in future energy systems. Energy 216
15. Li KK, Ashleigh C, Yu H (2016) Systematic study of aqueous monoethanolamine-based CO_2 capture process: model development and process improvement. Energ Sci Eng 4(1):23–39
16. Li KK, Philippe V, William C (2018) Mechanism investigation of advanced metal-ion-mediated amine regeneration: a novel pathway to reducing CO_2 reaction enthalpy in amine-based CO_2 capture. Environ Sci Technol 52(24):14538–14546
17. Mao SD, Liu Y, Zhang TA (2021) Nano-$CaCO_3$ synthesis by tangential jet from carbide slag. Mater Res Exp 8(9):095005
18. Mao SD, Liu Y, Zhang TA (2020) Nano-$CaCO_3$ synthesis by jet-reactor from calcium carbide slag. Mater Res Exp 7(11):115003
19. Zhu S, Zhao QY, Liu Y, Li XL (2022) Local bubble characteristics in a side-blown vortex smelting reduction reactor. Metall Mater Trans B 53(4):2303–2320

Author Index

© The Minerals, Metals & Materials Society 2024

C. Iloeje et al. (eds.), *Energy Technology 2024*, The Minerals, Metals & Materials Series, https://doi.org/10.1007/978-3-031-50244-6

Subject Index

© The Minerals, Metals & Materials Society 2024

C. Iloeje et al. (eds.), *Energy Technology 2024*, The Minerals, Metals & Materials Series, https://doi.org/10.1007/978-3-031-50244-6